Development of Methods to Study Secondary Organic Aerosol

Thesis by
Yuanlong Huang

In Partial Fulfillment of the Requirements for the
Degree of
Doctor of Philosophy

CALIFORNIA INSTITUTE OF TECHNOLOGY
Pasadena, California

2019
Defended May 14, 2019

Yuanlong Huang
ORCID: 0000-0002-6726-8904

ACKNOWLEDGEMENTS

My success at Caltech relies on help from many people.

First, I would like to thank my advisor, John Seinfeld, for his unlimited trust in me and the freedom he gave me to work on the topics that interest me. I am extremely fortunate to have John, a great scientist of atmospheric chemistry, as my advisor. I witnessed John's 50th year in Caltech and he is humble and eager to learn new things from others and responsive to his students. I am impressed by how efficiently John works. He is always there whenever I have a problem. I appreciate his patience on editing my writing. I also learned time management from him. In addition to his academic guidance, I also want to thank him for offering the annual mini-golf outing and Dodgers game. I am deeply grateful to him for his invitation to his house for Thanksgiving dinner.

I also want to thank Rick Flagan for his kind instruction on DMA theory and engineering. I enjoy talking with Rick about research ideas. I like to stop by his office, chat with him about my new ideas, and listen to his suggestions, which always surprise me. I appreciate that he spends time with me side-by-side to solve the problems I have encountered in research, no matter whether they are instrumentation or model. The Flagan Laboratory in Schlinger always looks like a big stock room of "toys", which I have a lot of fun playing with. I enjoy the time soldering and forging in Schlinger. Thanks to Rick for introducing these electrical and mechanical tools to me.

I would like to thank Paul Wennberg for serving as my committee chair. I am very impressed by how quickly he picks up my thoughts even though I describe them terribly. I still remember the time I went to ask him if he can serve as my committee member. After I said "Can I borrow you one minute", he replied "Yes, I am glad to be your committee member". I was so surprised since it looks like he can read from my mind. I like his question to me every time we casually meet in the hall "Have fun?", which always reminds me the origin of my motivation to do research. I always benefit from some random chats with him about the project I am working on. I also want to thank the Wennberg group members for teaching me CIMS, FTIR, UV-vis and GC techniques.

I thank Michael Hoffmann for being my committee member. I first met Michael in Shanghai, China and he impressed me with his diverse research background. I

am very fortunate to have the access to the Hoffmann Laboratory, where I have the chance to see ongoing research projects, like the very cool small electrical-chemical reaction chamber. Thanks to Michael for introducing the basic aqueous-phase chemistry and mass transport to me in his class. It is very generous of Michael to allow me to use the 3D printer in his lab, without which I could not construct the instrument I am building. Thanks to Michael for loaning me some of his book on chemical kinetics. I appreciate his input on aqueous-phase chemistry as well as the help from Hoffmann group members.

I want to thank Jack Beauchamp for sharing his sparkling ideas on mass spectrometry detection techniques and allowing me to get into his lab to see those fantastic techniques. I would like to thank Andy Thompson for his help as a representative advisor in ESE. I appreciate his advice on fluid dynamics after my qualifying exam. I also want to thank Prof. Shaocai Yu in Zhejiang University. During his visit in Caltech, I enjoyed discussing with Shaocai about the concept of instantaneous VOC yields and PM removal by water droplets. I thank him for generously insights his experience on CMAQ modeling. He taught me about taking actions whenever you have an idea. I want to thank my master advisor, Prof. Xin Yang in Fudan University, without whom I could not make it to Caltech. I can still turn to him for suggestions on my career plans. I really appreciate his help.

I would like to thank John Crounse for his unconditional help on instrumentation. I am impressed by John's broad knowledge on almost everything: coding and controlling theory, wiring and electrical engineering, chemical synthesis, reaction kinetics, etc. Every time I encounter a technical problem, I always have the feeling that once I turn to John for help it will be solved. And it does! During this process I learned a lot from him. I aspire to be a person like John who is trusted by all. The second person that gives me a similar feeling is Stavros Amanatidis. His knowledge on mechanical engineering is fantastic. I always feel the instruments he made are art pieces. Thanks to him for teaching me how to use the forging machines and thanks to him for spending time helping me design the instruments. I learned a lot from him!

I would like to thank Ran Zhao, not just as a mentor, but as a friend. Thanks for introducing me to the magic world of aqueous chemistry. It is a lot of fun to work and play ping-pong together. Your abilit to deal with different situations is impressive. Thanks for sharing your research and living experience with me. I'd also like to thank you (and Ini, Claire, Alina) for sharing your happiness in Canada

with me. I wish the best to you and your family!

Thanks to Matt Coggon for being my mentor. Thanks for transferring the CPOT you have built, teaching me Labview and basics of mechanical engineering. Thanks to Becky Schwantes for teaching me knowledge about CIMS as well as laboratory safety. I also want to thank Xuan Zhang, with whom I overlapped for a year. She taught me basic laboratory skills, especially GC calibration, DMA wiring and calibration, as well as chamber data processing. I thank Kelvin Bates for sharing his vision on IEPOX SOA chemistry. Though the project has many mysteries, I am sure we will make it fruitful. Thanks to Huajun Mai for teaching me DMA inversion and some electrical engineering knowledge. I am very happy to see you get a job you like. I thank Renee McVay for showing me how a chamber model is built. Thanks to Kevin Barraza for teaching me the FIDI technique. I am fortunate to be able to collaborate with you and publish my paper. I want to thank Xinxing Zhang for showing me the colorful world of physical chemistry while we ate together and the design of the acoustic levitator for droplets.

I would like to thank the current Seinfeld group members, from whom I got a lot of assistance, support, understanding, and fun. In addition to all the academic help (research ideas, background knowledge, instrumentation, scientific writing, and plotting, etc.), which I cannot list all since they happen everyday, I would like to thank them for all the fun I had outside the lab (e.g., the dodgeball and kickball games we played as a team): Chris Kenseth, thank you for introducing baseball to me; Weimeng Kong, thank you for showing me how to skateboard; Brigitte Rooney, thank you for keeping a GPS T-shirt for me; Sophia Charan, thank you for helping me rephrase my words; Elyse Pennington, thank you for hosting the white elephant party; Ben Schulze, thank you for arranging the magic castle; Reina Buenconsejo, thank you for preparing the birthday surprise. Though I cannot join you in the crossword game, I feel very fortunate to have you all in my life.

I also want to thank Yuan Wang and Lu Xu. Both of you have expanded my view from the field I focused on to another research field. Yuan taught me some basic ideas about how large-scale models are framed, and Lu taught me new technical skills and atmospheric chemistry. It is great to have both of you as lunch partners and I learned many interesting ideas about academy from you. I like how we searched for free food on campus together. I thank the Chinese-American Oceanic and Atmospheric Association Southern California Chapter (COAA-SCC), the Chinese-American Engineers and Scientists Association of Southern California (CESASC),

and the Southern California Chinese Environmental Protection Association (SC-CAEPA) for serving as excellent platforms to get to know more people not just from academy, but also from industry.

I thank all my roommates at Caltech: Max Lifson, I was very lucky to have you as my first foreign roommate from September 2014 to October 2016. I appreciate your patience on listening to my experience despite my poor oral English. Special thanks for inviting me to your wedding ceremony, I am so fascinated by the Jewish wedding. Best wishes to you and Lauren! Pengfei Sui, my second roommate from November 2016 to June 2018. It was a lot of fun to snowboard and play paintball with you. Thanks for introducing me to so many delicious restaurants. I wish the best for your professorial life at The Chinese University of Hong Kong, Shenzhen. Sang Chen, my current roommate since August 2018, thanks for taking me to grocery stores weekly before I got a car and thanks for sharing your cooking skills. I am glad to see both of us are graduating at the same time and will work as postdoc fellows in Caltech for the next year.

I thank Hao Xie for being my best man, meal partner, and playmate. It is a lot of fun to boulder, skateboard, and swim together with you. Through talking with you, I am impressed by your broad knowledge in every topic. Thanks to Siteng Fan, Xunyi Wu and Yanzhe Zhu for making me feel less lonely and younger. It is a lot of fun to eat and play with you guys. Thanks to Yang Yang and Siwen Wang (and also your cute boy Edmund) for inviting me to your house and hosting so many delicious BBQ parties. I wish the best for Professor Yang's career in Clarkson University. I want to thank Cheng Li, Qiong Zhang, Lucy Yin, Xiyue Zhang, Ho-Hsuan Wei, Wen Chen, Dandan Huang, Jinqiang Chen for being beside me and helping me when I have problems. I want to thank to Panqu Wang and Yuan Yuan for being my friends since we were undergraduates. It is great to have you in San Diego so I have an excuse to drive there for fun. Thanks to Hao Sun for driving a long way from Shanghai to attend my wedding.

I thank Christine and Dwight Landis for their unconditional support of instruments and grants to the Seinfeld Laboratory. I want to thank Martha Hepworth for helping me purchase all the materials and arranging the conferences. I thank Suresh Guptha for the assistance on computer issues. I also want to thank the L+R stuff: Nora Oshima, Kathy Young, Kathy Bravo, and Bronagh Glaser, for making L+R into a warm and big family house. I would like to thank the ISP stuff, Laura Kim and Daniel Yoder, for helping me prepare all the paper work for my status, visa and OPT

applications.

I also want to thank the Caltech Ping-pong club led by Peter Lee. I still remember how Peter and I got to know each other for the first time, which we review every time we have a party together. Thanks to Peter for hosting so many BBQ parties. I like Peter's cooking skill: the Korean style BBQ is so delicious. Thanks to Hiroyuki Hosokawa for training me in Ping-pong, which is a lot of fun. I would also like to thank Peter and Hiro for taking me to the Dodgers Stadium and the post-game dinner. I missed the Gam Ja Tang team a lot since Ran and Hiro left for their own careers. Good luck to you!

I would like to thank the GPS graduate students who began the same year as me: Elizabeth Bailey, Austin Chadwick, Sang Chen, Elle Chimiak, Alistair Hayden, Daniel Johnson, Voon Hui Lai, Ellen Leask, Jose Luis, Peter Martin, Kyle Metcalfe, John Naviaux, Leah Sabbeth, Nancy Thomas, and Chanel Valiente. Thank you for the projects we have done together, including preparing for the GPS social hour in our first year and hosting the Zilchbrau party in our second year. It was a lot of fun to work with all of you. I also like the picture we took together after all of us passed the qualifying exam. I am so proud of all of us.

I want to thank the softball leagues, the Flyball team and the Papa John's team. Though I got hit by a softball several times (and it really hurt) and we lost many games, I enjoyed when we fought together and the post-game beer on the roof of north parking structure. I also thank the Caltech Gym for providing all facilities to keep me healthy and strong. Thanks to Jin Yang for working out and running together with me. Hope the best to your postdoc life at the University of Wisconsin.

I want to thank the Caltech GPS Division for hosting the Pahoehoe travel to the Island of Hawai'i for all GPS graduating students. Through this trip I saw many gorgeous geological phenomena for the first time: the huge crater, the Pahoehoe and A'A all over the mountains and plains, the large lava tube, the ice lake that is 4000 m above sea level, etc. I was also impressed by how bio-diverse the island is: plants, birds, fruits (especially bananas), and the agriculture. Thanks to John Naviaux's instruction and protection, I learned how to snorkel and saw colorful fishes as well as a big turtle. I also got chance to know many new Hawaiians: the tree house guys - Elle Chimiak, Brooke Dallas, Michelle Dan, Cody Finke, Giuliana Viglione; the hot tub house guys - Elizabeth Eiden, Melissa Gutierrez, Lydia Kivrak, Lyn Li, Kabir Mohammed, Alyssa Poletti, Madeline Schemel; and the old volcano house guys (whom I lived with) - Elise Cutts, Voon Lai, Ellen Leask, Peter Martin,

John Naviaux, Sang Chen. Special thanks to Joe Kirschvink and Jason Saleeby for leading the team to explore the volcano. Thanks to Leticia Calderon for preparing all the paper work for flight tickets, brochures, and reimbursements. Thank you all for making this fantastic trip so exciting and fruitful, which will be my lifetime treasure. Mahalo!

It has been almost 15 years since I left my family to pursue my dream. I really missed them: my father Yu Huang, mother Feng Chen, and sister Qin Huang. I would like to thank my family for their understanding of and support to me. Lastly, I want to thank my wife, Lin Lin, for her support and love. In the past few years, we did not have many opportunities to spend time together. I missed you a lot. I love you all three thousand times. (It is quite odd that they are the most important people in my life, but I only have the fewest words to describe them.)

ABSTRACT

Secondary organic aerosol (SOA) in the atmosphere contributes significantly to air pollution and has profound impacts on regional and global climate change, as well as human health. SOA, as opposed to directly emitted particles, refers to those particles formed from oxidation of gas-phase compounds followed by nucleation and/or gas-particle partitioning, as well as those modified by gas-phase oxidants (e.g., O_3, OH radical, and NO_3 radical) through heterogeneous reactions within their lifetime in the atmosphere. Investigations of SOA formation in the laboratory have been carried out in batch reactors (e.g., environmental smog chambers) and continuous flow reactors (e.g., oxidation flow reactors). Compared with the real atmosphere, the reactors in the laboratory have boundaries and defined residence times under different operation conditions. To better constrain the experimental results and derive reliable parameters for aerosol models (e.g., yields of volatile organic compounds), a full understanding of the role of the reactors on the gas-phase components and suspended particles is needed.

In this thesis research, a number of studies were carried out to understand the role of the reactor itself on the behavior of SOA-forming systems. This includes the effect of the Teflon-walled Caltech Environmental Chamber on vapor molecules and characterization of the newly-built Caltech PhotoOxidation Flow Tube reactor (CPOT) for atmospheric chemistry studies.

Vapor-wall interactions in Teflon-walled environmental chambers have been studied; however, conflicting results existed in the literature concerning the basic timescales of vapor-wall loss in environmental chambers. The competition between vapor-particle and vapor-wall interactions determines the fate of vapor molecules in the reactor. A unified theory and empirical equations have been developed in this thesis to explain the observed vapor-wall interaction timescales. About 100 compounds have been studied to verify this theory. In characterizing the flow reactor performance, computational fluid dynamics (CFD) simulations have been combined with residence time distribution (RTD) experiments, revealing, among others, the importance of the inlet design of the reactor and the effect of temperature gradients on radial mixing in the reactor. An axial-dispersed plug flow reactor (AD-PFR) model framework was developed as a basis on which to simulate photochemistry occurring in the CPOT. An analytical solution for the cumulative RTD, which uses data during the transition period to steady state, can be applied to diagnose the

dispersion condition inside the flow rector.

Since SOA formation involves interactions among gas-phase molecules, particle surfaces and particle bulk phases, a state-of-the-art experimental technique (field-induced droplet ionization mass spectrometry, FIDI-MS) and a comprehensive model coupling gas-surface-aqueous multiphase transport and chemical reactions have been applied to investigate the gas-phase OH initiated oxidation of pinonic acid (PA) at the air-water interface. The interfacial oxidation mechanism has been found to differ from that of homogeneous reactions, and the kinetics depend on both OH diffusion from gas-phase to the interface and aqueous-phase reaction of pinonic acid + OH. The model calculation shows that, under typical ambient OH levels, PA is oxidized exclusively at the air-water interface of droplets with a diameter of 5 μm, demonstrating the critical importance of air-water interfacial chemistry in determining the fate of surface-active species.

PUBLISHED CONTENT AND CONTRIBUTIONS

Huang, Yuanlong and John H. Seinfeld (2019). "A note on flow behavior in axially-dispersed plug flow reactors with step input of tracer". In: *Atmos. Environ.: X* 1, p. 100006. DOI: 10.1016/j.aeaoa.2019.100006.
Y. H. performed experiments, derived solution, analyzed data, and wrote the paper for this project.

Huang, Yuanlong, Kevin M. Barraza, Christopher M. Kenseth, Ran Zhao, Chen Wang, J. L. Beauchamp, and John H. Seinfeld (2018a). "Probing the OH Oxidation of Pinonic Acid at the Air–Water Interface Using Field-Induced Droplet Ionization Mass Spectrometry (FIDI-MS)". In: *J. Phys. Chem. A* 122.31, pp. 6445–6456. DOI: 10.1021/acs.jpca.8b05353.
Y. H. developed model, analyzed data, ran simulation, and wrote the paper for this project.

Huang, Yuanlong, Ran Zhao, Sophia M. Charan, Christopher M. Kenseth, Xuan Zhang, and John H. Seinfeld (2018b). "Unified Theory of Vapor–Wall Mass Transport in Teflon-Walled Environmental Chambers". In: *Environ. Sci. Technol.* 52.4, pp. 2134–2142. DOI: 10.1021/acs.est.7b05575.
Y. H. developed model, conducted experiments, analyzed data, and wrote the paper for this project.

Kenseth, Christopher M., Yuanlong Huang, Ran Zhao, Nathan F. Dalleska, J. Caleb Hethcox, Brian M. Stoltz, and John H. Seinfeld (2018). "Synergistic O_3 + OH oxidation pathway to extremely low-volatility dimers revealed in β-pinene secondary organic aerosol". In: *Proc. Natl. Acad. Sci. U.S.A.* 115.33, pp. 8301–8306. DOI: 10.1073/pnas.1804671115.
Y. H. assisted in filter sample collection and ran MCM simulation.

Zhang, Xuan, John Ortega, Yuanlong Huang, Stephen Shertz, Geoffrey S. Tyndall, and John J. Orlando (2018). "A steady-state continuous flow chamber for the study of daytime and nighttime chemistry under atmospherically relevant NO levels". In: *Atmos. Meas. Tech.* 11.5, pp. 2537–2551. DOI: 10.5194/amt-11-2537-2018.
Y. H. wrote CSTR model to run MCM for this project.

Zhao, Ran, Christopher M. Kenseth, Yuanlong Huang, Nathan F. Dalleska, Xiaobi M. Kuang, Jierou Chen, Suzanne E. Paulson, and John H. Seinfeld (2018a). "Rapid Aqueous-Phase Hydrolysis of Ester Hydroperoxides Arising from Criegee Intermediates and Organic Acids". In: *J. Phys. Chem. A* 122.23, pp. 5190–5201. DOI: 10.1021/acs.jpca.8b02195.
Y. H. assisted in filter sample collection and did UV-Vis measurement.

Zhao, Ran, Christopher M. Kenseth, Yuanlong Huang, Nathan F. Dalleska, and John H. Seinfeld (2018b). "Iodometry-Assisted Liquid Chromatography Electrospray Ionization Mass Spectrometry for Analysis of Organic Peroxides: An Application to Atmospheric Secondary Organic Aerosol". In: *Environ. Sci. Technol.* 52.4,

pp. 2108–2117. DOI: 10.1021/acs.est.7b04863.
Y. H. assisted in filter sample collection and did UV-Vis measurement.

Huang, Yuanlong, Matthew M. Coggon, Ran Zhao, Hanna Lignell, Michael U. Bauer, Richard C. Flagan, and John H. Seinfeld (2017). "The Caltech Photooxidation Flow Tube reactor: design, fluid dynamics and characterization". In: *Atmos. Meas. Tech.* 10.3, pp. 839–867. DOI: 10.5194/amt-10-839-2017.
Y. H. performed CFD simulation, conducted experiments, developed model, analyzed data, and wrote the paper for this project.

TABLE OF CONTENTS

LIST OF ILLUSTRATIONS

Number *Page*

LIST OF TABLES

Chapter 1

INTRODUCTION

1.1 Background and Motivation

Particulate matter (PM) suspended in the atmosphere can scatter/absorb solar radiation, act as cloud condensation nuclei, impacting the climate directly or indirectly (IPCC, 2013). $PM_{2.5}$ refers to particles with a diameter smaller than 2.5 μm, which can profoundly damage human health since they can penetrate into deep stages of the lung (EPA, 2016). During PM lifetime in the atmosphere, particles interact with each other as well as the gas molecules/radicals surrounding them. Thus the properties (e.g., chemical composition, size, and phase state etc.) of these suspended particles are always changing.

The term aerosol is used to describe a relatively stable system of solid or liquid fine particles surrounded by gas molecules. Secondary organic aerosols (SOA) refer to those sub-micrometer particles containing a large mass fraction of organic compounds (Jimenez et al., 2009) that are formed through gas-particle partitioning or modified by multi-phase oxidation, compared with those from direct emission (primary organic aerosols, POA). The physicochemical properties of SOA in the atmosphere are complex, constantly changing, and have profound effects on climate and human health (Pope III et al., 2002). The formation and evolution of SOAs depend on gas-phase oxidants and volatile organic compounds (VOCs), and the particle-phase compositions and viscosities (George and Abbatt, 2010). We are interested in learning how these properties evolve so we can predict and evaluate their effect on air pollution and regional/global climate by models. Aside from direct field observations of SOAs, extensive laboratory studies have focused on the formation of SOA and parameterizing the key processes that can be used in chemical transport models.

The laboratory studies of SOA formation are usually carried out in atmospheric reactors, which, depending on the research purpose can be divided into batch mode and continuous mode. The batch-mode atmospheric reactor is best known as the environmental smog chamber, which is usually made of chemically inert materials (e.g., Teflon film), but without rigid boundaries so the pressures inside and outside the reactor remain the same. The continuous-mode atmospheric reactors usually

have rigid boundaries, so as the sampling goes on, some gas flux has to be added to keep the pressure inside the reactor constant. Based on the fluid dynamics, ideally, the continuous-mode reactor can be divided into continuously stirred tank reactor (CSTR) and plug flow reactor (PFR). For a batch-mode reactor, the reactants and products evolve with time, which is most similar to the real atmosphere where the components of an air parcel change over time; while a continuous-mode reactor usually runs at a steady state so one can examine closely the mechanisms under a specific condition. The other important aspect for these two modes is the effect of walls. The walls of a reactor can bias the quantitative results from a batch-mode reactor if one does not account for them since the boundaries keep interacting with both vapors and particles inside the reactor. In contrast, for continuous-mode reactors, wall effects are less critical since the system is at a steady state. However, there are also some special reactors that do not belong to either type. For example, the Cosmics Leaving Outdoor Droplets reactor (CLOUD, 2019) has rigid boundaries (stainless steel) and is running at a continuous mode but since the residence time is long relative to the reaction time, the system can be treated as a batch-mode reactor.

The Caltech Atmospheric Chemistry Laboratory has a dual environmental smog chamber (batch mode), which has made great contributions to the community by providing one of the important parameters for SOA formation to regional and global transport models, i.e., the yields of various precursor VOCs. To get a reliable value of VOC yield, one has to account for wall effects carefully. In this thesis, efforts have been taken to parameterize the wall effect on gas-phase vapors in a batch-mode Teflon-walled reactor. In addition, this thesis considers the continuous flow reactor, which is a complementary reactor to the chamber reactor. Besides characterizing the reactors by experiments, this thesis emphasizes developing models so one can either make predictions to compare with the data or retrieve key parameters from the data.

1.2 Organization of Thesis

In Chapter 2, we present the design and characterization of the Caltech PhotoOxidation flow Tube reactor (CPOT). We show how computational fluid dynamics (CFD) simulation can help design the inlet of a flow reactor. By comparing the residence time distributions (RTD) determined by the CFD simulation with those measured by experiments, we learn that temperature inhomogeneity can cause recirculation inside the flow reactor. We propose an axial-dispersed plug flow reactor (AD-PFR) to simplify the 3D flow reactor into a 1D model framework by parameterizing the inevitable turbulence as an eddy diffusivity. We also measure the particle transmission efficiency as a function of particle size under dry conditions. The CPOT is designed to run experiments at steady state under specific conditions that can perform a much higher exposure (reagent concentration $\times$ residence time) than a chamber reactor. We further propose a correction factor to calculate the exposure under the AD-PFR framework.

In Chapter 3, based on the studies in Chapter 2, we propose a new method to retrieve the eddy diffusivity inside a flow reactor. Instead of measuring the RTDs by pulse injection of species, one can take advantage of the data during the transition time, i.e., the data from the beginning of the experiment before the system reach steady state. We derive an analytical expression for this accumulative RTD and verified that the eddy diffusivity derived from this method is ~50% higher than that derived from pulse RTDs. We suggest using accumulative RTD to determine the eddy diffusivity, since it can better reflect the working condition of the flow reactor.

In Chapter 4, we present a study quantifying chamber wall effect on vapors. Compared with the real atmosphere, all the experiments in the lab must address such wall interactions because the air parcel is not as free as those ambient ones. The interaction between vapor molecules and the Teflon-walled environmental chamber can be described as a multi-step dissolving process. In this chapter, we propose a unified model to describe two significantly different dissolving timescales. In this model, the vapor-wall interaction is described as kinetically dissolving in a thin surface layer and then diffusing into the deep layer. Over 100 compounds have been used to develop and test this model. By parameterizing the vapor-wall accommodation coefficient and the activity coefficient, this model can be easily incorporated into the chamber models.

In Chapter 5, a multi-phase transport and reaction model is developed to derive the reaction rate constant between pinonic acid and hydroxyl radical at the air-

water interface. In this chapter, we build a model that can be used to simulate multi-phase (gas-interface-aqueous phases) mass transport and reaction with the experimental technique called field induced droplet ionization mass spectrometry (FIDI-MS) that focuses on in-situ air-water interfacial reaction and detection. The model framework follows the PRA definition (Pöschl et al., 2007). By introducing the interfacial reaction into the traditional gas-aqueous phase reaction model, we demonstrate that the air-water interfacial multi-phase reactions could be an important sink for surface-active and OH-reactive organic species in the atmosphere through multi-phase reactions.

Chapter 2

THE CALTECH PHOTOOXIDATION FLOW TUBE REACTOR - DESIGN, FLUID DYNAMICS AND CHARACTERIZATION

Huang, Yuanlong, Matthew M. Coggon, Ran Zhao, Hanna Lignell, Michael U. Bauer, Richard C. Flagan, and John H. Seinfeld (2017). "The Caltech Photooxidation Flow Tube reactor: design, fluid dynamics and characterization". In: *Atmos. Meas. Tech.* 10.3, pp. 839–867. DOI: 10.5194/amt-10-839-2017.

Abstract

Flow tube reactors are widely employed to study gas-phase atmospheric chemistry and secondary organic aerosol formation. The development of a new laminar-flow tube reactor, the Caltech PhotoOxidation flow Tube (CPOT), intended for the study of gas-phase atmospheric chemistry and secondary organic aerosol (SOA) formation, is reported here. The present work addresses the reactor design based on fluid dynamical characterization and the fundamental behavior of vapor molecules and particles in the reactor. The design of the inlet to the reactor, based on computational fluid dynamics (CFD) simulations, comprises a static mixer and a conical diffuser to facilitate development of a characteristic laminar flow profile. To assess the extent to which the actual performance adheres to the theoretical CFD model, residence time distribution (RTD) experiments are reported with vapor molecules (O_3) and submicrometer ammonium sulfate particles. As confirmed by the CFD prediction, the presence of a slight deviation from strictly isothermal conditions leads to secondary flows in the reactor that produce deviations from the ideal parabolic laminar flow. The characterization experiments, in conjunction with theory, provide a basis for interpretation of atmospheric chemistry and secondary organic aerosol studies to follow. A 1D photochemical model within an axially dispersed plug flow reactor (AD-PFR) framework is formulated to evaluate the oxidation level in the reactor. The simulation indicates that the OH concentration is uniform along the reactor, and an OH exposure (OH_{exp}) ranging from $\sim 10^9$ to $\sim 10^{12}$ molecules cm^{-3} s can be achieved from photolysis of H_2O_2. A method to calculate OH_{exp} with a consideration for the axial dispersion in the present photochemical system is developed.

2.1 Introduction

Experimental evaluation of atmospheric chemistry and aerosol formation is typically carried out in laboratory reactors. Such reactors comprise both chambers and flow reactors. The flow tube reactor has emerged as a widely-used platform (Bruns et al., 2015; Chen et al., 2013; Ezell et al., 2010; Kang et al., 2007, 2011; Karjalainen et al., 2016; Keller and Burtscher, 2012; Khalizov et al., 2006; Lambe et al., 2011a, 2015, 2011b, 2012; R. Li et al., 2015; Ortega et al., 2013, 2016; Palm et al., 2016; Peng et al., 2016, 2015; Simonen et al., 2017; Tkacik et al., 2014).

The flow tube reactor is generally operated under steady-state conditions. An attribute of the flow tube reactor is that, by control of the inlet concentration and oxidation conditions, it is possible to simulate atmospheric oxidation under conditions equivalent to multiple days of atmospheric exposure with a reactor residence time over a range of minutes. It should be noted that the chemistry occurring in such a highly oxidizing environment may differ from that in the atmosphere and batch chamber, even though no discrepancy between the components of the SOA generated in the flow tube reactor and the batch chamber has yet to be reported (Lambe et al., 2015). Moreover, under the steady state operating conditions, it is possible to accumulate sufficient products for detailed analytical evaluation. Key factors relevant to atmospheric processes, such as gas-phase kinetics (Donahue et al., 1996; Howard, 1979; Thornton and Abbatt, 2005), nucleation rates (Mikheev et al., 2000), uptake coefficients of vapors on particles (Matthews et al., 2014), and heterogeneous reactions on particle surfaces (George et al., 2007), can be evaluated via flow tube studies.

Since the concept of Potential Aerosol Mass (PAM) was proposed, the PAM reactor, operated as a flow tube reactor, has been widely used in laboratory and field studies of SOA formation (Chen et al., 2013; Kang et al., 2007, 2011; Keller and Burtscher, 2012; Kroll et al., 2009; Lambe et al., 2011a, 2015, 2012; Ortega et al., 2013, 2016; Palm et al., 2016; Slowik et al., 2012; Smith et al., 2009). A powerful attribute of the PAM and subsequent flow reactors is the capability to generate hydroxyl radical (OH) levels that lead to integrated OH exposure ranging as high as $\sim 10^{12}$ molecules cm^{-3} s, at which it is possible to simulate atmospheric oxidation conditions comparable to those occurring over $\sim$ 1 week. Chemical kinetic modeling studies have investigated the free radical chemistry in the oxidation flow reactor (OFR) (e.g., R. Li et al., 2015; Peng et al., 2016, 2015).

Flow tube designs vary in dimension, detailed construction, and strategy for gener-

ating the oxidizing environment. Each specific design aspect of a flow reactor can significantly affect both the fluid dynamics and the chemistry within the reactor. For example, the design of the inlet to the reactor determines the extent of initial mixing of the reactants as well as the development of concentration profiles in the reactor. The classical flow tube for gas-phase kinetic measurements employs a movable inlet in the axial position surrounded by a carrier gas to achieve the flexibility in varying reaction time (Howard, 1979). The wavelength-dependent radiation source determines the choice of oxidants that initiate free radical chemistry. In the atmosphere, the ubiquitous oxidant OH is generated largely by the reaction of H_2O with $O(^1D)$, which is produced by the photolysis of O_3 at wavelengths < 320 nm. In the flow reactor, a variety of OH generation strategies exist. One option is to use blacklights that center around 350 nm to gently photolyze OH precursors such as H_2O_2, HONO, and CH_3ONO. The material of the flow tube determines the placement of radiation sources. For example, the PAM reactor described by Kang et al. (2007) is constructed of Teflon, which is transparent to UV radiation; consequently, the UV lamps that drive the photochemistry can be positioned outside the reactor itself. By contrast, another class of flow reactors is constructed of aluminum, for which the UV lamps must be positioned inside the reactor itself (Ezell et al., 2010; R. Li et al., 2015). Characterization of the behavior of the flow tube reactor requires, ideally, a combination of flow and residence time modeling and experiment, chemical kinetic modeling and experiment, and modeling and experimental measurement of interactions of vapor molecules and particles with reactor walls.

We present here the development and characterization of the Caltech Photooxidation flow Tube reactor (CPOT). The CPOT has been constructed as a complement to the Caltech 24 m^3 batch chambers (Bates et al., 2014, 2016; Hodas et al., 2015; C. L. Loza et al., 2013, 2014; R. C. McVay et al., 2014; Renee C. McVay et al., 2016; Nguyen et al., 2015, 2014; Schilling Fahnestock et al., 2015; Rebecca H. Schwantes et al., 2015; Yee et al., 2013; Xuan Zhang et al., 2014, 2015) in carrying out studies of SOA formation resulting from the oxidation of volatile organic compounds (VOCs) by oxidants OH, O_3, and NO_3 over timescales not accessible in a batch chamber. Due to its steady-state operation, the CPOT also affords the capability to collect sufficient quantities of SOA generated in the reactor for comprehensive composition determination by off-line mass spectrometry.

While the reactor itself is not unlike a number of those already developed and cited above, we endeavor here to describe in some detail the theoretical/experimental

characterization of the reactor. Using computational fluid dynamics (CFD) simulations, we describe the design and characterization of the CPOT. We highlight fundamental consideration of the design of a laminar flow tube reactor, including methods of injection of gases and particles, the behavior of vapor molecules and particles in the reactor, and effects of non-isothermal conditions on the flow in the reactor. We evaluate the extent to which the fluid dynamics modeling agrees with experimental residence time distribution (RTD) measurements.

Experimental measurements of SOA formation in laboratory Teflon chambers are influenced by deposition of both particles and vapors to the chamber walls, and evaluation of the SOA yield from VOC oxidation must take careful accounting for such wall losses (e.g., Nah et al., 2017, 2016; Xuan Zhang et al., 2014). We seek to assess the extent to which both vapor and particle deposition onto the entrance region and quartz wall of the flow tube is influential in flow tube reactor studies. While experimental measurements of these processes will be presented in future studies, the transport modeling presented here provides a basis for evaluating the effect of reactor surfaces on experimental measurements of atmospheric chemistry and SOA formation.

A photochemical kinetic model is formulated to simulate OH production in the reactor. Typically, at steady state, the flow tube reactor gives only one data point under a specific condition. Such a model is essential in evaluating oxidation data in the reactor since the model predicts how the reactants evolve along the reactor. Generally, the ideal plug flow reactor (PFR) framework is used in the modeling of a flow tube system (R. Li et al., 2015; Peng et al., 2016, 2015). For a non-ideal flow reactor, the axially-dispersed plug flow reactor (AD-PFR) framework couples the RTD with the chemical reaction system. The axial dispersion plays the role of backward and forward mixing of the reactants, smoothing the concentration gradients. By the comparison between AD-PFR and PFR models, we will show how the non-ideal flow reactor impacts the data interpretation and suggest a method for correction.

2.2 Design and Experimental Setup

2.2.1 CPOT Reactor

The CPOT comprises three sections: the inlet section, the main reaction section, and the outlet section (Fig. 2.1A). The inlet consists of two components: the static mixer and the conical diffuser (Fig. 2.1B). The static mixer is designed to thoroughly

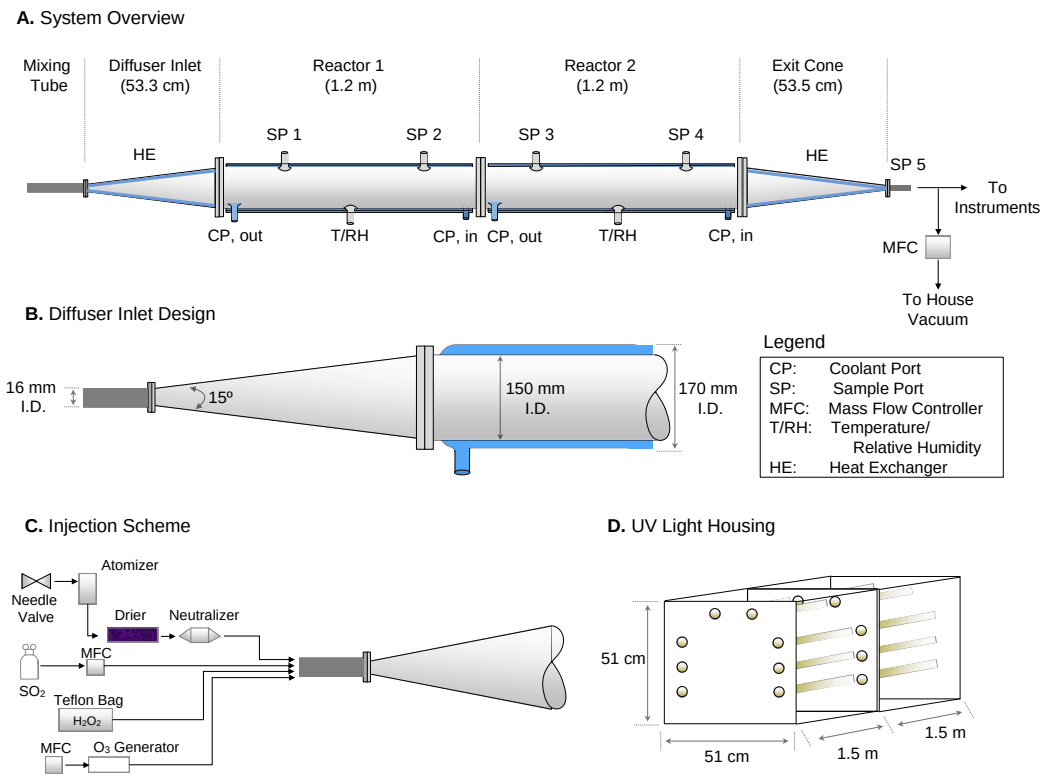

Figure 2.1: Overall schematic of the Caltech PhotoOxidation flow Tube (CPOT). (A) The inlet design. (B) The injection scheme. (C) Schematic for the housing chamber. (D) UV lamps.

mix reactant streams, whereas the diffuser serves to expand the mixed flow to the diameter of the reaction section while maintaining an idealized laminar flow profile. The static mixer is constructed of stainless steel and consists of 12 helical elements (StaticMixCo, NY). The Pyrex glass diffuser section expands from an inner diameter of 1.6 cm to 15 cm at an angle of 15°. The diffuser angle was chosen based on CFD simulations in order to minimize flow separation and recirculation. Detailed design of the inlet section is discussed in Section 2.3.

The CPOT reaction section consists of two 1.2 m × 17 cm ID cylindrical quartz tubes surrounded by an external water jacket (1 cm thickness) and flanged together with clamps and chemically resistant o-rings. Four ports along the reactor axis allow sampling of the reactor contents at different residence times. A transition cone at the end of the reactor concentrates the reactants into a common sampling line that can be split among multiple instruments; thus, samples extracted at the end of the reactor represent the so-called cup-mixed average of the entire reactor cross section. This design is similar to the exit cone of the UC Irvine flow tube reactor (Ezell et al.,

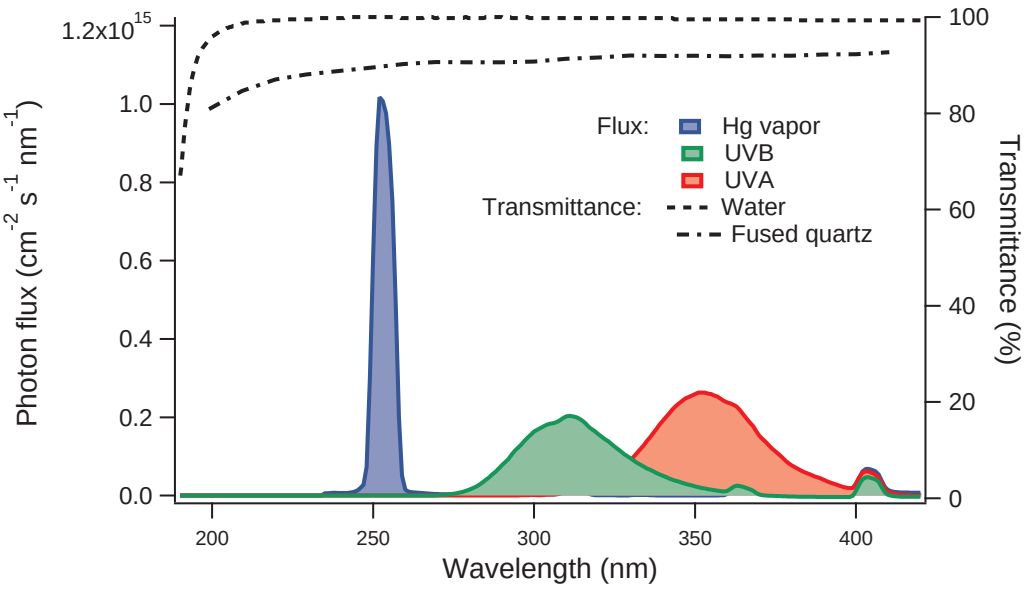

Figure 2.2: Photon fluxes inside the reactor, as well as the transmittance of water and fused quartz (Beder et al., 1971).

2010). The Pyrex glass exit cone gradually reduces the diameter of the reactor from 15 cm to 0.72 cm at an angle of 15°. Similar to the inlet diffuser, the exit cone is temperature-controlled (Section 2.2.3).

The CPOT is designed to operate under laminar flow. The essential dimensionless group that differentiates laminar vs. turbulent flow is the Reynolds number, Re $= \frac{\rho U D}{\mu}$, where ρ is the fluid density, U is a characteristic velocity of the fluid, μ is the fluid viscosity, and D is the tube diameter. For cylindrical tubes, the flow is considered laminar when Re < 2100. Under the typical CPOT flow rate (2 L min^{-1}), the Reynolds numbers at the inlet cone, in the cylindrical section, and at the exit cone are 150, 20, and 450, respectively, well below the transition to turbulent flow.

2.2.2 Photolytic Environment

The reactor is housed within a 51 × 51 × 300 cm chamber containing 16 wall-mounted UV lamps. The arrangement of the lamps is outlined in Fig. 2.1D. Light intensity is adjustable (0, 25%, 50%, 75%, and 100%), and the UV spectrum can be set to a specific wavelength range with the installation of various T12 UV lamps, including Hg vapor lamps (emit narrow bands at 254 nm and 185 nm), UVB lamps (polychromatic irradiation centered at 305 nm) and UVA lamps (polychromatic irradiation centered at 350 nm), based on the experimental goals.

Quantification of light fluxes for each type of lamp is the prerequisite for performing photochemical experiments. A challenge associated with quantifying photon fluxes is that the flux emitted by the lamps is not necessarily that perceived by a molecule inside the reactor. Attenuation of photon fluxes can potentially arise from: 1) attenuation by the quartz wall and the water jacket surrounding the experimental sections; 2) reflection and/or refraction of light inside the chamber; and 3) absorption of light by gas-phase molecules (e.g. absorption of the 185 nm band by O_2 molecules). To overcome this challenge, we employ a method combining direct measurements and gas-phase chemical actinometry, where the directly recorded emission spectra are adjusted to the the observed photolysis rate of NO_2 (j_{NO_2}). The advantage of this method is that the actual output spectra of the lamps are used, since the quantification of fluxes is based on what the molecules perceive inside the reactor. The water coolant in the jacket surrounding the tube is transparent at the UV wavelengths of interest, with the exception that it absorbs at the 185 nm band emitted by the Hg vapor lamps. Although the general UV cutoff of water is at 190 nm, we observed formation of 60 ppb of O_3 with a 2 L min^{-1} flow rate under the full power of the Hg vapor lamp. The radiation intensity at 185 nm that penetrates into the reaction section is calculated to be about 10^{-5} of that at 254 nm. The photon fluxes in the CPOT from the three types of lamps are shown in Fig. 2.2 with a detailed description of the determination of photon fluxes provided in Section 2.8.1.

2.2.3 Temperature Control in the Reaction Section

At full photolytic intensity, the lamps generate as much as 550 W of heat. To maintain a constant temperature and minimize convective mixing in the tube due to temperature inhomogeneity, each of the two reaction sections is fitted with a quartz-cooling jacket, in which chilled water is circulated at a rate of 13 L min^{-1}. Coolant is introduced into the jacket near the exit cone and exits at the inlet (Fig. 2.1A). Under typical operation, the cooling jacket can maintain the steady-state reactor temperature at a desired value between 20 and 38°C. Under full photolytic intensity of the UVA lamps, which produce the most heating among the three types of lamps, the temperature rise of air in the reactor is $\leq$ 0.3 K at steady state. Reactor temperature control is further addressed in Section 2.3.3.

2.2.4 Experimental Testing

Particles and vapor species are used to experimentally characterize the fluid dynamics inside the reactor. The injection scheme is illustrated in Fig. 2.1C. Polydisperse

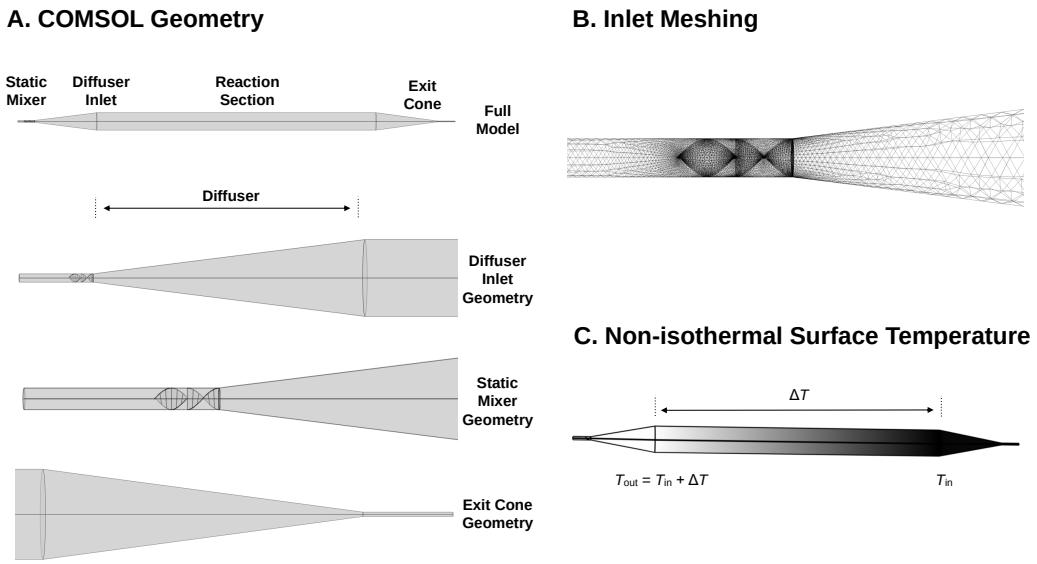

Figure 2.3: (A) Overview of the geometry used to simulate flow and species transport within the CPOT. (B) Inlet meshing for static mixer. (C) Schematic illustration of the temperature gradient used in non-isothermal simulations.

ammonium sulfate particles were generated by atomizing a 0.01 M aqueous solution with a constant rate atomizer (Liu and K. W. Lee, 1975). The atomized particles were immediately dried by a silica gel diffusion drier. The size distribution of particles was measured by a custom-built scanning mobility particle sizer (SMPS). For the particle RTD measurement, the particle counts were monitored with a TSI 3010 Condensation Particle Counter (CPC, Minneapolis, MN). Gas-phase RTD studies were performed under dark conditions. O_3 was generated by passing purified air through an O_3 generator (UVP, 97-0067-01), and the O_3 mixing ratio was monitored by a O_3 monitor (Horiba APOA-360). A Teledyne NO_x Analyzer (Model T200) was used to monitor NO, NO_2, and NO_x in the experiment of the determination of photon flux. To measure the penetration efficiency of gas-phase species, a SO_2 monitor (Meloy Lab, SA285E) was used to detect SO_2 and a chemical ionization mass spectrometry (CIMS, Crounse et al., 2006; St. Clair et al., 2010) was employed to detect H_2O_2.

2.2.5 CFD Simulations

CFD simulations were performed using COMSOL Multiphysics 5.0 software (Stockholm, Sweden. www.comsol.com) to assist the design and characterization of the reactor. COMSOL uses a finite element method and has a number of built-in modules that can be utilized to simulate a specific experimental condition. Recently,

several research groups have employed COMSOL in atmospheric and aerosol chemistry studies (Grayson et al., 2015; Sellier et al., 2015; Y. Zhang et al., 2015). Here, the model geometry replicates that of the actual design; thus, the simulations include a static mixer, diffuser inlet, reaction section, and exit cone with exact dimensions (Fig. 2.3A).

At the design stage, the performance of the inlet section was simulated numerically using CFD models (Section 2.2.5). The actual static mixer containing 12 mixing elements was simulated by a 2-element mixer using the COMSOL built-in static mixer model. Flow profiles calculated using the 2-element static mixer model were found to be identical to those using static mixers with 4 or more elements. Since static mixers yield asymmetric flow patterns, the model was solved in a 3D geometry. The entire 3D model was discretized with a fine mesh composed of approximately 1.25×10^6 tetrahedral elements (Fig. 2.3B). The average element quality, which is a reflection of cell distortion (a value of 1 reflects a perfect element shape), was 0.77 with a minimum of 0.12. A finer mesh within the domain of the static mixer was applied to capture flow dynamics near the entrance to the diffuser cone (Fig. 2.3B). Model sensitivity to meshing was tested using a finer mesh density, and results were found to be identical. An impermeable and no-slip boundary condition was applied to all surfaces. The flow at the entrance into the static mixer was set to be 2 L min^{-1}, and the outlet pressure was assumed to be atmospheric. Simulations were conducted until a steady state was achieved, and the errors converged to $< 10^{-6}$.

Navier-Stokes equations were solved using the COMSOL laminar flow package in the CFD module assuming compressible, isothermal flow. The isothermal assumption will be relaxed subsequently. To evaluate the effect of reactor temperature gradients, the COMSOL laminar flow package was coupled to the convective and diffusive heat transfer interface. To visualize fluid flow through the reactor, transient simulations were performed using the COMSOL dilute species transport package. This model, when coupled to the Navier-Stokes equations, enables one to track convection and diffusion of a tracer species, as described in Section 2.4. After first generating the steady-state laminar flow profile, a 30 s rectangular pulse of a 0.1 mol m^{-3} tracer was introduced numerically into the reactor at the entrance to the static mixer to generate the RTD. No wall uptake of gases or particles was assumed in this computation. Molecular or Brownian diffusivity can be varied over several orders of magnitude to represent that of vapor molecules and particles. The simulation was run for 80 min with data output every 15 s (consistent with the data acquisition of the instruments,

e.g. O_3 monitor and CPC). Simulations were performed for a variety of different inlet geometries, flow rates, and reactor temperature gradients. These simulations served to evaluate the design against alternative configurations and also demonstrate the sensitivity of fluid field to various flow conditions.

2.2.6 Photochemical Model

While the CFD simulation serves as a comprehensive method to understand the fluid dynamics, it is not efficient to solve a complex chemical kinetic system within this framework. A simplified 1D axial-dispersion photochemical model based on the RTD measurement is built here to evaluate the oxidation level. The mechanism presented here is that in the absence of NO_x. The oxidation of 100 ppb SO_2 by the OH radical is studied. H_2O_2 at 1 ppm serves as the OH precursor. The three types of UV lamps are considered, sequentially, to investigate the effect of the radiation source on OH exposure. Each simulation is carried out at RH = 5% and T = 295 K (corresponding to $[H_2O]$ = 1500 ppm). The case in the absence of H_2O_2 input is also simulated to check the background OH level. Reactions of the full mechanisms and the rate coefficients including photolysis rate under different lamps that are necessary for the chemical kinetic modeling are listed in Section 2.8.2.

The AD-PFR model setup is used in the present study and described in Section 2.8.3. The Danckwerts boundary condition is employed to ensure the flux continuity at both the inlet and outlet (M. E. Davis and R. J. Davis, 2003). This model system is solved in MATLAB (R2015b) by a boundary value problem solver `bvp4c`. The PFR model is run simultaneously as a comparison. No wall interaction and new particle formation are considered in the models. The result will be discussed in Section 2.6.

2.3 Design of the Flow Tube Reactor

Essential elements of the design of a flow tube reactor are: (1) the manner by which reactants are introduced into the reactor; (2) the nature of the flow inside the reactor; (3) the type and location of the radiation source relative to the reactor itself; and (4) the management of heat generation owing to the radiation source. The first two correspond to the inlet section design, while the latter two address the problem of possible non-isothermal conditions in the reaction section.

2.3.1 Injection Method

A number of possible arrangements exist to introduce material into a flow tube reactor (Fig. 2.4). The nature of the injection manifold has the potential to profoundly

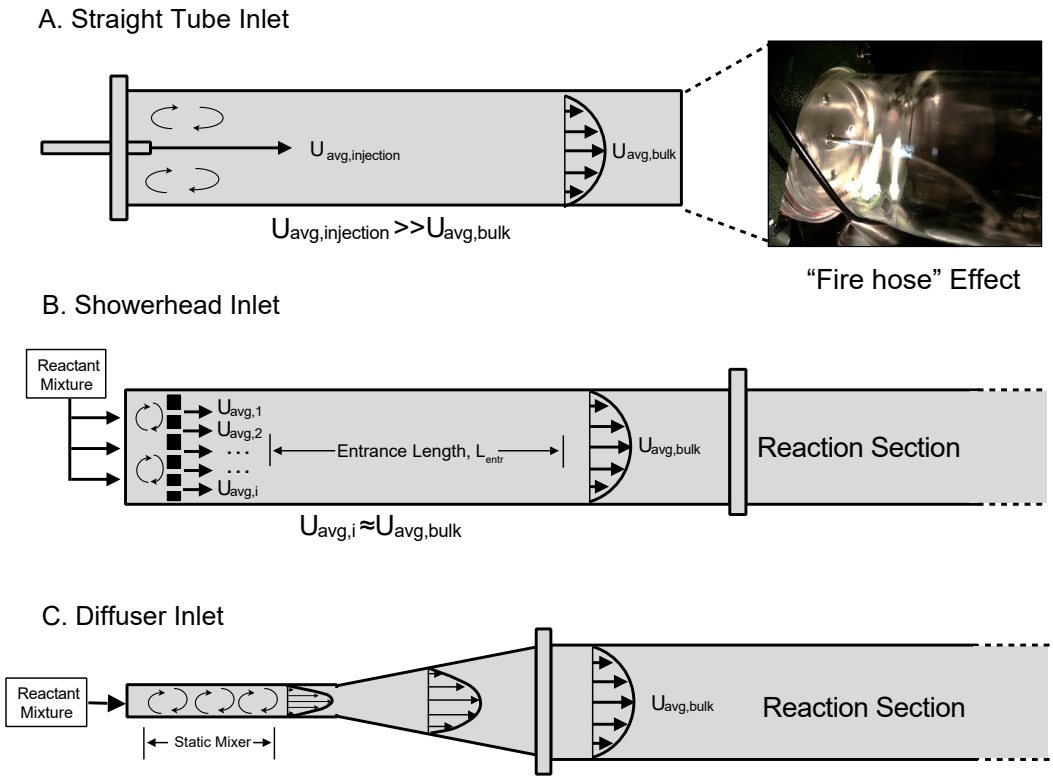

Figure 2.4: Inlet designs exemplified by (A) straight tube injection, (B) showerhead injection, and (C) diffuser injection. $U_{\text{avg,injection}}$, $U_{\text{avg,bulk}}$, and $U_{\text{avg,i}}$ values denote the average velocities at the inlet, in the bulk reaction section, and at the exit of a showerhead hole, respectively. Inlet (A) also illustrates the "fire hose" effect, as demonstrated by the visualization of smoke in a Pyrex glass tube.

affect the flow profile in the subsequent reaction section. In the case of a laminar flow reactor, it is desirable to minimize such "end effects" in order to establish parabolic flow quickly within the reaction section; otherwise, phenomena such as jetting and recirculation have the potential to impact flow patterns throughout the entire reactor. Figure 2.4A depicts the simplest injection method, by which vapor and particles are introduced into the reaction section through a short injection tube. While a benefit of this design is its simplicity, with this mode of injection, it is challenging to distribute reactant mixtures evenly across the reactor cross section. We tested this inlet method on a cylindrical Pyrex glass tube and visualized the flow pattern by the injection of smoke (Fig. 2.4A). With flow controlled by a vacuum line attached to the exit section, the gas-particle mixture is pulled into the reaction tube at a rate that is dictated by mass conservation. Smoke visualization studies illustrate that the mixture concentrates in a plug at the center of the reactor. This ”fire hose” effect arises from the enhanced velocity at the exit of the injection tube ($U_{\text{avg, injection}}$).

Such flow behavior is typical for that occurring with a sudden expansion (Bird et al., 2007).

Some flow tube designs address inlet issues using flow management devices, e.g. a spoked-hub/showerhead disk inlet (Bonn et al., 2002; Ezell et al., 2010) that distributes the reactants evenly about the reactor cross-section and provides sufficient mixing (Fig. 2.4B). Even when reactants are introduced gently into the tube, an axial distance is still required for the flow to develop to the characteristic parabolic laminar flow profile. This entrance length, L_{entr}, is estimated to be $0.035D\text{Re}$ (Bird et al., 2007). The inlet section should be designed with a sufficient entrance length L_{entr} to ensure the development of the laminar profile prior to the reaction section.

In the CPOT, reactants are injected via a conical diffuser (Fig. 2.4C) which has the advantage of gradually decreasing the velocity, thereby assisting with the formation of the laminar parabolic profile. The employment of a diffuser cone essentially replaces L_{entr}, and a parabolic profile is fully developed when the reactants reach the reaction section.

In addition to the flow field inside the reactor introduced by the inlet design, the transmission of different reactants (i.e. gas-phase species and particles) in the inlet system should also be considered (Karjalainen et al., 2016; Ortega et al., 2013, 2016; Palm et al., 2016; Simonen et al., 2017; Tkacik et al., 2014). Generally, a larger surface area means more interaction between the reactants and the walls, especially for "sticky" molecules. The effect of static mixer on the transmission of gas-phase species will be investigated in Section 2.5.1.

2.3.2 Angle of the Diffuser

A key consideration in designing a diffuser is avoiding flow separation that occurs when streamlines detach from the diffuser wall. Separation may be characterized by two flow patterns: stall and jetting flow. In stall, an asymmetrical flow pattern develops due to an adverse pressure gradient. Fluid is accelerated along one wall of the diffuser and recirculates slowly back along the other wall to the point of streamline detachment (Tavoularis, 2005). As demonstrated in Fig 2.4A, jetting flow is characterized by a symmetric flow pattern where the fluid is accelerated at the center of the diffuser and recirculates slowly along the walls. Recirculation introduces non-ideality since it accelerates gases and particles down the reactor, thereby affecting the residence time distribution (RTD) and leading to uncertain reaction times.

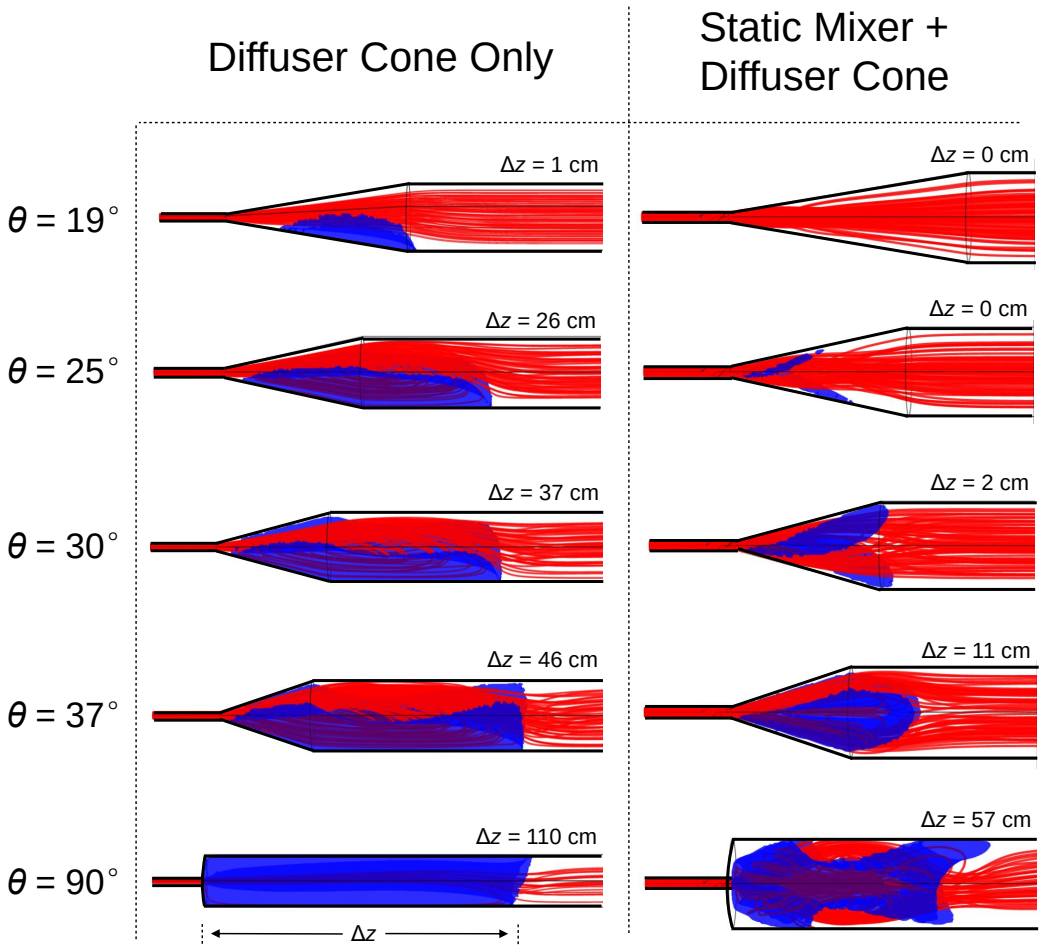

Figure 2.5: COMSOL simulation results for a suite of diffuser angles assuming isothermal conditions. Images in the left column are from simulations conducted in the absence of a static mixer. Images in the right column are from simulations employing a 2-element static mixer upstream of the diffuser cone. The red traces are streamlines demonstrating the flow pattern of fluid introduced upstream of the static mixer. The blue surfaces illustrate regions where the axial velocity < 0 m s^{-1}. Together, these traces illustrate the recirculation zone. Δz is the length that the recirculation zone penetrates into the reaction section. All simulations were performed for a volumetric reactor flow of 2 L min^{-1}.

Diffusers are routinely applied in larger systems such as wind tunnels and turbines; therefore, most literature on diffuser design focuses on flow patterns at high Re (Re $>$ 5000, e.g., Mehta and Bradshaw, 1979; Prakash et al., 2014; Seltsam, 1995; Tavoularis, 2005). As a rule of thumb for high Re systems, flow separation can be suppressed if the diffuser half-angle is $\leq 5°$; however, smaller angles are needed if the area ratio between the diffuser inlet and reactor section is much greater than 5 (Mehta and Bradshaw, 1979). We are unaware of studies that report diffuser

performance at modest Re (< 500). Fried and Idelchik (1989) recommend that diffusers be designed with an angle of divergence $< 7°$ to avoid flow separation; alternatively, F. M. White (2008) recommends an angle $< 15°$. Sparrow et al. (2009) modeled the flow of fluid through diffuser cones at various Re. For further discussion about flow separation within diffusers, see Tavoularis (2005).

Under a typical working flow rate (2 L min^{-1}), the value of Re at the entrance of the conical diffuser is ~ 200. Figure 2.5 shows simulated flow profiles for a range of diffuser angles. The red traces represent streamlines, whereas the blue surface illustrates points where flow recirculation occurs, that is, where the axial velocity < 0 cm s^{-1}. Collectively, these traces provide a visualization of the recirculation zone. We present flow profiles in the presence and absence of a static mixer since swirling flow has been shown to improve diffuser performance for systems with appreciable separation (McDonald et al., 1971).

As the diffuser angle increases, separation becomes more appreciable, and the recirculation zone penetrates farther into the reaction section ($\Delta z > 0$). At the most extreme angle we considered ($\theta = 37°$), the simulation predicts that the first 46 cm of the reaction section is impacted by recirculation. For reference, the extreme of a sudden expansion ($\theta = 90°$) exhibits recirculation that penetrates nearly halfway through the reactor ($\Delta z = 110$ cm). For flow tube systems operated at similar Re as here, if a parabolic flow profile is desired, it is recommended that one utilizes a diffuser with $\theta < 20°$ in order to minimize laminar flow disturbance within the reaction section.

The presence of a static mixer tends to quell separation at moderate diffuser angles. The recirculation zone appears to propagate into the reaction section only at diffuser angles $> 30°$; however, the extent of this recirculation is substantially reduced compared to simulations in the absence of a static mixer. Furthermore, the recirculation zone is predicted to be symmetric; fluid from the static mixer is directed radially towards the walls of the diffuser and recirculates back towards the center. In contrast, the recirculation zone in diffusers without static mixers is predicted to be asymmetric (Fig. 2.5), with flow recirculating at one wall of the diffuser. With flow introduced via a sudden expansion, the presence of a static mixer does little to minimize recirculation. The improvement in diffuser performance with swirling flow at the inlet is consistent with observations at high Re (ibid.), suggesting that the addition of a static mixer may help to mitigate moderate separation in systems employing wide-angled diffusers.

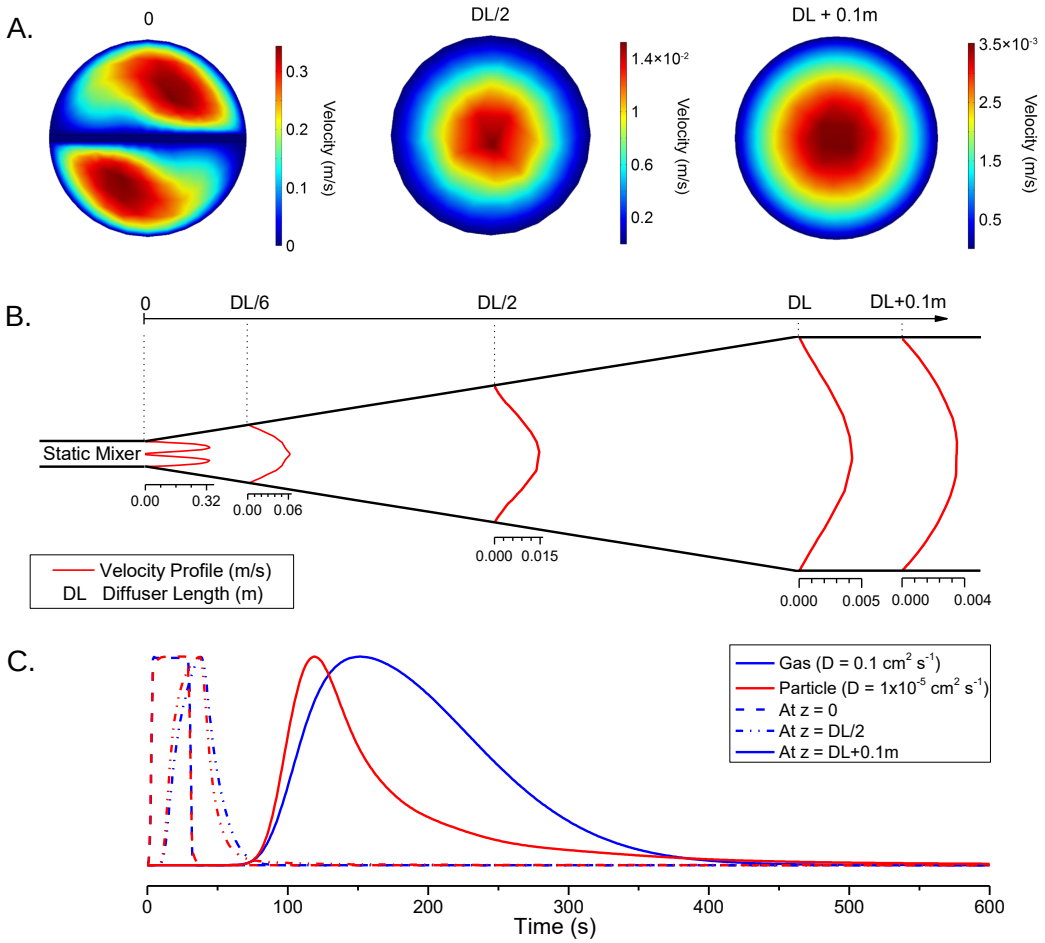

Figure 2.6: COMSOL simulated velocity field at the reactor inlet under isothermal conditions. Simulations were performed for the actual CPOT design: a 15° diffuser cone coupled to a static mixer. The velocity magnitude at various axial positions is shown in (A), and 1D axial velocity profiles within the "inlet-affected" region are shown in (B). The velocity magnitude in (B) is presented on the axis below each velocity profile. Note that DL = Diffuser Length (53.3 cm). (C) shows the normalized residence time of vapor molecules and monodisperse particles at various axial positions. A 30 s square wave pulse is used as the input.

Figure 2.6 further illustrates the CFD-modeled velocity profiles for the actual CPOT design, with a 15° diffuser cone coupled to a static mixer, in the region of the reactor extending from the inlet cone to the first 10 cm of the reaction section. We refer to this section of the reactor as the "inlet-affected" region, since axial positions farther downstream exhibit fully-developed laminar profiles. Figure 2.6A visualizes the entire velocity field along select cross-sections within the inlet-affected region, whereas Fig. 2.6B presents 1D velocity profiles at various axial positions. Note that Fig. 2.6A presents the velocity magnitude, whereas Fig. 2.6B illustrates the axial

velocity component (i.e., flow in the z-direction) to facilitate identification of regions impacted by flow recirculation. In general, the simulation predicts the absence of recirculation within the reactor under isothermal conditions. As demonstrated by Fig. 2.6B, the simulated axial velocity profile immediately downstream of the static mixer exhibits two jets with a maximum axial velocity of 31 cm s^{-1}. The jets quickly dissipate as the flow develops through the diffuser cone. At the exit of the diffuser cone, the flow is nearly parabolic, and the maximum velocity slows to 0.5 cm s^{-1}. Within 10 cm of the diffuser exit, the flow becomes parabolic with a maximum centerline velocity of 0.4 cm s^{-1}. We also simulated the fluid field under higher flow rates (e.g. 4 and 6 L min^{-1}) and found no separation of flow within the diffuser. These results demonstrate that the CPOT inlet is within the design limits for a diffuser with non-separated flows and that the presence of a static mixer has little effect on the parabolic profile in an isothermal reaction section. However, the presence of the static mixer does have an impact on the residence time of the reactants. Fig. 2.6C shows the corresponding residence time at the three positions for both vapor molecules and monodisperse particles, both of which are a 30 s square wave input. Section 2.4.3 addresses RTD.

2.3.3 Non-isothermal Effect

Precise control of temperature is crucial in maintaining as well-characterized a laminar flow as possible in the reaction section (Jonsson et al., 2008; Khalizov et al., 2006). In one class of flow tube design, the radiation source is positioned within the flow tube reactor itself, and the reactor walls are constructed of a UV blocking material. In that design, the effect of the internal heat source on the flow must be taken into account. In the present design, with the reaction tube suspended at the center of the chamber and the lights positioned on the outside of the tube, an exterior water jacket provides a heat transfer medium, while allowing penetration of UV radiation to the reactor. If water recirculation in the jacket is sufficiently rapid, axial temperature gradients in the cooling jacket can be minimized. Any jacket temperature maintained appreciably below or above that in the reactor itself will lead to temperature gradients that may induce secondary flows in the reactor.

Although the CPOT is equipped with a temperature control system (Section 2.2.3), maintaining a target temperature under UV irradiation is challenging. The measured rise in coolant temperature at steady state under full irradiation conditions is ≤ 0.2 K. Given the absence of heat sources within the reactor itself, the increase in coolant temperature is a result of the absorption of heat generated by the exterior UV

lamps. Temperature gradients along the reactor wall have the potential to induce recirculation from changes in density. The establishment of radial temperature gradients near the wall induces recirculation cells as density variations force the flow to stratify.

The dimensionless group that characterizes the effect of free convection on flow is the Richardson number, which relates the strength of buoyancy forces to that of convective forces. The Richardson number (Holman, 2010), Ri, can be expressed as the ratio of the Grashof number, Gr, to the square of the Reynolds number, Re:

$$\mathrm{Ri} = \frac{\mathrm{Gr}}{\mathrm{Re}^2} = \frac{g\beta D^3 \Delta T/\nu^2}{(\rho U_{\mathrm{avg}} D/\mu)^2} \sim \frac{gD}{TU_{\mathrm{avg}}^2}\Delta T \tag{2.1}$$

where g is the gravitational acceleration, β is the thermal expansion coefficient of air ($\frac{1}{T}$ for ideal gases), U_{avg} is the average fluid velocity, ν is the kinematic viscosity of air ($\frac{\mu}{\rho}$), and ΔT is a characteristic temperature difference between the tube wall and centerline. When $\mathrm{Ri} < 0.1$, convective forces dominate, and effects of buoyancy on the flow are small. When $\mathrm{Ri} > 10$, buoyancy forces may lead to flow bifurcation and recirculation. Under typical CPOT operating conditions, a radial temperature gradient between the fluid and wall of ~ 0.007 K is required to maintain $\mathrm{Ri} < 10$. Because this is a very small temperature difference, modest inequalities in temperature are anticipated to affect flow patterns within the reactor.

To investigate the effect of wall temperature differences on flow within the reaction section, we performed COMSOL simulations, assuming a non-isothermal reactor wall. The COMSOL laminar flow package was coupled to the convective and diffusive heat transfer interface. Since water is assumed to flow uniformly through the annular water jacket cross section from the exit to the entrance, we apply an axial temperature gradient to the simulation. A schematic illustration of the simulation setup is shown in Fig. 2.3C. At the exit of the reaction section, the temperature of the reactor wall is set to that of water entering the cooling jacket (T_{in}). At the entrance to the reaction section, we assume that the wall temperature is that of the water exiting the cooling jacket ($T_{\mathrm{out}} = T_{\mathrm{in}} + \Delta T$). The wall temperature is assumed to change linearly between the entrance and exit. The diffuser cone is prescribed at a constant temperature equivalent to the cooling jacket temperature T_{out}, whereas the exit cone is prescribed a constant temperature of T_{in}. In the following discussion, we focus on results with $T_{\mathrm{in}} = 23\ ^{\circ}\mathrm{C}$, which is the typical room temperature in the Caltech Laboratory. Note that this model setup is a simplified case, since in actual experiments the entrance and exit cones should be kept at the same temperature

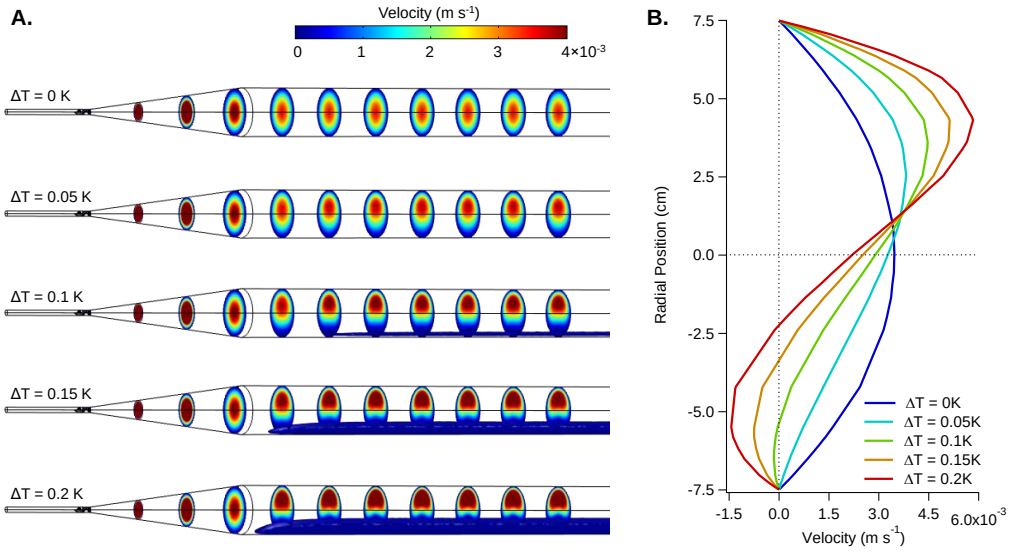

Figure 2.7: COMSOL simulated flow profiles as a function of reactor wall temperature gradient ΔT. (A) 3D simulation results demonstrating cross-sectional velocity profiles and consequential recirculation zones (blue isosurface). (B) 1D velocity profiles at axial position z = 150 cm.

(i.e., T_{in}); this will introduce temperature discontinuity between the entrance cone and the reaction tube. Nonetheless, this idealized model provides insight into the temperature difference induced flow perturbation within the flow tube reactor.

Figure 2.7 demonstrates the simulated effect of an axial temperature gradient (ΔT) on flow profiles within the reactor. Figure 2.7A illustrates 2D velocity profiles at various axial positions and a blue isosurface where the axial velocity < 0 cm s^{-1}. Figure 2.7B illustrates 1D velocity profiles at the midpoint of the reactor. As the temperature gradient within the reactor increases, the velocity profiles skew owing to the buoyancy of the warm air. This bifurcation induces recirculation and is predicted to affect the entire reactor region. For a temperature gradient of 0.2 K (equivalent to that actually measured), the recirculation zone exhibits a maximum velocity of -0.15 cm s^{-1}.

The simulations demonstrate the sensitivity of the velocity profile in the reactor to small temperature gradients within the reaction section. Such disturbances will manifest in shorter, broader residence times due to induced recirculating flow. As demonstrated in Fig. 2.7, a critical temperature difference exists at which recirculation becomes important. At a volumetric flow of 2 L min^{-1}, this critical temperature difference between the exit and the entrance is estimated to be ~0.08 K. The Ri

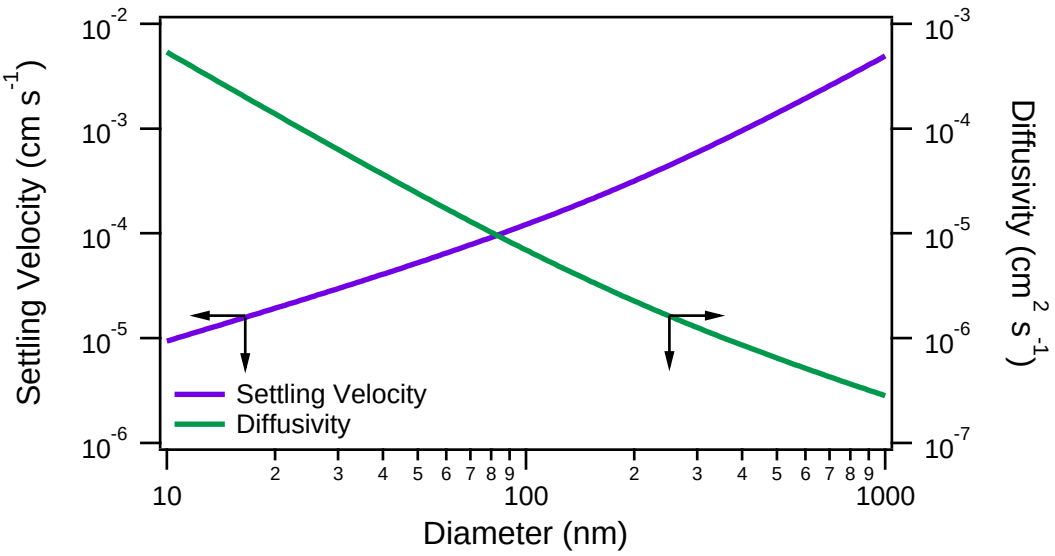

Figure 2.8: Particle settling velocity and Brownian diffusivity for spherical particles of unit density as a function of particle diameter (J. H. Seinfeld and S. N. Pandis, 2016).

number criterion indicates that higher flow rates reduce the reactor sensitivity to temperature gradients. We find the critical temperature differences at 4 L min^{-1} and 6 L min^{-1} are 0.18 K and 0.3 K, respectively. Even at higher flow rates, relatively small temperature gradients along the walls of the reactor can have potential consequences on reactor flow patterns.

2.4 Behavior of Gaseous and Particulate Species in a Laminar Flow Tube Reactor

2.4.1 Fluid Field in the Reaction Section

At the typical operating flow rate (2 L min^{-1}), flow within the reaction section is laminar (Re $\cong$ 20), under which the axial fluid velocity is given by the parabolic distribution,

$$v_z(r) = U_{\max}\left[1 - \left(\frac{r}{R}\right)^2\right] \tag{2.2}$$

where $U_{\max}$ is the centerline velocity, r is the radial coordinate in the tube, and R is the tube radius. The residence time of fluid elements in laminar flow differs along streamlines, for which the average residence time of fluid elements is precisely calculated. Due to the sensitivity to small temperature difference, as noted above, the actual velocity profile in the reactor under non-isothermal condition will not adhere to an ideal parabolic distribution.

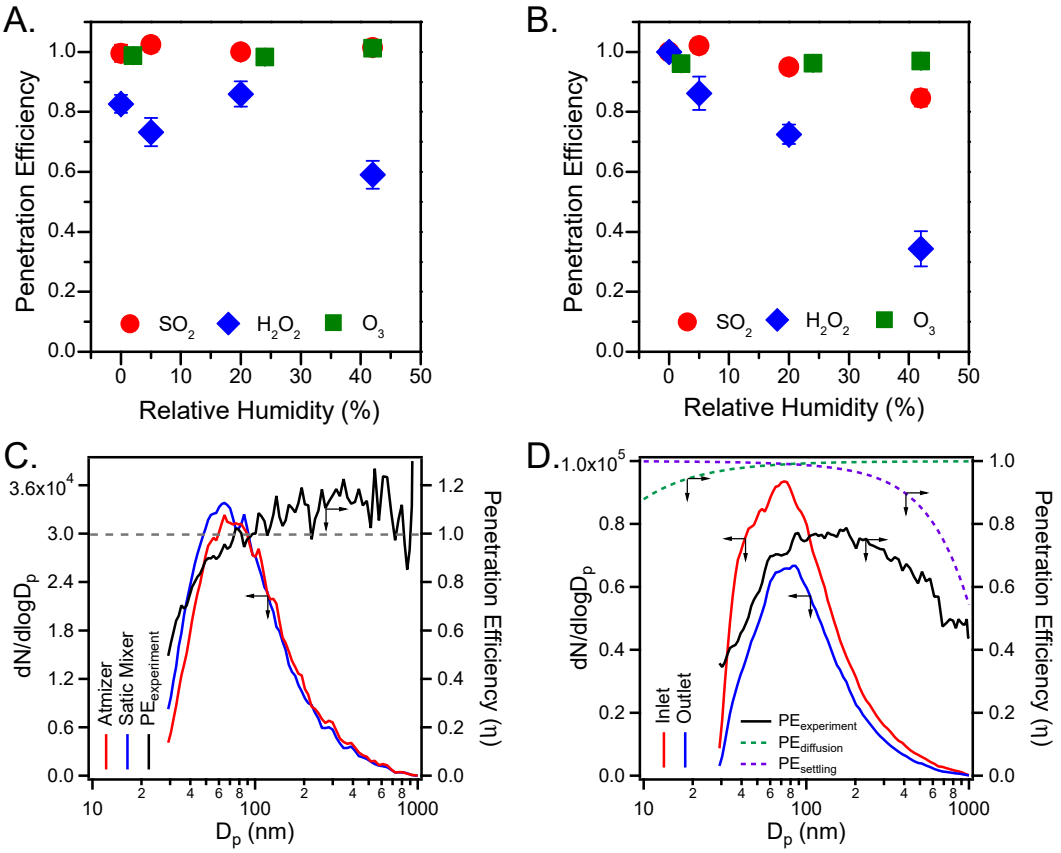

Figure 2.9: Penetration efficiency (η) of gases and particles in the static mixer and the flow tube. (A) Relative humidity (RH) dependent η of SO_2, H_2O_2, and O_3 in the static mixer. (B) RH dependent η of SO_2, H_2O_2, and O_3 in the flow tube. Error bar indicates the measured uncertainty. (C) Measured ammonium sulfate particle size distributions before and after the static mixer, as well as the η derived from these measurements. The gray dashed line indicates $\eta = 1$, i.e. no particle loss. (D) Measured ammonium sulfate particle size distributions at the inlet and outlet of the flow tube, as well as the η derived from these measurements. The calculated η with respect to particle diffusion loss (Eq. (2.4)) and gravitational settling (Eq. (2.34)) are indicated by the dashed lines.

2.4.2 Penetration Efficiency (η)

The penetration efficiency η is defined as the fraction of material entering the reactor that leaves in the absence of chemical reaction. If no removal occurs during flow through the reactor, then $\eta = 1$. Diffusional loss in a laminar cylindrical tube is addressed in Section 2.8.4. The mass conservation Eqs. (2.19) to (2.22) can be solved either numerically or analytically (E. J. Davis, 2008) to determine the penetration efficiency η, given a first-order loss rate to the wall, k_{wi}. For the case of complete removal of species i at the wall, in which $k_w \rightarrow \infty$, corresponding to the

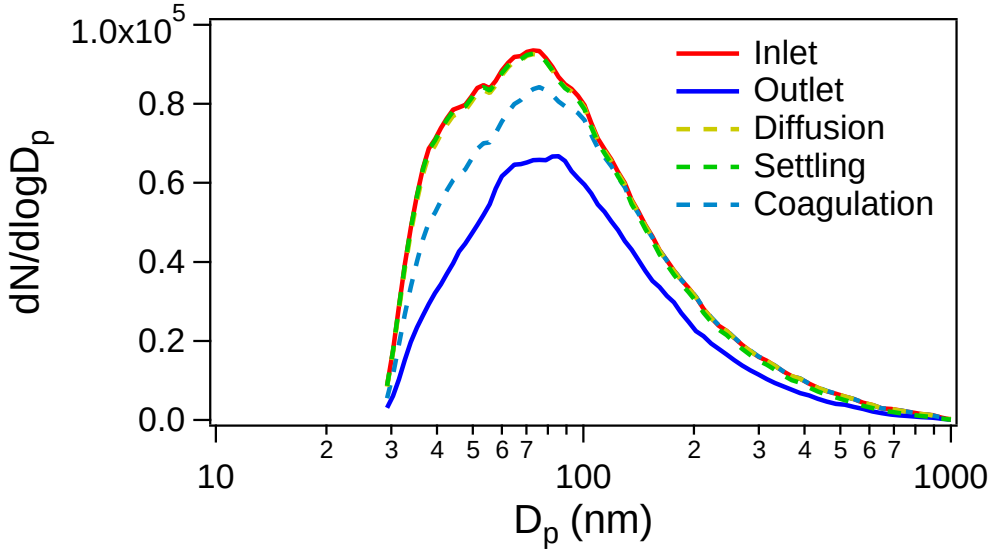

Figure 2.10: Particle size distributions at the outlet when diffusion, gravitational settling, and coagulation precosses are coupled separately with the size distribution at the inlet. The measured size distribution at the outlet is plotted as a reference. The coupling of diffusion and gravitational settling with the inlet size distribution is the product of dashed lines and the red line in Fig. 2.9D. The coagulation process is calculated in a coagulation model, which uses a PFR model with an average residence time of 1520 s by assuming a unity coagulation efficiency and no wall deposition. The coagulation model input is the size distribution at the inlet.

boundary condition $c_i = 0$ at the wall, the analytical solution for η is (Fuchs, 1964):

$$\eta = 0.8191 \exp(-3.657\xi) + 0.0975 \exp(-22.3\xi) + 0.0325 \exp(-57\xi) + \ldots \quad (2.3)$$

where ξ is the dimensionless length ($\frac{\pi \mathscr{D} L_{\text{cyld}}}{Q}$), $\mathscr{D}$ is the diffusivity of the species, L_{cyld} is the length of the cylindrical tube, and Q is the volumetric flow rate. For small ξ, i.e. < 0.02, an alternative equation is available (Gormley and Kennedy, 1948):

$$\eta = 1 - 2.56\xi^{2/3} + 1.2\xi + 0.177\xi^{4/3} \quad (2.4)$$

The penetration efficiency for particles is size dependent, i.e. $\eta(D_p)$. We will address the RTD of particles in Section 2.4.3.2 and Section 2.8.6.

2.4.3 Residence Time Distribution (RTD)

In a laminar flow field, idealized non-diffusing vapor or non-diffusing and non-settling particles, introduced as a pulse at the entrance of the tube, will first emerge as a pulse at the residence time of the centerline, followed by a decaying curve as the

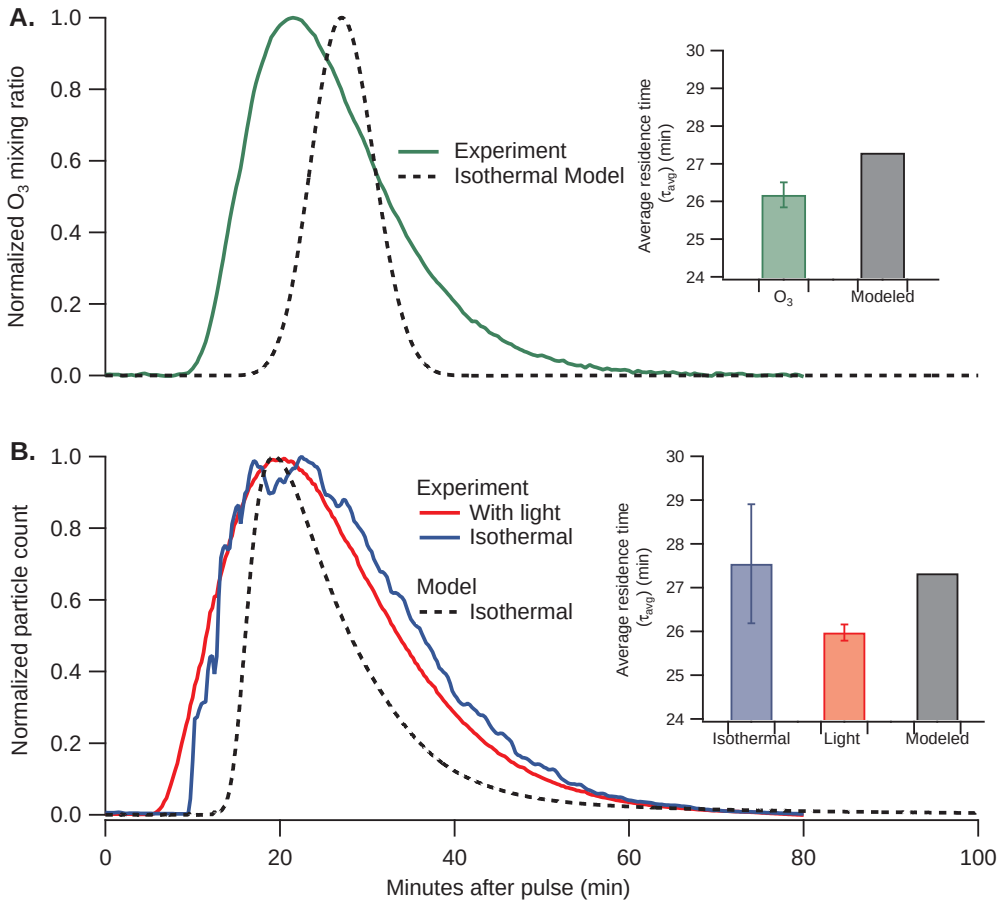

Figure 2.11: Experimental and COMSOL simulated residence time distributions of (A) O_3 vapor molecules and (B) polydisperse ammonium sulfate particles. The diffusivity used in COMSOL for O_3 is that for a generic gas-phase species 1×10^{-5} m^2 s^{-1} and for particles is 1×10^{-9} m^2 s^{-1} corresponding to a particle size of ~ 100 nm. The average residence time in each case is compared in the insets as reference.

.

material on the slower streamlines reaches the exit. Under actual conditions, vapor molecules undergo molecular diffusion in both the radial and axial directions, and particles are subject to Brownian diffusion and gravitational settling.

2.4.3.1 Vapor Molecule RTD

Vapor molecules in laminar flow in a tube undergo molecular diffusion in both the radial and axial directions. With molecular diffusion coefficient $\mathscr{D}_i$, the characteristic diffusion time in the radial direction is $\tau_{c,\mathscr{D}_i} = \frac{R^2}{\mathscr{D}_i}$. To assess the importance of radial diffusion as a mechanism for smearing vapor molecules across the tube cross-section during convection down the tube, one can compare the characteristic

timescale for radial diffusion with the characteristic residence time in the cylindrical tube, $\tau_{c,\text{cyld}} = \dfrac{L_{\text{cyld}}}{U_{\text{avg}}}$. If $\tau_{c,\mathcal{D}_i} \ll \tau_{c,\text{cyld}}$, for example, the vapor molecules will diffuse more or less uniformly across the tube radius in the time it takes for the fluid to flow to the tube exit. Likewise, if $\tau_{c,\mathcal{D}_i} \gg \tau_{c,\text{cyld}}$, each vapor molecule will effectively remain on the streamline upon which it entered. Vapor molecules also diffuse in the axial direction; this process is represented by the axial diffusion term, $\mathcal{D}_i \dfrac{\partial^2 c_i}{\partial z^2}$, on the right hand side of Eq. (2.18). As noted earlier, for flow velocities of the magnitude of those here, the effect of this axial diffusion is negligible when compared with axial convection. However, an apparent axial diffusion can arise from the interaction of radial molecular diffusion and the laminar flow, a process known as Taylor dispersion (Bird et al., 2007; G. I. Taylor, 1953). Under the criterion, $\tau_{c,\text{cyld}} \gg \dfrac{\tau_{c,\mathcal{D}_i}}{3.83^2}$, the concentration becomes approximately uniform over the cross-section of the tube. Section 2.8.5 presents a discussion of the application of Taylor dispersion based RTDs with respect to different initial conditions.

In the PAM reactor (Lambe et al., 2011a), the Taylor dispersion criteria do not strictly meet the working conditions, however, the two flow regime fitting results suggest that two types of flow may exist in the reactor: a direct flow with minor dispersion and a secondary recirculation flow with significant dispersion. Under the current flow rate of 2 L min^{-1} and characteristic vapor molecular diffusivity $\sim 1 \times 10^{-5}$ m^2 s^{-1}, $\tau_{c,\text{cyld}} = 1290$ s $\gg \dfrac{\tau_{c,\mathcal{D}_i}}{3.83^2} = 50$ s; therefore, the Taylor dispersion approximation for the gas-molecule RTD applies, and Taylor dispersion can be expected to be important. Note that the presence of the static mixer and conical diffuser in the inlet section alters the input distribution of vapor molecules and particles at the entrance of the reaction section (Fig. 2.6C) from an idealized uniform initial condition, and Eq. (2.25) will not hold exactly for the fitting of the results from actual pulse RTD experiments. The convolution (Eq. (2.28)) of the skewed input shape must be numerically calculated. The actual RTD of the reactor should also include the RTDs in the exit cone and sample line.

2.4.3.2 Particle RTD

For the behavior of particles in the reactor, in general, the following processes need to be accounted for: (1) advection; (2) Brownian diffusion; (3) gravitational settling; (4) growth/shrinkage owing to mass transfer from or to the gas phase; and (5) coagulation. The particle number concentration distribution as a function of particle diameter D_p is denoted as $n(D_p, r, z)$. Processes (1) - (4) are related to the penetration

efficiency, while the total mass of particles are conserved during the coagulation process with the size distribution being shifted. To discuss the penetration efficiency, coagulation is not included here, which will be further discussed in Section 2.5.1.2

In general, particles undergo both Brownian diffusion in the flow and settling under the influence of gravity. Collectively, these processes give rise to particle loss by deposition on the wall during transit through a laminar flow tube reactor. The Brownian diffusion coefficient of a 80 nm diameter particle is approximately four orders of magnitude smaller than that of a typical vapor molecule. Consequently, for typical particle sizes and residence times in the reactor, the Brownian diffusion of particles can be neglected, except in the region very close to the wall, wherein particle uptake at the wall because of diffusion can occur. Gravitational settling of particles in a horizontal tubular flow reactor occurs as particles fall across streamlines and deposit on the lower half of the tube. To assess the effect of gravitational settling of particles, one needs to compare the characteristic settling distance during transit through the reactor, $v_s \tau_{c,\mathrm{cyld}}$, with the tube radius, R, where v_s is the particle settling velocity. Figure 2.8 shows the size-dependent settling velocity and particle diffusivity for spherical particles. Under typical operating conditions, particles introduced uniformly across the entrance will tend to settle somewhat during transit down the reactor, so this process needs to be accounted for in analyzing particle RTDs. The full equation describing the motion of particles in the horizontal tubular laminar flow under simultaneous diffusion and settling cannot be easily solved. As suggested by the particle-size dependence of settling velocity and diffusivity in Fig. 2.8, consideration of the two separate regimes, i.e., diffusion and settling, respectively, can simplify the problem. Here we define the diffusion regime as that for particles with diameter $\leq$ 80 nm and otherwise for the settling regime. In each regime, we will consider only one process, i.e. either diffusion or settling.

A discussion of the motion of particles in the settling regime is presented in Section 2.8.6. The corresponding RTD (Eq. (2.32)) can be calculated based on the particle trajectories. In the diffusion regime, the settling velocity can be ignored, and Taylor dispersion is not applicable. The RTD of a pulse input can be approximated by the residence time along each streamline (Eq. (2.35)). Since actual particles undergo some degree of radial Brownian diffusion, which is not considered in Eq. (2.35), the full RTD should exhibit a broader and smoother profile than that predicted by Eq. (2.35) (as simulated by COMSOL, see Section 2.5.2.2).

The penetration efficiency (η) for mono-disperse particles can be calculated in their

respective regimes. In the settling regime, Equation (2.34) calculates the size dependent η. The behavior of particles in the diffusion regime can be calculated by Eqs. (2.3) and (2.4), where removal of particles at the wall is assumed. This is consistent with the boundary condition of the particles in the settling regime.

2.5 Results and Discussion

2.5.1 Experimental Evaluation of Penetration Efficiency

The penetration efficiency (η) was determined by using a constant input of either gas-phase species (SO_2, O_3, and H_2O_2) or polydisperse ammonium sulfate particles through the static mixer or through the flow tube. The relative humidity (RH)-dependent penetration efficiency is investigated for both gas-phase species and particles. The results are shown in Fig. 2.9.

2.5.1.1 Vapor Molecules

The η of O_3 in both the static mixer and the flow tube is constant ($\eta \sim 98\%$) over a wide RH range. SO_2 shows no removal by the static mixer, while H_2O_2 exhibits a lose of 20% to 40% in the static mixer. The measured η values in the flow tube of all the gas-phase species (O_3, SO_2, and H_2O_2) are essentially 100 % under dry conditions (RH < 5%). In the flow tube, the η values of both SO_2 and H_2O_2 decrease with RH. At RH = 42%, about 70% of H_2O_2 is lost, while at this RH about 20% of SO_2 is lost. These results show the complexity of the η of gas-phase species. The extent of wall deposition of organic vapors in the flow tube reactor requires a comprehensive study and will be addressed in a future publication.

2.5.1.2 Particles

The η values for polydisperse ammonium sulfate particles are also investigated at different RH. No RH-dependence was found for RH < 50 %, which is below the deliquescence RH of ammonium sulfate (results not shown). Figures 2.9C and D show the measured size distributions before and after the static mixer and the flow tube, as well as the size-dependent penetration efficiency obtained as a ratio. Figure 2.9C indicates that about half of the small particles (< 50 nm) are lost in the static mixer, while large particles (> 100 nm) penetrate essentially entirely through the static mixer. This is reasonable since the flow inside the static mixer is laminar (Re = 150). The smaller particles diffuse to the static mixer, while the larger ones follow the flow streamline.

The theoretical particle η curves under the influence of loss by gravitational settling and diffusion have also been calculated by applying the relevant parameters to Eqs. (2.4) and (2.34) (Fig. 2.9D). Only the reaction sections were considered in this theoretical calculation (i.e. the inlet and exit cones are excluded). We consider this calculation as a qualitative guideline for η. Settling velocity and diffusivity of particles are size-dependent (Fig. 2.8), resulting in reduced transmission for very small and large particles, due to diffusion loss and gravitational settling, respectively. Both measurements and theory indicate that η is maximized at a particle diameter of approximately 100 nm. The measured maximum penetration efficiency is $\sim$ 80 %, indicating a loss of particles, which is likely caused by secondary flow that actively conveys particles closer to the wall. This secondary flow will be discussed in Section 2.5.3. The behavior of particles in the exit cone is also difficult to predict and may reflect a certain extent of particle loss.

A numerical coagulation model is used to check the influence of coagulation on particle size distribution. This model uses a PFR framework with an average residence time of 1520 s, which is the measured particle average residence time (Section 2.5.2.2). A unity coagulation efficiency is assumed and no wall deposition of particles. The result is shown in Fig. 2.10. The comparison indicates that the coagulation process lowers the small particle number, accounting for about half of the missing small particles. The total particle number concentration and average residence time are the two key parameters that impact the coagulation process. Coagulation will have a negligible influence in the case of smaller particle number and shorter residence time. The CPOT typically uses particle number and surface concentrations in the order of magnitude of 10^4 cm^{-3} and 10^3 μm^2 cm^{-3}. It should be note that coagulation process itself has an impact only on the size distribution not the total particle mass. However, the presence of coagulation may enhance the gravitational settling effect owing to the production of larger particles.

2.5.2 Experimental Evaluation of RTD

We present here the results of experimental evaluation of the RTD for both vapor molecules and particles. The RTD profiles were determined by introducing a 30 s pulse of O_3 or polydisperse ammonium sulfate particles into the reactor under dry conditions (RH < 5%). All experiments were performed at the typical operating flow rate of 2 L min^{-1} in at least triplicate. The average residence time (τ_{avg}) was

obtained from each RTD profile according to:

$$\tau_{\text{avg}} = \frac{\Sigma I_j t_j}{\Sigma I_j}, \tag{2.5}$$

where I_i is the signal recorded at each time step t_j.

2.5.2.1 Vapor Molecules

As noted earlier, a typical value of diffusivity, 1×10^{-5} m^2 s^{-1}, is used in COMSOL to predict the gas-phase RTD. Measured and predicted gas-phase RTDs are shown in Fig. 2.11A. A large discrepancy is observed between the measured and theoretical RTD under presumed isothermal conditions. The predicted gas-phase RTD exhibits a symmetrical distribution centered at approximately 27 min. However, the measured RTD of gas-phase O_3 exhibits an asymmetrical feature, somewhat similar to the particle RTD (Fig. 2.11B). The τ_{avg} values obtained from the O_3 pulse experiments and simulations are also summarized in Fig. 2.11A. The measured τ_{avg} value of O_3 is shorter than predicted by 1.5 min. Potential explanations for measured RTDs are discussed in Section 2.5.3.

2.5.2.2 Particles

A typical value of particle diffusivity, 1×10^{-9} m^2 s^{-1}, corresponding to that of a $\sim$ 100 nm diameter particle, is used in COMSOL to predict the RTD. Figure 2.11B compares the measured RTD of polydisperse ammonium sulfate particles to that of the COMSOL simulation. Under isothermal conditions, the particle RTD exhibits a zigzag feature which is likely due to the static mixer that may distribute particles somewhat unevenly across streamlines, as can be seen in the velocity profile in Fig. 2.6A. As laminar flow develops in the reaction section, particles follow their respective streamlines until the exit cone, appearing as the zigzag pattern on the RTD profile. This zigzag feature is absent in the vapor molecule RTD, likely due to the larger diffusivity of vapor molecules. The theoretical RTD of particles in an idealized laminar flow reactor exhibits a sharp peak when the center line first arrives at the exit (Eq. 2.35). The experimental RTD observed exhibits a rather gradual rise instead of a sharp pulse likely due to the method of introduction (Fig. 2.6C). Figure 2.11B shows that, under isothermal conditions, the modeled RTD reproduces the shape and the peak time of the observed RTD, and the τ_{avg} values also show excellent agreement. However, the modeled RTD appears narrower than that observed. This indicates that particles arrive earlier and remain for a longer time than COMSOL predicts.

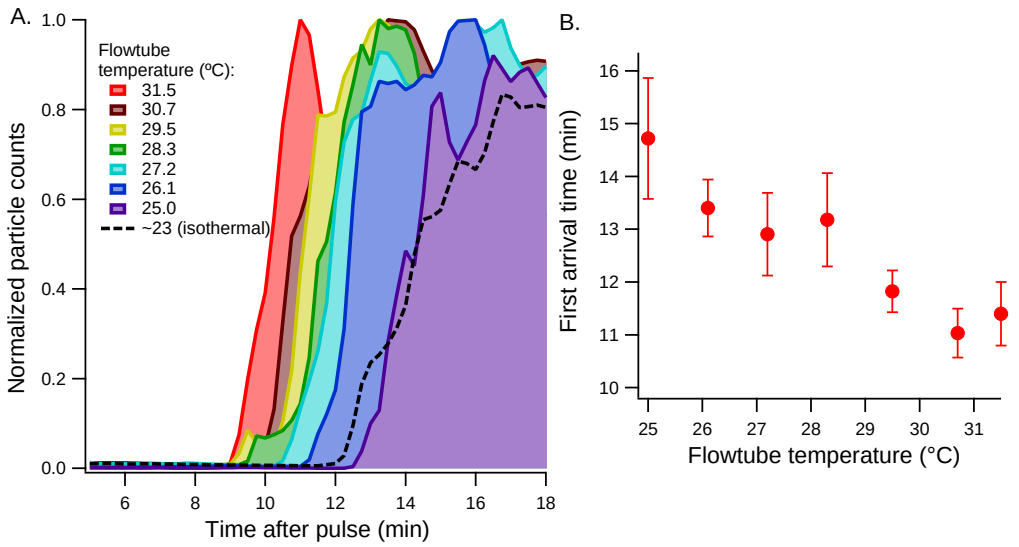

Figure 2.12: Non-isothermal effects on particle RTD. The water jacket temperature was raised systematically against the room temperature (~23 °C). (A) Normalized ammonium sulfate particle counts recorded at the exit are plotted against time after a pulse is introduced at the inlet. The experiment at each temperature is repeated 3 to 4 times. The results from a set of isothermal experiments are also included (dashed line) for reference. (B) Arrival times of the first major peak of each experiment.

.

Overall, the experimental RTD results of both gas-phase species and particles in the CPOT are essentially comparable to those of present flow reactors (ibid.), given the arrival time and the width of the peak. This discrepancy of the RTDs between the theoretical laminar flow and the real flow indicates the presence of non-ideal flow in the reactor.

2.5.3 Non-ideal Flow in the Reactor

The discrepancy between isothermal laminar flow theory and the experimental results can be attributed in part to non-isothermal conditions in the reactor. As noted earlier, the Richardson number (Eq. (2.1)) criterion indicates that a small temperature difference (~ 0.007 K) between the bulk and the wall can induce recirculation flows. The measured particle RTDs under isothermal conditions are compared to that obtained under maximum UVA radiation in Fig. 2.11B. A pronounced difference is that the RTD curve under radiation appears much smoother. The τ_{avg} value under irradiation is shortened by 1.5 min compared to that under isothermal conditions. Given the close agreement between the two RTD profiles, it is unlikely that a recirculation within the tube exists; more likely, the slight non-isothermal condition has created secondary flows that mix the tracers both radially and axially.

To further investigate non-isothermal effects, the temperature of the water jacket was raised in a step-wise manner to approach a significant temperature difference between the bulk flow and the wall. The experiments were conducted in the absence of UV radiation. The injected air was at room temperature (approximately 23°C), so a higher water jacket temperature exacerbates the deviation from isothermal conditions. The results of these experiments are shown in Fig. 2.12. The RTD at each temperature is the average of 3 to 4 replicates. As shown in Fig. 2.12A, the RTD at 25°C appears indistinguishable from that at quasi-isothermal conditions (the dashed line, we use "quasi-isothermal" here to distinguish from strict isothermal conditions in the model). Particles arrive at the exit cone earlier at higher water jacket temperatures, mirroring the observed discrepancy between the modeled and observed RTD profiles. This trend is clearly illustrated by Fig. 2.12B, where the arrival time of particles in each experiment is shown as a function of the water jacket temperature. This observation is consistent with the hypothesis that a difference in temperature between the wall and the inlet flow leads to the non-ideal conditions.

Consider that the wall of the reactor is at a constant room temperature as slightly cooler air is introduced into the reactor. Two orthogonal forces interact with each other in the horizontal flow tube when they are of similar orders of magnitude: forced convection by the pressure gradient (horizontal) and buoyancy-induced free convection (vertical). The actual velocity field in this situation is challenging to simulate (Faris and Viskanta, 1969; Iqbal and Stachiewicz, 1966; Mori and Futagami, 1967; Siegwarth et al., 1969). Generally, to satisfy mass conservation, the air close to the wall is warmed and rises along the sidewall, inducing a downward flow in the center of the tube, forming two symmetric vortices. Superposition of the primary forced convective and the secondary free convective flows convert the vertical recirculation into spiral motions along the tube. The spiral flow developed in the reaction section plays a similar role as the static mixer in the inlet section. The spiral flow is more easily established if there are hot spots inside, which can be likely, as the sample ports on the reaction sections are not heat-insulated by the water jacket. To quantitatively represent this effect, one can introduce an enhanced isotropic eddy-like diffusivity ($\mathscr{D}_e$), a statistical fluid field related property.

To verify the presence of the spiral secondary flow in the CPOT, we systematically increased the diffusivity used in the COMSOL simulations. The agreement between simulated and observed RTD improves, as the value of $\mathscr{D}_e$ is increased in the COMSOL simulation, with the optimal agreement achieved when $\mathscr{D}_e = 4.5 \times 10^{-4}$

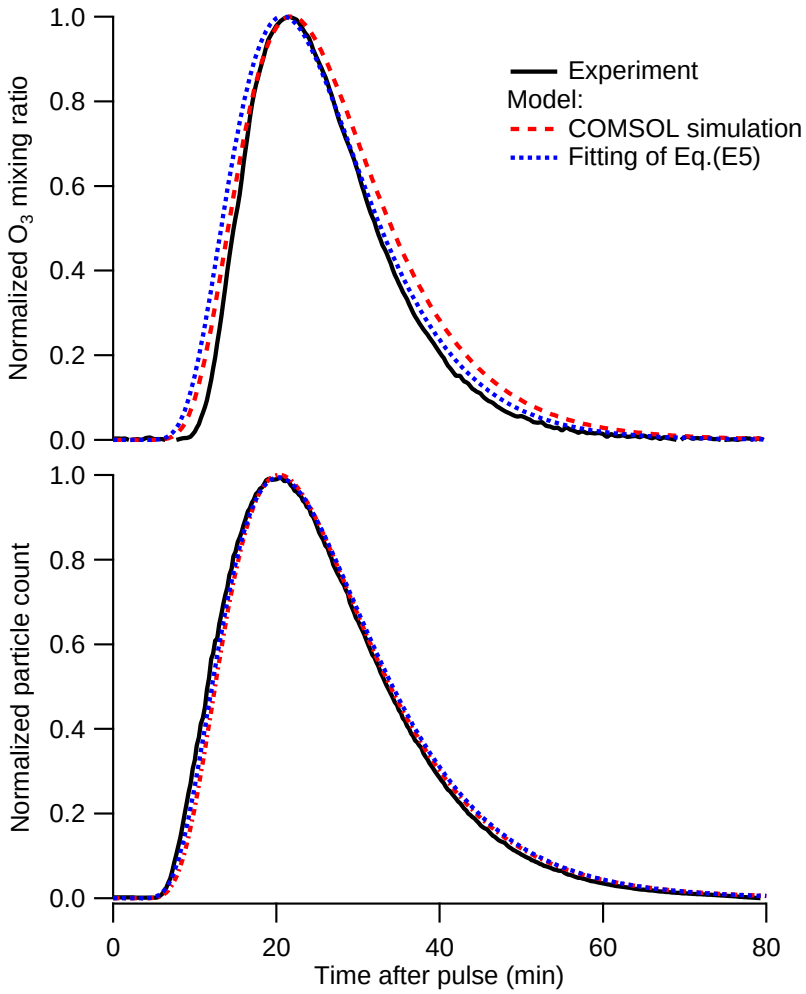

Figure 2.13: Comparison of experimentally determined RTD of (A) O_3 vapor molecules and (B) polydisperse ammonium sulfate particles to optimized simulation results employing an eddy-like diffusivity ($\mathscr{D}_e$) in the Taylor dispersion model. The COMSOL simulation employs an optimal $\mathscr{D}_e$ values of 4.5×10^{-4} m^2 s^{-1} for O_3 and 6.0×10^{-4} m^2 s^{-1} for particles. The fittings of Eq. (2.27) employs the same optimal $\mathscr{D}_e$, as well as an optimal average velocity ($U_{avg,fit}$) of 2.1×10^{-3} m s^{-1} and an optimal characteristic residence time ($\tau_{c,cyld,fit}$) of 1360 s.

m^2 s^{-1} and 6.0×10^{-4} m^2 s^{-1} for O_3 and particles, respectively (Fig. 2.13). These $\mathscr{D}_e$ values are, respectively, 45 and 6×10^5 times the diffusivity of vapor molecules and particles from the strictly parabolic flow base case (Fig. 2.11). The vapor molecule RTD (Fig. 2.13A) no longer exhibits the symmetrical feature of the base case, due to the enhanced Taylor dispersion. The particle RTD (Fig. 2.13B) is also substantially broadened compared to the base case and exhibits close agreement with the observations. The optimal $\mathscr{D}_e$ values for vapor molecules and particles are similar, suggesting that the molecular diffusion in the CPOT is dominated by the

secondary flows. This offers an explanation for the similarity in the observed RTD profiles of O_3 and particles, despite orders of magnitude difference in their inherent diffusivity.

To further evaluate the $\mathscr{D}_e$ values determined from the COMSOL simulations and the hypothesis of secondary flows, one can adopt a separate approach to examine $\mathscr{D}_e$. Given the mixing provided by the static mixer and the conical diffuser, the optimal values of $\mathscr{D}_e$ can be applied in Eq. (2.27). The values of $U_{avg,fit}$ and $\tau_{c,cyld,fit}$ are adjusted to find the best match between Eq. (2.27) and the observed RTD profiles. The optimal fitting results are shown in Fig. 2.13. The fitted average flow velocity ($U_{avg,fit}$) is 2.1×10^{-3} m s^{-1}, which results in a characteristic residence time $\tau_{c,cyld,fit}$ of 1360 s. This $U_{avg,fit}$ value agrees well with the designed average velocity (2.0×10^{-3} m s^{-1}). This observation again suggests that the non-isothermal secondary flow induced eddy-like diffusion dominates the mass transport process in the tube.

Overall, these results highlight the importance of temperature effects in approaching an ideal flow condition in a gas-phase laminar flow reactor. Even a small temperature deviation can likely create secondary flows in the flow field that affect both the RTD and the τ_{avg} of tracers. It is to be noted that these secondary flows occurring at Re $\cong$ 20 should be distinguished from the classic turbulent flow.

2.6 Photochemical Model

2.6.1 Behavior of Species in the Models

The fitted parameters in Section 2.5.3 have been used in the simulation of the photochemical reactions, and the results are shown in Fig. 2.14. The absorption cross section of H_2O_2 increases exponentially towards shorter wavelengths; hence, the Hg vapor lamp (Fig. 2.2) is highly efficient in photolyzing H_2O_2, whereas the efficiency drops substantially when UVB and UVA lamps are employed (Fig. 2.14A). The decay of SO_2 (Fig. 2.14B) and the steady-state concentration of the OH radical (Fig. 2.14C) follow the photolysis rates of H_2O_2 under each type of radiation. The model simulation also confirms that the OH radical reaches a steady state immediately, with its steady-state concentration, ranging from $\sim 10^6$ to $\sim 10^9$ molecules cm^{-3}, staying uniform along the entire tube in the presence of a high mixing ratio of H_2O_2.

As mentioned in Section 2.2.2, a small amount of the 185 nm radiation is present in the CPOT when Hg vapor lamps are equipped. Radiation at 185 nm generates

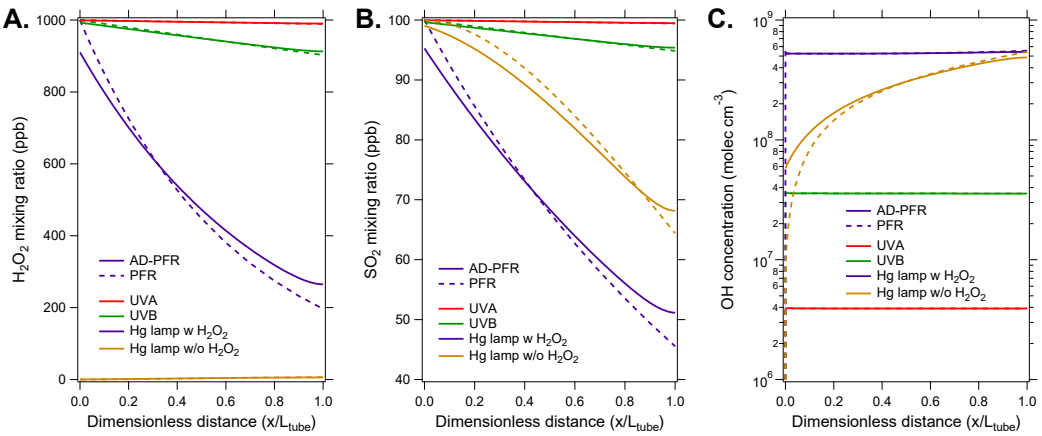

Figure 2.14: 1D photochemical model using axially-dispersed assumption (AD-PFR, solid line) and plug flow assumption (PFR, dashed line). 1 ppm H_2O_2 and 100 ppb SO_2 at RH = 5% and T = 295 K is used in the simulation. Hg vapor (purple), UVB (green), and UVA (red) lamps at full emission are used to drive the photochemical reactions. (A) Axial profile of H_2O_2, (B) Axial profile of SO_2, and (C) Axial profile of OH.

additional OH radicals via photolysis of O_2 and subsequent reaction between $O(^1D)$ and H_2O. We have performed control simulations to investigate the relative contribution of the OH radical generated from this pathway. No OH was generated in the absence of photolysis of O_2 that happens only in the presence of the 185 nm radiation (data not shown). With the full Hg vapor emission, even at an RH as low as 5%, a significant amount of the OH radical was generated in the absence of H_2O_2. The SO_2 decay without H_2O_2 was approximately half that with H_2O_2 (Fig. 2.14B). The OH concentration at the end of the reactor reached the same level as the case in which H_2O_2 is added (Fig. 2.14C) but a major difference was observed in the concentration profile of the OH radical along the tube. Without H_2O_2, the OH concentration increases along the tube, and consequently, the decay profiles of SO_2 do not follow that of a first-order decay.

Discrepancies were observed in the H_2O_2 and SO_2 concentration profiles near the inlet and exit of the CPOT between the PFR and AD-PFR models (Fig. 2.14A and B). These discrepancies arise from the necessary Danckwerts boundary condition, which is more significant at higher oxidation levels. The profiles indicate the effect from the axial dispersion, which arises from the axial mixing induced by secondary flow inside the reactor. The axial dispersion lowers the conversion of the reactant by smoothing the concentration gradient caused by reactions.

2.6.2 OH Exposure Calculation

The OH exposure (OH_{exp}) is commonly obtained based on the PFR assumption, using the initial and final concentrations of SO_2, i.e. $[SO_2]_0$ and $[SO_2]_\tau$. However, to use the PFR assumption, the effects of radial and axial dispersion need to be addressed. Under the PFR framework, radial diffusion is considered to be rapid, such that the concentration is uniform within a cross section. This assumption can be justified by comparing the radial diffusion timescale ($\frac{R^2}{\mathscr{D}}$) with the axial convection timescale ($\frac{L}{U}$), i.e. $\frac{R}{L}$Pe, where Pe is the Péclet number. A ratio of ~ 0.01 with the fitted parameters indicates that radial diffusion is approximately 100 times faster than axial convection and that a uniform cross-section concentration can be expected in the absence of any chemical reactions. The dimensionless group that relates the reaction rate to the diffusion rate is the Damköhler number (Da = $\frac{k^I R^2}{\mathscr{D}}$, where k^I is a first-order reaction rate constant). In the case of the oxidation of SO_2 by OH, $k^I = k^{II}_{SO_2{}^+OH}[OH]$. If Da $\ll 1$, the radial diffusion rate is much faster than the reaction rate, and a uniform cross-section concentration results. In the current chemical system, even with the Hg vapor lamps (the largest $j_{H_2O_2}$ and therefore the most rapid k^I), the Da value is $0.011 \ll 1$. We conclude that radial diffusion will dominate in the reactor and that the simplified 1D model framework is valid.

The effect of axial dispersion, on the other hand, should be accounted for in interpreting experimental data (Donahue et al., 1996; Howard, 1979). For the first-order reaction system, Howard (1979) showed that the presence of axial dispersion lowers the effective rate constant of a pseudo-first-order reaction by the factor ($1 - \frac{\mathscr{D}k^I}{U^2}$). This correction factor also applies to the OH_{exp} calculation.

Starting from the continuity equation, by the assumption of pseudo-first-order reaction ($k^I = k^{II}[OH]$), the equation governing the steady state concentration of the tracer down the tube $C(z)$ is:

$$U\frac{dC}{dz} = \mathscr{D}\frac{d^2C}{dz^2} - k^I C \tag{2.6}$$

Given two appropriate boundary conditions (B.C.s), one can obtain an analytical solution to Eq. (2.6). In order to use the same initial condition in the AD-PFR model as that in the PFR model, the 2nd order differential equation can be reduced to a 1st order equation through scale analysis. Scaling $C \sim C_0$, where C_0 is the

concentration of the tracer in the feed, and $z \sim \frac{U}{k^I}$, Eq. (2.6) becomes:

$$f\frac{d^2\tilde{C}}{d\tilde{z}^2} - \frac{d\tilde{C}}{d\tilde{z}} - \tilde{C} = 0 \tag{2.7}$$

where $\tilde{C} = \frac{C}{C_0}$, $\tilde{z} = \frac{k^I}{U}z$, and $f = \frac{\mathscr{D}k^I}{U^2}$. In the CPOT system, typical parameter values are: $\mathscr{D} \sim 10^{-4}$ m^2 s^{-1}, $k^I \sim 10^{-4}$ s^{-1}, and $U \sim 10^{-3}$ m s^{-1}, thus $f \sim 10^{-2}$. Owing to the relatively small magnitude of f, neglecting the second-order derivative term in Eq. (2.7), the solution of Eq. (2.7) is

$$C(z) = C_0 \exp\left(-\frac{k^I}{U}z\right) \tag{2.8}$$

Although f is small, it is not identically zero. To account for the perturbation that occurs due to the small axial dispersion term in Eq. (2.6), we substitute (2.8) into the diffusion term but retain the advection term in derivative form:

$$U\frac{dC}{dz} = \mathscr{D}\left(-\frac{k^I}{U}\right)^2 C - k^I C = -k^I(1-f)C \tag{2.9}$$

Then substituting $dt = \frac{dz}{U}$ and $k^I = k^{II}[\mathrm{OH}]$ in Eq. (2.9) one obtains:

$$\frac{dC}{dt} = -k^{II}(1-f)C[\mathrm{OH}] \tag{2.10}$$

In doing so, the diffusion-advection equation has been reduced to a single advection equation, in which the effect of axial dispersion is incorporated into the factor $1-f$.

Integrating Eq. (2.10), we obtain the $\mathrm{OH}_{\mathrm{exp}}$ expression that accounts for the presence of axial dispersion:

$$\mathrm{OH}_{\mathrm{exp}} = \int [\mathrm{OH}]dt = \frac{1}{k^{II}(1-f)} \ln\frac{C_0}{C_\tau} \tag{2.11}$$

Eq. (2.11) offers two ways to calculate $\mathrm{OH}_{\mathrm{exp}}$.

The left-hand term is a direct calculation based on the definition of exposure, and the integration incorporates the RTD induced by non-ideal flow conditions. This direct calculation of $\mathrm{OH}_{\mathrm{exp}}$ is most feasible by integrating a mechanism of OH-tracer chemistry, since OH is expected to be a function of t, which can be simulated. Specifically, if OH is uniform along the tube, $\int [\mathrm{OH}]dt = [\mathrm{OH}]\tau_{\mathrm{avg}}$, where τ_{avg} is the average residence time. This corresponds to the usual mode of operation. The

Table 2.1: Simulated OH exposure under full light emission

Lamp type	**OH_{exp}**[a] (molecules cm^{-3} s)		**Atmos. Equiv.**[b] (h)	
	PFR	AD-PFR_{corr}[c]	PFR	AD-PFR_{corr}
Hg vapor	8.0×10^{11}	7.3×10^{11}	222	203
UVB	5.4×10^{10}	4.9×10^{10}	15	13.6
UVA	6.0×10^{9}	5.4×10^{9}	1.7	1.5

[a]Input of OH exposure (OH_{exp}) simulation: 1 ppm H_2O_2 and 100 ppb SO_2 at RH = 5% and T = 295 K ([H_2O] = 1500 ppm).
[b]Atmospheric equivalent (Atmos. Equiv.) OH_{exp} values are converted to their equivalent hours of OH exposure in the ambient atmosphere, assuming a typical ambient OH concentration of 1×10^6 molecules cm^{-3}.
[c]PFR and AD-PFR_{corr} are calculated by Eqs. (2.12) and (2.11), respectively.

right-hand expression in Eq. (2.11) is an indirect calculation, OH_{exp}, based on the measured concentrations of the tracer at the inlet and the outlet of the reactor, C_0 and C_τ, respectively. Due to the presence of axial dispersion, the actual measured concentration C_τ at the outlet is higher than it would be in the absence of axial dispersion. If no correction for the axial dispersion is applied, the calculated OH_{exp} will be lower than it actually is. However, since f is generally small, the increase of OH_{exp} due to the presence of axial dispersion is limited to a factor of $\sim f$ (since $\frac{1}{1-f} \approx 1 + f$ as $f \ll 1$). For example, the largest $f = 0.05$ occurs in the Hg lamp system. If $f > 0.1$, e.g. more significant axial dispersion or much higher OH level, additional terms should be included in the approximate solution (2.8), and Eq. (2.10) has to be modified correspondingly. By comparison, in the typical advection system in the absence of axial dispersion, OH_{exp} is calculated simply as:

$$OH_{exp} = \frac{1}{k^{II}} \ln \frac{C_0}{C_\tau} \tag{2.12}$$

According to Eq. 2.11, the effect of axial dispersion is enhanced when the OH oxidation proceeds more rapidly (i.e. at higher k^I values) or the axial dispersion is stronger. There are several ways to estimate the OH exposure in the axially-dispersed flow system. R. Li et al. (2015) calculate the residence time dependent OH_{exp} first and then couple this relationship with the RTD. Because of the uniform OH concentration along the tube, the methods by R. Li et al. (ibid.) and Eq. (2.12) give the same OH_{exp}. In this work, we employ Eq. (2.11) for the AD-PFR model and compare the results with those calculated by Eq. (2.12) for the PFR model. The

simulated OH_{exp} results are summarized in Table 2.1, along with their atmospheric equivalent timescale. The results show that the PFR model always gives a higher OH_{exp} value and there is about an $8 \sim 10\%$ difference between the values calculated by the PFR and AD-PFR models, indicating the effect from axial dispersion. Peng et al. (2015) performed a detailed comparison of OH_{exp} calculated with the PFR model, the coupling of RTD with PFR model, and the experimental tracer decay method. The authors recommended using the experimental tracer decay method. For a non-ideal flow reactor, we suggest using Eq. (2.11) to account for axial dispersion in the evaluation of OH_{exp}.

Overall, the current photochemical model indicates that with H_2O_2 as the OH precursor in the absence of NO_x, the CPOT can achieve a wide range of steady-state OH concentrations and OH_{exp} that are comparable to the PAM system (Lambe et al., 2011a; R. Li et al., 2015).

2.7 Conclusions

We report the development of a laminar flow tube reactor for studies of atmospheric VOC oxidation and formation of secondary organic aerosol. The flow tube reactor has been designed to achieve a relatively well-defined flow environment for interpretation of reaction conditions. As has been recognized in existing flow tube reactors, inlet design plays a significant role in establishing the fluid dynamic environment in the reactor. The current design comprises a static mixer followed by a conical diffuser. Computational fluid dynamics (CFD) simulations demonstrate that this injection scheme introduces flow into the reaction section that avoids flow separation from the wall, assisting a rapid transition to a parabolic profile under idealized, isothermal conditions. Some loss of reactive species, H_2O_2, used as an OH precursor, occurs in the static mixer; however, this loss can be compensated by an increased feed concentration designed to generate the desired OH level in the reactor.

The fluid dynamics in the reactor was examined experimentally by comparing the penetration efficiency (η) and residence time distribution (RTD) of vapor molecules and particles to those predicted under ideal laminar flow conditions. O_3 and SO_2 molecules exhibit $\sim$ 100% transmission in the static mixer. H_2O_2 losses in the static mixer are 20% to 40%, increasing as RH increases. Small particles are lost at $\sim$ 50% in the static mixer. The penetration efficiency of polydisperse ammonium sulfate particles under dry conditions was measured and compared with theoretical

predictions accounting for diffusional deposition and gravitational sedimentation in laminar flow. The penetration efficiency calculated with this theory captures the trend in the two regimes; i.e. in the diffusion regime, the smaller the particles, the more loss they exhibit, while in the settling regime, the larger the particles, the more the deposition. A simple coagulation model calculation suggests that the coagulation process accounts for half of the particle number loss over the small size range.

As has been noted in prior studies of flow regime behavior in flow tube reactors, comparison of theoretically predicted and observed RTDs of vapors and particles reveal the importance of small temperature gradients in inducing a departure from the ideal laminar flow. Despite the presence of a temperature-controlled water jacket, the RTD profiles are affected by slightly non-isothermal conditions in the reactor that lead to secondary flows. This conclusion is supported by substantially improved agreement between observed and predicted RTDs when an enhanced eddy-like diffusivity ($\mathscr{D}_e$) is employed in the CFD simulations. The best-fit ($\mathscr{D}_e$) values, 4.5×10^{-4} m^2 s^{-1} and 6.0×10^{-4} m^2 s^{-1} for O_3 and particles, respectively, are sufficiently large to indicate that the transport of tracers is likely dominated by secondary flow.

Despite these flow non-idealities, the observations and simulations demonstrate that the combination of the static mixer/conical diffuser allows a radially uniform and axially dispersed flow system to develop within the reactor, useful for quantitative kinetics studies. A 1D photochemical model is formulated correspondingly. When H_2O_2 is employed as the OH precursor, the model predicts that the OH concentration is uniform along the whole tube. The extent to which this uniformity depends on the external OH reactivity, i.e. [tracer]$k_{\text{tracer+OH}}$, will be evaluated in future work. The system can produce a wide range of OH_{exp} under different radiation conditions for specific scientific objectives. Future work will focus on detailed studies of secondary organic aerosol formation, with particular attention given to wall interactions of gases and particles.

2.8 Supporting Information

2.8.1 Determination of Photon Fluxes

The irradiance of the three types of lamps from 190 to 850 nm ($E_{e,\lambda}$) was recorded using an Ocean Optics fiber optic spectroradiometer (HR2000CG-UV-NIR). The unit is pre-calibrated by the manufacturer and is equipped with a 20 cm long fiber optic cable, which can be inserted into the CPOT through one of the sampling ports so that the recorded spectra reflect those inside the CPOT.

The j_{NO_2} values were determined by photolyzing 200 ppb of NO_2 that is continuously supplied to the reactor. Mixing ratios of NO_2, NO and O_3 were monitored at the exit cone. Experimental results employing the UVA lamps are shown in Fig. 2.15. A fraction of NO_2 is photolyzed, forming an equivalent amount of NO and O_3. The j_{NO_2} value can be obtained using the photo-stationary state assumption (J. H. Seinfeld and S. N. Pandis, 2016):

$$j_{NO_2} = \frac{k_{NO+O_3}[O_3][NO]}{[NO_2]} \tag{2.13}$$

where $[O_3]$, $[NO_2]$ and [NO] are the concentrations of these three species at photo-stationary state, respectively. k_{NO+O_3} is the rate coefficient of the reaction NO + O_3, and a value of 1.9×10^{-14} cm^3 $molec^{-1}$ s^{-1} (298 K) is used here (ibid.). The j_{NO_2} value obtained from this experiment is 5.36×10^{-3} s^{-1}. The validity of the photo-stationary phase was confirmed by solving a simple kinetic model of relevant species (i.e. the mixing ratios of the three species did not further change within the CPOT run time).

The UVA flux was adjusted until we obtained a light intensity $I(\lambda)$ that best represents the observed j_{NO_2}. The photolysis rate of species i, j_i, can be obtained as the integral of its quantum yield ($\phi_i(\lambda)$), absorption cross section ($\sigma_i(\lambda)$) and the photon flux ($I(\lambda)$) over wavelengths λ_1 to λ_2:

$$j_i = \int_{\lambda_1}^{\lambda_2} \phi_i(\lambda)\sigma_i(\lambda)I(\lambda)d\lambda \tag{2.14}$$

Determination of j_{NO_2} under the Hg vapor lamps and UVB lamps, however, was difficult because photolysis of NO_2 leads to a net loss of NO_x when these lamps were used (i.e. the photo-stationary state was not achieved). We suspect the reason is that light with shorter wavelengths created an excess amount of $O(^1D)$.

Alternatively, we determined the fluxes of the Hg vapor lamp and the UVB lamp by relating the signal strength obtained from these two types of lamp to that from

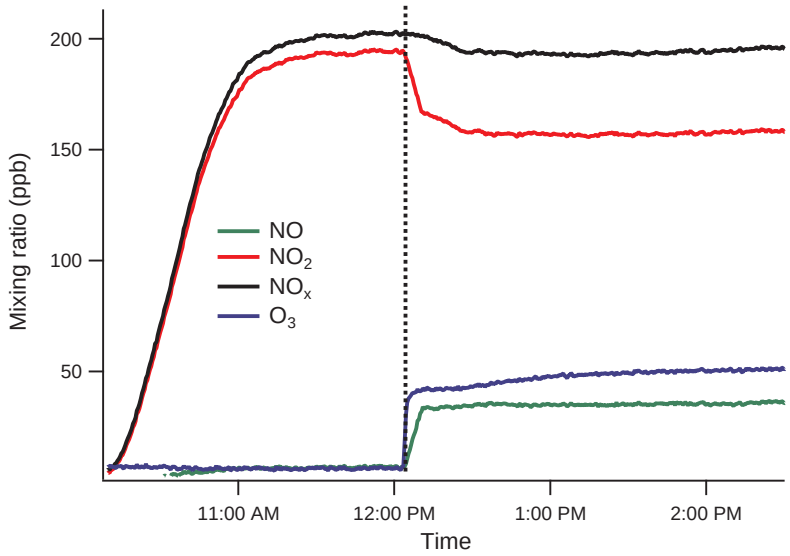

Figure 2.15: The temporal profiles of NO_2, NO, NO_x and O_3 at the end of the CPOT during a NO_2 photolysis experiment. The lamps were turned on at the time indicated by the dashed line.

the UVA lamp. We fixed the fiber optics probe at the same position while changing the type of lamps surrounding the CPOT. By doing this, we assume that the ratio between the recorded spectra represents the ratio of their photon fluxes.

The Hg vapor lamp emits wavelength at 185 nm at an intensity typically less than 1 % of that at 254 nm (R. Li et al., 2015). Direct quantification of 185 nm light in the CPOT is difficult because the fiber optic spectrometer cannot record radiation with wavelengths shorter than 190 nm. Instead, the intensity of the 185 nm light can be roughly estimated from O_3 formation. Under full emission of the Hg vapor lamp with 2 L min^{-1} of clean air flowing through, we observe 60 ppb of O_3 at the exit cone. Assuming all of O_3 has arisen from O_2 photolysis, the radiation intensity at 185 nm can be evaluated based on the Chapman mechanism (J. H. Seinfeld and S. N. Pandis, 2016) with an average residence time of 1520 s (Section 2.5.2.2). The intensity of the 185 nm band is estimated to be 10^{-5} that of the 254 nm band, the majority of which is likely absorbed by the water jacket.

2.8.2 Photochemical Reactions

Table 2.2: Photolysis reactions in OH generation

#	Reaction	Photolysis Rate @ Hg Lamps[s^{-1}]	Photolysis Rate @ UVB Lamps[s^{-1}]	Photolysis Rate @ UVA Lamps[s^{-1}]
1	$H_2O_2 \xrightarrow{h\nu} 2\,OH$	5.48×10^{-4}	3.54×10^{-5}	4.44×10^{-6}
2	$O_2 \xrightarrow{h\nu} 2\,O$	1.97×10^{-11}	0	0
3	$O_3 \xrightarrow{h\nu} O_2 + O(^1D)$	7.64×10^{-2}	1.94×10^{-3}	1.53×10^{-5}
4	$O_3 \xrightarrow{h\nu} O_2 + O$	8.50×10^{-3}	3.22×10^{-4}	2.61×10^{-5}
5	$H_2O \xrightarrow{h\nu} OH + H$	5.79×10^{-10}	0	0
6	$HO_2 \xrightarrow{h\nu} OH + O(^1D)$	2.60×10^{-3}	3.86×10^{-5}	1.76×10^{-7}

Absorption cross sections and quantum yields come from Burkholder et al. (2015) and IUPAC (`http://iupac.pole-ether.fr/`). The photon flux was measured in the current study conducted in Caltech. O refers to $O(^3P)$. All lamps are at full emission.

Table 2.3: Reactions in OH generation and SO_2 oxidation

#	Reaction	Rate Constant $[(cm^3/molecule)^{n-1}s^{-1}]^a$	Low-pressure limit rate constant (k_0)	High-pressure limit rate constant (k_∞)
1	$O^b + O_2 + M \longrightarrow O_3 + M$	$6.0 \times 10^{-34} M (300/T)^{2.4}$		
2	$O + O_3 \longrightarrow 2\,O_2$	$8.0 \times 10^{-12} \exp(-2060/T)$		
3	$H + HO_2 \longrightarrow H_2 + O_2$	6.9×10^{-12}		
4	$H + HO_2 \longrightarrow 2\,OH$	7.2×10^{-11}		
5	$H + HO_2 \longrightarrow H_2O + O$	1.6×10^{-12}		

(Continued)

#	**Reaction**	**Rate Constant** $[(\mathrm{cm}^3/\mathrm{molecule})^{n-1}\mathrm{s}^{-1}]^a$	**Low-pressure limit rate constant** (k_0)	**High-pressure limit rate constant** (k_∞)
6	$H + O_2 + M \longrightarrow HO_2 + M$	Eq(1)[c]	$4.4 \times 10^{-32} M (300/T)^{1.3}$	$7.5 \times 10^{-11} (300/T)^{-0.2}$
7	$H + O_3 \longrightarrow OH + O_2$	$1.4 \times 10^{-10} \exp(-470/T)$		
8	$O + OH \longrightarrow O_2 + H$	$1.8 \times 10^{-11} \exp(180/T)$		
9	$O + HO_2 \longrightarrow OH + O_2$	$3.0 \times 10^{-11} \exp(200/T)$		
10	$O + H_2O_2 \longrightarrow OH + HO_2$	$1.4 \times 10^{-12} \exp(-2000/T)$		
11	$OH + H_2 \longrightarrow H_2O + H$	$2.8 \times 10^{-12} \exp(-1800/T)$		
12	$2\,OH \longrightarrow H_2O + O$	1.8×10^{-12}		
13	$2\,OH + M \longrightarrow H_2O_2 + M$	Eq(1)	$6.9 \times 10^{-31} (300/T)$	2.6×10^{-11}
14	$OH + HO_2 \longrightarrow H_2O + O_2$	$4.8 \times 10^{-11} \exp(250/T)$		
15	$OH + H_2O_2 \longrightarrow H_2O + HO_2$	1.8×10^{-12}		
16	$OH + O_3 \longrightarrow HO_2 + O_2$	$1.7 \times 10^{-12} \exp(-940/T)$		
17	$HO_2 + HO_2 \longrightarrow H_2O_2 + O_2$	$(3.0 \times 10^{-13} \exp(460/T) + 2.1 \times 10^{-33} \exp(920/T)) (1 + 1.4 \times 10^{-21} [H_2O] \exp(2200/T))$		
18	$HO_2 + O_3 \longrightarrow OH + O_2 + O_2$	$1.0 \times 10^{-14} \exp(-490/T)$		
19	$O(^1D) + O_2 \longrightarrow O + O_2$	$3.3 \times 10^{-11} \exp(55/T)$		
20	$O(^1D) + N_2 \longrightarrow O + N_2$	$2.15 \times 10^{-11} \exp(110/T)$		
21	$O(^1D) + O_3 \longrightarrow 2\,O_2$	1.2×10^{-10}		
22	$O(^1D) + O_3 \longrightarrow O_2 + 2\,O$	1.2×10^{-10}		

(Continued)

#	**Reaction**	**Rate Constant** $[(\mathrm{cm}^3/\mathrm{molecule})^{n-1}\mathrm{s}^{-1}]^a$	**Low-pressure limit rate constant** (k_0)	**High-pressure limit rate constant** (k_∞)
23	$O(^1D) + H_2 \longrightarrow OH + H$	1.2×10^{-10}		
24	$O(^1D) + H_2O \longrightarrow 2\,OH$	$1.63 \times 10^{-10} \exp(60/T)$		
25	$O + SO_2 + M \longrightarrow SO_3 + M$	Eq(1)	$5.3 \times 10^{-29}(300/T)^{4.4}$	$1.9 \times 10^{-11}(300/T)^{1.8}$
26	$OH + SO_2 + M \longrightarrow HOSO_2 + M$	Eq(1)	$3.3 \times 10^{-31}(300/T)^{4.3}$	1.6×10^{-12}
27	$SO_3 + 2\,H_2O \longrightarrow H_2O + H_2SO_4$	$8.5 \times 10^{-41} \exp(6540/T)[H_2O]^2$		
28	$HOSO_2 + O_2 \longrightarrow HO_2 + SO_3$	$1.3 \times 10^{-12} \exp(-330/T)$		

Rate constants from Burkholder et al. (2015) and IUPAC (`http://iupac.pole-ether.fr/`).

[a]Note that n represents the reaction order *not* including the effects of the bath gas M. The bath gas is already considered in the calculation of each rate constant.

[b]Without any specific indication, O refers to $O(^3P)$.

[c]Eq(1): $k(M,T) = \dfrac{k_0 M}{1 + k_0 M/k_\infty} 0.6^{\left\{1+\left[\log_{10}(k_0 M/k_\infty)\right]\right\}^{-1}}$

2.8.3 Danckwerts Boundary Condition

At steady state, the simplified 1D governing equation is:

$$\mathscr{D}_{\mathrm{e}} \frac{d^2 c_i}{dz^2} - U_{\mathrm{avg,fit}} \frac{dc_i}{dz} + \sum_i R_i = 0 \tag{2.15}$$

The first term is the axial diffusion, the second term is the convection, and the third term contains all the sources and sinks. Equation (2.15) has incorporated the Taylor dispersion derived RTD information. Thus we can solve it as a RTD coupled transport problem. We also employ the Danckwerts boundary condition, which ensures the continuity of the flux:

$$U_{\mathrm{avg,fit}} c_i \Big|_{0_-} = \left[U_{\mathrm{avg,fit}} c_i - \mathscr{D}_{\mathrm{e}} \frac{dc_i}{dz} \right] \Bigg|_{0_+} \tag{2.16}$$

$$\frac{dc_i}{dz} \Bigg|_{L_-} = 0 \tag{2.17}$$

In Eq. (2.16), $c_i\big|_{0_-}$ is the input concentration, while $c_i\big|_{0_+}$ is unknown and should be solved. It is this form that determines the discontinuity of the concentration at the inlet. With all the known reactions (Section 2.8.2), one can solve Eqs. (2.15) to (2.17) numerically. If one wants to add the wall loss terms, assuming a first-order wall loss rate, k_{wi}, the surface-to-volume ratio ($\frac{S}{V}$) of the reactor should be added, i.e. $\frac{S}{V} k_{wi} c_i$. The k_{wi} value can be preset if we are interested in the output, or can be determined as long as we know the output. The parameters used in these equations are: $\mathscr{D}_{\mathrm{e}} = 4.5 \times 10^{-4}$ m^2 s^{-1}, $U_{\mathrm{avg,fit}} = 2.1 \times 10^{-3}$ m s^{-1}, $\tau_{\mathrm{c,cyld,fit}} = 1360$ s, and $L = U_{\mathrm{avg,fit}} \tau_{\mathrm{c,cyld,fit}}$. As a comparison, a plug flow reactor model runs at the same time, with the only parameter as $\tau_{\mathrm{avg}} = 1520$ s.

2.8.4 Diffusional Loss in A Laminar Cylindrical Tube

The full conservation equation for gas-phase species i, $c_i(t, r, z)$, is

$$\frac{\partial c_i}{\partial t} + v_z(r)\frac{\partial c_i}{\partial z} = \mathscr{D}_i \left[\frac{1}{r}\frac{\partial}{\partial r}\left(r\frac{\partial c_i}{\partial r}\right) + \frac{\partial^2 c_i}{\partial z^2}\right] + P_i - S_i \tag{2.18}$$

where $\mathscr{D}_i$ is the molecular diffusivity of species i in air, and P_i and S_i are the rates of generation and consumption of species i, by chemical reaction and gas-particle partitioning, respectively. A typical order of magnitude estimate of the molecular diffusion coefficient for vapor molecules in air is $\sim 10^{-5}$ m^2 s^{-1}. Under conditions typical of the operation of the flow tube reactor, the magnitude of the axial molecular diffusion term in Eq. (2.18) is small relative to that of the other terms in the equation and may be neglected. E. J. Davis (2008) gives a thorough discussion on the analytical solution for this system that is at steady state. Without any generation and consumption of species i, Eq. (2.18) becomes:

$$v_z(r)\frac{\partial c_i}{\partial z} = \mathscr{D}_i \left[\frac{1}{r}\frac{\partial}{\partial r}\left(r\frac{\partial c_i}{\partial r}\right)\right] \tag{2.19}$$

Equation 2.19 is subject to a boundary condition at the reactor entrance, $z = 0$:

$$c_i(r, 0) = c_{i0} \tag{2.20}$$

where a uniform concentration c_{i0} is assumed at the inlet of the reactor, and the symmetry condition at the centerline of the reactor, $r = 0$:

$$\frac{\partial c_i}{\partial r}(0, z) = 0 \tag{2.21}$$

A general boundary condition at the reactor wall allows for the possible deposition of species i on the wall, is

$$\mathscr{D}_i \frac{\partial c_i}{\partial r}(R, z) = -k_{wi} c_i \tag{2.22}$$

where k_{wi} is a first-order wall deposition coefficient for species i. k_{wi} can be expressed in terms of the uptake coefficient for species i, γ_i, as $k_{wi} = \frac{1}{4}\gamma_i \omega_i$, where ω_i is the mean molecular speed of species i. Either k_{wi} or γ_i must be determined experimentally. If no uptake of species i occurs at the wall, then $k_{wi} = 0$.

2.8.5 Taylor Dispersion-Based RTD

By cross-section averaging of Eq. (2.18) (without sources and sinks), the average concentration at any cross section obeys:

$$\frac{\partial \langle c_i \rangle}{\partial t} + U_{\text{avg}} \frac{\partial \langle c_i \rangle}{\partial z} = \mathscr{D}_{\text{eff},i} \frac{\partial^2 \langle c_i \rangle}{\partial z^2} \tag{2.23}$$

where $\mathscr{D}_{\text{eff},i} = \mathscr{D}_i \left(1 + \frac{\text{Pe}^2}{192}\right)$ which accounts for the convective enhancement in diffusivity (Aris, 1956), where Pe, the Péclet number, is $\frac{2RU_{\text{avg}}}{\mathscr{D}_i}$.

The solution of Eq. (2.23) for a pulse input at the entrance to the reactor, of N_0 moles over the cross section area A of the tube, is:

$$\langle c_i \rangle(t, z) = \frac{1}{\sqrt{4\pi \mathscr{D}_{\text{eff},i} t}} \frac{N_0}{A} \exp\left[-\frac{(z - U_{\text{avg}} t)^2}{4\mathscr{D}_{\text{eff},i} t}\right] \tag{2.24}$$

The RTD of the diffusive species in the flow tube, i.e. at $z = L_{\text{cyld}}$, is:

$$\langle c_i \rangle(t, L_{\text{cyld}}) = \frac{1}{\sqrt{4\pi \tilde{\mathscr{D}}_{\text{eff},i} \tilde{t}}} \frac{N_0}{V} \exp\left[-\frac{(1 - \tilde{t})^2}{4\tilde{\mathscr{D}}_{\text{eff},i} \tilde{t}}\right] \tag{2.25}$$

where V is the volume of the tube, $\tilde{\mathscr{D}}_{\text{eff},i} = \frac{\mathscr{D}_{\text{eff},i}}{\tau_{c,\text{cyld}} U_{\text{avg}}^2}$, and $\tilde{t} = \frac{t}{\tau_{c,\text{cyld}}}$.

For a pulse input, of finite duration t_0,

$$\langle c_i \rangle(t, z = 0) = \begin{cases} \dfrac{N_0}{A U_{\text{avg}} t_0} & 0 \le t \le t_0 \\ 0 & t > t_0 \end{cases} \tag{2.26}$$

The RTD at $z = L_{\text{cyld}}$ is:

$$\langle c_i \rangle(t, L_{\text{cyld}}) = \frac{N_0}{2V} \left[\text{erf}\left(\frac{1 - \tilde{t}}{\sqrt{4\tilde{\mathscr{D}}_{\text{eff},i} \tilde{t}}}\right) - \text{erf}\left(\frac{1 - \tilde{t} - \tilde{t}_0}{\sqrt{4\tilde{\mathscr{D}}_{\text{eff},i} \tilde{t}}}\right)\right] \tag{2.27}$$

where $\text{erf}(x) = \frac{2}{\sqrt{\pi}} \int_0^x \exp(-\eta^2) d\eta$ and $\tilde{t}_0 = \frac{t_0}{\tau_{c,\text{cyld}}}$. More generally, by transforming $t = -\frac{z}{U_{\text{avg}}} = -\frac{z}{L_{\text{cyld}}} \frac{L_{\text{cyld}}}{U_{\text{avg}}} = -\tilde{z} \tau_{c,\text{cyld}}$, where $\tilde{z} = \frac{z}{L_{\text{cyld}}}$, the RTD for a non-ideal pulse input $f(t)$ (e.g. the solid profile in Fig. 2.6C) is in the form of:

$$\langle c_i \rangle(t, L_{\text{cyld}}) = \frac{1}{\sqrt{4\pi \tilde{\mathscr{D}}_{\text{eff},i} \tilde{t}}} \frac{N_0}{V} \int_{-\infty}^{+\infty} f(-\tilde{z} \tau_{c,\text{cyld}}) \exp\left[-\frac{(1 - \tilde{t} - \tilde{z})^2}{4\tilde{\mathscr{D}}_{\text{eff},i} \tilde{t}}\right] d\tilde{z} \tag{2.28}$$

where $\tilde{\mathscr{D}}_{\text{eff},i}$ and $\tilde{t}$ are defined as in Eqs. (2.25) and (2.27).

2.8.6 Particle Size Dependent RTDs

Figure 2.8 can be used to define two separate regimes of particle behavior, i.e. settling regime (diameter larger than 80 nm) and diffusion regime (otherwise).

While cylindrical coordinates are usually employed in a flow tube reactor, it will prove to be advantageous to use a Cartesian coordinate framework for the numerical simulation of particle settling in horizontal laminar flow in a tubular geometry. In the settling regime, particle motion in a horizontal tubular laminar flow is governed by the following differential equations for particle position, $(x(t),\ y(t),\ z(t))$, in a Cartesian coordinate system (with origin at the center of the tube at $t = 0$, as shown in Fig. 2.16):

$$\frac{dx}{dt} = 0 \tag{2.29}$$

$$\frac{dy}{dt} = -v_y(D_p) = -v_s(D_p) \tag{2.30}$$

$$\frac{dz}{dt} = v_z(x, y) = U_{\max}\left(1 - \frac{x^2 + y^2}{R^2}\right) \tag{2.31}$$

Given an initial particle position, $x(0) = x_0$, $y(0) = y_0$, $z(0) = z_0$, this set of equations can be solved either numerically or analytically. Examples of the numerical simulation of particle trajectories are shown in Fig. 2.16.

The analytical solution of Eqs. (2.29) – (2.31) for the time τ that a particle resides in the flow is:

$$\tilde{t}^3 - 2\tilde{y}\tilde{t}^2 - (1 - \tilde{x}^2 - \tilde{y}^2)\tilde{t} + t_1/t_2 = 0 \tag{2.32}$$

where $\tilde{x} = x_0/R$, $\tilde{y} = y_0/R$, $t_1 = L_{\text{cyld}}/U_{\max}$, $t_2 = R/v_s$, and $\tilde{t} = t/t_2$. $\tilde{x}$ and $\tilde{y}$ are subject to the condition:

$$\tilde{y}(1 - \tilde{x}^2) - \frac{1}{3}\tilde{y}^3 - \frac{t_1}{t_2} + \frac{2}{3}(1 - \tilde{x}^2)^{3/2} \le \tilde{x}^2 + \tilde{y}^2 \le 1 \tag{2.33}$$

The integral over this closed space leads to the penetration efficiency η for non-diffusive monodisperse particles:

$$\eta = \frac{2}{\pi}(-2\epsilon\sqrt{1 - \epsilon^{2/3}} + \epsilon^{1/3}\sqrt{1 - \epsilon^{2/3}} + \arcsin\sqrt{1 - \epsilon^{2/3}}) \tag{2.34}$$

where $\epsilon = \dfrac{3t_1}{4t_2}$ and the implicit condition here is that $\epsilon \le 1$, i.e. $v_s \le \dfrac{4R}{3L_{\text{cyld}}}U_{\max}$, otherwise $\eta = 0$. Calculated theoretical RTD and η are shown in Fig. 2.17.

The RTD of non-diffusing materials along each streamline for a pulse input is:

$$\langle n\rangle(t, L_{\text{cyld}}) = \begin{cases} 0 & 0 \le t < t_1 \\ \dfrac{2N_0 t_1^2}{AU_{\text{avg}}t^3} & t \ge t_1 \end{cases} \tag{2.35}$$

where N_0 is the total input quantity of the pulse, the same as defined in Section 2.8.5.

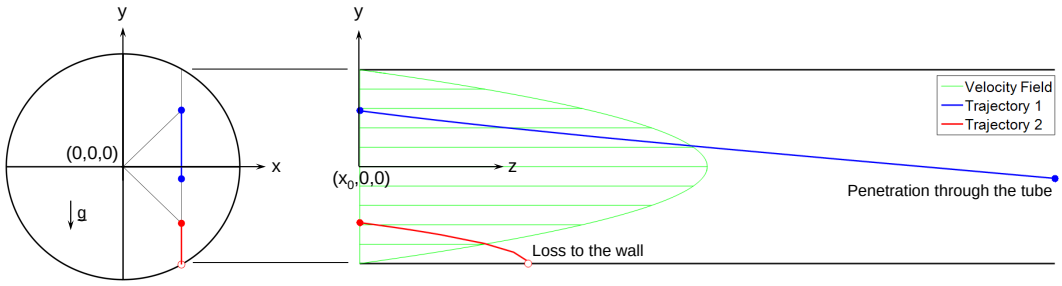

Figure 2.16: Particle trajectories in a vertical plane in a laminar flow tube. Particles are of the same size and are subject to gravitational settling and fluid advection. The Cartesian coordinate framework is indicated. Two different cases are shown: blue particles are those that can successfully penetrate through the tube, while red particles eventually deposit on the tube wall.

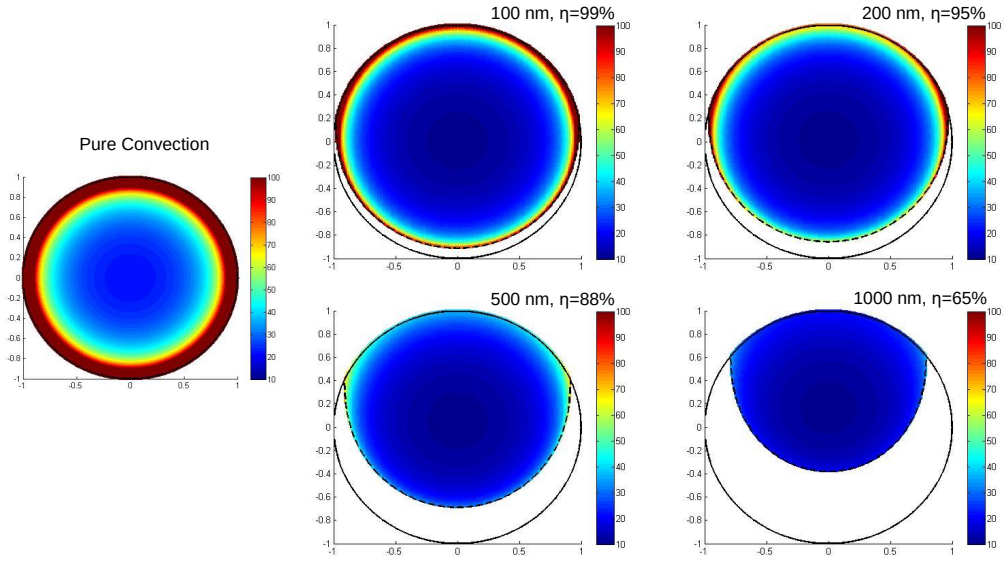

Figure 2.17: Theoretical residence time distribution (Eq. (2.32)) and penetration efficiency (Eq. (2.34)) of particles with different diameters in a horizontal flow tube. Only gravitational settling and convection are considered. The simulation assumes a uniform distribution of monodisperse particles at the entrance of a well-developed laminar flow with no interaction between particles. Each point corresponds to the residence time and the initial position of the particle. The color bar indicates the residence time (min). The open space between the dashed curve and the tube wall indicates the region in which particles have deposited on the tube wall (η = 0%). The residence time of purely convective, non-diffusing particles (Eq. (2.35)) is shown for reference.

2.8.7 List of Symbols

Symbol	Meaning	unit
A	cross section of the reactor	m^2
c	concentration	mol m^{-3}
D	reactor diameter	m
D_p	particle diameter	nm
$\mathscr{D}$	diffusivity	m^2 s^{-1}
g	gravitational acceleration	m s^{-2}
k_w	mass transport coefficient to the wall	m s^{-1}
L	length of the reactor	m
n	particle number concentration	cm^{-3}
N_0	total moles or number of the pulse input	mole or number
P	generation rate of species	molec cm^{-3} s^{-1}
R	radius of the reactor	m
S	consumption rate of species	molec cm^{-3} s^{-1}
t_0	duration	s
T	temperature	K
U	characteristic velocity of the fluid	m s^{-1}
v	velocity	m s^{-1}
V	volume of the reactor	m^3
Q	volumetric flow rate	m^3 s^{-1}
Greek		
β	thermal expansion coefficient of fluid	K^{-1}
μ	viscosity of the fluid	kg m^{-1} s^{-1}
ν	kinematic viscosity	m^2 s^{-1}
ρ	density of fluid	kg m^{-3}
θ	angle of the cone	$^\circ$
τ	residence time	s
ω	mean molecular speed	m s^{-1}

Note: Some of the symbols appear in Section 2.8.4 - 2.8.6.

2.8.8 List of Dimensionless Numbers and Subscripts

Symbol	Name	Expression
Greek		
γ	uptake coefficient	
η	penetration efficiency	
ϵ	ratio of timescale of convection to that of settling	$3L_{\text{cyld}}v_s/4RU_{\text{max}}$
ξ	dimensionless length	$\pi\mathscr{D}L_{\text{cyld}}/Q$
Dimensionless groups		
Gr	Grashof number	$g\beta D^3\Delta T/\nu^2$
Pe	Péclet number	$2RU_{\text{avg}}/\mathscr{D}_i$
Re	Reynolds number	$\rho U_{\text{avg}}D/\mu$
Ri	Richardson number	Gr / Re^2
Subscripts		
c	characteristic value	
cyld	cylindrical tube	
e	eddy-like	
fit	fitted result	
i	species	
j	time step	
s	settling	
avg	average value	
eff	effective value	
entr	entrance	
in	inlet	
max	maximum value	
out	outlet	
r	r-component in cylindrical framework	
x	x-component in Cartesian framework	
y	y-component in Cartesian framework	
z	z-component in Cartesian or cylindrical framework	
Superscripts		
I	first-order reaction rate	
II	second-order reaction rate	
overbar		
˜	nondimensionalized variable	

Note: Some of the symbols appear in Section 2.8.4 - 2.8.6.

Chapter 3

A NOTE ON FLOW BEHAVIOR IN AXIALLY-DISPERSED PLUG FLOW REACTORS WITH STEP INPUT OF TRACER

Huang, Yuanlong and John H. Seinfeld (2019). "A note on flow behavior in axially-dispersed plug flow reactors with step input of tracer". In: *Atmos. Environ.: X* 1, p. 100006. DOI: 10.1016/j.aeaoa.2019.100006.

Abstract

Atmospheric chemistry studies are frequently conducted in flow reactors, such as the potential aerosol mass (PAM) reactor. To characterize the flow condition in such a reactor, an axially-dispersed plug flow reactor (AD-PFR) model has been applied to explain the observed residence time distribution (RTD). Compared with the traditional RTD analysis that directly fits the observed data from a pulse input or differentiates the data points from a step input, we introduce here a direct method to retrieve the axial diffusivity in an AD-PFR model by fitting an analytical formula to the rising profile of the tracer at the beginning of the experiment (the transition data before the reactor reaches steady state). This method can be readily used to determine the flow conditions inside an AD-PFR.

3.1 Introduction

Flow reactors have achieved a prominent status in the study of atmospheric chemistry. The nature of the flow in such reactors plays a role in interpretation of the kinetic data obtained within the reactor. For a cylindrical flow reactor with sufficiently low Reynolds number (Re), the fluid velocity field is parabolic laminar flow. After a sufficient distance downstream, a radial velocity gradient-induced concentration difference can be smoothed by radial molecular diffusion. In this case, the three-dimensional tubular transport becomes essentially a one-dimensional convective-diffusive flow known as Taylor dispersion (G. I. Taylor, 1953). Temperature differences between the fluid and the reactor wall may also serve to perturb the ideal parabolic profile and induce radial mixing (Huang et al., 2017). An axially-dispersed plug flow reactor (AD-PFR) model applies in these situations of non-ideal, low-Re flow reactors.

To better understand the chemical kinetics in the flow tube reactor within the AD-

PFR framework, the two necessary parameters are the intensity of axial dispersion and the average residence time, which can be derived from the residence time distribution (RTD) of a tracer that is non-interactive with the wall. Then the AD-PFR model can be parameterized to reproduce experimental data. In addition to simulation, the parameters can be used to adjust the measured oxidation exposure (residence time $\times$ concentration, e.g., OH exposure, ibid.), a common quantity to represent the degree of oxidation occurring in an oxidation flow reactor. In all cases, the RTD plays an important role in evaluating these parameters.

The residence time distribution (RTD), often referred to as an E-curve, is widely used to diagnose the physics of the transport in such flow reactors. An E-curve is generated by a pulse or step injection, with the temporal concentration profile being monitored at the outlet of the reactor. Measurement of the RTD at the exit of the reactor affords an analysis of the chemical kinetics occurring in the reactor (R. Li et al., 2015; Peng et al., 2015). A pulse input of tracer requires injection of a quantity of tracer within a period of time much shorter than the average residence time in the reactor; on the other hand, a step input requires a stable and constant source of tracer. The step input affords a smoother E-curve from which the rising portion of the curve (known as the F-curve) can be obtained more easily. Mitroo et al. (2018) also reported the step-down method, in which a reactor initially filled with tracer is replaced by clean air, and from which an E-curve with a smooth tail can be obtained. In summary, analysis of experimental data on the nature of flow in the flow reactor generally includes: (1) direct E-curve fitting from a pulse input (Huang et al., 2017; Lambe et al., 2011a; Simonen et al., 2017); (2) E-curve fitting by differentiating the F-curve from a step input of tracer (Mitroo et al., 2018); (3) F-curve fitting from the cumulative E-curve with a pulse input (Wolf and D. H. White, 1976).

We suggest here a fourth method to diagnose the nature of flow in a flow reactor, that is, analyzing the F-curve from a step input by directly fitting the observed concentration distribution to the analytical solution of the AD-PFR model with a continuous source of tracer. In this approach, differentiation of the F-curve is not required. This method takes advantage of the time-dependent data prior to the reactor reaching steady state. Such an approach can be carried out at the inception of an experiment. Two critical parameters relating to the behavior the flow reactor, i.e., the axial diffusivity $\mathcal{D}$ and the average residence time in the reactor, τ_r, can be obtained from fitting a reactor model to the F-curve. Since the volumetric flow rate through the reactor and the diameter of the reactor are known, τ_r can be replaced

with the effective length L of the reactor. By comparison with those parameters derived from injection of a pulse of tracer, we show that the direct fitting of data from a step input to the F-curve has the potential to be applied in the same situations as those to the E-curve. Since the flow condition for the measurement of the F-curve is the same as that in an actual experiment, i.e., continuous rather than pulse injection, parameters derived from the F-curve may be more representative of the AD-PFR model.

3.2 Formulation and Solution

The conservation equation describing the AD-PFR is:

$$\frac{\partial c(x,t)}{\partial t} = -u\frac{\partial c(x,t)}{\partial x} + \mathscr{D}\frac{\partial^2 c(x,t)}{\partial x^2} \tag{3.1}$$

where c is the concentration of the tracer, x and t are the variables of axial distance and time, u is the uniform convective velocity, and $\mathscr{D}$ is the axial diffusivity.

For a pulse input, the dimensionless RTD (E-curve) is

$$E_{\text{pulse}}(\theta) = \sqrt{\frac{\text{Pe}}{4\pi\theta}}\exp\left[-\frac{(1-\theta)^2}{4\theta/\text{Pe}}\right] \tag{3.2}$$

where $\text{Pe} = \frac{Lu}{\mathscr{D}}$ is the Péclet number, L is the length of the reactor, $\theta = \frac{t}{\tau_r}$, and $\tau_r = \frac{L}{u}$ is the average residence time in the reactor.

In reality, the pulse input usually persists for a short period of time (square-wave injection), e.g., τ_0, which should be $\ll \tau_r$. The E-curve can be described as (Huang et al., 2017):

$$E_{\text{period}}(\theta) = \frac{1}{2}\left[\text{erf}\left(\frac{1-\theta}{\sqrt{4\theta/\text{Pe}}}\right) - \text{erf}\left(\frac{1-\theta-\theta_0}{\sqrt{4\theta/\text{Pe}}}\right)\right] \tag{3.3}$$

where $\theta_0 = \frac{\tau_0}{\tau_r}$ and $\text{erf}(x) = \frac{2}{\sqrt{\pi}}\int_0^x \exp(-\eta^2)d\eta$.

With a fixed source at $x = 0$, i.e., $c(0,t) = c_0$, into an initially empty reactor, i.e., $c(x,0) = 0$, the downstream concentration far from the source remains 0, i.e., $c(+\infty,t) = 0$, for which an analytical solution exists (Ogata and Banks, 1961), the derivation of which is given in Section 3.6.1. The dimensionless form of the temporal profile of the tracer at the end of the AD-PFR for the step input (F-curve) is

$$F_{\text{step}}(\theta) = \frac{1}{2}\left[\text{erfc}\left(\frac{1-\theta}{\sqrt{4\theta/\text{Pe}}}\right) + \exp(\text{Pe})\text{erfc}\left(\frac{1+\theta}{\sqrt{4\theta/\text{Pe}}}\right)\right] \tag{3.4}$$

where $\mathrm{erfc}(x) = 1 - \mathrm{erf}(x)$. It should be noted that even though by definition the F-curve is the cumulative distribution function of the E-curve, Eq. (3.4) is not the integral form of Eq. (3.2), since deriving Eq. (3.2) only needs an initial condition, but two more boundary conditions are necessary to obtain Eq. (3.4).

Another common treatment of the AD-PFR model applies the so-called Danckwerts boundary conditions (Danckwerts, 1953). Instead of a fixed source at $x = 0$, a constant flux is assumed: upstream of $x = 0$ only convection holds, while downstream of $x = 0$ both convection and dispersion occur, leading to

$$uc(0_-, t) = uc(0_+, t) - \mathscr{D}\frac{\partial c(0_+, t)}{\partial x} \tag{3.5}$$

where $c(0_-, t)$ and $c(0_+, t)$ are concentrations right before and after the entrance ($x = 0$) of the reactor. Eq. (3.5) indicates that the concentration profile at $x = 0$ is non-continuous, and as axial dispersion increases, the difference between $c(0_-, t)$ and $c(0_+, t)$ gets larger. Correspondingly, Danckwerts (ibid.) suggested a smooth profile of the concentration at $x = L$, i.e.,

$$\frac{\partial c(L, t)}{\partial x} = 0 \tag{3.6}$$

A closed-form analytical solution to this case does not exist, but a numerical solution can be applied (see 3.6.2). To be consistent with Eq. (3.4), the reactor is assumed to be initially empty, i.e., $c(x, 0) = 0$.

To distinguish between the cases of Eq. (3.4) and the numerical solution of Eqs. (3.5) and (3.6), we refer to them as AD-PFR and Danckwerts, respectively. Compared with the continuity of tracer flux at the inlet as specified by Eq. (3.5), the inlet boundary condition in the AD-PFR requires a step change in diffusivity at the inlet of the reactor.

Figure 3.1 shows the calculated solutions of the F-curves for PFR, continuous stirred-tank reactor (CSTR), tubular laminar flow reactor (LFR), AD-PFR, and Danckwerts models. With the same extent of axial dispersion (Pe = 10, the same order of magnitude as those of typical flow tube reactors), the tracers in the AD-PFR and the Danckwerts models behave similarly, suggesting that the effects of different boundary conditions on the temporal profiles are limited under typical flow tube reactor operation conditions and both models can represent actual condition.

3.3 Experimental

Experiments were performed in the Caltech Photochemical Oxidation flow Tube reactor (CPOT, Huang et al., 2017). Briefly, the CPOT comprises a conic transition

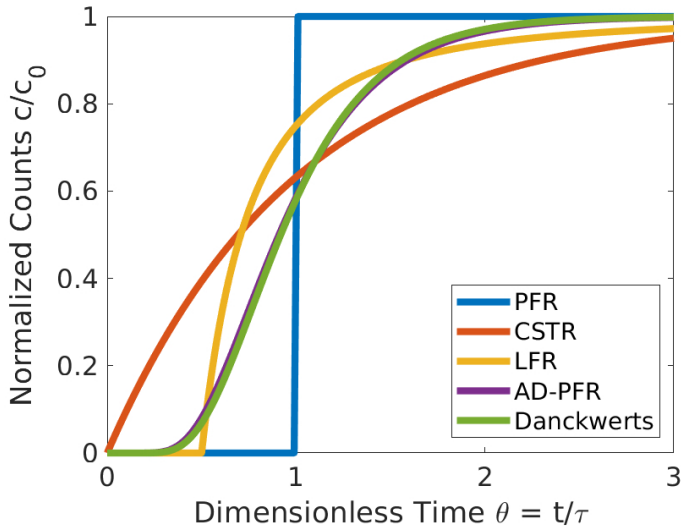

Figure 3.1: Theoretical temporal profiles (F-curve) of the tracer emerging from a flow reactor as described in different models. The analytical dimensionless expression for PFR is $F_{\mathrm{PFR}}(\theta) = H(\theta - 1)$, for CSTR is $F_{\mathrm{CSTR}}(\theta) = 1 - \exp(-\theta)$, for tubular LFR is $F_{\mathrm{LFR}}(\theta) = H(\theta - \frac{1}{2})(1 - \frac{1}{(2\theta)^2})$, for AD-PFR is Eq. (3.4) (Pe = 10), and for Danckwerts AD-PFR is numerical simulation (Pe = 10), where $H(x - a)$ is the Heaviside step function, i.e., $H(x - a) = 0$ as $x < a$, $H(x - a) = 0.5$ as $x = a$, and $H(x - a) = 1$ as $x > a$. Note that F-curves for AD-PFR and Danckwerts AD-PFR are similar when axial dispersion (Pe) is the same.

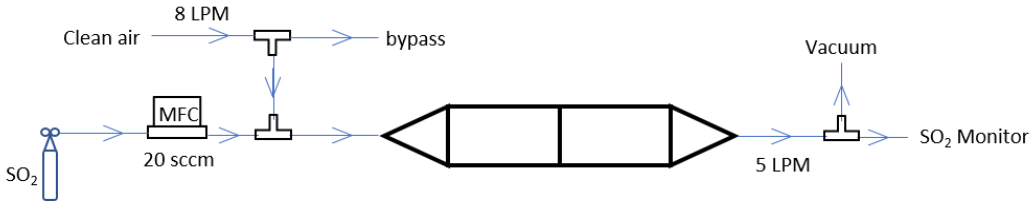

Figure 3.2: Experimental setup.

tube (53 cm) as the inlet, two straight quartz tubes (1.2 m × 17 cm I.D. each) as the main reactor, and a second conic tube (53 cm) to produce a cup-mixed-average output. A SO_2 cylinder of 10 ppm (Airgas) served as the source of tracer, and a SO_2 monitor (model 43i, ThermoFisher) was applied to record the temporal profile of SO_2 at the outlet (Figure 3.2). The overall volumetric flow rate through the CPOT was fixed at 5 L min^{-1} (Re ~ 20) at room temperature (~ 297 K). Prior to injection, purified clean air flowed through the reactor. Both pulse and step injections of SO_2 were carried out. The pulse injection lasted for 1 min with the flow of SO_2 set at 100 sccm. For the step injection, the start of the experiment was recorded at the inception of SO_2 flow at 100 sccm by a mass flow controller. For each type of

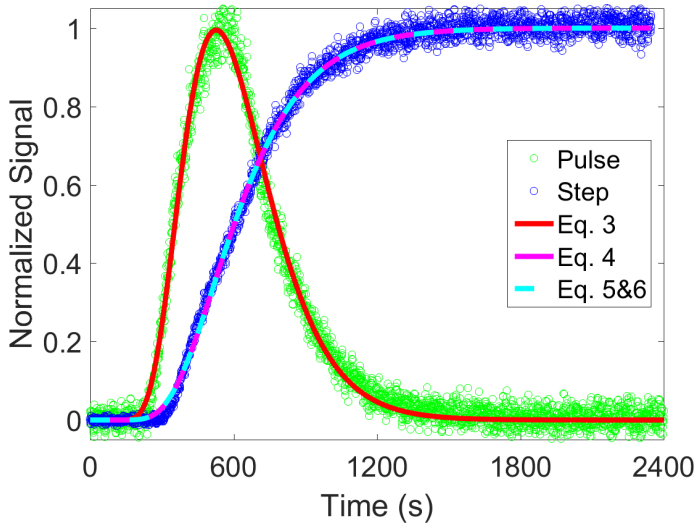

Figure 3.3: Experimental profiles with pulse injection (green circles) fitted by Eq. (3.3) (red solid line) and step input (blue circles) fitted by AD-PFR model (Eq. (3.4), magenta solid line) as well as the Danckwerts boundary condition model (Eq. (3.5)&(3.6), cyan dashed line).

injection, the experiment was repeated for at least three times. Since the flow system at the inlet is open to the ambient, the additional injection of SO_2 is not supposed to perturb the flow field inside the reactor. The experiments were carried out under dry condition (RH < 1%), since SO_2 can interact strongly with the wall at high RH (Lambe et al., 2011a) while Eq. (3.1) (and its solutions) does not incorporate this effect.

Figure 3.3 shows typical temporal patterns of tracer corresponding to the pulse (green circles) and step (blue circles) injections, respectively. Data points represent 1 s resolution.

3.4 Results and Discussion

The average residence time in the flow tube itself is ~ 510 s. Accounting for the two conic sections of the overall reactor assembly, the expected average residence time in the entire reactor assembly should exceed 510 s. With a pulse input lasting a period of 60 s, Eq. (3.3) is used to fit the observed data by the function `fit` in MATLAB (2016b). The parameter values obtained from the fitting are: $\mathcal{D}_{eq3} = (7.1 \pm 0.1) \times 10^{-4}$ m^2 s^{-1}, $\tau_{eq3} = 588 \pm 1$ s, and $L_{eq3} = 2.77 \pm 0.01$ m, with a $Pe_{eq3} = 18$. The inferred value of $\mathcal{D}_{eq3}$ is at least one order of magnitude larger than the inherent gas-phase molecular diffusivity of SO_2, confirming that the derived

value of the diffusivity is a result of the fluid field. This eddy-like diffusivity is consistent with the observation in Huang et al. (2017). The fitted effective length of the reactor exceeds that solely of the reactor section (2.4 m), reflecting the role of the two conic sections at the inlet and outlet.

Experimental data from the step input suggest that none of the PFR, CSTR, or LFR models explains the observation, whereas both the AD-PFR and Danckwerts models show strong potential to fit the data. Fitting results from both models are shown together with observations in Fig. 3.3. Both models fit the data with $R^2 > 0.99$, further demonstrating the 1D-convective-diffusive plug flow reactor model as a representation of the CPOT reactor. The fitting results from Eq. (3.4) are: $\mathscr{D}_{\mathrm{eq4}} = (1.09 \pm 0.02) \times 10^{-3}$ m^2 s^{-1}, $\tau_{\mathrm{eq4}} = 648 \pm 2$ s, and $L_{\mathrm{eq4}} = 3.05 \pm 0.02$ m, with $\mathrm{Pe}_{\mathrm{eq4}} = 13$. Those from Eq. (3.5)-(3.6) are: $\mathscr{D}_{\mathrm{eq5}} = (1.18 \pm 0.02) \times 10^{-3}$ m^2 s^{-1}, $\tau_{\mathrm{eq5}} = 651 \pm 2$ s, and $L_{\mathrm{eq5}} = 3.07 \pm 0.02$ m, with $\mathrm{Pe}_{\mathrm{eq5}} = 12$.

Eq. (3.5)-(3.6) predictions of $\mathscr{D}$, τ, and L are close to those of Eq. (3.4), consistent with the theoretical prediction (Fig. 3.1). As a result, the inferred values of the Péclet number, Pe, are similar, suggesting that, in the present case, either model can be used to characterize the reactor. Figure 3.3 also shows that the predictions of Eqs. (3.4) and (3.5)-(3.6) overlap closely. The comparison above suggests that Eq. (3.4) can be used as an inverse model to derive key parameters, e.g., $\mathscr{D}$, τ, and L, from the transitional profiles, because it has an analytical expression; while Danckwerts conditions are more practicable computationally, especially for the purpose of simulating nonlinear reactions and calculating OH exposure. Note that when modeling photochemical processes, the radiation intensity in the conical section can be much weaker than that in the main reactor; thus the length of the main reactor (as well as the residence time in the reaction section) should be used in the model instead of the effective length L (or τ) fitted from the E- or F-curves, while the diffusivity $\mathscr{D}$ stays the same.

The observed F-curve with step input started to rise ~ 35 s later than the observed E-curve with pulse input, consistent with the fitted average residence time that $\tau_{\mathrm{F}} > \tau_{\mathrm{E}}$. Moreover, the axial diffusivities derived from the F-curve exceed that derived from the E-curve. The Pe number inferred from F-curve is $\sim 30\%$ smaller than that inferred from E-curve, indicating that though the pulse and step injection methods are similar, the axial dispersion is larger in the step injection. This conclusion suggests that the fluid field may be slightly different in the two cases. Since the working conditions of the flow tube for the measurement of the F-curve are similar

to those of actual flow tube experiments (i.e., precursors are injected continuously rather than in pulses), the larger extent of axial dispersion by fitting of the F-curve may better reflect the actual conditions inside the reactor.

We attempted to differentiate the F-curve from both step-up and step-down injection to obtain the E-curve, following Mitroo et al. (2018), which, given the relatively finer data point resolution, the potential lack of smoothness in the E-curve precludes as close fitting as with the pulse injection method. Lambe et al. (2011a) show that inside the Potential Aerosol Mass (PAM) reactor two fluid field patterns exist, and thus the measured RTD is a superposition of two axially dispersed plug flows. The concept of superposition of two different flow patterns also applies to Eq. (3.4) since the number of unknown parameters is the same. Note that the idea of fitting the F-curve directly also applies for other theoretical residence time models, such as tanks-in-series (Mitroo et al., 2018), the advantages of which are: (1) the theories behind the F-curve are the same as those of the E-curve; (2) the experimental conditions needed to obtain the F-curve are similar to those actually performed, and (3) fewer data fluctuations exist relative to E-curve, since F-curve is always rising until it reaches steady state.

3.5 Conclusions

The axially-dispersed plug flow reactor (AD-PFR) model has shown potential to represent non-ideal reactors, the evidence for which is excellent fitting of the experimental data. We present here the successful application of fitting experimental data to the theoretical cumulative curve (the F-curve), which is a close representation of an actual tracer experiment. The derived parameters from the F-curve suggest relatively stronger axial dispersion than that suggested by the E-curve, which better represents the actual experimental condition in flow tube reactors, i.e., continuous injection of precursors rather than pulse injections.

We note here that though AD-PFR can be used to describe the residence time in non-ideal flow reactors, this model does not consider the interaction between the wall and the flow which is a common phenomenon, especially in sampling tubes (Pagonis et al., 2017). A gas-wall partition and convection model has been proposed to explain the observed signal delay that can occur from a step injection, which is beyond the treatment of this technical note.

3.6 Supporting Information

3.6.1 Derivation of PDE Solution

The partial differential equation (PDE) describing an axially-dispersed plug flow reactor (AD-PFR) is

$$\frac{\partial c(x,t)}{\partial t} = -u\frac{\partial c(x,t)}{\partial x} + \mathscr{D}\frac{\partial^2 c(x,t)}{\partial x^2} \tag{3.7}$$

When there is a fixed source at $x = 0$, Eq. (3.7) is subject to the following initial and boundary conditions (Eqs. (3.8)-(3.10)):

$$c(x,0) = 0 \tag{3.8}$$

$$c(0,t) = c_0 \tag{3.9}$$

$$c(+\infty,t) = 0 \tag{3.10}$$

Separation of variables or similarity solutions are not available here. Since the range of x is 0 to infinity, the method of Fourier transform does not apply. Ogata and Banks (1961) proposed the transformation

$$c(x,t) = \Gamma(x,t)\exp\left(\frac{ux}{2\mathscr{D}} - \frac{u^2 t}{4\mathscr{D}}\right) \tag{3.11}$$

and applied Duhamel's theorem to derive the solution; thus the solution (Eq. (3.4)) of Eqs. (3.7)-(3.10) is referred to as the Ogata-Banks Formula. The introduction of Eq. (3.11) transforms Eq. (3.7) into a pure diffusion equation but the boundary condition Eq. (3.9) becomes t-dependent, making the solution more complicated. The derivation we introduce here involves basic knowledge of complex analysis, in order to solve Eqs. (3.7)-(3.10).

First, we use the method of Laplace transform with respect to t, i.e.,

$$c(x,t) \rightarrow \mathscr{L}\{c(x,t)\}(x,s) = \int_0^\infty c(x,t)\exp(-st)dt = L(x,s) \tag{3.12}$$

To do this, multiplying both sides of Eq. (3.7) by $\exp(-st)$, and integrating from 0 to $+\infty$ with respect to t, the first term of Eq. (3.7) becomes $sL(x,s) - c(x,0)$ after integration by parts. The other two terms keep the same form because of linearity of the operator. Rearranging the equation, Eq. (3.7) becomes:

$$sL(x,s) - c(x,0) + u\frac{\partial L(x,s)}{\partial x} = \mathscr{D}\frac{\partial^2 L(x,s)}{\partial x^2} \tag{3.13}$$

which can be rearranged as:

$$\mathscr{D}\frac{\partial^2 L}{\partial x^2} - u\frac{\partial L}{\partial x} - sL = 0 \tag{3.14}$$

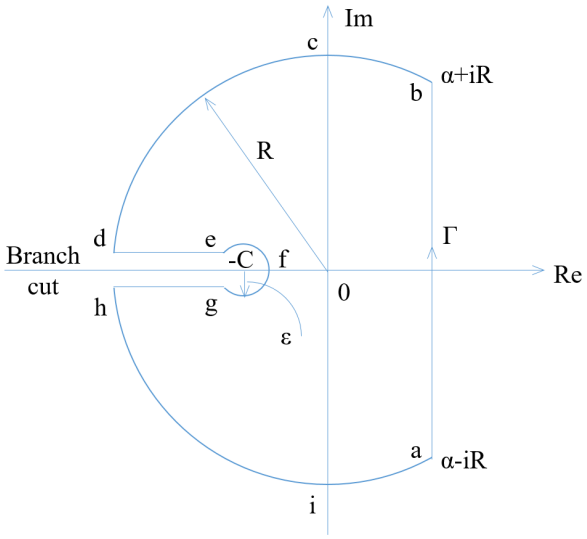

Figure A.1: Bromwich integral path over complex plane.

And boundary condition Eqs. (3.9) and (3.10) become:

$$\mathscr{L}\{C(0,t)\} = L(0,s) = \frac{c_0}{s} \tag{3.15}$$

$$\mathscr{L}\{C(\infty,t)\} = L(\infty,s) = 0 \tag{3.16}$$

The general solution for Eq. (3.14) is

$$L(x,s) = A\exp(\lambda_1 x) + B\exp(\lambda_2 x) \tag{3.17}$$

where $\lambda_1 = \frac{u+\sqrt{u^2+4\mathscr{D}s}}{2\mathscr{D}}$ and $\lambda_2 = \frac{u-\sqrt{u^2+4\mathscr{D}s}}{2\mathscr{D}}$. With Eqs. (3.15) and (3.16) we get $A = 0$ and $B = \frac{c_0}{s}$. So the solution for Eq. (3.14) is

$$\begin{aligned} L(x,s) &= \frac{c_0}{s}\exp\left(\frac{u-\sqrt{u^2+4\mathscr{D}s}}{2\mathscr{D}}x\right) \\ &= c_0\exp\left(\frac{ux}{2\mathscr{D}}\right)\frac{1}{s}\exp\left(-\frac{x}{\sqrt{\mathscr{D}}}\sqrt{\frac{u^2}{4\mathscr{D}}+s}\right) \end{aligned} \tag{3.18}$$

Then the key problem is how to obtain the inverse Laplace transform (iLT) to Eq. (3.18). We can simplify it in the form of $\frac{A}{s}\exp(-B\sqrt{C+s})$, where $A = c_0\exp(\frac{ux}{2\mathscr{D}})$, $B = \frac{x}{\sqrt{\mathscr{D}}}$, $C = \frac{u^2}{4\mathscr{D}}$. After applying the Bromwich contour integral over the complex plane (Fig. A.1), we will get the iLT result. We note here that the iLT result (Eq. (3.28)) can be verified by Mathematica (Wolfram), a detailed step-by-step contour

integration of iLT is provided here.

The iLT is in the form of

$$\begin{aligned} f(t) = \mathscr{L}^{-1}\{L(s)\} &= \frac{1}{2\pi i}\int_{\alpha-i\infty}^{\alpha+i\infty} L(s)\exp(st)ds \\ &= \frac{1}{2\pi i}\int_{\alpha-i\infty}^{\alpha+i\infty} \frac{A}{s}\exp(-B\sqrt{C+s}+st)ds \end{aligned} \tag{3.19}$$

The integral of Eq. (3.19) is on a complex plane along a vertical line $s = \alpha$ from $-i\infty$ to $+i\infty$, where α can be any value right of all singularities (poles, branch points, etc.). The Method of Residues will be applied to evaluate this integral, which states that the integration along a closed curve on a complex plane equals the sum of residues at all isolated singularities. Thus we construct a counterclockwise loop Γ as shown in Fig. A.1, also known as the Bromwich contour, to evaluate the integral. Note that there is a branch point at $s = -C$ (thus a branch cut from $-C$ to $-\infty$ in this case) and an isolated singular point at $s = 0$ on this contour. As $R \to \infty$, the path $\widehat{ab}$ approaches that we are looking for. As $\lim_{R\to\infty}|L(s)| = 0$, by Jordan's Lemma, the integration over $\widehat{bcd}$ and $\widehat{hia}$ will be zero when $R \to \infty$. Since the integration over path $\widehat{de}$, $\widehat{efg}$, and $\widehat{gh}$ can be calculated and the integration over the whole contour can be obtained by residue theorem, i.e.,

$$\oint_\Gamma = \lim_{R\to\infty}\left(\int_{\widehat{ab}} + \int_{\widehat{de}} + \int_{\widehat{efg}} + \int_{\widehat{gh}}\right) = \text{Res}(0) \tag{3.20}$$

Then we can get $\lim_{R\to\infty}\int_{\widehat{ab}} = \text{Res}(0) - \lim_{R\to\infty}\left(\int_{\widehat{de}} + \int_{\widehat{efg}} + \int_{\widehat{gh}}\right)$.

The residue at $s = 0$ is

$$\text{Res}(0) = 2\pi i(A\exp(-B\sqrt{C+s}+st))|_{s=0} = 2\pi i A\exp(-B\sqrt{C}) \tag{3.21}$$

Over $\widehat{de}$, we set $C + s = r\exp(i\pi) = -r$, then $\sqrt{C+s} = \sqrt{r}\exp(\frac{i\pi}{2}) = i\sqrt{r}$. So we get $ds = -dr$ and $\lim_{\varepsilon\to0}\int_{-R}^{-C-\varepsilon} L(s)ds = -\lim_{\varepsilon\to0}\int_{R-C}^{\varepsilon} L(r)dr = -\int_{R-C}^{0} L(r)dr$. The integration over $\widehat{de}$ becomes:

$$\begin{aligned} \int_{\widehat{de}} &= -\int_{R-C}^{0} \frac{A}{-r-C}\exp(-iB\sqrt{r}+(-r-C)t)dr \\ &= \int_{R-C}^{0} \exp(-(r+C)t)\frac{A}{r+C}\exp(-iB\sqrt{r})dr \end{aligned} \tag{3.22}$$

Over $\widehat{gh}$, we set $C + s = r\exp(-i\pi) = -r$, then $\sqrt{C+s} = \sqrt{r}\exp(-\frac{i\pi}{2}) = -i\sqrt{r}$ and also $ds = -dr$, and $\lim_{\varepsilon\to0}\int_{-C-\varepsilon}^{-R} L(s)ds = -\lim_{\varepsilon\to0}\int_{\varepsilon}^{R-C} L(r)dr = -\int_{0}^{R-C} L(r)dr$.

The integration over $\widehat{gh}$ becomes:

$$\begin{aligned}\int_{\widehat{gh}} &= -\int_0^{R-C} \frac{A}{-r-C}\exp\left(iB\sqrt{r}+(-r-C)t\right)dr \\ &= \int_0^{R-C} \exp\left(-(r+C)t\right)\frac{A}{r+C}\exp\left(iB\sqrt{r}\right)dr\end{aligned} \tag{3.23}$$

Over $\widehat{efg}$, we set $C+s=\varepsilon\exp(-i\theta)$, then $\sqrt{C+s}=\sqrt{\varepsilon}\exp(-\frac{i\theta}{2})$. So we get $ds=-i\varepsilon\exp(i\theta)d\theta$ and

$$\begin{aligned}\lim_{\varepsilon\to 0}\int_{\widehat{efg}} L(s)ds = \lim_{\varepsilon\to 0}\int_{\pi}^{-\pi} &-\frac{A}{\varepsilon\exp(-i\theta)-C}i\varepsilon\exp(i\theta) \\ &\exp\left[-B\sqrt{\varepsilon}\exp(-\frac{i\theta}{2})+(\varepsilon\exp(-i\theta)-C)t\right]d\theta = 0\end{aligned} \tag{3.24}$$

Then we get:

$$\begin{aligned}&\int_{\alpha-i\infty}^{\alpha+i\infty}\frac{A}{s}\exp\left(-B\sqrt{C+s}+st\right) = \lim_{R\to\infty}\int_{\widehat{ab}} = \mathrm{Res}(0) - \lim_{R\to\infty}\left(\int_{\widehat{de}}+\int_{\widehat{efg}}+\int_{\widehat{gh}}\right) \\ &= 2\pi i A\exp\left(-B\sqrt{C}\right) - \lim_{R\to\infty}\int_{R-C}^{0}\exp\left(-(r+C)t\right)\frac{A}{r+C}\exp\left(-iB\sqrt{r}\right)dr \\ &- \lim_{R\to\infty}\int_0^{R-C}\exp\left(-(r+C)t\right)\frac{A}{r+C}\exp\left(iB\sqrt{r}\right)dr \\ &= 2\pi i A\exp\left(-B\sqrt{C}\right) - \int_0^{\infty}\frac{A\exp\left(-(r+C)t\right)}{r+C}\left(-\exp\left(-iB\sqrt{r}\right)+\exp\left(iB\sqrt{r}\right)\right)dr \\ &= 2\pi i A\exp\left(-B\sqrt{C}\right) - 2iA\int_0^{\infty}\frac{\exp\left(-(r+C)t\right)}{r+C}\sin\left(B\sqrt{r}\right)dr\end{aligned} \tag{3.25}$$

Substituting Eq. (3.25) into Eq. (3.19) we get

$$f(t) = A\exp\left(-B\sqrt{C}\right) - A\int_0^{\infty}\frac{\exp\left(-(r+C)t\right)}{\pi(r+C)}\sin\left(B\sqrt{r}\right)dr \tag{3.26}$$

It can be shown that (`http://mathworld.wolfram.com/Erf.html`):

$$\begin{aligned}&\int_0^{\infty}\frac{\exp\left(-(x+p)t\right)}{\pi(x+p)}\sin\left(a\sqrt{x}\right)dx = \\ &-\sinh\left(a\sqrt{p}\right)+\frac{\exp\left(-a\sqrt{p}\right)}{2}\mathrm{erf}\left(\frac{a}{2\sqrt{t}}-\sqrt{pt}\right)+\frac{\exp\left(a\sqrt{p}\right)}{2}\mathrm{erf}\left(\frac{a}{2\sqrt{t}}+\sqrt{pt}\right)\end{aligned} \tag{3.27}$$

where $\mathrm{erf}(x)=\frac{2}{\sqrt{\pi}}\int_0^x\exp(-\eta^2)d\eta$. So Eq. (3.26) becomes:

$$f(t) = \frac{A}{2}\exp\left(-B\sqrt{C}\right)\mathrm{erfc}\left(\frac{B}{2\sqrt{t}}-\sqrt{Ct}\right)+\frac{A}{2}\exp\left(B\sqrt{C}\right)\mathrm{erfc}\left(\frac{B}{2\sqrt{t}}+\sqrt{Ct}\right) \tag{3.28}$$

where $\text{erfc}(x) = 1 - \text{erf}(x)$. Substituting A, B, and C into the above equation, the final iLT result of Eq. (3.19) is

$$c(x,t) = \frac{c_0}{2}\left[\text{erfc}\left(\frac{x-ut}{\sqrt{4\mathscr{D}t}}\right) + \exp\left(\frac{xu}{\mathscr{D}}\right)\text{eftc}\left(\frac{x+ut}{\sqrt{4\mathscr{D}t}}\right)\right] \tag{3.29}$$

3.6.2 Numerical Solution of the Danckwerts Boundary Problem

We use the pde solver pdepe in MATLAB (2016b) to numerically solve the Danckwerts boundary problem. Here is an example:

```
function C_t = fun_CD_nd(Pe,theta)
% This function returns numerically simulated temporal profile
% at the outlet of a convective-diffusive plug flow reactor.
% It uses the non-dimensional format.
% It applies Danckwerts B.C., with I.C. all zeros.
% It assumes C0_t is a constant input.
% ------------------------------------------- %
% Pe: Peclet number, LU/D
% L: length of reactor, m
% U: average convective velocity, m s-1
% D: axial diffusivity, m2 s-1
% theta: non-dimensional time
% ------------------------------------------- %
% C_t: time dependent concentration profile at outlet
% ------------------------------------------- %
% created: 2018/03/16, yhuang@caltech.edu
N = 100; % grid number
xmesh = linspace(0,1,N);
sol = pdepe(0,@mypde,@myic,@mybc,xmesh,theta);
C_t = sol(:,end);
% ------------------------------------------- %
    function [c,f,s] = mypde(x,t,u,DuDx)
        c = Pe;
        f = DuDx;
        s = -Pe*DuDx;
    end
% ------------------------------------------- %
    function u0 = myic(x)
        u0 = 0;
    end
% ------------------------------------------- %
    function [pl,ql,pr,qr] = mybc(xl,ul,xr,ur,t)
        pl = ul-1;
        ql = -1/Pe;
```

```
35          pr = 0;
36          qr = 1;
37      end
38 % ------------------------------------------- %
39 end
```

The following script shows how to use the above function:

```
1 theta = 0:0.01:4;
2 Pe = 10;
3 C_t = fun_CD_nd(Pe,theta);
4 plot(theta,C_t)
```

Chapter 4

UNIFIED THEORY OF VAPOR-WALL MASS TRANSPORT IN TEFLON-WALLED ENVIRONMENTAL CHAMBERS

Huang, Yuanlong, Ran Zhao, Sophia M. Charan, Christopher M. Kenseth, Xuan Zhang, and John H. Seinfeld (2018). "Unified Theory of Vapor–Wall Mass Transport in Teflon-Walled Environmental Chambers". In: *Environ. Sci. Technol.* 52.4, pp. 2134–2142. DOI: 10.1021/acs.est.7b05575.

Abstract

Secondary organic aerosol (SOA) formation is studied in laboratory chambers, in which volatile organic compounds (VOCs) are oxidized to produce low-volatility compounds that condense into the aerosol phase. It has been established that such oxidized low-volatility compounds can partition into the chamber walls, which traditionally consist of Teflon film. Several studies exist in which the rates of uptake of individual vapor compounds to the chamber walls have been measured, but a unified theory capable of describing the range of experimental measurements has been lacking. Here, a two-layer model of observed short and long vapor-wall interaction timescales in Teflon-walled environmental chambers is presented and shown to be consistent with experimental data on the rate of wall deposition of more than 90 compounds. Semi-empirical relationships between key parameters in the model and vapor molecular properties are derived, which can be used to predict the fate of gas-phase vapor in the chamber under dry conditions.

4.1 Introduction

The environmental chamber is a principal laboratory system used to study the formation, properties, and evolution of secondary organic aerosol (SOA) (R. H. Schwantes et al., 2017a). The typical material from which chambers are constructed is Teflon film (fluorinated ethylene propylene, FEP). The process of SOA formation involves oxidation of a volatile organic compound (VOC) to generate low-volatility gas-phase products that subsequently condense into the aerosol phase. It has been established that these oxidized products may also partition into the Teflon chamber walls (Bian et al., 2015; Cappa et al., 2016; Krechmer et al., 2015, 2016; La et al., 2016; Christine L. Loza et al., 2010; Matsunaga and Ziemann, 2010; R. C.

McVay et al., 2014; Nah et al., 2016; Trump et al., 2016; Ye et al., 2016; Yeh and Ziemann, 2014, 2015; Xuan Zhang et al., 2014, 2015). Such vapor-wall loss reduces the potential yield of SOA and must be accounted for in analysis of experiments. Current treatments of vapor-wall deposition in chambers consider the FEP film as an infinite medium into which vapor molecules dissolve.

The extent of partitioning of oxidized organic species typical of SOA into Teflon film has been studied experimentally by introducing species individually into a chamber and measuring their rate of decay from wall uptake. The uptake has been characterized by the timescale required to approach vapor-wall equilibrium (τ_w). Previous studies indicate that τ_w can be competitive with the timescales of other processes occurring in the chamber, such as the rate of VOC oxidation and the timescale associated with vapor-particle partitioning(R. C. McVay et al., 2014; Nah et al., 2016). The timescale τ_w is governed by gas-phase diffusion through the boundary layer adjacent to the chamber wall, followed by uptake into the wall itself. Two major studies of vapor-wall uptake of individual organic species typical of VOC oxidation products have reported significantly different timescales for vapor uptake, namely $\tau_w \sim 10$ min (Krechmer et al., 2016) and $\tau_w \sim 10$ h (Xuan Zhang et al., 2015). Possible reasons for the observed discrepancy in vapor-wall uptake rates include differences in the particular chemical systems studied or in the experimental protocol itself. The goal of the present work is to formulate and evaluate experimentally a unified theory of vapor-wall mass transport and uptake in Teflon-walled environmental chambers.

4.2 Two-Layer Kinetic Sorption Model

We introduce a two-layer kinetic sorption model (Fig. 4.1A), inspired by that proposed by Crank (1953), to explain the stress-dependent diffusion of vapor molecules into polymer film. In the two-layer model, after traversing a gas-phase boundary layer, vapor molecules enter a sharp, swollen outer layer in the Teflon that is thought to be stress-free, in which equilibrium with the gas phase is established relatively rapidly. It is estimated that a pseudo-steady state profile in the gas-phase boundary layer is achieved on a timescale of order 10 s (Section 4.5.1). Vapor molecules absorbed into the outer polymer layer (denoted the "Surface layer" in Fig. 4.1A) then slowly diffuse into the interior of the polymer film (the "Inner layer" in Fig. 4.1A) by breaking inter-chain bonds, impeded by the stress exerted by the polymer network.

4.2.1 Surface Layer

The Teflon FEP film is treated as a solution into which the molecules dissolve. Matsunaga and Ziemann (2010) proposed that vapor-wall partitioning equilibrium can be represented by an effective organic mass concentration of the wall itself, C_w, by analogy to the effective aerosol mass concentration used in describing vapor-particle uptake (John H. Seinfeld and James F. Pankow, 2003). Here, we introduce C_w and C'_w, respectively, to distinguish between the compound-independent and -dependent equivalent mass concentration of the Teflon wall. These quantities are related by $C'_w = \frac{C_w}{\gamma^\infty}$, where γ^∞ is the activity coefficient of the solute vapor dissolved in an infinitely dilute solution of Teflon film. The compound-dependent C'_w reflects, therefore, the effect of the compound's activity in Teflon film. The process of partitioning into C_w corresponds to the surface layer absorption.

It is advantageous to define an effective thickness of the surface layer, L'_e. L'_e is related to C'_w by $L'_e = \frac{V}{A}\frac{C'_w}{\rho_w}$, where V and A are the volume and surface area of the chamber, respectively, and the density of FEP film (Boedeker, 2017) is ρ_w = 2150 kg m^{-3}. Note that this effective thickness L'_e is related to the physical thickness of the surface layer L_e by $L'_e = \frac{L_e}{\gamma^\infty}$. Measurements of C_w suggest that L_e is of order 1 nm (Krechmer et al., 2016; Matsunaga and Ziemann, 2010; Yeh and Ziemann, 2015), corresponding to a sharp air-polymer interface. This behavior is similar to that of a typical vapor-liquid interface, wherein the density increases sharply from the bulk vapor to the bulk liquid over a distance of order 1 nm (10 − 20 nominal molecular diameters, Frezzotti, 2011). For water molecules, this distance is ∼ 3.3 − 8.4 Å(Davidovits et al., 1991). For Teflon film, in determining C'_w, Matsunaga and Ziemann (2010) assumed an effective molecular weight of Teflon film of 200 g mol^{-1}; we adopt this assumption here, for which the effective Teflon molecular diameter is 0.54 nm. We tentatively take L_e = 5 nm, corresponding to a value of C_w = 32.2 mg m^{-3} (assuming γ^∞ = 1 and $\frac{A}{V}$ = 3 m^{-1}), consistent with the suggestions by Krechmer et al. (2016) and Yeh and Ziemann (2015). The molecular diffusivity in the swollen and stress-free surface layer, that is of order 10^{-13} m^2 s^{-1} (Tokarev et al., 2006), establishes a timescale of ∼ 1 ms to achieve concentration uniformity within the surface layer.

A key parameter in the kinetic sorption model is the vapor-wall equilibrium constant, K_w, similar to a Henry's law constant. The dimensionless $K_w = \frac{\rho_w}{\gamma^\infty c^*}\frac{MW_{voc}}{MW_w}$, where MW_{voc} and MW_w are the mean molecular weights of the VOC vapor and FEP

film, respectively, and c^* is the saturation mass concentration of the vapor. Typically, the activity coefficient of a compound in Teflon film, γ^∞, is the only unknown parameter in the expression for K_w. Limited information exists to constrain the value of γ^∞, and the activity coefficient γ^∞ is often assumed to be unity (Krechmer et al., 2016; Matsunaga and Ziemann, 2010; Yeh and Ziemann, 2015). Within the consistent model framework developed here, γ^∞ is defined as the ratio of the physical thickness of the surface layer, L_e, to the effective thickness, L'_e, i.e. $\gamma^\infty = \frac{L_e}{L'_e}$. If $\gamma^\infty = 1$, the FEP film behaves as an ideal solution. If $\gamma^\infty > 1$, the vapor molecules prefer to remain in the gas phase; if $\gamma^\infty < 1$, vice versa. Values of γ^∞ for a wide variety of compounds calculated from the literature (Krechmer et al., 2016; Matsunaga and Ziemann, 2010; Yeh and Ziemann, 2014, 2015) as a function of c^* estimated by EVAPORATION (Compernolle et al., 2011; Tropo, 2014) as shown in Fig. 4.7A and Table 4.1 indicates that $\gamma^\infty > 1$. The inverse linear relationship between γ^∞ and c^* suggests that FEP polymer is not generally hospitable for VOCs. This behavior, however, does not conflict with the presence of low volatility compounds in the Teflon film, since the vapor-wall equilibrium constant depends more strongly on c^* than γ^∞, such that compounds with lower c^* will haver higher K_w values (see Table 1 for dependence of γ^∞ on c^*). Furthermore, the equilibrium fraction of solute remaining in the gas phase, F_g, (Fig. 4.7B) is consistent with the observation that less volatile compounds tend to reside preferentially in the wall.

4.2.2 Inner Layer

The magnitude of the inner layer (Fig. 4.1) effective diffusivity, $\mathscr{D}_{\text{eff}}$, is key to determining the temporal behavior of the bulk gas-phase concentration, $C_g^b(t)$, in a sufficiently long-duration experiment ($\sim$ 10 h). $\mathscr{D}_{\text{eff}}$ is considered to be influenced by the existence of FEP film in a glassy state, a coexistence of liquid and solid states, the latter of which comprises immobile micro-voids (Frisch, 1980). Dual sorption theory (Vieth et al., 1976) asserts that whereas free molecules can diffuse through the liquid layer, deeper diffusion must satisfy the Langmuir adsorption isotherm on the inner surface of local micro-voids (ibid.). As a result, the molecular diffusivity in polymer is lower than that in pure liquid ($10^{-13} - 10^{-9}$ m^2 s^{-1}) (Manabu Shiraiwa et al., 2011). The overall $\mathscr{D}_{\text{eff}}$ of molecules absorbed in the Teflon inner layer is of order $10^{-22} - 10^{-17}$ m^2 s^{-1}, well within the range of semi-solid diffusivities (Manabu Shiraiwa et al., 2013). By fitting time-dependent Teflon uptake rates of a variety of species, one can estimate the $\mathscr{D}_{\text{eff}}$ values.

4.2.3 Governing Equations Describing Uptake of Vapor Molecules in the Two-Layer Model

The mass transport coefficients across the gas-phase boundary layer and through the vapor-Teflon interface (Fig. 4.1) can be written as $v_e = \frac{2}{\pi}\sqrt{k_e \mathscr{D}_g}$ and $v_c = \frac{\alpha_w \omega}{4}$, respectively, where k_e is the eddy diffusivity coefficient for mixing in the chamber, $\mathscr{D}_g$ is the vapor molecular diffusivity in air, α_w is the vapor-wall accommodation coefficient (see discussion in Section 4.5.2), and ω is the vapor molecular mean speed. From mass transfer resistance theory, the overall mass transport coefficient across the gas-phase boundary layer and the air-Teflon interface is $v_l = \left(\frac{1}{v_e} + \frac{1}{v_c}\right)^{-1}$. For quasi-steady state gas-phase boundary layer diffusion (see discussion in Section 4.5.1), the bulk gas-phase mass flux J_b (μg s^{-1}) to the Teflon surface is:

$$J_b = A v_l \left(C_g^b(t) - \frac{C_s(t)}{K_w} \right) \tag{4.1}$$

where C_g^b is the gas-phase concentration in the bulk chamber and C_s is the concentration of vapor dissolved in the wall surface layer. The mass balance for C_g^b involving vapor-wall mass transfer and gas-phase chemical reactions is:

$$\frac{dC_g^b(t)}{dt} = -\left(\frac{A}{V}\right) v_l \left(C_g^b(t) - \frac{C_s(t)}{K_w} \right) + \sum^{i} R_i \tag{4.2}$$

where $\sum^{i} R_i$ represents the net generation or consumption of the species by chemical reaction.

Within the Teflon surface layer, the diffusive flux, J_d (μg s^{-1}), at the surface layer-inner layer boundary is:

$$J_d = -A \mathscr{D}_{\text{eff}} \left. \frac{\partial C_i(x,t)}{\partial x} \right|_{x=L_e} \tag{4.3}$$

where C_i is the concentration of vapor molecules in the wall inner layer. Time-dependent mass conservation for C_s is given by:

$$\frac{dC_s(t)}{dt} = \frac{v_l}{L_e} \left(C_g^b(t) - \frac{C_s(t)}{K_w} \right) + \frac{\mathscr{D}_{\text{eff}}}{L_e} \left. \frac{\partial C_i(x,t)}{\partial x} \right|_{x=L_e} \tag{4.4}$$

Diffusion of the dissolved solute in the inner Teflon layer obeys:

$$\frac{\partial C_i(x,t)}{\partial t} = \mathscr{D}_{\text{eff}} \frac{\partial^2 C_i(x,t)}{\partial x^2} \tag{4.5}$$

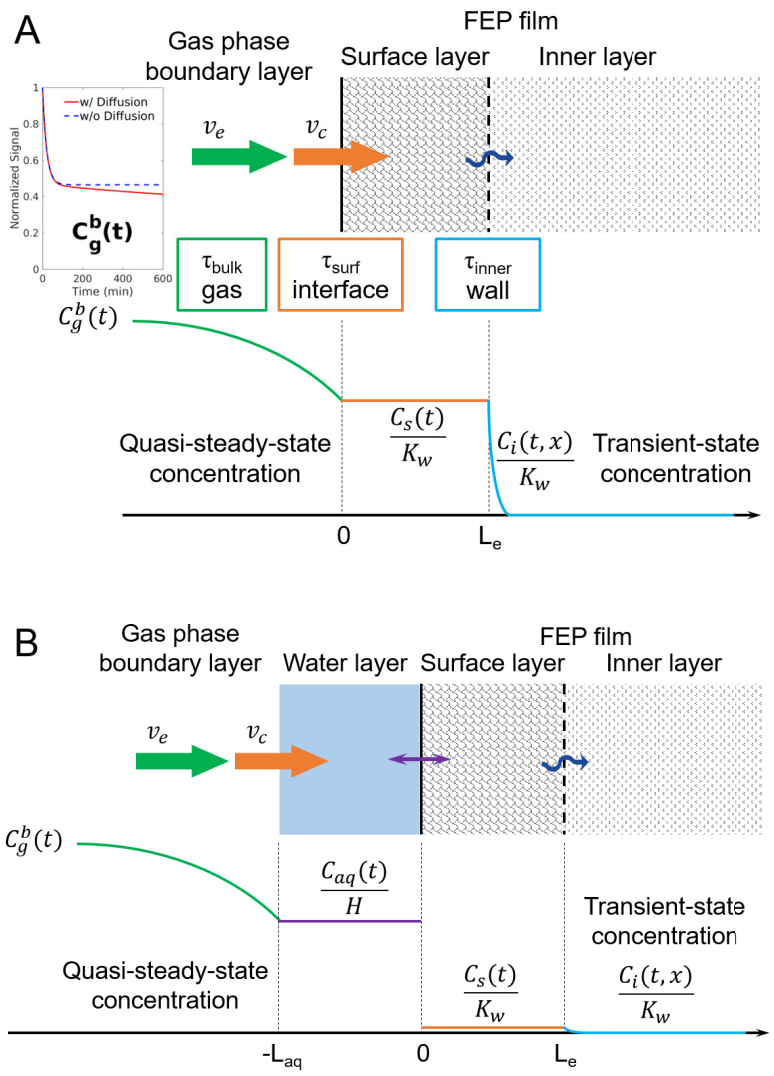

Figure 4.1: Two-layer (dry) and three-layer (moist) models of vapor uptake at the surface of Teflon film in a laboratory chamber. (A) Two-layer kinetic sorption model. v_e and v_c are gas-phase boundary layer and interfacial mass transport coefficients, respectively. $C_g^b(t)$ is the bulk gas-phase concentration, $C_s(t)$ is the concentration (assumed to rapidly achieve uniformity) within the Surface Layer, and C_i is the transient concentration in the Inner Layer. The vapor-Teflon wall equilibrium constant, K_w, plays a role similar to that of a Henry's law dissolution constant. Timescales, τ_{bulk}, τ_{surf}, and τ_{inner}, corresponding to each layer are indicated. (B) Vapor uptake process in the presence of a thin aqueous film on the Teflon wall. Assumption of $H \gg K_w$, where H is the corresponding Henry's law constant, is made. $C_{aq}(t)$ denotes the concentration of dissolved vapor in the aqueous film. L_e and L_{aq} represent the surface layer and aqueous film thicknesses, respectively.

Associated initial and boundary conditions are:

$$\begin{aligned} &C_g^b(0) = C_{g0}^b; \quad C_s(0) = C_{s0}; \\ &C_i(x,0) = 0; \quad C_i(0,t) = C_s(t); \quad C_i(\infty,t) = 0; \end{aligned} \tag{4.6}$$

C_{g0}^b and C_{s0} are appropriate initial concentrations. For example, $C_{s0} = 0$ corresponds to a pristine chamber condition, while $C_{g0}^b = \dfrac{C_{s0}}{K_w}$ applies if the bulk gas-phase and surface layer concentrations are at equilibrium at the beginning of an experiment. The boundary condition as $x \longrightarrow \infty$ expresses the consequence of the slow diffusion in the inner layer relative to the overall extent of the layer itself. If $\mathscr{D}_{\text{eff}}$ is sufficiently small such that penetration into the inner layer is negligible over an experiment, the mass conservation equations reduce to a single-layer sorption model, in which the corresponding vapor-wall equilibrium timescale (τ_{vwe}) is:

$$\tau_{vwe} = \left(\frac{A}{V}\right)^{-1} \left(1 + \frac{V}{K_w L_e A}\right)^{-1} v_l^{-1} \tag{4.7}$$

Table 4.1 summarizes the key parameters that represent vapor-wall deposition in chamber experiment simulations.

Table 4.1: Parameters Representing Vapor-Wall Deposition in Chambers

Parameter[a]	Expression
k_1: forward rate (s^{-1})	$\left(\frac{A}{V}\right) v_l$
k_{-1}: backward rate (s^{-1})	$\frac{10^9}{L_e K_w} v_l$ or $\left(\frac{A}{V}\right) v_l \frac{\gamma^\infty c^*}{10^3 C_w} \frac{MW_w}{MW_{voc}}$
k_2: first-order loss rate (s^{-1})	Fig. 4.5 or from measurement[b]
L_e: Surface layer thickness (nm)	5
K_w: dimensionless equilibrium constant	$\frac{10^9 \rho_w}{\gamma^\infty c^*} \frac{MW_{voc}}{MW_w}$
C_w: equivalent wall concentration (mg m^{-3})	$10.8 \left(\frac{A}{V}\right)$
γ^∞: activity coefficient in FEP	$10^{3.299} (c^*)^{-0.6407}$ (Fig. 4.7A)
v_l: wall deposition velocity (m s^{-1})	$\left(\frac{\pi}{2} \frac{1}{\sqrt{k_e \mathscr{D}_g}} + \frac{4}{\alpha_w \omega}\right)^{-1}$
α_w: wall accommodation coefficient	$10^{-2.744} (c^*)^{-0.6566}$ (Fig. 4.8)
$\mathscr{D}_{\text{eff}}$: effective diffusivity in FEP film (m^2 s^{-1})	$10^{-17.05} (\theta - 110.9)^{-1.695} (c^*)^{0.1831}$
ρ_w: Teflon FEP density (Boedeker, 2017, kg m^{-3})	2150
c^*: vapor saturation concentration (μg m^{-3})	species dependent (Tropo, 2014)
k_e: eddy diffusivity coefficient (Krechmer et al., 2016, s^{-1})	$0.004 + 10^{-2.25} (V)^{0.74}$
V: chamber volume (m^3)	chamber dependent
A: chamber surface area (m^2)	chamber dependent

(Continued)

Parameter[a]	Expression
$\mathscr{D}_g$: diffusivity in gas phase ($m^2\ s^{-1}$)	5×10^{-6}
ω: mean molecular velocity ($m\ s^{-1}$)	$\sqrt{\frac{8RT}{\pi MW_{voc}}}$
R: gas constant ($kg\ m^2\ s^{-2}\ K^{-1}\ mol^{-1}$)	8.314
MW_w: average molecular weight of FEP (Matsunaga and Ziemann, 2010, $g\ mol^{-1}$)	200
MW_{voc}: vapor molecular weight ($g\ mol^{-1}$)	species dependent
θ: molecular volume ($cm^3\ mol^{-1}$)	species dependent (Fig. 4.3)

[a] The parameters listed here correspond to the dynamic system $X \underset{k_{-1}}{\overset{k_1}{\rightleftharpoons}} Y \xrightarrow{k_2} Z$, where X is the species of interest. Detailed discussion of the incorporation of this model framework into chamber models can be found in Section 4.5.7.

[b] It is recommended to fit the measured signal decay of species X to the analytical equation in Section 4.5.6 to obtain k_2, or simply use the asymptotic relationship $k_w^X = \frac{K_{eq}}{1 + K_{eq}} k_2$, where k_w^X is the "apparent" first-order decay rate constant of species X, and $K_{eq} = \frac{k_1}{k_{-1}}$. In general, the use of the asymptote will not lead to a significant difference if the measurement lasts several hours.

4.2.4 Aqueous Film Model

Under sufficiently high relative humidity conditions (RH > 90%), it is assumed that an aqueous film of thickness L_{aq} exists on the chamber wall (Fig. 4.1B). Since the diffusivity of vapor molecules in water $\mathscr{D}_{aq}$ is $\sim 1 \times 10^{-9}$ m^2 s^{-1} (Schwarzenbach et al., 2005), the estimated timescale ($\frac{L_{aq}^2}{\mathscr{D}_{aq}}$) for the dissolved vapor concentration to reach uniformity in this thin layer of water is sufficiently small (e.g. $\sim 10^{-1}$ s if L_{aq} = 10 μm) such that the rate-limiting step for uptake is either gas-phase boundary layer diffusion or interfacial accommodation at the air-water interface.

Since oxidized VOCs tend to be polar molecules, γ^{∞} in aqueous solution should be smaller than that in Teflon polymer solution, such that partitioning in the aqueous phase is preferred over the polymer phase. Thus, in this case, a reasonable assumption is that vapor partitioning does not proceed beyond the thin water film on the Teflon surface.

For this single-layer model, EQ. (4.7) can be directly applied to the aqueous film uptake, replacing K_w and L_e with the Henry's law constant H and L_{aq}, respectively. As described in Section 4.5.2, based on measured timescale and equilibrium constants, it is possible to estimate the accommodation coefficient of the water surface.

4.3 Experimental Study of Vapor-Wall Uptake

To study vapor-wall interaction, we either (i) generated the compounds in situ by VOC oxidation in the chamber (Krechmer et al., 2016; Praske et al., 2015; R. H. Schwantes et al., 2017b, 2015; St. Clair et al., 2016; Teng et al., 2017; Xuan Zhang et al., 2015), or (ii) injected the compounds of interest (purchased or synthesized) into the chamber (Bates et al., 2014; C. L. Loza et al., 2014; Christine L. Loza et al., 2010; Matsunaga and Ziemann, 2010; Nguyen et al., 2014, 2016; Manabu Shiraiwa et al., 2013; Yeh and Ziemann, 2015). The two-layer kinetic model is applied to two laboratory data sets from the Caltech Environmental Chamber (24 m^3, $\frac{A}{V} \sim 2$ m^{-1}) on the dynamics of vapor-wall deposition of individual compounds: (i) Xuan Zhang et al. (2015) corresponding to in situ generation and (ii) deposition measurements of alcohols (1-hexanol 98%, 1-heptanol 98%, 1-octanol ≥ 99%, 1-nonanol 98%, 1-decanol ≥ 99%, 1-undecanol ≥ 97.5%, and 1-dodecanol 98%), aromatics (toluene 99.8%, *m*-xylene ≥ 99%, *o*-xylene 98%, and 1,3,5-trimethylbenzene 98%), alkanes (*n*-dodecane ≥ 99%, *n*-tridecane ≥ 99%, *n*-tetradecane ≥ 99%, *n*-octylcyclohexane 98%), and biogenics (isoprene 99%, methacrolein 95%, methyl vinyl ketone 99%, and α-pinene ≥ 99%) (all purchased through Sigma-Aldrich) by direct injection.

In the experiments conducted by Xuan Zhang et al. (ibid.), in situ oxidation of α-pinene, *n*-dodecane, toluene, and isoprene were carried out under high- and low-NO_x conditions, with oxidation periods varying from 1 to 7 h. A customized CF_3O^--CIMS (Crounse et al., 2006) (chemical ionization mass spectrometry) was used to monitor the vapor-wall decay rates. Refer to Xuan Zhang et al. (2015) for more experimental details. In the direct injection experiments, a bulb containing 10 to 50 μL of pure or mixed liquid VOCs was maintained at 65°C (as well as the 50 cm stainless injection line, 3/8 in. OD) to ensure complete injection at a flow rate of 5 L min^{-1} of clean air ($\sim$ 100 ppb in the chamber, several orders of magnitude lower than the saturation vapor pressure). Before each injection, the chamber has been flushed with clean air at a flow rate of 370 L min^{-1} for 24 h at 45°C. The injection period varied from minutes (biogenics) to hours (alcohols). After the injection period, 5 pulse injections of clean air were used to actively mix the chamber without significantly altering its volume. The chamber is considered well mixed $\sim$ 5 min after this operation, which is especially relevant for compounds with short injection periods. A series of RH-dependent studies was carried out in the chamber under 8%±5%, 50%±5% and, 80%±5% RH at 20°C.

Over $\sim$ 18 h in the dark, a gas chromatograph with flame ionization detector (GC/-FID, Agilent 6890N) was used to monitor the temporal concentration changes at a continuous sampling flow rate of 0.29 L min^{-1} through a perfluoroalkoxy (PFA) Teflon tube (1/4 in. OD, 3/16 in. ID, and 2.0 m length). Pagonis et al. (2017) note that use of a PFA Teflon tube induces a response time lag for "sticky" compounds; the continuous flow through the sampling tube and lower sampling time resolution ($\sim$ 10 min) act to smooth this effect. A HP-5 column (30 m $\times$ 0.32 mm ID $\times$ 0.25 μm film thickness) was used for alcohols, aromatics, alkanes, and α-pinene, and a HP-PLOT Q column (15 m $\times$ 0.53 mm ID $\times$ 40 μm film thickness) was used for isoprene, methacrolein (MACR), and methyl vinyl ketone (MVK). For mixtures, the GC temperature ramping procedure was adjusted to obtain full peak resolution. It is challenging to clearly define the start time for GC measurements of compound dark decay. We ignore the first 3 to 5 data points of the GC measurements, which is $\sim$ 1 h after injection, on the assumption that the vapor concentrations in the gas phase and the surface layer have reached equilibrium.

Additionally, studies of in situ 20 s-pulse generated compounds (Krechmer et al., 2016) from isoprene oxidation under 8%±5%, 50%±5% and > 90% RH were carried out. When RH > 90%, an aqueous film was introduced to the surface of Teflon

film by injecting water vapor into the chamber at 30°C until the RH reached ~ 80% and cooling to 20°C to facilitate a uniform water film condensation on the wall, as evidenced visually by the blurry appearance of the chamber. Isoprene (~200 ppb), ~ 1.2 ppm NO (Airgas, 500 ppm ±1%), and ~ 1.2 ppm CH_3ONO (synthesized following W. D. Taylor et al. (1980)) were injected to the chamber, respectively. UV lights were turned on for 20 s (j_{NO_2} = 0.0044 s^{-1}), and no nucleation was observed after lights off. Oxidation products were monitored with a custom-modified I^--CIMS (B. H. Lee et al., 2014) with a 2 L min^{-1} sampling rate through 1/4 in. PFA tube. A permeation tube with pure liquid CH_3I (Sigma-Aldrich, 99%) was used for reagent ion generation in I^--CIMS, where vapor molecules X are detected as the cluster $(X \cdot I^-)$.

In the two-layer kinetic model simulation, the values of k_e and $\mathscr{D}_g$ used are 0.075 s^{-1} and 5×10^{-6} m^2 s^{-1}, respectively, for all compounds (Xuan Zhang et al., 2014). The accommodation coefficient α_w is calculated by a fitted empirical equation based on literature data (Table 4.1 and Fig. 4.8, see Section 4.5.2 for details). Activity coefficients for the compounds studied in Xuan Zhang et al. (2015) are predicted by the equation in Table 4.1 and Fig. 4.7A. Since the oxidation period in Xuan Zhang et al. (ibid.) varied from 1 to 7 h, it is reasonable to assume that an equilibrium state between the bulk chamber and the surface layer had been reached, i.e. $C_g^b = \frac{C_s}{K_w}$, when lights were off. This assumption excludes the oxidation period from the fitting process. We will address subsequently the effect of the oxidation period on the temporal profile of bulk concentration.

4.4 Results and Discussion

4.4.1 Effect of Oxidation Period on Vapor-Wall Partitioning

To study vapor-wall interaction, the species of interest is introduced to the chamber by either direct injection or in situ generation. During injection, the more volatile compounds generally require less time to inject, but achieve wall partitioning more slowly (e.g. *n*-alkanes (Matsunaga and Ziemann, 2010)), whereas less volatile compounds require a longer injection time, during which the bulk chamber and the wall may have already reached equilibrium when injection is completed. Even though the injection period can be shortened by heating the bulb and the injection line (Matsunaga and Ziemann, 2010; Yeh and Ziemann, 2015), for passively mixed chambers, the chamber mixing timescale may be the limiting factor to obtain a well-mixed concentration. This mixing issue is avoided with in situ generation of oxidation products. Ideally, the VOC oxidation period is short, so as to approximate

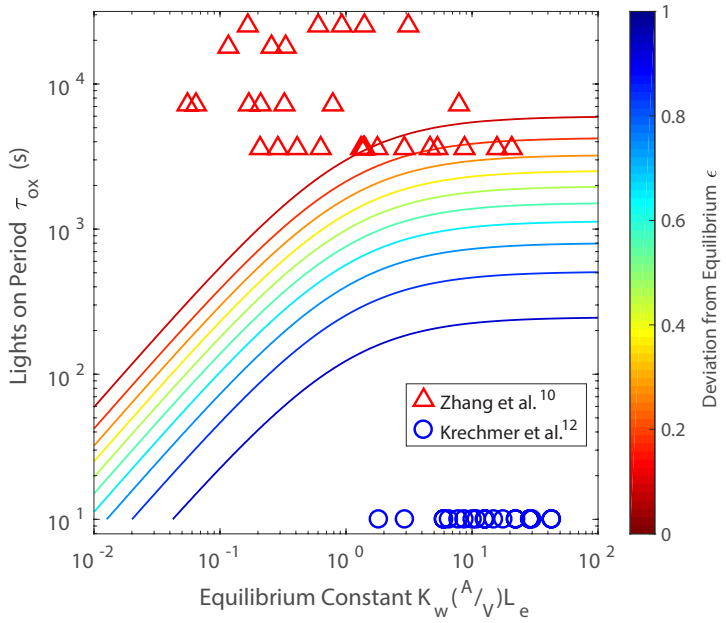

Figure 4.2: Deviation from equilibrium state at the end of oxidation period τ_{ox} as a function of equilibrium constant $K_w \frac{A}{V} L_e$ and oxidation period τ_{ox} for the system represented by G $\xrightarrow{k_0}$ X $\underset{k_{-1}}{\overset{k_1}{\rightleftharpoons}}$ Y, where $k_0 = \frac{0.05}{\tau_{ox}}$ (s^{-1}, assume 5% of G is consumed at the end of oxidation period τ_{ox}), $k_1 = \frac{A}{V} v_l$ (s^{-1}), $k_{-1} = \frac{1}{L_e K_w} v_l$ (s^{-1}), $\frac{A}{V}$ is the surface area to volume ratio of the chamber (m^{-1}), v_l is the vapor-to-wall mass transport coefficient (m s^{-1}), L_e is the surface layer thickness (m), K_w is the dissolution equilibrium constant of vapor molecule in Teflon film. The equilibrium constant $K_{eq} = \frac{k_1}{k_{-1}} = K_w \frac{A}{V} L_e$.

as closely as possible a pulse input of oxidation products (Krechmer et al., 2016). This is important, as the anticipated equilibration time between generation in the chamber and absorption by the surface layer of Teflon is of order 10^3 s (ibid.). However, generation of detectable concentration of products usually requires a relatively long oxidation time (OH concentration is typically $\sim 10^6$ molecules cm^{-3}), during which period equilibrium between the bulk chamber and the surface layer is likely to be achieved.

An idealized kinetic model is useful to describe the interplay between in situ oxidation and the approach to vapor-wall equilibrium. Let us assume that the VOC oxidation can be represented by the first-order reaction G $\xrightarrow{k_0}$ X, where G is the

VOC precursor, X is the oxidation product (i.e. the bulk concentration $C_g^b(t)$ in Eq. (4.2)), and k_0 is an effective first-order rate constant. Since diffusion in the inner layer of the Teflon film is sufficiently slow, it is reasonable to ignore the inner layer uptake of the vapors during the oxidation period, i.e. the second term in Eq. (4.4). By multiplying a scaling factor $\frac{A}{V}L_e$ to $C_s(t)$ in Eq. (4.4), the system can be represented kinetically by $G \xrightarrow{k_0} X \underset{k_{-1}}{\overset{k_1}{\rightleftharpoons}} Y$, where $Y = \frac{A}{V}L_e C_s(t)$, $k_1 = \frac{A}{V}v_l$, and $k_{-1} = \frac{1}{L_e K_w}v_l$. The equilibrium constant for this system is $K_{eq} = \frac{k_1}{k_{-1}} = K_w\frac{A}{V}L_e$. By this representation, vapor-wall partitioning during the VOC oxidation period is mathematically analogous to a classical equilibrium reaction system.

The departure from vapor-wall equilibrium at the end of the reaction period is defined by the normalized deviation $\epsilon = \frac{Y_e - Y_0}{Y_e} = \frac{X_0 - X_e}{X_e K_{eq}}$, where X_0 and Y_0 are the concentrations of X and Y at the end of the oxidation period, and X_e and Y_e are the concentrations at equilibrium. Thus, a value of $\epsilon = 0$ indicates that equilibrium has already been reached at the end of the oxidation period, whereas a value of ϵ close to 1 suggests that from the measured concentration change of X, one can derive the characteristic timescale and equilibrium constant for vapor-wall deposition. Note that it is necessary to focus only on species X, since that is the compound being measured. An analytical solution for the time-dependent dynamics of this kinetic system is given in Section 4.5.3.

For the compounds examined in this study and by Xuan Zhang et al. (2015), the oxidation period τ_{ox} varies from $\sim$ 10 s to $\sim$ 7 h. Assuming that 5% of the precursor G is consumed at the end of the oxidation period, the reaction rate constant k_0 follows the relationship $\tau_{ox}k_0 = 0.05$. The forward rate constant k_1 is determined by the mixing timescale in the chamber (k_e), as well as the surface accommodation coefficient (α_w). Using $k_e = 0.075\ s^{-1}$, $\mathcal{D}_g = 5 \times 10^{-6}\ m^2\ s^{-1}$, and $\alpha_w = 10^{-5}$ (discussion in Section 4.5.2 suggests that most of the compounds studied here are located in the gas-phase boundary layer diffusion regime, where the critical $\alpha_w \sim 10^{-6}$, for simplicity, a fixed value of 10^{-5} for α_w is assumed here), a value of $k_1 = 4.02\times10^{-4}\ s^{-1}$ is obtained, which is of the same order of magnitude as the values reported in the wall deposition study by Krechmer et al. (2016). A contour plot (Fig. 4.2) of ϵ as a function of vapor-wall equilibrium constant, $K_w\frac{A}{V}L_e$, and oxidation period, τ_{ox}, indicates that the majority ($\sim$ 75%) of the compounds studied in Xuan Zhang et al. (2015) had already reached vapor-wall equilibrium at the end of the relatively lengthy oxidation period. In such a case, it is reasonable

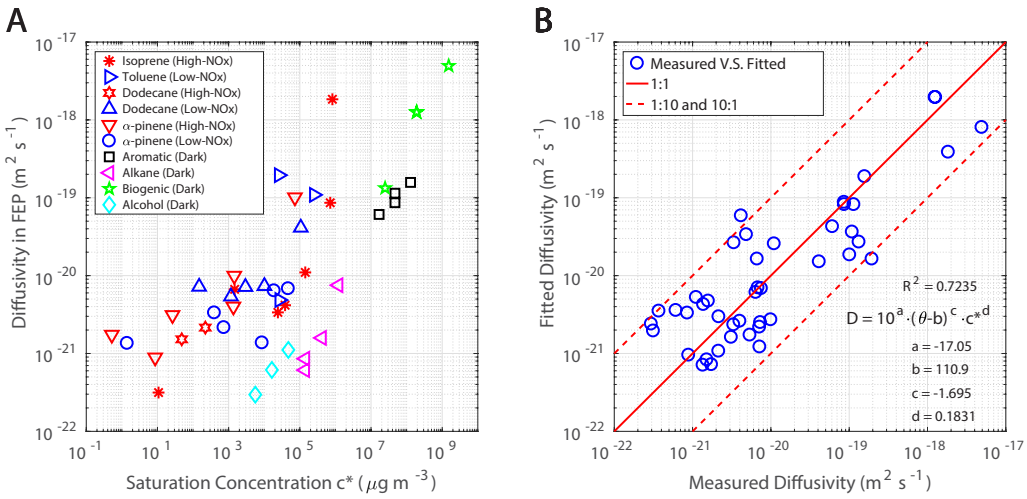

Figure 4.3: (A) Diffusivity in FEP film inferred from measurements by Xuan Zhang et al. (2015) using CIMS and from this study using GC/FID as a function of saturation concentration (c^*) predicted by EVAPORATION (Compernolle et al., 2011; Tropo, 2014). (B) Comparison between measured and fitted diffusivity ($\mathscr{D}_{\text{eff}}$ in $\text{m}^2\ \text{s}^{-1}$) in Teflon film. The molecular volume (θ in $\text{cm}^3\ \text{mol}^{-1}$) and saturation vapor concentration (c^* in $\mu\text{g}\ \text{m}^{-3}$) dependent fitting equation in (B) is used. Molecular volume is estimated by summing the characteristic atomic volumes (θ = C×16.35 + H×8.71 + O×12.43 + N×14.39 $\text{cm}^3\ \text{mol}^{-1}$, where C, H, O, and N represent the number of carbon, hydrogen, oxygen, and nitrogen atoms in the compound)(Abraham and McGowan, 1987). Note: this equation applies only for molecules with volume exceeding 110.9 $\text{cm}^3\ \text{mol}^{-1}$.

to estimate the diffusivity in the inner layer by assuming equilibrium between the bulk chamber and the surface layer. The small value of the wall accommodation coefficient reported by Xuan Zhang et al. (ibid.) likely represents a combination of surface accommodation and inner layer diffusion. Fig. 4.2 shows explicitly the effect of the length of the oxidation period on the surface-layer equilibrium process, since inner-layer diffusion will dominate the dynamics of the vapor sink in a long-duration oxidation experiment.

4.4.2 Diffusion in Teflon Polymer

The inferred diffusivities $\mathscr{D}_{\text{eff}}$ of species dissolved in Teflon film obtained by fitting data to the two-layer model as a function of the molecular saturation concentration c^* are shown in Fig. 4.3A. $\mathscr{D}_{\text{eff}}$ values are in the range of $10^{-22} - 10^{-17}\ \text{m}^2\ \text{s}^{-1}$, which is of order 10^6 smaller than those of small organic molecules in polymer film (Bagley and Long, 1955; Manabu Shiraiwa et al., 2011; Tokarev et al., 2006), a result that

is consistent with the higher energy barrier for larger molecules (Bagley and Long, 1955; Crank, 1953). A transition state between solid and liquid diffusivities of this order of magnitude is well within the range of those in semi-solid organic aerosol particles (Manabu Shiraiwa et al., 2011).

With the assumption that the molecular diffusivity in FEP film can be expressed as a function of molecular volume, we apply a semi-empirical equation to correlate the diffusivity as a function of vapor molecular volume (θ in $cm^3\ mol^{-1}$) (Abraham and McGowan, 1987) and vapor saturation concentration (c^* in $\mu g\ m^{-3}$). c^* is used as the parameter that incorporates the contribution from different functional groups, and, as noted earlier, is estimated by the empirical routine EVAPORATION (Compernolle et al., 2011; Tropo, 2014). The diffusivities obtained from the semi-empirical equation (Table 4.1) are shown in Fig. 4.3B. 95% of the predicted diffusivities lie within an order of magnitude of those inferred $\mathcal{D}_{\text{eff}}$. The high order of negative molecular volume dependence is consistent with the expectation that the larger the molecule, the smaller the diffusivity. The critical volume in the semi-empirical equation ($110.9\ cm^3\ mol^{-1}$) can be viewed as a characteristic "hole" in the film; thus, small molecules only have to overcome the crosslinks between polymer chains. The fitted value of the critical volume is found to exceed those of most of the molecules studied previously (Bagley and Long, 1955; Tokarev et al., 2006); thus the semi-empirical relation given in Fig. 4.3B cannot be used for molecules smaller than the critical volume. The diffusivity is found to be mildly dependent on vapor saturation concentration, reflecting the effect of the presence of functional groups (or molecular shape) on molecular diffusivity.

Diffusivities of vapor molecules in fresh and aged Teflon chambers have also been investigated. Though the absorption properties of the surface layer were reported to be unchanged in either fresh or aged Teflon chambers (Matsunaga and Ziemann, 2010), by fitting experimental data in the Caltech chamber (Xuan Zhang et al., 2015), we found that the inner layer diffusivity increased with use of chambers, consistent with the observations by Christine L. Loza et al. (2010). Such behavior could be attributed to alteration of inter-chain bonds, such that subsequent diffusion is characterized by internal stress relaxation Bagley and Long (1955) and Crank (1953). See discussion in Section 4.5.4 for additional details.

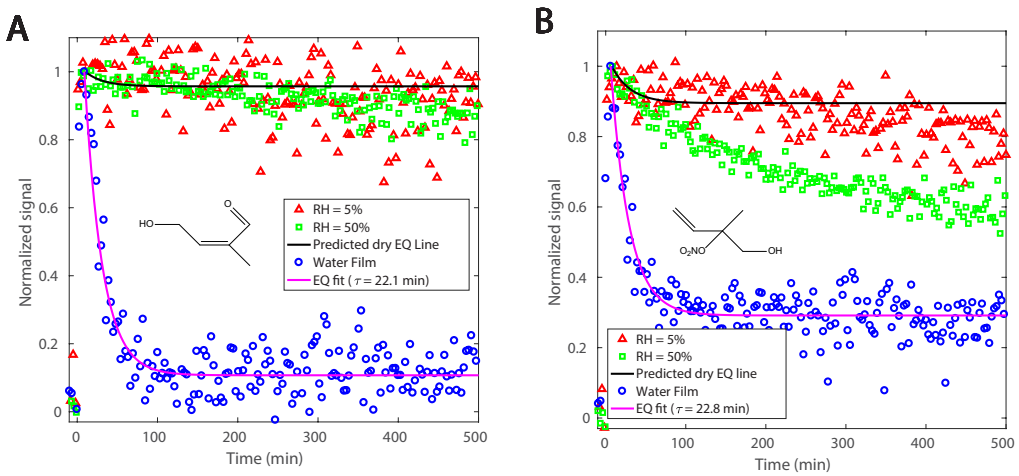

Figure 4.4: Signal decay after 20 s of in situ generation of isoprene oxidation products: (A) $C_5H_8O_2$ and (B) $C_5H_9O_4N$ at RH = 5%, 50% and > 90% (with aqueous film). Because of the signal decay caused by the "memory effect" arising from the sampling tube and instrument inlet (Pagonis et al., 2017), the peaks show up ~ 5 min after lights off.

4.4.3 Humidity Effect

For polymer film chambers, permeation of ubiquitous ambient water vapor through the film is possible given the small molecular volume and high diffusivity ($\sim 10^{-12}$ m^2 s^{-1}) of water in such polymer films (Linossier et al., 1997). The dissolution of water molecules in the Teflon film can exert an impact on the behavior of organic molecules therein. For hydrophilic compounds, the water could facilitate the absorption of the vapors into the film, while for hydrophobic compounds, it could exert a retarding effect. In the high humidity case, in which an aqueous film is hypothesized to be present on the Teflon surface (Panel B of Fig. 4.1), it is evident that hydrophilic compounds would dissolve in the aqueous film.

The limited studies of RH-dependent vapor-wall interaction in chambers that exist report that the vapor-wall loss rate increases at higher RH (> 50%) (Bates et al., 2014; Christine L. Loza et al., 2010; Nguyen et al., 2014, 2016). It is notable that the compounds that have been studied in this regard are either reactive with water (e.g. IEPOX (Bates et al., 2014; Nguyen et al., 2014)) or highly water soluble (e.g. HCOOH, H_2O_2 (Nguyen et al., 2016) and glyoxal (Christine L. Loza et al., 2010)). These observations are consistent with the existence of water molecules in the Teflon film facilitating the absorption of hydrophilic compounds. We used two experimental strategies to investigate the role of RH in vapor-wall interaction.

In the first class of experiments, we injected into the chamber at different RH levels several groups of compounds (alcohols, alkanes, aromatics, and biogenics) that are not highly water soluble and have relatively large molecular volume. A GC/FID was used to monitor the long-term dark decay of these compounds. The inferred diffusivities of the alcohols, alkanes, aromatics, and biogenics in Teflon are shown in Fig. 4.10, indicating that most of the diffusivities decrease as RH increases. It is expected that at high RH, more water molecules dissolve in the Teflon film, such that intrusion of hydrophobic compounds is hindered.

Second, we carried out the same experimental protocol as that of Krechmer et al. (2016) based on an in situ pulse generation of oxidation products (OH concentration is $\sim 10^8$ molecules cm^{-3}). The temporal profiles of two isoprene oxidation products ($C_5H_8O_2$ and $C_5H_9O_4N$) are shown in Fig. 4.4. Under dry conditions (RH $\sim$ 5%), $C_5H_8O_2$ and $C_5H_9O_4N$ exhibit essentially the same diffusivities as those observed by Xuan Zhang et al. (2015). However, at RH $\sim$ 50%, the two compounds behave differently; a faster decay rate is observed for $C_5H_9O_4N$, which is likely attributable to hydrolysis of the compound containing a $-ONO_2$ group (Bean and Hildebrandt Ruiz, 2016). When a water film is introduced intentionally (RH > 90%), the signals of both compounds decrease rapidly after the lights are off at almost the same rates, reaching a constant level for the next 8 h. By fitting the data at RH > 90% in Fig. 4.4 to the aqueous film model (Fig. 4.1B), a characteristic timescale is found to be $\sim$ 22 min for each compound, considerably faster than that due to inner layer diffusion under dry conditions. This value is in the range of vapor-wall equilibrium timescales (τ_w) reported by Krechmer et al. (2016) and Matsunaga and Ziemann (2010). With an estimated chamber eddy diffusivity of 0.075 s^{-1} (Xuan Zhang et al., 2014), the calculated accommodation coefficients of $C_5H_8O_2$ and $C_5H_9O_4N$ at the water surface are 3.06×10^{-5} and 1.32×10^{-5}, respectively, consistent with gas-phase boundary layer mass transport being the rate-limiting step in the fast equilibrium sorption process.

The water film serves as a substantial reservoir given that both compounds are water active (soluble or reactive). By comparison, the inferred equilibrium constants, K_{eq}, for both compounds in the aqueous film exceed those in the dry Teflon film by factors of 186 and 21, suggesting that the majority of the vapor molecules remain within the aqueous layer. The results of this aqueous film experiment are consistent with the conclusion that in SOA formation experiments under high RH conditions, the presence of a condensed water film on the wall will exacerbate vapor-wall loss

of hydrophilic oxidation products.

4.4.4 Mechanistic Representation of Vapor-Wall Deposition

After the introduction of vapors into the chamber (either by injection or in situ generation), loss due to wall uptake is generally reported as first order. The experimental results reported here show that, in addition to the establishment of rapid equilibrium between the bulk gas phase and the surface layer of the chamber wall ($\tau_{\text{surf}} \sim 10^3$ s), inner layer diffusion as well as chemical reactions (e.g. hydrolysis) can lead to a continuous decay of the gas-phase vapors in the bulk chamber. This process can be represented kinetically by the following system: Source $\longrightarrow$ X $\underset{k_{-1}}{\overset{k_1}{\rightleftharpoons}}$ Y $\xrightarrow{k_2}$ Z, where Source represents injection or in situ oxidation. Species X and Y represent the same compound in different phases, and species Z is the same compound in the third phase (e.g the inner layer in this case). Correspondingly, k_2 represents either the first-order chemical reaction rate constant or the mass transfer coefficient. The forward and backward rate constants k_1 and k_{-1} govern the approach to phase equilibrium of X and Y.

When injection or in situ oxidation has ceased, the above dynamic system can be represented simply as X $\underset{k_{-1}}{\overset{k_1}{\rightleftharpoons}}$ Y $\xrightarrow{k_2}$ Z. If species X and Y have reached equilibrium, and if $k_2 \ll k_1 + k_{-1}$, a slow decay follows a rapid equilibrium. The time-dependent analytical solution of this kinetic system is presented in Section 4.5.6. The apparent first-order decay rate constant, k_w^X, of species X exhibits the long-time asymptote $\frac{K_{eq}}{1+K_{eq}}k_2$, where $K_{eq} = \frac{k_1}{k_{-1}}$ as defined above.

The net loss rate constant k_2 is a function of diffusivity $\mathscr{D}_{\text{eff}}$. To obtain a relationship between k_2 and $\mathscr{D}_{\text{eff}}$, an empirical equation can be fitted as shown in Fig. 4.5, where k_2 and $\mathscr{D}_{\text{eff}}$ both emerge from fitting experimental data from the equilibrium reaction model and the two-layer diffusion model. For comparison, k_2 values derived from reported apparent first-order loss rates, k_w, by the asymptotic relationship, $k_w = \frac{K_{eq}}{1+K_{eq}}k_2$, and the inferred diffusivities are shown in Fig. 4.5. Many of these reported data points lie within the uncertainty of the empirical relationship. The small reported k_2 values may be the result of different chamber conditions (Bates et al., 2014; Praske et al., 2015; St. Clair et al., 2016), or the use of the asymptote, since some of the data are from the observation within 2 h (as indicated in Section 4.5.6, in the short time period, the apparent k_w is small). Note that this empirical relationship does not account for the presence of heterogeneous reactions, which

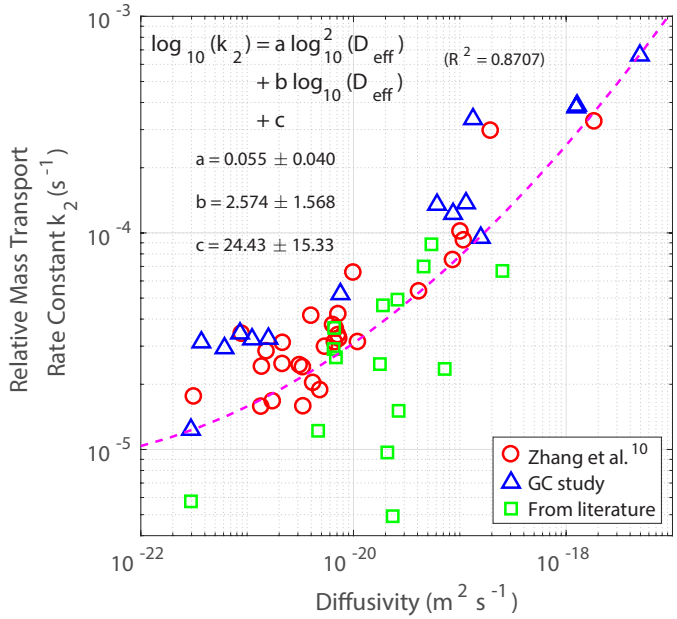

Figure 4.5: Empirical relationship between compound molecular diffusivity $\mathscr{D}_{\text{eff}}$ (m^2 s^{-1}) and relative inner layer mass transport rate constant k_2 (s^{-1}). k_2 is derived by fitting the analytical solution in Section 4.5.5 to the experimental data, whereas data points from the literature (Bates et al., 2014; C. L. Loza et al., 2014; Christine L. Loza et al., 2010; Praske et al., 2015; R. H. Schwantes et al., 2017b, 2015; Manabu Shiraiwa et al., 2013; St. Clair et al., 2016) are calculated by the asymptotic relationship between k_w (reported data) and k_2. Diffusivity is predicted by the equation in Fig. 4.3.

may change the value of k_2.

4.4.5 Atmospheric Implications

Teflon-walled laboratory chambers serve as the predominant system for the study of atmospheric SOA formation. Clear evidence exists for the deposition of VOC oxidation products on polymeric Teflon chamber walls. Such deposition removes products that would otherwise condense onto particles as SOA. Since the presence of wall deposition of vapors leads to an underestimate of the atmospheric SOA-forming potential of the parent VOC, data that have been influenced by such wall deposition will lead to an underprediction of SOA formation when extrapolated to the atmosphere.

The wall deposition process involves transport of vapor molecules from the core of the chamber to a boundary layer on the wall of the chamber, through which vapors are transported to the wall surface by a combination of molecular diffusion and

macroscopic mixing. Vapor molecules diffuse into the Teflon polymer matrix by a process akin to that of uptake into a condensed phase. Observed rates of molecular uptake into Teflon polymer are found to be consistent with a model of the Teflon film consisting of two layers: (1) a thin surface layer into which vapor molecules penetrate first through the gas-phase boundary layer and second across the interface, over a timescale of order 10^3 s; and (2) a deeper layer of effectively semi-infinite extent into which the absorbed vapor molecules diffuse from the surface layer. The uptake rates by Teflon-walled chamber of over 90 individual organic vapor species are found to depend upon their molecular saturation vapor concentration (c^*) and molecular size (θ).

Semi-empirical equations have been formulated to describe the absorptive properties (γ^∞ and α_w) of the surface layer and the diffusivity in the inner layer of FEP film. Additional studies are needed to characterize the temperature effect on the vapor uptake process. Water molecules dissolved in the Teflon film provide extra sinks on the wall for hydrophilic compounds. Under sufficiently high RH conditions, where a thin film of condensed water is present on the Teflon surface, the wall becomes an increasingly competitive reservoir for hydrophilic compounds. The challenge is to design VOC oxidation chamber experiments under different RH levels so as to minimize vapor transport to the chamber walls. To better constrain the measured vapor-wall loss rate (e.g. the "apparent" first-order rate constant k_w), recommended parameters and guidelines are given in Table 4.1, which can facilitate a comprehensive consideration of the sinks of gas-phase species in a typical SOA formation experiment.

4.5 Supporting Information

4.5.1 Gas-Phase Boundary Layer Transport

The governing equation for gas-phase boundary layer mass transport of a tracer molecule of concentration C_g^δ across a layer of thickness δ on the wall of a chamber is :

$$\frac{\partial C_g^\delta}{\partial t} = \frac{\partial}{\partial x}\left[(\mathscr{D}_g + k_e x^2)\frac{\partial C_g^\delta}{\partial x}\right] = (\mathscr{D}_g + k_e x^2)\frac{\partial^2 C_g^\delta}{\partial x^2} + 2xk_e\frac{\partial C_g^\delta}{\partial x} \tag{4.8}$$

where $\mathscr{D}_g$ is the vapor molecular diffusivity in the gas phase, and k_e is the eddy diffusivity coefficient characteristic of mixing in the bulk of the chamber (Corner and Pendlebury, 1951; Crump and John H. Seinfeld, 1981).

The boundary condition at the outer extent of the boundary layer, $x = \delta$, is:

$$C_g^\delta(\delta, t) = C_g^b(t) \tag{4.9}$$

where $C_g^b(t)$ is the concentration in the bulk of the chamber.

The rate of change of $C_g^b(t)$ owing to removal from the bulk by transport to and uptake by the chamber wall is:

$$V\frac{dC_g^b(t)}{dt} = -A\left[(\mathscr{D}_g + k_e x^2)\frac{\partial C_g^\delta}{\partial x}\right]\Bigg|_{x=\delta} \tag{4.10}$$

where V and A are the volume and surface area of the chamber, respectively.

The boundary condition on C_g^δ at the wall surface, $x = 0$, owing to equality of fluxes, is:

$$\mathscr{D}_g\left(\frac{\partial C_g^\delta}{\partial x}\right)\Bigg|_{x=0} = \frac{\alpha_w \omega}{4}\left(C_g^\delta|_{x=0} - \frac{C_s}{K_w}\right) \tag{4.11}$$

where α_w is the accommodation coefficient at the wall, ω is the mean molecular velocity of the species, and $K_w = \dfrac{C_w}{\gamma^\infty c^*}$. γ^∞ is the activity coefficient of vapor molecules dissolved in the wall, c^* is the species mass saturation concentration, C_w is the effective organic mass concentration of the wall, by analogy to the effective aerosol mass concentration used in describing vapor-particle uptake (John H. Seinfeld and James F. Pankow, 2003), and C_s is the species concentration uniformly dissolved in the wall surface layer.

Correspondingly, the rate of change of $C_s(t)$ is:

$$V\frac{dC_s(t)}{dt} = A\left[(\mathscr{D}_g + k_e x^2)\left(\frac{\partial C_g^\delta}{\partial x}\right)\right]\Bigg|_{x=0} \tag{4.12}$$

The concentration profile of vapors in the boundary layer will eventually relax to a quasi-steady state, under which the governing equation for the gas-phase concentration reduces to:

$$0 = \frac{\partial}{\partial x}\left[(\mathscr{D}_g + k_e x^2)\frac{\partial C_g^\delta}{\partial x}\right] \tag{4.13}$$

The boundary conditions on Eq. (4.13) are $C_g^\delta(\delta, t) = C_g^b(t)$ and $C_g^\delta(0, t) = C_{g,0}^\delta(t)$, where $C_{g,0}^\delta(t)$ is the gas-phase concentration immediately above the wall surface. Note that the time t refers to that in the period after which quasi-steady state conditions have been reached. The solution to Eq. (4.13) subject to its boundary conditions is:

$$C_g^\delta(x,t) = \left(C_g^b(t) - C_{g,0}^\delta(t)\right)\arctan\left(x\sqrt{\frac{k_e}{\mathscr{D}_g}}\right)/\arctan\left(\delta\sqrt{\frac{k_e}{\mathscr{D}_g}}\right) + C_{g,0}^\delta(t) \tag{4.14}$$

The rates of change of $C_g^b(t)$ and $C_s(t)$ over the entire chamber are:

$$\begin{aligned} V\frac{dC_g^b(t)}{dt} &= -A\left[(\mathscr{D}_g + k_e x^2)\frac{\partial C_g^\delta}{\partial x}\right]\Bigg|_{x=\delta} \\ &= -\left(C_g^b(t) - C_{g,0}^\delta(t)\right)\sqrt{k_e\mathscr{D}_g}/\arctan\left(\delta\sqrt{\frac{k_e}{\mathscr{D}_g}}\right) = -\frac{\alpha_w\omega}{4}\left(C_{g,0}^\delta(t) - \frac{C_s(t)}{K_w}\right) \\ &= -A\,\mathscr{D}_g\left(\frac{\partial C_g^\delta}{\partial x}\right)\Bigg|_{x=0} = -V\frac{dC_s(t)}{dt} \end{aligned} \tag{4.15}$$

Since $C_{g,0}^\delta(t)$ is unknown, we can rewrite Eq. (4.15) as:

$$\frac{dC_g^b(t)}{dt} = -\left(\frac{A}{V}\right)\left(\frac{1}{v_e} + \frac{1}{v_c}\right)^{-1}\left(C_g^b(t) - \frac{C_s(t)}{K_w}\right) = -\frac{dC_s(t)}{dt} \tag{4.16}$$

where $v_e = \sqrt{k_e\mathscr{D}_g}/\arctan\left(\delta\sqrt{\frac{k_e}{\mathscr{D}_g}}\right)$ and $v_c = \frac{\alpha_w\omega}{4}$. Under typical chamber conditions, $\frac{\delta^2 k_e}{\mathscr{D}_g} \gg 1$, $v_e = \frac{2}{\pi}\sqrt{k_e\mathscr{D}_g}$. The initial condition is: at $t = 0$, $C_g^b = C_{g0}^b$ and $C_s = 0$. From Eq. (4.16), we can solve for the time evolution of C_g^b and C_s.

If we define $\Delta C(t) = C_g^b(t) - \frac{C_s(t)}{K_w}$ as the deviation from equilibrium, we can derive the rate of change of $\Delta C(t)$ from Eq. (4.16):

$$\frac{d\Delta C(t)}{dt} = \frac{d\left[C_g^b(t) - \frac{C_s(t)}{K_w}\right]}{dt} = -\left(\frac{A}{V}\right)\left(1 + \frac{1}{K_w}\right)\left(\frac{1}{v_e} + \frac{1}{v_c}\right)^{-1}\Delta C(t) \tag{4.17}$$

So the vapor-wall equilibration timescale (τ_{vwe})is:

$$\tau_{vwe} = \left(\frac{A}{V}\right)^{-1} \left(1 + \frac{1}{K_w}\right)^{-1} \left(\frac{1}{v_e} + \frac{1}{v_c}\right) \tag{4.18}$$

The two key parameters in the vapor-wall interaction are the accommodation coefficient on the wall α_w and the vapor-wall equilibrium constant K_w. Of interest is the extent to which α_w and K_w impact the time for the gas-phase concentration to reach quasi-steady state within the boundary layer. For example, for the Caltech chamber, the eddy diffusion coefficient $k_e = 0.075$ (s^{-1}) (Xuan Zhang et al., 2014), and $\frac{A}{V} = 2.08$ (m^{-1}); we assume $\mathscr{D}_g = 5 \times 10^{-6}$ (m^2 s^{-1}), and $\omega = 200$ (m s^{-1}). To satisfy the condition $\frac{\delta^2 k_e}{\mathscr{D}_g} \gg 1$, the boundary layer thickness δ is on the order of 10^{-1} m (Corner and Pendlebury, 1951). We will consider as well δ values of 10^{-2} and 10^{0} m. α_w and K_w are varied to estimate the timescale for the gas-phase concentration to reach 95% of its quasi-steady state profile with the boundary layer thickness $\delta = 10^{-1}$, 10^{-2}, and 10^{0} m, respectively.

The timescales are shown in Fig. 4.6, indicating that for a wide range of boundary layer thickness δ, the gas-phase boundary layer reaches quasi-steady state within $\sim$ 10 s. Based on this conclusion, it is reasonable to use the quasi-steady-state flux directly in calculations.

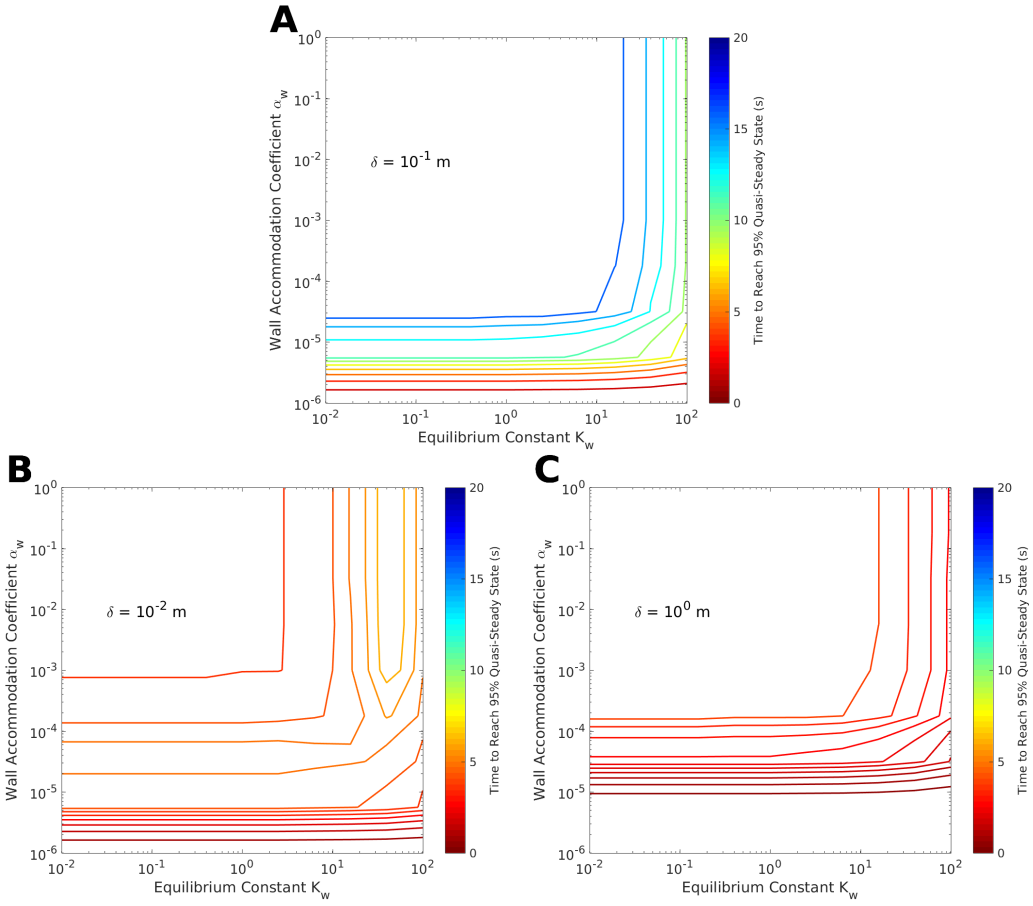

Figure 4.6: Timescale for gas-phase concentration to reach 95% of the quasi-steady state in a boundary layer of thickness of (A) $\delta = 0.1$ m, (B) $\delta = 0.01$ m, and (C) $\delta = 1$ m.

4.5.2 Activity and Accommodation Coefficients

This section addresses the information used to calculate γ^{∞} and α_w based on data from the literature (Krechmer et al., 2016; Matsunaga and Ziemann, 2010; Yeh and Ziemann, 2014, 2015).

The activity coefficient γ^{∞} in Teflon film can be calculated by the following equation:

$$\gamma^{\infty} = \frac{MW_{voc}}{MW_w} \cdot \frac{C_w}{c^* \cdot C_s/C_g} \tag{4.19}$$

where MW_{voc} and MW_w are the molecular weight of the compound (varies, listed in the following table) and the wall (assumed 200 g mol^{-1}) (Matsunaga and Ziemann, 2010), C_w is the equivalent wall mass concentration (e.g., 32.2 mg m^{-3} for the chambers used by Krechmer et al. (2016) and Ziemann et al. (Yeh and Ziemann, 2014, 2015)), c^* is the saturation concentration (μg m^{-3}, estimated by EVAPORATION (Compernolle et al., 2011)), and C_s/C_g is the ratio of vapor concentration dissolved in the wall surface layer to that in the gas phase at equilibrium (data from the literature (Krechmer et al., 2016; Matsunaga and Ziemann, 2010; Yeh and Ziemann, 2014, 2015)). See the caption of Fig. 4.7 for details.

The characteristic equilibration timescale τ_{vwe} for gas-wall partitioning is:

$$\tau_{vwe} = \frac{1}{k_{g\rightarrow w} + k_{g\leftarrow w}} = \frac{1}{k_{g\rightarrow w}} \frac{1}{1 + 1/K_{eq}} \tag{4.20}$$

where $k_{g\rightarrow w} = \left(\frac{A}{V}\right)\left(\frac{4}{\alpha_w \omega} + \frac{\pi}{2}\frac{1}{\sqrt{k_e \mathcal{D}_g}}\right)^{-1}$, $K_{eq} = \frac{k_{g\rightarrow w}}{k_{g\leftarrow w}} = \left(\frac{C_s}{C_g}\right)_{eq}$, and $\omega = \sqrt{\frac{8RT}{\pi MW_{voc}}}$, R is the gas constant, and T is temperature. Both the gas-to-wall transfer constant $k_{g\rightarrow w}$ and the equilibrium constant K_{eq} determine the characteristic timescale τ_{vwe}. $k_{g\rightarrow w}$ is determined by both the surface accommodation coefficient α_w and the eddy diffusivity k_e in the chamber. For either monofunctional or multifunctional compounds, Krechmer et al. (2016) recommended constant timescales (1800 s and 600 s) in the same chamber simulation, even though the equilibrium constants are different. Such an assumption (τ_{vwe} is fixed, but K_{eq} varies) requires that the accommodation coefficient α_w is compound-dependent.

We can calculate the surface accommodation coefficient α_w with the following equation derived from EQ. (4.20):

$$\alpha_w = \frac{4}{\omega}\left[\tau_{vwe}\left(\frac{A}{V}\right)\left(1 + \frac{1}{C_s/C_g}\right) - \frac{\pi}{2}\frac{1}{\sqrt{k_e \mathcal{D}_g}}\right]^{-1} \tag{4.21}$$

Estimates of the characteristic timescale τ_{vwe} and the ratio C_s/C_g at equilibrium can be obtained from measurements in the literature (Krechmer et al., 2016; Matsunaga and Ziemann, 2010; Yeh and Ziemann, 2014, 2015). Krechmer et al. (2016) suggested the eddy diffusivity k_e could be calculated by:

$$k_e = 0.004 + 5.6 \times 10^{-3} V^{0.74} \tag{4.22}$$

With a chamber volume of $V = 8$ m^3, $k_e = 0.03$ s^{-1}. The gas-phase diffusivity $\mathcal{D}_g$ is set as a constant 5×10^{-6} m^2 s^{-1} for all compounds. The calculated values of α_w are listed in Table. 4.2 and shown in Fig. 4.8. An empirical equation fitted to the data clearly indicates a negative dependence of α_w on the vapor saturation concentration, which is consistent with the expectation that less volatile compounds are more "sticky". Note that when $k_e = 0.03$ s^{-1}, negative values of α_w result from the NO_3^--CIMS data (ibid.), suggesting that under their chamber conditions, the limiting step is gas-phase boundary layer diffusion (Fig. 4.8, left upper grean area), which was verified by turning on the fan inside the chamber (so that k_e increases) leading to a much faster decay rate. For the Caltech chamber, $k_e = 0.075$ s^{-1}, calculated based on the particle-wall deposition rate (Xuan Zhang et al., 2014), yields a critical $\alpha_w = 7.80 \times 10^{-6}$ ($\omega = 200$ m s^{-1}), corresponding to $c^* = 4 \times 10^3$ μg m^{-3} from the fitting expression (Fig. 4.8). The range of saturation concentration c^* of the compounds studied by Xuan Zhang et al. (2015) is $10^{-1} - 10^6$ μg m^{-3}. We apply this fitting expression (Fig. 4.8) to predict α_w.

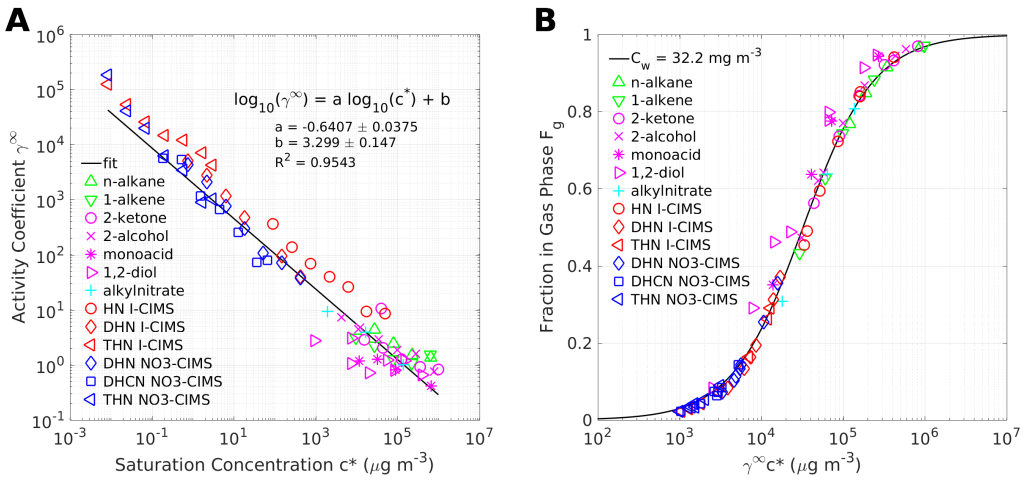

Figure 4.7: Panel (A) Activity coefficients γ^{∞} in FEP film calculated from the literature (Krechmer et al., 2016; Matsunaga and Ziemann, 2010; Yeh and Ziemann, 2014, 2015) as a function of vapor saturation concentration (c^*) estimated by EVAPORATION (Compernolle et al., 2011; Tropo, 2014). Raw data used to calculate γ^{∞} are provided in Table 4.2. *n*-alkanes and 1-alkenes (green) are from Matsunaga and Ziemann (2010). 2-ketones, 2-alcohols, monoacids, and 1,2-diols (magenta) are from Yeh and Ziemann (2015). Alkylnitrates (cyan) are from Yeh and Ziemann (2014). I^--CIMS (red) and $NO_3{}^-$-CIMS (blue) are from Krechmer et al. (2016). SIMPOL.1 (J. F. Pankow and Asher, 2008) predicts vapor pressure by summation of group contributions, and EVAPORATION considers group position effect for multifunctional isomers. The difference in vapor pressure estimated by these two methods is within a factor of $2 \sim 3$. For multifunctional isomers, all HNs (Krechmer et al., 2016) (hydroxynitrates) are 1-OH-5-alkylnitrates, DHNs (dihydroxynitrates) are 1,5-OH-2-alkylnitrates, THNs (trihydroxynitrates) are 1,2,5-OH-6-alkylnitrates, and DHCNs (dihydroxycarbonylnitrates) are 1,2-OH-5-carbonyl-6-alkylnitrates. Measurements by I^--CIMS (Krechmer et al., 2016) are thought to be biased by "memory" effects arising from sampling tube and instrument inlet; thus, they are excluded in the fitting. Panel (B) Fraction F_g at vapor-wall equilibrium remaining in the gas phase (Krechmer et al., 2016) as a function of $\gamma^{\infty}c^*$. $F_g = \dfrac{1}{1 + C_w/(\gamma^{\infty}c^*)}$, where $C_w = 32.2$ mg m^{-3} corresponding to $L_e = 5$ nm and surface-to-volume ratio $\dfrac{A}{V} = 3$ m^{-1}.

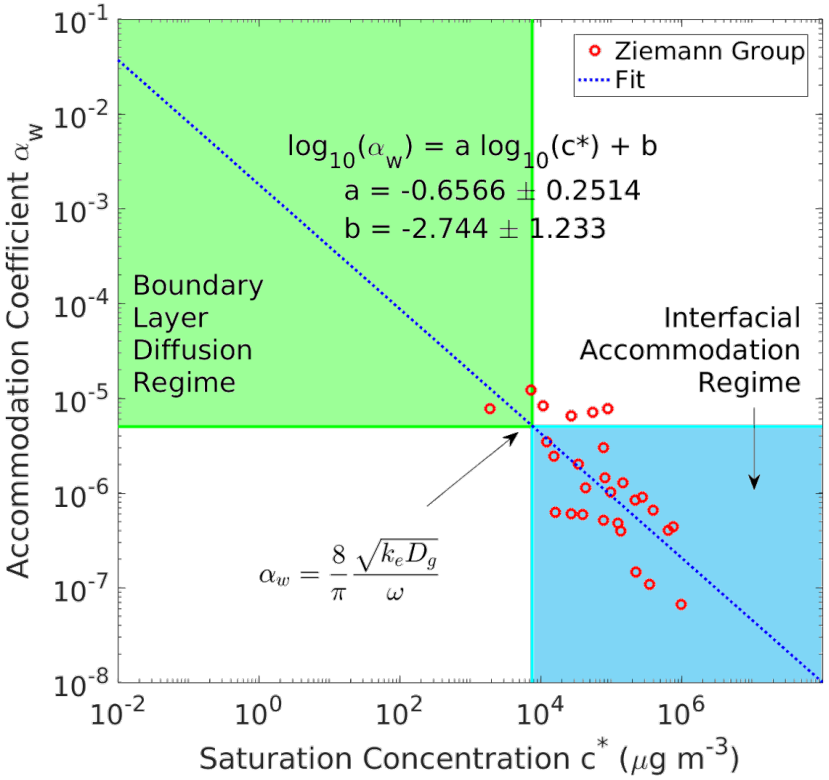

Figure 4.8: Accommodation coefficient of vapor molecules on the Teflon wall α_w versus saturation concentration c^*. Data are from the Ziemann group (Matsunaga and Ziemann, 2010; Yeh and Ziemann, 2014, 2015). An empirical relationship is fitted to the data points. The critical α_w point (McMurry and Grosjean, 1985) (5.12×10^{-6}, corresponding to $k_e = 0.03$ s^{-1}, marked by an arrow) is that at which the rate of mass transport to the wall shifts from the gas-phase boundary layer diffusion regime (green area) to the interfacial accommodation regime (blue area). The fitted line indicates that the compounds studied by Krechmer et al. (2016) (c^* in the range of 10^{-2} – 10^4 μg m^{-3}) lie in the gas-phase boundary layer diffusion regime.

Table 4.2: Literature data used to calculated activity coefficient γ^{∞} and accommodation coefficient α_w

	T	$\mathscr{D}_g$	L_e	ρ_{FEP}	A/V	V	MW_{FEP}	C_w^{eq}
	(K)	(m^2 s^{-1})	(nm)	(kg m^{-3})	(m^{-1})	(m^3)	(g mol^{-1})	(μg m^{-3})
	298	5×10^{-6}	5	2150	3	8	200	3.22E+04
Source				min	g mol^{-1}	atm		
2-ketone (Yeh and Ziemann, 2015)		F_g	C_w/C_g	τ_{vwe}	MW_{voc}	EVAPORATION	α_w	γ^{∞}
	2-decanone	0.970	0.031	50	156	1.55E-04	6.72E-08	8.24E-01
	2-undecanone	0.921	0.085	85	170	5.06E-05	1.09E-07	9.14E-01
	2-dodecanone	0.841	0.188	43	184	1.65E-05	4.83E-07	1.26E+00
	cyclododecanone	0.933	0.072	15	184	5.23E-06	5.96E-07	1.05E+01
	2-tridecanone	0.736	0.359	35	198	5.41E-06	1.13E-06	2.03E+00
	2-tetraecanone	0.563	0.776	33	212	1.77E-06	2.43E-06	2.87E+00
				min	g mol^{-1}	atm		
2-alcohol (ibid.)		F_g	C_w/C_g	τ_{vwe}	MW_{voc}	EVAPORATION	α_w	γ^{∞}
	2-nonanol	0.962	0.040	10	144	1.31E-04	4.41E-07	7.65E-01
	2-decanol	0.945	0.058	8	158	4.27E-05	9.04E-07	1.59E+00
	2-undecanol	0.868	0.152	18	172	1.40E-05	1.02E-06	1.86E+00
	2-dodecanol	0.770	0.300	19	186	4.56E-06	2.01E-06	2.89E+00
	cyclododecanol	0.621	0.610	14	186	1.44E-06	8.36E-06	4.48E+00
	2-tridecanol	0.642	0.558	21	200	1.49E-06	3.46E-06	4.74E+00
	2-tetradecanol	0.473	1.114	-	214	4.88E-07	-	7.25E+00
				min	g mol^{-1}	atm		

monoacid (ibid.)		F_g	C_w/C_g	τ_{vwe}	MW_{voc}	EVAPORATION	α_w	γ^∞
	pentanoic acid	0.943	0.060	14	102	1.57E-04	4.01E-07	4.15E-01
	heptanoic acid	0.775	0.290	8	130	1.68E-05	7.73E-06	8.09E-01
	octanoic acid	0.637	0.570	-	144	5.49E-06	-	1.26E+00
	nonanoic acid	0.351	1.849	-	158	1.80E-06	-	1.19E+00

				min	g mol^{-1}	atm		
1,2-diol (ibid.)		F_g	C_w/C_g	τ_{vwe}	MW_{voc}	EVAPORATION	α_w	γ^∞
	1,2-butanediol	0.947	0.056	8	90	1.06E-04	6.53E-07	6.62E-01
	1,2-pentanediol	0.914	0.094	8	104	3.48E-05	1.28E-06	1.20E+00
	1,4-pentanediol	0.799	0.252	17	104	1.95E-05	1.45E-06	8.05E-01
	1,5-pentanediol	0.462	1.165	-	104	4.68E-06	-	7.23E-01
	1,2-hexanediol	0.778	0.285	8	118	1.14E-05	7.10E-06	1.21E+00
	1,6-hexanediol	0.290	2.448	-	118	1.53E-06	-	1.05E+00
	1,2-octanediol	0.488	1.049	16	146	1.22E-06	1.22E-05	3.09E+00
	1,8-octanediol	0.010	95.618	-	146	1.64E-07	-	2.52E-01
	1,2-decanediol	0.083	11.048	-	174	1.30E-07	-	2.74E+00
	1,10-decanediol	0.010	98.010	-	174	1.75E-08	-	2.30E+00

				min	g mol^{-1}	atm		
alkane (Matsunaga and Ziemann, 2010)		F_g	C_w/C_g	τ_{vwe}	MW_{voc}	EVAPORATION	α_w	γ^∞
	N-tridecane	0.967	0.034	-	184	8.47E-05	-	1.36E+00
	N-tetradecane	0.915	0.093	74	198	2.77E-05	1.48E-07	1.52E+00
	N-pentadecane	0.848	0.180	41	212	9.06E-06	5.18E-07	2.42E+00
	N-hexadecane	0.767	0.303	56	226	2.96E-06	6.06E-07	4.39E+00

				min	g mol^{-1}	atm		
alkene (ibid.)		F_g	C_w/C_g	τ_{vwe}	MW_{voc}	EVAPORATION	α_w	γ^{∞}
	1-tridecene	0.971	0.030	-	182	8.47E-05	-	1.55E+00
	1-tetradecene	0.884	0.132	20	196	2.77E-05	8.42E-07	1.08E+00
	1-pentadecene	0.744	0.345	17	210	9.06E-06	2.99E-06	1.26E+00
	1-hexadecene	0.627	0.595	16	224	2.96E-06	6.52E-06	2.24E+00
	1-heptadecene	0.433	1.311	-	238	9.68E-07	-	3.11E+00

				min	g mol^{-1}	atm		
alkylnitrate (Yeh and Ziemann, 2014)		F_g	C_w/C_g	τ_{vwe}	MW_{voc}	EVAPORATION	α_w	γ^{∞}
	2-decyl nitrate	0.807	0.239	65	203	1.64E-05	3.99E-07	1.00E+00
	2-dodecyl nitrate	0.638	0.568	85	227	1.76E-06	6.24E-07	3.95E+00
	2-tetradecyl nitrate	0.307	2.252	28	251	1.88E-07	7.71E-06	9.32E+00

				min	g mol^{-1}	atm		
HN I^--CIMS (Krechmer et al., 2016)		F_g	C_w/C_g	τ_{vwe}	MW_{voc}	EVAPORATION	α_w	γ^{∞}
	$C_6H_{13}NO_4$	0.941	0.063	-	163	7.36E-06	-	8.56E+00
	$C_7H_{15}NO_4$	0.851	0.175	-	177	2.41E-06	-	9.39E+00
	$C_8H_{17}NO_4$	0.839	0.192	-	191	7.87E-07	-	2.62E+01
	$C_9H_{19}NO_4$	0.723	0.383	-	205	2.57E-07	-	4.00E+01
	$C_{10}H_{21}NO_4$	0.594	0.684	-	219	8.41E-08	-	6.87E+01
	$C_{11}H_{23}NO_4$	0.490	1.041	-	233	2.75E-08	-	1.38E+02
	$C_{12}H_{25}NO_4$	0.454	1.203	-	247	8.99E-09	-	3.64E+02

				min	g mol^{-1}	atm		
DHN I^--CIMS (ibid.)		F_g	C_w/C_g	τ_{vwe}	MW_{voc}	EVAPORATION	α_w	γ^∞
	$C_6H_{13}NO_5$	0.371	1.695	-	179	5.77E-08	-	4.03E+01
	$C_7H_{15}NO_5$	0.312	2.205	-	193	1.89E-08	-	9.48E+01
	$C_9H_{19}NO_5$	0.194	4.155	-	221	2.02E-09	-	4.71E+02
	$C_{10}H_{21}NO_5$	0.163	5.135	-	235	6.59E-10	-	1.17E+03
	$C_{11}H_{23}NO_5$	0.133	6.519	-	249	2.16E-10	-	2.80E+03
	$C_{12}H_{25}NO_5$	0.083	11.048	-	263	7.05E-11	-	5.06E+03

				min	g mol^{-1}	atm		
THN I^--CIMS (ibid.)		F_g	C_w/C_g	τ_{vwe}	MW_{voc}	EVAPORATION	α_w	γ^∞
	$C_6H_{13}NO_6$	0.290	2.448	-	195	3.79E-10	-	4.26E+03
	$C_7H_{15}NO_6$	0.262	2.817	-	209	1.96E-10	-	7.15E+03
	$C_8H_{17}NO_6$	0.163	5.135	-	223	6.42E-11	-	1.20E+04
	$C_9H_{19}NO_6$	0.072	12.831	-	237	2.10E-11	-	1.46E+04
	$C_{10}H_{21}NO_6$	0.043	22.364	-	251	6.86E-12	-	2.57E+04
	$C_{11}H_{23}NO_6$	0.030	32.898	-	265	2.24E-12	-	5.33E+04
	$C_{12}H_{25}NO_6$	0.023	42.860	-	279	7.34E-13	-	1.25E+05

				min	g mol^{-1}	atm		
DHN NO_3^--CIMS (ibid.)		F_g	C_w/C_g	τ_{vwe}	MW_{voc}	EVAPORATION	α_w	γ^∞
	$C_6H_{13}NO_5$	0.355	1.817	9	179	5.77E-08	-	3.76E+01
	$C_7H_{15}NO_5$	0.254	2.937	11.8	193	1.89E-08	-	7.13E+01
	$C_8H_{17}NO_5$	0.143	5.993	11.2	207	6.17E-09	-	1.07E+02
	$C_9H_{19}NO_5$	0.133	6.519	12.6	221	2.02E-09	-	2.99E+02

	$C_{10}H_{21}NO_5$	0.114	7.772	10.2	235	6.59E-10	-	7.68E+02
	$C_{11}H_{23}NO_5$	0.103	8.709	11.8	249	2.16E-10	-	2.10E+03
	$C_{12}H_{25}NO_5$	0.072	12.831	9.8	263	7.05E-11	-	4.36E+03

				min	g mol^{-1}	atm		
DHCN NO_3^--CIMS (ibid.)		F_g	C_w/C_g	τ_{vwe}	MW_{voc}	EVAPORATION	α_w	γ^∞
	$C_6H_{11}NO_6$	0.143	5.993	8.2	193	8.35E-09	-	7.89E+01
	$C_7H_{13}NO_6$	0.074	12.587	10	207	4.32E-09	-	7.25E+01
	$C_8H_{15}NO_6$	0.084	10.862	8.6	221	1.41E-09	-	2.57E+02
	$C_9H_{17}NO_6$	0.072	12.831	9.4	235	4.62E-10	-	6.65E+02
	$C_{10}H_{19}NO_6$	0.043	22.364	8	249	1.51E-10	-	1.17E+03
	$C_{11}H_{21}NO_6$	0.063	14.898	9	263	4.94E-11	-	5.36E+03
	$C_{12}H_{23}NO_6$	0.023	42.860	7.4	277	1.62E-11	-	5.68E+03

				min	g mol^{-1}	atm		
THN NO_3^--CIMS (ibid.)		F_g	C_w/C_g	τ_{vwe}	MW_{voc}	EVAPORATION	α_w	γ^∞
	$C_6H_{13}NO_6$	0.090	10.148	10.2	195	3.79E-10	-	1.02E+03
	$C_7H_{15}NO_6$	0.043	22.364	11.2	209	1.96E-10	-	8.99E+02
	$C_8H_{17}NO_6$	0.054	17.692	9.4	223	6.42E-11	-	3.48E+03
	$C_9H_{19}NO_6$	0.032	30.153	11.4	237	2.10E-11	-	6.24E+03
	$C_{10}H_{21}NO_6$	0.034	28.851	9.8	251	6.86E-12	-	1.99E+04
	$C_{11}H_{23}NO_6$	0.023	42.860	11.6	265	2.24E-12	-	4.09E+04
	$C_{12}H_{25}NO_6$	0.034	28.851	10.4	279	7.34E-13	-	1.86E+05

4.5.3 Analytical Solution for the Kinetics of the System $\mathbf{G} \xrightarrow{\mathbf{k_0}} \mathbf{X} \underset{\mathbf{k_{-1}}}{\overset{\mathbf{k_1}}{\rightleftharpoons}} \mathbf{Y}$

The system dynamics are described by the set of linear ODEs:

$$\frac{d}{dt}\mathbf{W} = \mathbb{A} \cdot \mathbf{W} \tag{4.23}$$

where $\mathbf{W} = \begin{pmatrix} G \\ X \\ Y \end{pmatrix}$, $\mathbb{A} = \begin{pmatrix} -k_0 & 0 & 0 \\ k_0 & -k_1 & k_{-1} \\ 0 & k_1 & -k_{-1} \end{pmatrix}$. The initial condition is $\mathbf{W}_0 = \begin{pmatrix} G_0 \\ 0 \\ 0 \end{pmatrix}$. The eigenvalues of $\mathbb{A}$ are $\lambda_1 = -k_0$, $\lambda_2 = 0$, and $\lambda_3 = -(k_1 + k_{-1})$.

When $k_0 \neq k_1 + k_{-1}$, the analytical solution for the concentrations of the three species is:

$$\frac{1}{G_0}\mathbf{W} = \begin{pmatrix} 1 \\ \dfrac{-k_0 + k_{-1}}{k_0 - k_1 - k_{-1}} \\ \dfrac{k_1}{k_0 - k_1 - k_{-1}} \end{pmatrix} \mathrm{e}^{-k_0 t} + \begin{pmatrix} 0 \\ \dfrac{k_{-1}}{k_1 + k_{-1}} \\ \dfrac{k_1}{k_1 + k_{-1}} \end{pmatrix} + \begin{pmatrix} 0 \\ \dfrac{k_0 k_1/(k_1 + k_{-1})}{k_0 - k_1 - k_{-1}} \\ -\dfrac{k_0 k_1/(k_1 k_{-1})}{k_0 - k_1 - k_{-1}} \end{pmatrix} \mathrm{e}^{-(k_1 + k_{-1})t} \tag{4.24}$$

When $k_0 = k_1 + k_{-1}$, the solution is:

$$\frac{1}{G_0}\mathbf{W} = \begin{pmatrix} 1 \\ -\dfrac{k_{-1}}{k_1 + k_{-1}} \\ -\dfrac{k_1}{k_1 + k_{-1}} \end{pmatrix} \mathrm{e}^{-k_0 t} + \begin{pmatrix} 0 \\ \dfrac{k_{-1}}{k_1 + k_{-1}} \\ \dfrac{k_1}{k_1 + k_{-1}} \end{pmatrix} + \begin{pmatrix} 0 \\ \dfrac{k_0 k_1}{k_1 + k_{-1}} \\ -\dfrac{k_0 k_1}{k_1 + k_{-1}} \end{pmatrix} t\mathrm{e}^{-(k_1 + k_{-1})t} \tag{4.25}$$

After the oxidation period of duration t_0, during which G is oxidized to X, $X(t_0) + Y(t_0) = X_e + Y_e = 1 - \mathrm{e}^{-k_0 t_0}$, where X_e and Y_e are equilibrium concentrations of X and Y and have a relationship of $\dfrac{Y_e}{X_e} = K = \dfrac{k_1}{k_{-1}}$. Thus the derivation from equilibrium $\epsilon(t_0, K)$ is

$$\epsilon(t_0, K) = \frac{X(t_0) - X_e}{Y_e} = \frac{X(t_0) - (1 - \mathrm{e}^{-k_0 t_0})\dfrac{1}{1 + K}}{(1 - \mathrm{e}^{-k_0 t_0})\dfrac{K}{1 + K}} \tag{4.26}$$

4.5.4 Fresh versus Aged Teflon Chambers

Ratios of the inferred molecular diffusivities in fresh vs. aged Teflon as a function of c^* are shown in Fig. 4.9, based on the measurements of Xuan Zhang et al. (2015) It is found that the inferred diffusivity in fresh Teflon chambers is $\sim$ 1 order of magnitude lower than that in an aged chamber. No apparent trend for high-NO_x and low-NO_x conditions is evident. Over 330 experiments were carried out in the "aged" Caltech chambers from 2012 to 2014, whereas the "fresh" data were obtained immediately after installation of new chambers. A change in polymer diffusivity over time has been reported (Bagley and Long, 1955), attributed to unrecoverable inter-chain bonds, such that subsequent diffusion events are characterized by internal stress relaxation (Crank, 1953).

Differences in measured vapor-wall deposition rates between fresh and aged Teflon chambers are consistent with the observations by Christine L. Loza et al. (2010) that the first-order vapor-wall loss rate is essentially negligible in new chambers but increases as more and more experiments are performed. However, this observation is not in conflict with that by Matsunaga and Ziemann (2010) of a lack of chamber age dependence for surface layer absorption Crank (1953), since the surface layer, i.e. the sharp and swollen boundary interface, is the same in either fresh or aged Teflon chambers.

The effect of temperature on vapor-wall deposition was studied at 45°C and 20°C for three relatively volatile species (isoprene, MACR, and MVK, Fig. 4.9). The data indicate that at higher temperature, these three species exhibit a slower wall deposition rate. The reason is unclear; it could be a result of decreased surface accommodation at higher temperature, as parameterized by α_w.

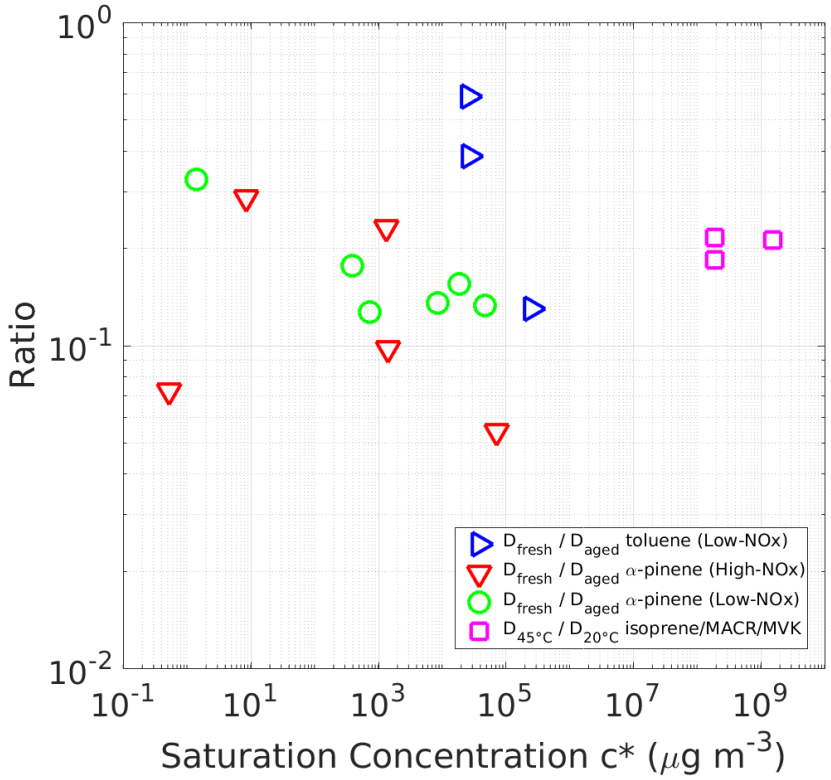

Figure 4.9: Ratio of inferred diffusivity in fresh to aged Teflon film as well as that at 45°C to 20°C as a function of saturation concentration c^*. Since the wall accommodation coefficient, α_w, at 45°C is assumed the same as that at 20°C, the smaller inferred diffusivity at 45°C could also be caused by lower α_w at higher temperature.

4.5.5 Humidity Effect on Teflon Inner Layer Diffusivity

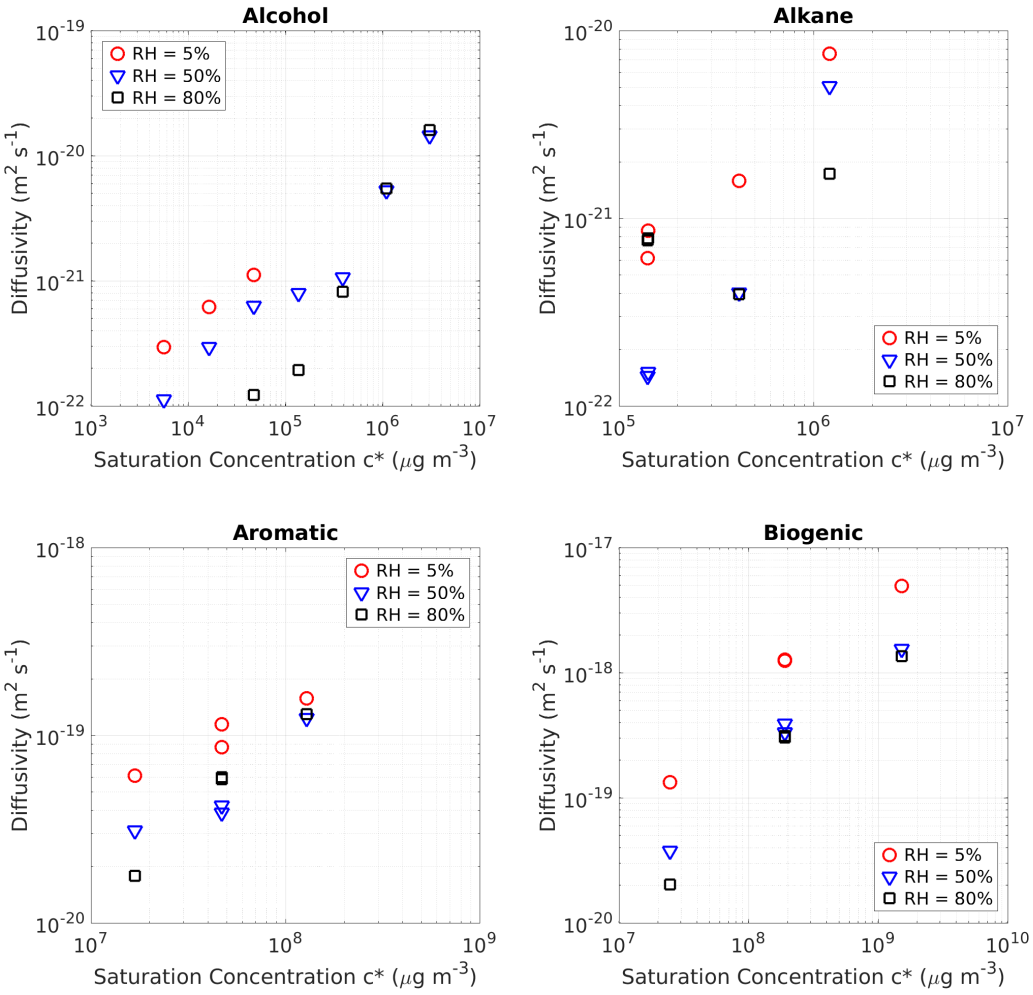

Figure 4.10: Inferred Diffusivity $\mathcal{D}_{\text{eff}}$ (m^2 s^{-1}) in FEP Teflon film as a function of saturation concentration c^* (μg m^{-3}) at different relative humidities for alcohols (C_6-C_{12} 1-alcohols), alkanes (C_{12}-C_{14} *n*-alkanes and *n*-octylcyclohexane), aromatics (toluene, *m*-, *o*-xylene, and 1,3,5-trimethylbenzene), and biogenic compounds (isoprene, MACR, MVK, and α-pinene).

4.5.6 Exact and Approximate Solutions for the Kinetics of the System $\mathbf{X} \underset{\mathbf{k_{-1}}}{\overset{\mathbf{k_1}}{\rightleftharpoons}} \mathbf{Y} \xrightarrow{\mathbf{k_2}} \mathbf{Z}$

The system dynamics are described by the set of linear ODEs:

$$\frac{d}{dt}\mathbf{W} = \mathbb{A} \cdot \mathbf{W} \tag{4.27}$$

where $\mathbf{W} = \begin{pmatrix} X \\ Y \end{pmatrix}$, and $\mathbb{A} = \begin{pmatrix} -k_1 & k_{-1} \\ k_1 & -k_{-1} - k_2 \end{pmatrix}$. It is assumed that X and Y rapidly come to equilibrium. The initial condition is $\mathbf{W}_0 = X_0 \begin{pmatrix} 1 \\ k_1/k_{-1} \end{pmatrix}$.

The eigenvalues of $\mathbb{A}$ are:

$$\begin{aligned} \lambda_1 &= \frac{-(k_1 + k_{-1} + k_2) - \sqrt{(k_1 + k_{-1} + k_2)^2 - 4k_1k_2}}{2} \\ \lambda_2 &= \frac{-(k_1 + k_{-1} + k_2) + \sqrt{(k_1 + k_{-1} + k_2)^2 - 4k_1k_2}}{2} \end{aligned} \tag{4.28}$$

The solution of Eq. (4.27) is

$$\frac{1}{X_0}\mathbf{W} = \frac{1}{X_0}\begin{pmatrix} X(t) \\ Y(t) \end{pmatrix} = -\frac{\lambda_2}{\lambda_1 - \lambda_2}\begin{pmatrix} 1 \\ \dfrac{k_1 + \lambda_1}{k_{-1}} \end{pmatrix} e^{\lambda_1 t} + \frac{\lambda_1}{\lambda_1 - \lambda_2}\begin{pmatrix} 1 \\ \dfrac{k_1 + \lambda_2}{k_{-1}} \end{pmatrix} e^{\lambda_2 t} \tag{4.29}$$

And by mass balance:

$$Z(t) = X_0\left(1 - X(t) + \frac{k_1}{k_{-1}}(1 - Y(t)\right) \tag{4.30}$$

Under conditions that $k_2 \ll k_1 + k_{-1}$, that is, rapid equilibrium established by X and Y, we can derive approximate solutions.

First, the eigenvalues can be simplified as:

$$\begin{aligned} \lambda_1 &= -(k_1 + k_{-1}) - \frac{k_{-1}}{k_1 + k_{-1}}k_2 \\ \lambda_2 &= -\frac{k_1}{k_1 + k_{-1}}k_2 \end{aligned} \tag{4.31}$$

We note that $\dfrac{\lambda_2}{\lambda_1} \ll 1$. If the equilibrium constant $K_{eq} = \dfrac{k_1}{k_{-1}} \gg 1$, $\lambda_1 = -k_1 - k_{-1}$ and $\lambda_2 = -k_2$. If $K_{eq} \ll 1$, $\lambda_1 = -k_1 - k_{-1} - k_2$ and $\lambda_2 = -\dfrac{k_1}{k_{-1}}k_2$.

Second, the slow change of X owing to the slow conversion of Y to Z is usually described in terms of a first-order rate constant k_w^X, in the units of time^{-1}:

$$k_w^X = \frac{1}{X}\frac{dX}{dt} = \frac{\frac{\lambda_1\lambda_2}{\lambda_1-\lambda_2}e^{\lambda_1 t}\left(e^{(\lambda_2-\lambda_1)t}-1\right)}{\frac{\lambda_1}{\lambda_1-\lambda_2}e^{\lambda_1 t}\left(e^{(\lambda_2-\lambda_1)t}-\frac{\lambda_2}{\lambda_1}\right)} = \lambda_2\frac{e^{(\frac{\lambda_2}{\lambda_1}-1)\lambda_1 t}-1}{e^{(\frac{\lambda_2}{\lambda_1}-1)\lambda_1 t}-\frac{\lambda_2}{\lambda_1}} \sim \lambda_2\frac{e^{-\lambda_1 t}-1}{e^{-\lambda_1 t}}$$
$$= \lambda_2\left(1-e^{\lambda_1 t}\right) \tag{4.32}$$

EQ. (4.32) indicates that at the outset when t is small, the rate of change of X is $k_w^X \sim -\lambda_2\lambda_1 t$, which results in a relatively flat profile of X. As $t \to \infty$, $k_w^X \sim -\lambda_2$, suggesting that, X and Y can be viewed as a group, for which the net loss rate is λ_2.

4.5.7 Application in Chamber Simulations

This two-layer model can be readily incorporated into models of vapor and particle dynamics in chambers, since only the fates of vapor molecules in gas phase and in the surface layer have to be tracked. The scheme $\mathrm{X} \underset{\mathrm{k_{-1}}}{\overset{\mathrm{k_1}}{\rightleftharpoons}} \mathrm{Y} \xrightarrow{\mathrm{k_2}} \mathrm{Z}$ can simplify this incorporation, where X is the gas-phase concentration of concern and Y corresponds to its concentration in the surface. Thus the ordinary differential equations for X and Y are:

$$\frac{dX}{dt} = -k_1 X + k_{-1} Y + \sum P_{iX} - \sum L_{iX} \tag{4.33}$$

$$\frac{dY}{dt} = k_1 Y - k_{-1} Y - k_2 Y \tag{4.34}$$

where $\sum P_{iX}$ and $\sum L_{iX}$ are the production and loss processes for gas-phase species X in the chamber, respectively, e.g. chemical reactions or interaction with particles (J. H. Seinfeld and S. N. Pandis, 2016). Expressions for $\mathrm{k_1}$, $\mathrm{k_{-1}}$, and $\mathrm{k_2}$ can be found in Table 1.

Initial conditions are required to apply this model. We suggest that: if Compound X is introduced into the chamber through injection, the initial conditions for EQs. (4.33) and (4.34) are $X = X_0$ and $Y = X_0 \frac{k_1}{k_{-1}}$; if Compound X is generated in-situ chemically, the initial conditions are $X = Y = 0$.

Another key aspect is the value of $\mathrm{k_2}$. From Table 1, $\mathrm{k_2}$ can be found through $\mathscr{D}_{\mathrm{eff}}$, while $\mathscr{D}_{\mathrm{eff}}$ can be predicted based on the molecular volume (θ) and the vapor saturation concentration (c^*). If one wants to account for the history of use of the chamber, a rough expression for the corrected diffusivity is $\mathscr{D}_{\mathrm{eff}}^{corr} = \frac{0.015n}{330}\mathscr{D}_{\mathrm{eff}}$, where n is the number of experiments performed in that chamber, and we assume the diffusivity increases by $\sim 1.5\%$ per experiment based on the finding in Section IV. However, the semi-empirical expression for $\mathrm{k_2}$ applies only to dry conditions at room temperature and a chamber constructed of 50 μm Teflon film. For other conditions, e.g. different RH or temperature, we suggest that $\mathrm{k_2}$ be determined experimentally. One has to find the "apparent" first-order decay rate k_w^X by exponentially fitting the experimental data, similar to the GC measurement in this study, and apply $k_w^X = \frac{k_1}{k_1 + k_{-1}} k_2$ to find k_2.

Chapter 5

PROBING THE OH OXIDATION OF PINONIC ACID AT THE AIR-WATER INTERFACE USING FIELD-INDUCED DROPLET IONIZATION MASS SPECTROMETRY (FIDI-MS)

Huang, Yuanlong, Kevin M. Barraza, Christopher M. Kenseth, Ran Zhao, Chen Wang, J. L. Beauchamp, and John H. Seinfeld (2018). "Probing the OH Oxidation of Pinonic Acid at the Air–Water Interface Using Field-Induced Droplet Ionization Mass Spectrometry (FIDI-MS)". In: *J. Phys. Chem. A* 122.31, pp. 6445–6456. DOI: 10.1021/acs.jpca.8b05353.

Abstract

Gas and aqueous phases are essential media for atmospheric chemistry and aerosol formation. Numerous studies have focused on aqueous-phase reactions as well as coupled gas/aqueous-phase mass transport and reaction. Few studies have directly addressed processes occurring at the air-water interface, especially involving surface-active compounds. We report here the application of field-induced droplet ionization mass spectrometry (FIDI-MS) to chemical reactions occurring at the atmospheric air-water interface. We determine the air-water interfacial OH radical reaction rate constants for sodium dodecyl sulfate (SDS), a common surfactant, and pinonic acid (PA), a surface-active species and proxy for biogenic atmospheric oxidation products, as 2.87×10^{-8} and 9.38×10^{-8} cm^2 molec^{-1} s^{-1}, respectively. In support of the experimental data, a comprehensive gas-surface-aqueous multiphase transport and reaction model of general applicability to atmospheric interfacial processes is developed. Through application of the model, PA is shown to be oxidized exclusively at the air-water interface of droplets with a diameter of 5 μm under typical ambient OH levels. In the absence of interfacial reaction, aqueous- rather than gas-phase oxidation is the major PA sink. We demonstrate the critical importance of air-water interfacial chemistry in determining the fate of surface-active species.

5.1 Introduction

The hydroxyl radical (OH) is the fundamental oxidant in the atmosphere. In addition to reaction with gas-phase molecules (e.g., volatile organic compounds), OH reaction can modify the physico-chemical properties (e.g., surface tension, hygroscopicity, composition, etc.) of airborne particles through heterogeneous chemistry

(George and Abbatt, 2010). Heterogeneous OH-initiated oxidation of particles can be confined to the interface due to the particle bulk properties, such as high viscosity (Houle et al., 2018). The air-water interface is ubiquitous in the atmosphere owing to the high surface-to-volume ratio of cloud and fog droplets. Moreover, heterogeneous reaction at the air-water interface can be facilitated if the air-water interface lowers the reaction energy barrier (Zhong et al., 2018). In addition, organic molecules at the air-water interface may have preferred orientation as a result of hydrogen bonding involving substituent groups (Wren et al., 2015); thus, the reaction mechanisms at the air-water interface can differ from those of gas- and aqueous-phase reactions (Enami and Colussi, 2017; Heath and Valsaraj, 2015; Hua et al., 2015; Jones et al., 2017; Kumar et al., 2018; Martins-Costa et al., 2015; Wellen et al., 2017). Studies of the air-water interfacial oxidation of organic compounds have focused on the effects of substitutions (Pillar and Guzman, 2017), unsaturation (King et al., 2009; Xiao et al., 2017), and chain length (Sebastiani et al., 2018) on reaction kinetics and mechanisms.

Pinonic acid (PA) is a major oxidation product of α-pinene, one of the most abundant biogenic volatile organic compounds emitted to the atmosphere (global emissions estimated at 66.1 Tg/y, Guenther et al., 2012). Studies have focused on gas- and aqueous-phase oxidation of PA by OH (Müller et al., 2012; Witkowski and Gierczak, 2017). Upon oxidation by OH, PA has been shown to have a high potential to form the secondary organic aerosols (SOA, Aljawhary et al., 2016; A. K. Y. Lee et al., 2011). With a saturation vapor pressure of $\sim 7 \times 10^{-5}$ Pa at 296 K (Bilde and Spyros N. Pandis, 2001), PA partitions between the gas and particle phases. Given its high Henry's law constant of $\sim 2 \times 10^{7}$ M atm^{-1} (Lignell et al., 2013), PA tends to reside in the aqueous phase under cloudy and foggy conditions, or in the presence of aerosol liquid water. Although PA has been shown to be a highly surface-active species in the atmosphere (X. Li et al., 2010), limited studies have been directed to its behavior at the air-water interface (Enami and Colussi, 2017; Enami and Sakamoto, 2016). Enami and Sakamoto (2016) showed that PA resides at the air-water interface and observed peroxyl radicals and hydroperoxides at the early stage of exposure of PA solution droplets to OH. Though OH oxidation of PA at the air-water interface is rapid, kinetic data of the interfacial reaction are lacking. Lai et al. (2015) estimated the atmospheric lifetime of PA as 2.1 - 3.3 days under environmentally relevant humidity conditions based on heterogeneous OH oxidation of PA film as opposed to an actual air-water interface. Given its high surface activity and tendency to partition to the aqueous phase, investigation of

mechanisms and kinetics of interfacial oxidation of PA by OH under atmospheric conditions is addressed here.

We employ field-induced droplet ionization mass spectrometry (FIDI-MS) to investigate the OH oxidation of pinonic acid at the air-water interface (Grimm and Beauchamp, 2003, 2005). FIDI-MS is differentiated from other mass spectrometric techniques by the ability to perform online detection of chemical species at the air-water interface via a surface-selective sampling mechanism, for which the ionization process has been studied extensively. The FIDI sampling apparatus produces millimeter-sized water droplets containing analytes at concentrations relevant to the ambient atmosphere (i.e., clouds, fog, and aerosol liquid water). Because of the specificity of sampling, FIDI-MS has been employed to monitor the adsorption and heterogeneous chemistry of organic compounds at the air-water interface of both atmospherically (Grimm et al., 2006; Thomas et al., 2016; X. Zhang et al., 2017) and biologically (Kim et al., 2010a,b; X. Zhang et al., 2018) relevant systems. The controllable timescale for reaction in FIDI-MS makes it possible to track the kinetics of interfacial reactions over many half-lives and multiple generations of oxidation.

Through study of the OH oxidation of PA at the air-water interface with FIDI-MS, we seek to elucidate the mechanistic details of its surface reaction. To interpret the kinetic data, we develop a gas-surface-aqueous multiphase transport and reaction model that describes the heterogeneous OH oxidation of PA and constrains the surface reaction rate constant of PA + OH at the air-water interface. For the first time, the interplay between chemistry, diffusion, and phase-partitioning occurring at a droplet's air-water interface is investigated. We demonstrate that under typical ambient OH levels ($\sim 10^6$ molec cm^{-3}), the majority of the multiphase PA oxidation occurs on the surface of water droplets representative of cloud/fog water. In short, the present study addresses the importance of interfacial oxidation for surface-active atmospheric species.

5.2 Methods

5.2.1 Experimental Setup

A schematic diagram of the FIDI-MS setup is depicted in Figure 5.1; a detailed description of the FIDI-MS method is presented elsewhere (Grimm and Beauchamp, 2003, 2005). Briefly, an aqueous droplet of ~2 mm diameter (~ 4 μL volume) is suspended on the end of a stainless steel capillary held equidistant between two parallel plate electrodes separated by 6.3 mm (Fig. 5.1a). Droplets are formed

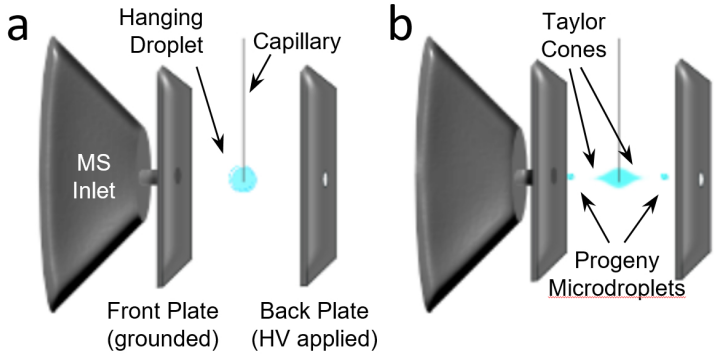

Figure 5.1: Schematic of FIDI-MS for oxidation studies, as viewed from the side. a: A droplet hanging between two parallel plate electrodes. b: A snapshot of the elongated droplet when the pulsed voltage is employed to the plate electrodes.

from analyte solutions fed through the capillary using a motorized syringe pump. The parallel plates are mounted on a translation stage to allow alignment of an aperture in the electrically grounded front plate with the atmospheric pressure inlet of an LTQ-XL mass spectrometer (Thermo-Fischer, Waltham, MA) that is open to ambient lab air. Following droplet formation, a period of 60 s is allowed for diffusion of surface-active species to achieve equilibrium coverage at the air-water interface. The sampling of the hanging droplet proceeds by applying a high voltage pulse (3 - 5 kV, 100 ms duration, variable polarity) to the back plate electrode and to the capillary at half the magnitude supplied to the back plate, establishing a homogeneous electric field. The electric field induces an aligned dipole that stretches the suspended droplet until dual Taylor cones are formed at opposite ends, ejecting charged sub-micrometer progeny droplets of opposite polarity toward the appropriately biased electrodes (Fig. 5.1b). Progeny droplets of a specific polarity pass through the aperture in the grounded front plate and enter the inlet of the mass spectrometer, resulting in the detection of gas-phase ions. As FIDI sampling causes significant perturbation to the droplet, a fresh droplet is generated for each measurement. In many respects, the FIDI process is similar to that of electrospray ionization (ESI), except that sampling occurs only from the sheared electrical double layer at the droplet surface. In this study, a negative voltage was applied to the back plate and capillary to detect deprotonated $[M-H]^-$ ions.

A dielectric barrier discharge source (DBDS) was used to generate hydroxyl radicals. The DBDS consists of a 38 mm borosilicate tube (6.45 mm O.D., 3.91 mm I.D.) with a tungsten rod (1.02 mm diameter) inner electrode and a conductive silver epoxy outer electrode. A bubbler provides water-saturated helium through the DBDS with

flow monitored by a Type πMFC digital mass flow controller (model PFC-50, MKS Instruments). A high voltage AC power supply (Trek PM04015, Trek, Inc) biases the inner electrode during experiments, while the outer electrode remains grounded. The operational conditions of the DBDS are as follows: 12 kVpp (peak-to-peak AC voltage) bias, 1 kHz sine waveform, 1.414 mA current, and 1000 cm^3 min^{-1} He/H_2O flow. The proposed mechanism of OH generation proceeds either directly via an electron capture reaction with water ($e^- + H_2O \longrightarrow H^- + OH$), or through a two-step process ($e^- + H_2O \longrightarrow H_2O^+ + 2\,e^-$ and $H_2O^+ + H_2O \longrightarrow H_3O^+ + OH$, Barraza, 2018). No H, O, or HO_2 is anticipated to form in the DBDS. The characterization of gas-phase OH concentration will be discussed subsequently.

Ultra-pure water (18 MΩ, < 3 ppb TOC, Millipore Milli-Q) and HPLC grade methanol (J.T.Baker) were used as solvents. Aqueous stock solutions of *cis*-pinonic acid (PA, 98%, Sigma-Aldrich) and sodium dodecyl sulfate (SDS, 98%, Fischer Scientific) were prepared at concentrations of 5 mM and 2 mM, respectively, and diluted as needed. Settings for FIDI-MS were optimized for deprotonated *cis*-pinonic acid $[PA-H]^-$ using a 20 μM solution of PA in 99.2:0.8 methanol:water (v/v%).

To study the interfacial OH + PA reaction mechanism, an aqueous PA droplet with an average bulk concentration of 50 μM is exposed to OH from the DBDS for varying reaction times, at which concentration, based on its equilibrium constant, ~19% of PA is estimated to remain on the surface of the droplet with a radius of 1 mm. Droplets of 20 μM SDS were exposed to the OH source for different durations to characterize the gas-phase OH concentration. To constrain the surface reaction rate constant for OH + PA, a mixture of PA and SDS solution is diluted to 50 and 20 μM, respectively. Under each reaction condition, 5 droplets were repeated and averaged to overcome drop-to-drop variation.

5.2.2 Diffusion-Reaction Interfacial Model

We present the development of a diffusion-reaction model designed to describe the air-water interfacial reaction on a droplet between gas-phase OH and a surface-active component, PA in this study. In addition to its surface reaction with OH, PA can evaporate into the gas phase, diffuse into the bulk droplet, and undergo bulk oxidation if dissolved OH is present. Sodium dodecyl sulfate (SDS) is used as a reference compound that, in contrast to PA, given its high molecular weight and long alkyl chain, undergoes only surface reaction, i.e., no evaporation and no diffusion

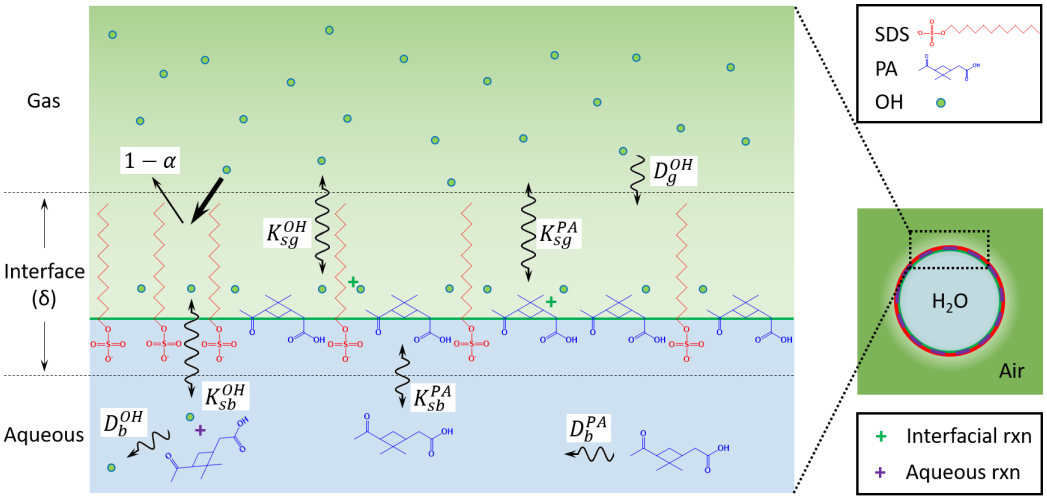

Figure 5.2: Multiphase transport and reaction model for OH reaction with sodium dodecyl sulfate (SDS) and pinonic acid (PA) at the air-water interface. Key parameters of corresponding processes are labeled and explanation can be found in Section 5.5.1 and Table 5.1.

into the bulk. Moreover, SDS oxidation products are easy to characterize at early timescales as SDS undergoes sequential oxygenation with negligible fragmentation. As such, by measuring the rate of decay of SDS on the surface, one can infer the gas-phase OH concentration, and, in turn, calculate the surface reaction rate constant with OH for the surface-active species. The model accounts for each of these transport and reaction processes explicitly, for both PA and SDS, in order to extract the surface reaction rate of PA + OH from the experimental data.

The physical system to which this model is applied is depicted in Fig. 5.2; additional details of the model are discussed in Section 5.5.1. The following reactions describe the transport and reaction processes:

$$\mathrm{OH}(gs) \rightleftharpoons \mathrm{OH}(s) \tag{R 1}$$

$$\mathrm{PA}(gs) \rightleftharpoons \mathrm{PA}(s) \tag{R 2}$$

$$\mathrm{PA}_p(gs) \rightleftharpoons \mathrm{PA}_p(s) \tag{R 3}$$

$$\mathrm{OH}(s) + \mathrm{SDS}(s) \longrightarrow \mathrm{SDS}_{p1}(s) \xrightarrow{\mathrm{OH}(s)} \mathrm{SDS}_{p2}(s) \xrightarrow{\mathrm{OH}(s)} \mathrm{SDS}_{p3}(s) \xrightarrow{\mathrm{OH}(s)} \ldots \tag{R 4}$$

$$\mathrm{OH}(s) + \mathrm{PA}(s) \longrightarrow \mathrm{PA}_p(s) \tag{R 5}$$

$$\mathrm{OH}(s) \rightleftharpoons \mathrm{OH}(b) \tag{R 6}$$

$$\mathrm{PA}(s) \rightleftharpoons \mathrm{PA}(b) \tag{R 7}$$

$$\mathrm{PA}_p(s) \rightleftharpoons \mathrm{PA}_p(b) \tag{R 8}$$

$$\mathrm{OH}(b) + \mathrm{PA}(b) \longrightarrow \mathrm{PA}_p(b) \tag{R 9}$$

where s refers to the surface, b represents the bulk aqueous phase, and gs denotes the gas phase within one molecular mean free path above the surface. Note that gs is distinct from g, the bulk gas phase sufficiently far from the surface. Differences in concentrations between gs and g is described in Section 5.5.1.

R1, R2, and R3 correspond to the surface adsorption and desorption of OH, PA, and PA products (PA_p), respectively. R4 and R5 are the surface reaction of SDS + OH and PA + OH. R6, R7, and R8 represent surface to bulk droplet transport. R9 represents the bulk aqueous-phase reaction of PA + OH. The forward and reverse reaction rate constants for R1 - R3 and R6 - R8 follow the multi-phase transport theory in Pöschl et al. (2007) and are explicitly discussed in Section 5.5.1. The bulk aqueous-phase rate constant of PA + OH in R9 is adopted from Aljawhary et al. (2016). R4 and R5 are the key processes on which we focus here. Values of key parameters are summarized in Table 5.1.

The gas-phase OH concentration sufficiently far from the droplet surface is assumed to be constant, based on the assumption that the OH concentration from the DBDS is constant. Close to the droplet, however, a concentration gradient exists that depends on the OH uptake coefficient (γ_{gs}). During the reaction period, the droplet size is assumed to be constant, i.e., no water evaporation occurs. However, evaporation of surface-active PA is considered (R2). The Langmuir adsorption model (monolayer) is used to calculate the initial surface coverage of PA given the bulk concentration of the PA solution from which the droplet is formed (See Section 5.5.2). When PA and SDS coexist in the droplet, we assume that PA and SDS do not interact, that the surface coverages of PA and SDS are equivalent (i.e., $\theta_{0,\mathrm{PA}} = \theta_{0,\mathrm{SDS}} = 1$), and that the surface coverage is homogeneous. An implicit assumption is the absence of reaction between PA, SDS, and their products.

OH surface reactions are assumed to follow Langmuir-Hinshelwood kinetics (Pöschl et al., 2007; Socorro et al., 2017), i.e., OH first adsorbs to the organic surface (R1) and then reacts interfacially with PA and SDS (R4 and R5). This assumption is consistent with the experimental data, as will be discussed subsequently. The adsorption property of OH follows Vácha et al. (2004). Adsorbed OH can also diffuse into the droplet (R6) and react with PA in the bulk aqueous phase (R9) (Svishchev and Plugatyr, 2005). The oxidation products of SDS + OH are assumed

to stay in the interface, since even after several generations of oxidation the long alkyl chain remains largely intact (i.e., functionalization predominates). The SDS oxidation products are assumed to continue to react with adsorbed OH at different rates (R4). For simplicity, the first-generation oxidation products of the PA + OH reactions at the interface (R5) and in the bulk (R9) are represented as single lumped products, $PA_p(s)$ and $PA_p(b)$. $PA_p(s)$ and $PA_p(b)$ are assumed to have equivalent compositions and properties, even though their formation rates and mechanisms may differ. Depletion of the $PA(s)$ by reaction with OH is replenished by aqueous-phase diffusion of $PA_p(b)$ toward the surface (R7). Equilibrium partitioning of PA and PA_p between the gas phase, the surface and the aqueous phase was estimated using the quantum chemical program COSMOtherm based on density functional theory calculations (see Section 5.5.3 for details, Goss, 2009; Wang et al., 2015). The predicted surface/water and surface/air equilibrium constants for PA and proposed products of the interfacial reaction of PA + OH (see Results and Discussion) are listed in Table S1. The predicted equilibrium constants for the PA oxidation products span several orders of magnitude. For simplicity, the lumped PA oxidation product PA_p is assumed to have the same equilibrium constants as PA. Subsequent reactions of the lumped PA products, PA_p, with OH are also represented in the model.

Table 5.1: Parameters and Reaction Rate Constants Used in This Work

Symbol	Parameter	Value
α_s^i	surface accommodation coefficient for species i	1
δ	interface thickness (m)	6.9×10^{-10} (Vácha et al., 2004)
$\mathscr{D}_g^{OH}$	gas-phase OH diffusivity ($m^2\ s^{-1}$)	2.67×10^{-5}
$\mathscr{D}_b^{OH}$	aqueous-phase OH diffusivity ($m^2\ s^{-1}$)	2.30×10^{-9} (Ivanov et al., 2007)
$\mathscr{D}_b^{PA}$	aqueous-phase PA diffusivity ($m^2\ s^{-1}$)	1×10^{-10}
K_{sg}^{OH}	surface-gas adsorption equilibrium constant of OH (m)	6.07×10^{-6} (Vácha et al., 2004)
K_{sb}^{OH}	surface-bulk adsorption equilibrium constant of OH (m)	5.52×10^{-9} (Vácha et al., 2004)
K_{sg}^{PA}	surface-gas adsorption equilibrium constant of PA (m)	9.62×10^{4}
K_{sb}^{PA}	surface-bulk adsorption equilibrium constant of PA (m)	2.01×10^{-4}
$k_{\text{bulk}}^{\text{OH+PA}}$	bulk reaction rate constant of OH + PA ($M^{-1}\ s^{-1}$)	3.30×10^{9} (Aljawhary et al., 2016)
$k_{\text{surf}}^{\text{OH+SDS}}$	surface reaction rate constant of OH + SDS ($cm^2\ molec^{-1}\ s^{-1}$)	2.87×10^{-8} [a]
$k_{\text{surf}}^{\text{OH+PA}}$	surface reaction rate constant of OH + PA ($cm^2\ molec^{-1}\ s^{-1}$)	9.38×10^{-8} [a]

[a] These values are from fitting of the experimental data. Refer to Results and Discussion for details.

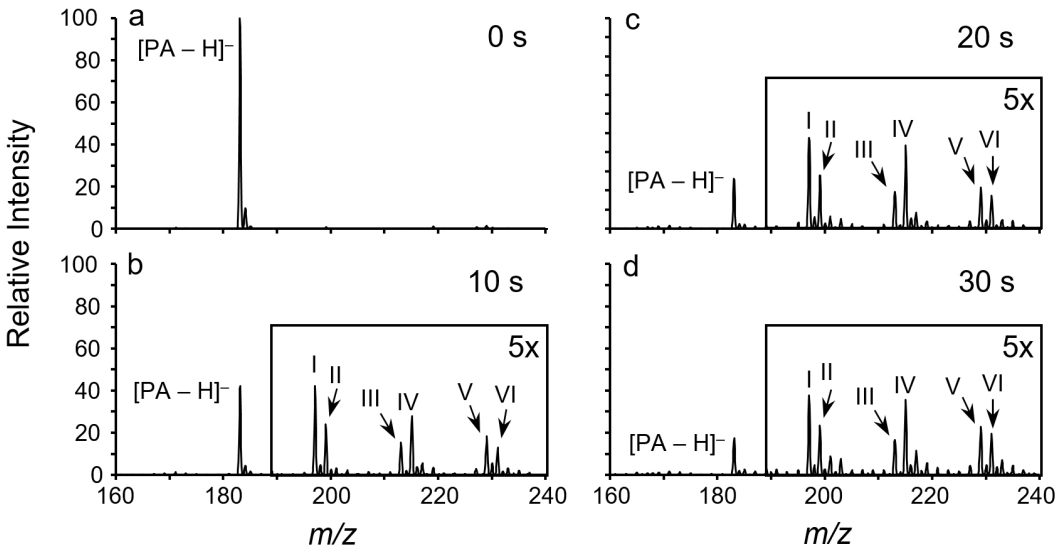

Figure 5.3: Pinonic acid (PA) oxidation at the air-water interface by gas-phase OH detected by FIDI-MS OH exposure. a. 0 s; b. 10 s; c. 20 s; d. 30 s. m/z of identified products are as follows: I = 197, II = 199, III = 213, IV = 215, V = 229, and VI = 231. Mass spectra are reported as averages of replicate samples (N = 5). The peak intensities in b, c, and d have been normalized with respect to the peak intensity of $[PA-H]^-$ in a.

5.3 Results and Discussion

5.3.1 OH Oxidation of Pinonic Acid Droplet

As a compound of intermediate volatility (Wang et al., 2015), we first examined the extent to which PA evaporates from the droplet. Both experimental and simulation results (Section 5.5.4) suggest that changes in PA concentration due to evaporation within the experimental timescale of 100 s are negligible. Figure 5.3 depicts the mass spectra of a PA droplet, in 10 s intervals, over a 30 s OH exposure. A series of six major oxidation products, at m/z 197 (I), 199 (II), 213 (III), 215 (IV), 229 (V), and 231 (VI) are identified. Since FIDI-MS provides only unit-mass resolution, each peak likely represents the combination of several isomers and isobars. As a first approximation, $[PA-H]^-$+14 is assumed to represent the addition of one carbonyl (>C=O), $[PA-H]^-$+16 the addition of one hydroxyl (-OH), $[PA-H]^-$+30 the addition of one carboxylic acid (-C(=O)OH) or one hydroxyl and one carbonyl, and $[M-H]^-$+32 the addition of two hydroxyls or one hydroperoxyl (-OOH).

As shown in Fig. 5.4, the initial H-abstraction by OH from PA can occur at 7 possible sites (a - g). Quantum chemical calculations suggest that in gas-phase OH oxidation, H-abstraction occurs most likely on carbon f (Müller et al., 2012; Vereecken and Peeters, 2002). However, results of structure activity relationships (SAR) for OH

oxidation in the aqueous-phase indicate that carbons a and c are preferred positions (Witkowski and Gierczak, 2017). At the air-water interface, molecular dynamics simulations (X. Li et al., 2010) suggest that PA molecules are oriented such that the hydrophilic functional groups (-C(=O)OH and >C=O) are embedded in the droplet, while the hydrophobic cyclobutyl ring is exposed on the droplet surface (see Fig. 5.2), making carbons a-c the most vulnerable to OH attack. Following the initial H-abstraction (Fig. 5.4), the resulting alkyl radical combines exclusively with O_2 at the air-water interface to form a peroxyl radical (RO_2), which may undergo the same competitive reaction channels as those in the gas phase (Atkinson and Arey, 2003). The three dominant gas-phase bimolecular reactions are RO_2 + RO_2 ($k_{RO2} \sim 10^{-14} - 10^{-12}$ cm^3 molec^{-1} s^{-1}), RO_2 + NO ($k_{NO} = 7 - 10 \times 10^{-12}$ cm^3 molec^{-1} s^{-1}), and RO_2 + HO_2 ($k_{HO_2} = 5 - 20 \times 10^{-12}$ cm^3 molec^{-1} s^{-1}, Atkinson and Arey, 2003; Orlando and Tyndall, 2012). Note that the aqueous-phase RO_2 + RO_2 and RO_2 + HO_2 reactions have similar rate constants (10^9 M^{-1} s^{-1} $\sim 1.7 \times 10^{-12}$ molecule^{-1} cm^3 s^{-1}, Ervens and Volkamer, 2010; Sonntag and Schuchmann, 1991) as those in the gas-phase. Assuming NO and HO_2 have similar air-water interfacial adsorptive and reactive properties, and given that the FIDI source is exposed to the ambient atmosphere and typical daily average NO mixing ratio in the Los Angeles area is $\sim$ 1 ppb ($10^{11} - 10^{12}$ molec cm^{-3}, CARB, 2018; Praske et al., 2018) and indoor HO_2 mixing ratio < 10 ppt ($\sim 10^9$ molec cm^{-3}, Carslaw, 2007), it is expected that reaction with NO is the dominant fate of PA peroxyl radicals at the air-water interface, with a small fraction of RO_2 + RO_2 and RO_2 + HO_2 reactions (Fig. 5.4). Reaction of RO_2 + NO yields alkoxy radicals (RO) that undergo decomposition, isomerization, or reaction with O_2 (J. H. Seinfeld and S. N. Pandis, 2016).

To aid in identification of the compounds that contribute to the six major mass spectral peaks detected by FIDI-MS, collision-induced dissociation (CID) was employed for detailed analysis of molecular structure. The MS/MS fragmentation patterns of the six parent ions are shown in Fig. 5.12. The daughter ions in each MS/MS spectrum can be explained by neutral losses of H_2O, CO_2, C_3H_6O, and $C_6H_{10}O$ (Yasmeen et al., 2010, Fig. 5.12). Certain neutral losses are characteristic to specific functional groups, e.g., carboxylic acid ions exhibit losses of 18 u (H_2O) and 44 u (CO_2, Demarque et al., 2016). All structures proposed in Fig. 5.4 are consistent with the observed MS/MS spectra. The peak at m/z 197 can be explained by a $C_{10}H_{14}O_4$ species derived from the RO_2 formed by H-abstraction from carbon a via successive reactions with NO and O_2 or through Russell disproportionation (Russell, 1957). The compound at m/z 199 can also form through the Russell mechanism.

The RO formed through OH-attack on carbon a can undergo ring-opening processes via scission of either the a-b or a-c bonds (for simplification, Fig. 5.4 depicts only the cleavage of the a-c bond), yielding a new alkyl radical, which after reacting with O_2 and NO forms another RO. This intermediate RO can undergo 1,5 H-shift to form the species at m/z 229 and m/z 231, react with O_2 to yield m/z 213, or react with RO to yield what is believed to be a minor product at m/z 215. H-abstraction from carbons b or c leads to the formation of a RO, which will decompose, react with O_2 and NO, and ultimately yield a tertiary RO. The resulting tertiary alcohol at m/z 215 (shown in Fig. 5.4) is expected to be the major isobaric contributor at this m/z, given its agreement with the major fragments observed in the MS/MS spectrum.

The aqueous-phase pH can affect the reaction mechanism as well as the reaction rate (Witkowski and Gierczak, 2017). Given pK_a = 4.82 (Howell and Fisher, 1958), the pH in the bulk droplet of PA solution at equilibrium with the surface is at most 5.2 and the ratio of deprotonated PA to PA is $\sim$ 2.2 (assuming the surface and the bulk are decoupled). Deprotonated PA has an additional reaction pathway in the aqueous phase, i.e., electron transfer (Ervens et al., 2003). However, the undissociated PA is expected to dominate at the surface (M.-T. Lee et al., 2016). Thus Fig. 5.4 only illustrates the mechanism of undissociated PA reacted with OH at the air-water interface.

The kinetic behavior of PA and its 6 oxidation products are shown in Fig. 5.13. The relative rates of appearance of each product are consistent with the PA reaction pathways proposed based on MS/MS analysis. While I and II are both the lowest mass products, the considerably slower rate of appearance of II suggests that this product is formed by a slower and/or more complex mechanism. Fig. 5.4 proposes a fragmentation product (H-abstraction from carbons d or e) as one of the possible structures of II, whereas I is suggested to be predominantly due to functionalization. The highest level of oxidation characterize the highest mass species (V and VI). The kinetic behavior of V and VI indicates a net balance between formation and degradation pathways for these species, suggesting that as the O/C ratio increases, the interfacial OH + PA oxidation system exhibits a propensity to shift from functionalization to fragmentation products.

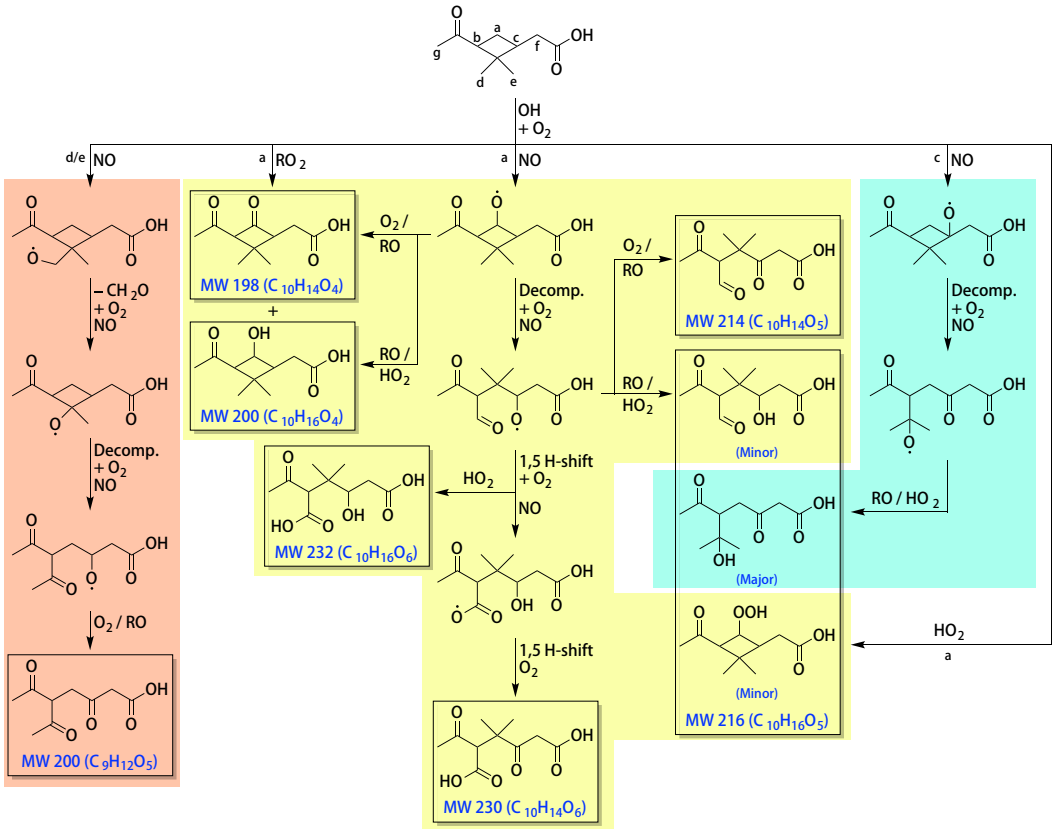

Figure 5.4: Mechanism of OH-initiated oxidation of PA under NO-dominant conditions.

5.3.2 Characterization of Gas-Phase OH Concentration

To study the kinetics of interfacial OH oxidation of PA, a sufficient constraint on the gas-phase OH concentration is necessary. By monitoring the heterogeneous OH oxidation of surfactant (i.e., SDS in this study), and assuming that the surfactant remains exclusively on the surface, one can infer the gas-phase OH concentration. As stated in the Model description section, it is necessary to incorporate all possible processes (i.e., adsorption and reaction on the surface, as well as diffusion in the bulk droplet, into a unified model), from which the gas-phase OH concentration can be inferred.

Assuming an effective cross-section area of 30 $Å^2$ for SDS (A. Tan et al., 2002) and that the SDS resides solely at the surface, a monolayer of SDS is formed on the surface of a droplet with a radius of 1 mm. Mass spectra of the interfacial OH oxidation of SDS are shown in Fig. 5.14, and the measured decay of SDS is shown in Fig. 5.5a. Due to the linear alkyl chain, the successive increases of m/z 14 and 16 indicate that alcohols and carbonyls are the most likely products via RO_2 / RO

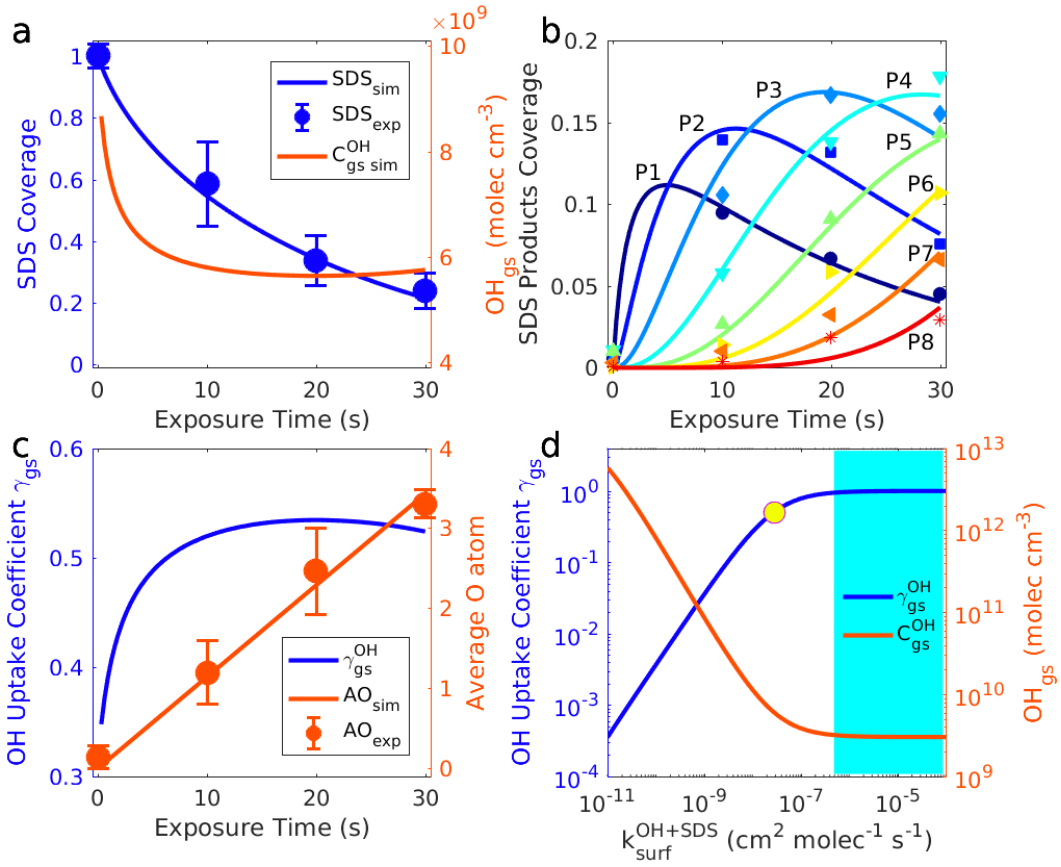

Figure 5.5: Experimental and fitted results of the OH oxidation of the SDS droplet. a. Temporal profiles of SDS coverage (blue dots, measured values averaged by 5 repeats; blue line, fitting result) and the modeling gas-phase OH concentration above the surface (orange line). b. Temporal profiles of 8 generations of SDS + OH products (lines are fitting results and dots are experimental results). c. Temporal profiles of predicted OH uptake coefficient (blue line) and the average number of oxygen atoms incorporated into SDS via OH oxidation (orange dots, measured values averaged by 5 repeats; orange line, fitting result). d. Calculated OH uptake coefficient and the gas-phase OH concentration above the surface as a function of the optimally fitted surface reaction rate constant for SDS + OH system. Yellow dot represents the value adopted in this study and cyan background marks the gas-phase diffusion limit regime for the determination of $k_{\text{surf}}^{\text{OH+SDS}}$.

chemistry in the SDS + OH reaction. However, other functionalities, e.g., carboxylic acids (m/z + 30), are possible. Instead of assigning specific formula to each m/z peak, the products can be clustered into groups, i.e., peaks at m/z $[\text{DS}]^-$ + 14 and $[\text{DS}]^-$ + 16 are grouped into the products that contain one oxygen atom, while products at m/z $[\text{DS}]^-$ + 28, $[\text{DS}]^-$ + 30, and $[\text{DS}]^-$ + 32 are those with two oxygen atoms, etc. Figure 5.5b presents the temporal profiles of 8 generations of identified SDS + OH oxidation products. Assuming that SDS incorporates one oxygen after

reacting with one OH, by defining the average oxygen atom as the signal-intensity-weighted sum of the oxygen content in the identified oxidation products (m/z 265 - 400), the experimental results indicate that ~10 s is required for OH to react with the entire monolayer of SDS (Fig. 5.5c). The near-linear relationship in Fig. 5.5c suggests Langmuir-Hinshelwood kinetics govern the air-water system, since if OH were to react with the interfacial molecules upon collision (Eley-Rideal mechanism), the rate of oxygen atom incorporation would increase as the reaction progresses, given that more reactive C-H bonds are formed (e.g., those adjacent to a carbonyl group).

By fitting the experimental data in Fig. 5.5a-c, we seek to estimate the gas-phase OH concentration, as well as the surface reaction rate constants for both SDS and SDS products. The best-fit gas-phase OH mixing ratio is found to be ~698 ppb. The experimental distribution patterns of the eight oxidation generations and the decay curve of SDS determine the reaction rate constants of SDS_p + OH to relative that of SDS + OH, i.e., $k_{\text{surf}}^{\text{OH+SDS}}$. All generations are found to react faster with OH than SDS. Nonetheless, without any constraint on the surface concentration of OH, the optimally fitted $k_{\text{surf}}^{\text{OH+SDS}}$ values span from 10^{-11} to 10^{-4} cm^2 molec^{-1} s^{-1}, within which range, $k_{\text{surf}}^{\text{OH+SDS}}\theta_{\text{OH}}$ (Fig. 5.15a) is nearly constant, suggesting that the decay of SDS is a quasi-first-order reaction (~0.0516 s^{-1}). Figure 5.5d shows the estimated average OH uptake coefficient γ_{gs} and the gas-phase OH concentration above the surface C_{gs}^{OH} as functions of the optimally fitted $k_{\text{surf}}^{\text{OH+SDS}}$. In the regime where $k_{\text{surf}}^{\text{OH+SDS}} > 10^{-7}$ cm^2 molec^{-1} s^{-1}, both γ_{gs} and C_{gs}^{OH} remain constant, which is a result of the fast surface reaction rate, causing gas-phase diffusion of OH to the surface to become the rate-limiting step in this system. γ_{gs} of OH onto thin organic film is typically ≥ 0.1 (George and Abbatt, 2010) and the gas-phase diffusion limit is unlikely in the FIDI experiment since the DBDS aims directly at the droplet. Adopting a median value $\gamma_{gs} = 0.5$, we find the average values $C_{gs}^{OH} \approx 6 \times 10^9$ molec cm^{-3}, $k_{\text{surf}}^{\text{OH+SDS}} \approx 2.87 \times 10^{-8}$ cm^2 molec^{-1} s^{-1}, and $\theta_{\text{OH}} \approx 10^{-9}$. Figure 5.5a and c show the calculated temporal profiles of C_{gs}^{OH} and γ_{gs}.

The simulation suggests that in the absence of bulk reaction consuming aqueous-phase OH, OH radicals can diffuse to the center of the droplet and reach ~1 nM after 30 s (Fig. 5.15b), indicating that the bulk droplet serves as a significant sink of OH in the OH + SDS interfacial reaction system. The high gas-phase OH concentration above the surface gives ~ 10^{11} molec cm^{-3} s OH exposure in the FIDI system, corresponding to ~ 1 day exposure under typical atmospheric conditions

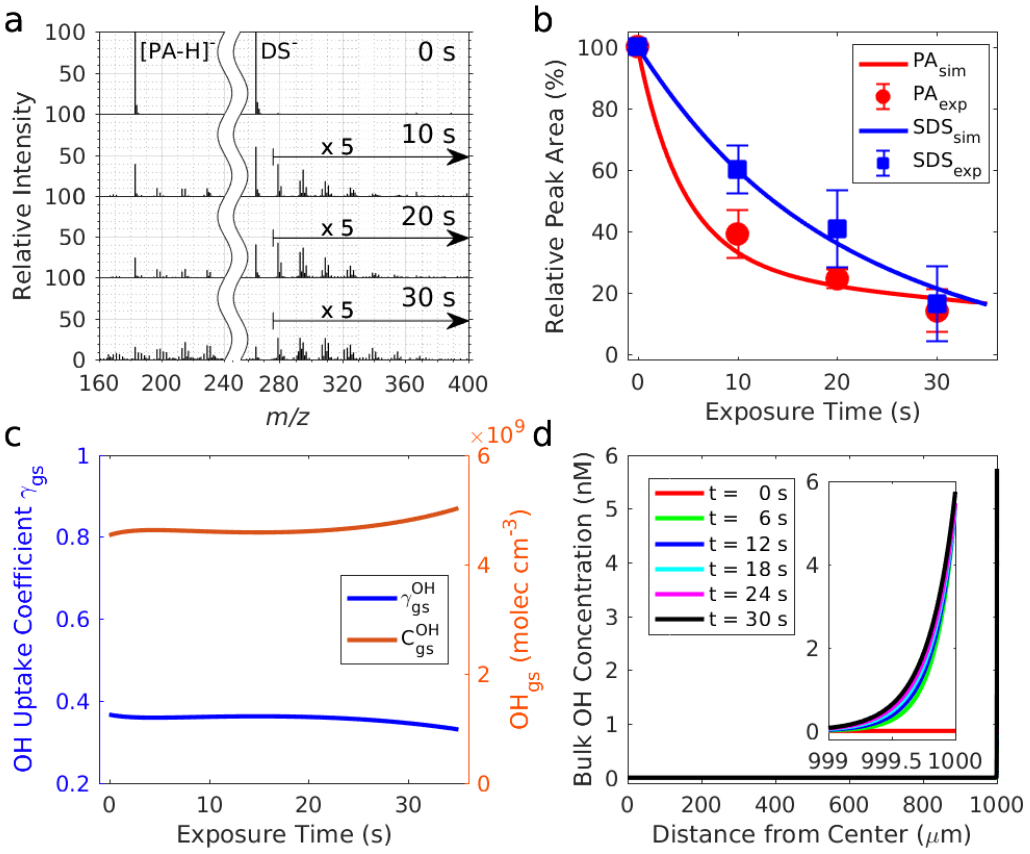

Figure 5.6: Experimental and simulation results of the OH oxidation of the mixture of PA and SDS droplet. a. Mass spectra of the sampling under different OH exposure (left is the PA regime and right is the SDS regime). b. Temporal profiles of the surface coverage of PA and SDS. Dots represent experimental measurements (averaged by 5 repeats) and lines represent simulated results. c. Predicted temporal profiles of the OH uptake coefficient and the gas-phase OH concentration. d. Simulated bulk aqueous-phase OH distribution at different exposure time. Inset panel is the zoom-in near the surface regime.

(assuming ambient OH concentration of 1×10^6 molec cm^{-3}). The air-interface-water properties of OH employed in the model and the best-fit surface reaction rate constant of SDS + OH are summarized in Table 5.1.

5.3.3 Kinetics of Interfacial OH Oxidation of Pinonic Acid

PA partitions between the droplet surface and bulk. Because of diffusion to the bulk of both PA and PA oxidation products, one cannot use the same strategy as employed for OH + SDS to determine the surface reaction rate constant. As discussed above, the products of PA + OH are complex, and it is impossible to track the fractions of all the PA products that diffuse into the bulk. By adding a reference compound to

the system, such as a surfactant that undergoes only surface reaction, we can better constrain the OH concentration on the surface and determine the surface reaction rate constant for OH + PA. The resulting mass spectra under different exposure times are shown in Fig. 5.6a. The decay of both PA and SDS is shown in Fig. 5.6b. The apparent decay rate of PA exceeds that of SDS, which is indicative of the relative reactivity of PA. One cannot, however, rule out the possibility that bulk aqueous-phase transport and oxidation can affect the decay rate.

By fitting to the data points in Fig. 5.6b, where the surface reaction rate constants for both SDS and SDS products are known, the bulk gas-phase OH concentration is estimated as ~678 ppb, consistent with the value evaluated for SDS + OH experiments, demonstrating the reproducibility of DBDS employed for air-water interfacial oxidation studies. The surface reaction rate constant of PA + OH is determined to be 9.38×10^{-8} cm^2 molec^{-1} s^{-1}, ~3 times of that of SDS + OH. The fitted surface rate constant of PA + OH is not sensitive to the surface coverage of PA and SDS. The gas-phase OH concentration above the surface is $\sim 5\times10^9$ molec cm^{-3} and the OH uptake coefficient is ~0.35 (Fig. 5.6c).

The calculated average oxygen atom incorporation into SDS products fits the experimental data (Fig. 5.16a) as well. The simulated bulk aqueous-phase OH distribution (Fig. 5.6d) predicts that OH is confined to the surface region (within a distance of ~1 μm). The heterogeneous nature of the reactions can be quantified by utilizing the concept of a reacto-diffusive length L_{OH} (Pöschl et al., 2007):

$$L_{OH} = \sqrt{\frac{\mathscr{D}_b^{OH}}{k_b^{OH+PA} C_b^{PA}}} \tag{5.1}$$

where $\mathscr{D}_b^{OH}$ is the bulk diffusion coefficient of OH (2.3×10^{-9} m^2 s^{-1}), k_b^{OH+PA} is the bulk reaction rate constant of PA + OH (3.3×10^9 M^{-1} s^{-1}) (Aljawhary et al., 2016), and C_b^{PA} is the bulk concentration of PA ($\sim (1-19\%)\times 50$ μM). In this system, $L_{OH} \approx 0.6$ μm, is consistent with the prediction of the simulation (Fig. 5.6d). To replenish its consumption by OH in the sub-surface region, a continuous diffusive flux of PA from the bulk aqueous phase has to be established (Fig. 5.16b). Though the surface reaction rate constant of PA + OH is faster than that of SDS + OH, the simulated decay curves of PA and SDS cross after 30 s exposure to OH, since at that point, replenishment of PA from the bulk competes with the surface reaction rate.

In summary, to determine the air-water interfacial reaction rate constant of a surface-

active species, one has to account for simultaneous aqueous-phase diffusion and reaction. For a system with high bulk OH reactivity ($k_b^{II} C_b$, where k_b^{II} is a second-order aqueous-phase reaction rate constant and C_b is the bulk aqueous-phase concentration of the surface-active species), the heterogeneous reaction is enhanced, since the penetration of OH into the droplet bulk is confined to the sub-surface region. If the bulk reaction rate is smaller than that on the surface, a slower "apparent" decay rate of the surface coverage can be expected due to the replenishment from bulk diffusion.

5.3.4 Atmospheric Implications

In the atmosphere in which cloud and fog droplets or aerosol water are present, for species with high Henry's law constants, a large fraction will partition to the aqueous phase, where aqueous phase chemistry can be significant (Blando and Turpin, 2000; Ervens et al., 2011; Y. B. Lim et al., 2010). The Henry's law constant relates the gas and bulk aqueous phases and is routinely adopted in the cloud or aqueous aerosol chemistry models (H.-J. Lim et al., 2005; McNeill et al., 2012). However, by accounting for the surface activity, the fraction that partitions in the gas phase, on the surface, and in the bulk aqueous phase may be quite different. The fraction partitioning on the surface of the droplet, F_{surf}, can be estimated by

$$F_{\text{surf}} = \frac{\frac{3w_L}{\overline{R_p}}}{\frac{1}{\mathrm{K}_{sg}} + \frac{w_L}{\mathrm{K}_{sb}} + \frac{3w_L}{\overline{R_p}}} \tag{5.2}$$

where K_{sg} and K_{sb} are the surface/gas phase and surface/bulk aqueous phase equilibrium constants, respectively. The ratio $\frac{\mathrm{K}_{sg}}{\mathrm{K}_{sb}}$ can be viewed as the effective Henry's law constant. w_L is the liquid water mixing ratio in the air and $\overline{R_p}$ is the volume-weighted average radius of the droplets. For PA in the present study, Fig. 5.81 indicates that the smaller the droplet, the higher the fraction of PA that resides on the surface.

If the sole source of OH is from the gas phase (thus ignoring possible aqueous-phase photolysis reactions, Aljawhary et al., 2016; Lignell et al., 2013), multiphase OH oxidation can be divided into sequential processes: gas-phase reaction, gas-surface adsorption/desorption, surface reaction, surface-bulk aqueous transport, and bulk aqueous phase reaction. Given reaction rate constants in the gas phase, on the surface, and in the aqueous phase, the following questions concerning oxidation of a surface-active species arise: What is the rate-limiting step in ambient OH

multiphase oxidation? Is the gas-surface-bulk system always at equilibrium? What is the major sink of surface-active species?

The FIDI studies simulate processes occurring within 1 min with an equivalent OH exposure of 1 day under typical ambient conditions. Within a relatively short period, interfacial transport is the rate-limiting step under extremely high OH levels (Fig. 5.6d). For ambient OH levels, the conclusion that OH oxidation of PA occurs predominately at the air-water interface may not be directly extrapolated to typical environmental conditions. To clarify this point, we apply the derived rate constant of PA + OH in a case study simulation of the ambient OH oxidation of PA in cloud and fog droplets.

We assume an air parcel with a typical liquid water mixing ratio ($w_L = 3 \times 10^{-7}$, J. H. Seinfeld and S. N. Pandis, 2016) equivalent to ~0.6 cm^{-3} droplets of 100 μm diameter or $\sim 5 \times 10^3$ cm^{-3} droplets of 5 μm diameter (Fig. 5.17a), and an overall PA concentration of 0.5 nmol m^{-3} (~100 ng m^{-3}, Kavouras et al., 1999; Vestenius et al., 2014). The gas-phase OH concentration is assumed constant, 1×10^6 molec cm^{-3}. The multiphase reactions are studied in two ambient cloud droplet sizes (Bréon et al., 2002; J. H. Seinfeld and S. N. Pandis, 2016), i.e., 5 μm and 100 μm. The reaction of PA + OH occurs in the gas phase (Müller et al., 2012), on the surface, and in the bulk aqueous phase (Aljawhary et al., 2016) with rate constants of 1.125×10^{-11} $molec^{-1}$ cm^3 s^{-1}, 9.38×10^{-8} $molec^{-1}$ cm^2 s^{-1}, and 3.30×10^9 M^{-1} s^{-1}, respectively. The fractions of remaining PA in the gas phase, on the surface, and in the bulk aqueous phase are tracked. Initial partitioning of PA between the surface/air and surface/water is at equilibrium (see Section 5.5.8 for detailed calculation), indicating that >99% of PA remains on the surface of a 5 μm droplet, while ~90% remains on the surface of a 100 μm droplet.

By matching the mass flux through the interface with accommodation coefficients and relating the gas phase to the aqueous phase via Henry's law constants (Mai et al., 2015; J. H. Seinfeld and S. N. Pandis, 2016), one can, in a simplified model, exclude the effect of the interfacial reaction. To distinguish between the two models, we call the former M1 and the latter M2. To minimize the effect of interfacial transport in M2, we adopt the accommodation coefficients as unity for PA, PA products, and OH. The effective Henry's law constant is $H = \frac{K_{sg}}{K_{sb}} = 1.95 \times 10^7$ M atm^{-1} for PA and PA products, consistent with that reported in Lignell et al. (2013), and 39 M atm^{-1} for OH (Vácha et al., 2004). As opposed to M1, partition of PA between gas phase and aqueous phase at equilibrium (Ervens et al., 2011) in M2 is independent of droplet

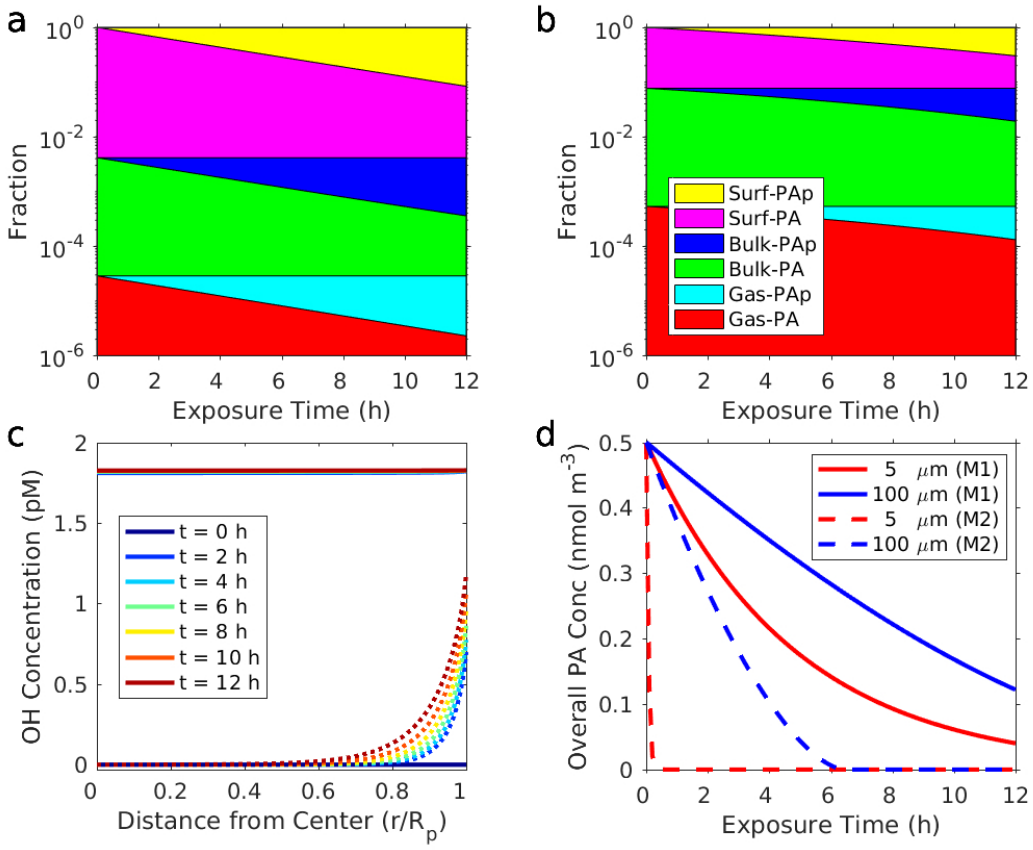

Figure 5.7: Simulated multi-phase OH oxidation of PA in droplets of 5 μm (a) and 100 μm (b), with an overall PA concentration of 0.5 nmol m^{-3} under typical ambient conditions (gas-phase OH concentration $\sim 10^6$ molec cm^{-3}). a and b: Fraction of the overall quantities of PA and PA products that resides on the surface, in the bulk aqueous phase, and in the gas phase. c: Predicted bulk aqueous-phase distribution of OH at different OH exposure times by M1 (solid lines: 5 μm droplets, dashed lines: 100 μm droplets). d: Temporal profiles of overall PA as exposed to OH.

size ($F_{\text{aq}} = \frac{Hw_L}{1+Hw_L} > 99\%$), and diffusion of OH inside the droplet is found to be the rate-limiting step of the multiphase oxidation.

For both models, an overall simulation time is taken as 12 h, corresponding to an equivalent OH exposure as used in the FIDI experiments. Shrinkage or growth of the droplets is not considered during the 12 h simulation, given that water vapor is at equilibrium in the cloud.

Figures 5.7a and b present the predicted fractions of different PA fates in the systems in droplets of 5 μm and 100 μm, respectively. Since the surface properties of PA and PA products are identical in M1, the constant fraction of the sum of PA and PA products within any phase during the simulation indicates that the partitioning of

PA and PA products between the gas phase, the surface, and the bulk aqueous phase remains at equilibrium. This quasi-equilibrium partitioning can be attributed to the fact that the reaction rates are sufficiently slow (because of the relatively low OH concentration) such that mass transport between the gas phase, the surface, and the bulk aqueous phase is no longer a rate-limiting step. The consumption of PA in the 5 μm system occurs exclusively at the air-water interface, while ~10% is contributed by the aqueous-phase OH oxidation in the 100 μm system. Both Fig. 5.7a and b suggest that gas-phase oxidation of PA is unimportant in the cloud and fog system, which also applies to M2 (i.e., without accounting for interfacial effects, aqueous phase oxidation predominates).

The simulated bulk aqueous-phase OH distributions (Fig. 5.7c) suggest that the smaller the droplet, the more uniform the bulk. For larger droplets, the reaction is constrained to the sub-surface region, which is characterized by the OH reactive-diffusive length (EQ. (5.1)), since less PA resides on the surface, leaving the bulk aqueous-phase with relatively stronger OH reactivity ($k_b^{OH+PA}C_b^{PA}$). The OH uptake coefficient by 5 μm droplet surface is ~1 order of magnitude smaller than that by 100 μm droplet surface (Fig. 5.17b). However, given the much larger surface area concentration in the 5 μm droplet system, under the same OH exposure, the overall PA concentration is predicted to decay ~90%, higher than ~75% in the 100 μm droplet system (Fig. 5.7d). By comparison, if the interfacial interaction is not considered (M2), the model predictions suggest that PA is depleted in ~30 min in the 5 μm system and ~6 h in the 100 μm system. The longer lifetime of PA in the larger droplet system reflects the fact that in the absence of the interfacial resistance, i.e., interfacial reaction and accommodation, the rate-limiting step is bulk aqueous-phase diffusion of OH.

5.4 Conclusions

Interfacial effects of surfactants have been recognized to lower the surface tension and facilitate cloud droplet formation (Nozière, 2016; Ruehl et al., 2016). The present case study highlights the significance of air-water interfacial partitioning and reaction of surface-active species (e.g., PA). For the cloud and fog system with characteristically higher air-water surface area concentration, the sink of the surface-active species can be expected to occur predominantly on the surface, so that the surface reaction rate is the rate-limiting step in the multiphase OH oxidation. The quasi-equilibrium partitioning state during the oxidation suggests that in the absence of a source of surface-active species (either from outside of the air parcel or from

oxidation of precursors), multiphase OH oxidation can be simplified as occurring in three individual regions (gas phase, surface, and bulk aqueous phase), for which the explicit dynamic multiphase model applies. For species that are less surface-active, e.g., glyoxal (Ervens et al., 2011; Galloway M. M. et al., 2011; Y. Tan et al., 2009), the effect of air-water interfacial processes may not be as significant as those for surface-active species. Since the simulation treats the gas-phase OH as the sole source, given the high solubility of H_2O_2 (Henry's law constant = 8.70×10^4 at 298 K, Burkholder et al., 2015), potential photolysis of dissolved H_2O_2 can serve as a large source of aqueous-phase OH (Kameel et al., 2013) and the fate of surface-active species may change. Moreover, photosensitized chemistry has been proved to play a critical role on the radical-radical reaction at the air-water interface (Bernard et al., 2016; Rossignol et al., 2016; Tinel et al., 2016). Additional studies are needed to clarify the competitive OH oxidations of surface-active species among gas phase, surface, and bulk aqueous phase under different conditions.

5.5 Supporting Information

5.5.1 Model Description

This section presents the details of the physico-chemical model of the experimental system. Interfacial adsorption, surface reaction, and aqueous-phase reaction can be represented by the elementary reactions R1 - R9. Reactions R1, R2, and R3 correspond to the surface adsorption and desorption of OH, PA, and PA_p. The relationship between the concentration above the surface $C_{gs,i}$ and that far from the surface $C_{g,i}$ is:

$$C_{gs,i} = F_{Kn_i,\gamma_i} C_{g,i} = \frac{1}{1 + \gamma_i \frac{0.75+0.28Kn_i}{Kn_i(1+Kn_i)}} C_{g,i} \tag{5.3}$$

where F_{Kn_i,γ_i} is a correction factor to account for the transition of gas-phase diffusion from the continuum regime to the kinetic regime (Pöschl et al., 2007), i is the index for species i, Kn_i is the Knudsen number $Kn_i = \frac{\lambda_i}{R_p}$, where λ_i is the mean free path of species i in the gas phase and R_p is the radius of the droplet. λ_i will be approximated by $\lambda_i = \frac{3\mathcal{D}_{g,i}}{\omega_i}$, where $\mathcal{D}_{g,i}$ is the gas-phase molecular diffusivity, and ω_i is the gas-phase mean molecular velocity. For OH, $\mathcal{D}_{g,\mathrm{OH}} = 2.17\times10^{-5}$ m^2 s^{-1} (Ivanov et al., 2007). For PA and PA_p, $\mathcal{D}_{g,\mathrm{PA}} = \mathcal{D}_{g,\mathrm{PA}_p} = 1\times10^{-5}$ m^2 s^{-1}. γ_i is the uptake coefficient of species i by the surface, as defined:

$$\gamma_i = \frac{J_{ads,i} - J_{des,i}}{J_{colid,i}} = \frac{\frac{1}{4}\alpha_{0,i}(1 - \sum\theta_i)\omega_i C_{gs,i} - \frac{1}{\tau_{des,i}} C_{s,i}}{\frac{1}{4}\omega_i C_{gs,i}} \tag{5.4}$$

where $J_{ads,i}$, $J_{des,i}$, and $J_{colid,i}$ are the adsorption, desorption, and collision flux of gas-phase molecules i to the surface. The expression for $J_{ads,i}$ is based on Langmuir-Hinshelwood kinetics, wherein $\alpha_{0,i}$ is the surface accommodation coefficient on species i free surface. α_0 of OH on an organic surface is usually assumed to be unity (Socorro et al., 2017). To simplify the case, $\alpha_{0,\mathrm{PA}}$ and α_{0,PA_p} are both taken to be unity. The further assumption made here is that α_0 is independent of the surface components, an assumption that can be relaxed later. $\omega_i = \sqrt{\frac{8R_gT}{\pi M_i}}$ is the mean speed of gas molecule, where R_g is the gas constant, T is the ambient temperature, and M_i is the molecular weight of species i. $\sum\theta_i$ is the coverage of all adsorbed species. $\tau_{des,i}$ is the desorption lifetime, which can be derived from the surface-gas adsorption equilibrium $K_{sg,i}$. $K_{sg,i}$ can be calculated through density functional theory (DFT, Vácha et al., 2004, COSMOtherm2017, see discussion in Section 5.5.3)), and $\tau_{des,i} = \frac{4K_{sg,i}}{\alpha_{0,i}\omega_i}$. σ_i is the effective cross section area of species i. The surface concentration of species i is $C_{s,i} = \frac{\theta_i}{\sigma_i}$, where θ_i is the surface coverage of species i. By tracking $C_{g,\mathrm{OH}}$ and $C_{g,\mathrm{PA}}$ through mass balance and differential

equations and substituting EQ. (5.3) into EQ. (5.4), one can determine the uptake coefficient γ_i and $C_{gs,i}$ expressed by the gas-phase concentration $C_{g,i}$ at a specific time. Correspondingly, the rate of change of surface concentration of species i as a result of surface-gas exchange is:

$$\frac{d}{dt}C_{s,i}^{\mathrm{gs-s}} = \frac{1}{4}\alpha_{0,i}\left(1-\sum\theta_i\right)\omega_i C_{gs,i} - \frac{1}{\tau_{des,i}}C_{s,i} \tag{5.5}$$

Reactions R4 and R5 are surface reactions between adsorbed OH, and SDS and PA, the products of which are $\mathrm{SDS_{pl}}$ (l = 1, 2, 3,..., m) and PA_p, respectively.

For SDS and $\mathrm{SDS_{pl}}$, the only sink and source is R4. In summary, the differential equations with stoichiometric coefficient matrix are:

$$\frac{d}{dt}\begin{pmatrix} C_{s,\mathrm{SDS}} \\ C_{s,\mathrm{SDS}_{p1}} \\ C_{s,\mathrm{SDS}_{p2}} \\ C_{s,\mathrm{SDS}_{p3}} \\ \vdots \end{pmatrix} = k_{s,\mathrm{OH+SDS}}C_{s,\mathrm{OH}}\begin{pmatrix} -1 & 0 & 0 & 0 & \dots \\ 1 & -f_1 & 0 & 0 & \dots \\ 0 & f_1 & -f_2 & 0 & \dots \\ 0 & 0 & f_2 & -f_3 & \dots \\ \vdots & \vdots & \vdots & \vdots & \ddots \end{pmatrix}\begin{pmatrix} C_{s,\mathrm{SDS}} \\ C_{s,\mathrm{SDS}_{p1}} \\ C_{s,\mathrm{SDS}_{p2}} \\ C_{s,\mathrm{SDS}_{p3}} \\ \vdots \end{pmatrix} \tag{5.6}$$

where $C_{s,\mathrm{SDS}}$, $C_{s,\mathrm{SDS_{pl}}}$, and $C_{s,\mathrm{OH}}$ are surface concentrations of SDS, SDS products, and OH, and $k_{s,\mathrm{OH+SDS}}$ is the second-order surface reaction rate constant, and f_l (l = 1, 2, 3, ...) is the ratio of the reaction rate constant of $\mathrm{SDS_{pl}}$ + OH to $k_{s,\mathrm{OH+SDS}}$. The overall consumption rate of adsorbed OH by SDS is:

$$\frac{d}{dt}C_{s,\mathrm{OH}}^{\mathrm{OH+SDS}} = -k_{s,\mathrm{OH+SDS}}C_{s,\mathrm{OH}}(C_{s,\mathrm{SDS}} + \sum_{l=1} f_l C_{s,\mathrm{SDS}_{p2}}) \tag{5.7}$$

For PA, the rate of surface concentration change rate as a result of surface reaction R5 is:

$$\frac{d}{dt}C_{s,\mathrm{OH}}^{\mathrm{OH+PA}} = \frac{d}{dt}C_{s,\mathrm{PA}}^{\mathrm{OH+PA}} = -\frac{d}{dt}C_{s,\mathrm{PA}_p}^{\mathrm{OH+PA}} = -k_{s,\mathrm{OH+PA}}C_{s,\mathrm{OH}}C_{s,\mathrm{PA}} \tag{5.8}$$

where $k_{s,\mathrm{OH+PA}}$ is the surface reaction rate constant of OH + PA. Additional surface reaction mechanisms of OH + PA can be considered if appropriate.

Reactions R6-R8 represent surface-bulk aqueous-phase transport. This can be viewed as one of the boundary conditions of the bulk aqueous-phase diffusion problem. The transport rate from the bulk aqueous phase to the surface is limited by the available sites on the surface, following the monolayer assumption. The surface concentration change rate of species i as a result of the surface-bulk aqueous exchange is:

$$\frac{d}{dt}C_{s,i}^{\mathrm{s-sb}} = k_{bs,i}\left(1-\sum\theta_i\right)C_{bs,i} - k_{sb,i}C_{s,i} \tag{5.9}$$

where $k_{bs,i}$ is the mass transport coefficient of species i from the bulk aqueous phase to the surface, units of which are the same as velocity. $k_{bs,i}$ can be estimated based on the aqueous-phase diffusivity based on the average distance traveled in one direction through diffusion is $\delta_i = \langle x_i \rangle = \sqrt{\frac{4\mathscr{D}_{b,i}t}{\pi}}$. The migration velocity is the ratio of distance to time, where in this case the distance is the thickness of the monolayer. Thus the mass transport coefficient from bulk to interface $k_{bs,i} \approx \frac{4\mathscr{D}_{b,i}}{\pi\delta}$. $\mathscr{D}_{aq,i}$ is the diffusivity of species i in the aqueous phase, taking ($\mathscr{D}_{b,\mathrm{OH}} = 2.3 \times 10^{-9}$ m^2 s^{-1}, Svishchev and Plugatyr, 2005) and a typical value 10^{-10} m^2 s^{-1} for PA and PA$_p$. $C_{bs,i}$ is the bulk concentration beneath the surface, which can be approximated as $C_{b,i}(R_p)$, the bulk aqueous-phase concentration at $r = R_p$. $k_{sb,i}$ is the first-order mass transport rate coefficients of species i from surface to aqueous bulk, which can be derived from the surface-aqueous equilibrium constant $K_{sb,i}$ and the bulk-to-surface transport coefficient $k_{bs,i}$ by $k_{sb,i} = \frac{k_{bs,i}}{K_{sb,i}}$.

So far, the gas-surface-bulk transfers have been addressed. The overall rate of change of surface concentration of OH is the summation of EQs. (5.5), (5.7) - (5.9), while the overall rates of change for PA and PA$_p$ on the surface are the summation of EQs. (5.5), (5.8), and (5.9).

For the rates of change of $C_{b,i}$, one has to consider simultaneous the bulk diffusion and the bulk reaction. Reactions R9 is the aqueous-phase second-order reaction between OH and PA. The reaction rate is:

$$\mathrm{RXN}_b = k_{b,\mathrm{OH+PA}} C_{b,\mathrm{OH}} C_{b,\mathrm{PA}} \tag{5.10}$$

where $k_{b,\mathrm{OH+PA}}$ is the second-order volume reaction rate constant. Note that the aqueous-phase reaction product is the same as that through surface reaction. Overall, the bulk diffusion-reaction equation in a spherical droplet is:

$$\frac{\partial C_{b,i}}{\partial t} = \mathscr{D}_{b,i} \frac{\partial^2 C_{b,i}}{\partial r^2} + \frac{2\mathscr{D}_{b,i}}{r} \frac{\partial C_{b,i}}{\partial r} + \mathrm{RXN}_b \tag{5.11}$$

constrained by the boundary and initial conditions:

$$\begin{aligned}
\frac{\partial C_{b,i}}{\partial r}(0,t) &= 0, && t \geq 0 \\
\frac{\partial C_{b,i}}{\partial t}(R_p,t) &= \frac{1}{\Delta r}\left[-\frac{d}{dt} C_{s,i}^{\mathrm{s-sb}} - \mathscr{D}_{b,i} \frac{\partial C_{b,i}}{\partial r}(R_p,t)\right], && t \geq 0 \\
C_{b,i}(r,0) &= C_{b,i}^0, && 0 \leq r \leq R_p
\end{aligned} \tag{5.12}$$

where R_p is the radius of the droplet, $C_{b,i}(R_p,t) = C_{bs,i}(t)$, and Δr is the thickness of the boundary layer. The method of lines (MOL) can be applied to solve EQs.

(5.11) and (5.12) by discretization in space and continuation in time. Central finite difference is used for $r < R_p$, and three-term backward difference is used for $r = R_p$. The spatial grid points correspond to $r_k = k\Delta r$, where $k = 0, 1, 2, ..., N$ and $R_p = N\Delta r$. So EQs. (5.11) and (5.12) become

$$\frac{dC_{b,k,i}}{dt} = \begin{cases} \mathrm{RXN}_{b,k,i} + \dfrac{6\mathscr{D}_{b,i}}{\Delta r^2}(C_{b,k+1,i} - C_{b,k,i}), & k = 0 \\ \mathrm{RXN}_{b,k,i} + \dfrac{\mathscr{D}_{b,i}}{k\Delta r^2}((k+1)C_{b,k+1,i} - kC_{b,k,i} + (k-1)C_{b,k-1,i}), & k = 1, 2, ..., N-1 \\ \mathrm{RXN}_{b,k,i} + \dfrac{1}{\Delta r}\left(-\dfrac{d}{dt}C_{s,i}^{\mathrm{s-sb}} - \mathscr{D}_{b,i}\dfrac{3C_{b,k,i} - 4C_{b,k-1,i} + C_{b,k-2,i}}{2\Delta r}\right), & k = N \end{cases} \tag{5.13}$$

where $\mathrm{RXN}_{b,k,i} = -\mathrm{RXN}_{b,k}$ for OH and PA, and $\mathrm{RXN}_{b,k,i} = \mathrm{RXN}_{b,k}$ for PA_p.

The total number of variables involved in the ODE calculation is $3(N+1)+3+(m+1)$. The first term "$3(N+1)$" accounts for the diffusion and reaction of OH, PA and PA_p in the bulk aqueous phase, where N is the grid discretization number. The second term "3" accounts for the surface coverage of OH, PA and PA_p. And the third term "$(m+1)$" accounts for the surface coverage of SDS and the products, where m is the number of product generations.

5.5.2 Surface Coverage of PA at Surface-Bulk Equilibrium

In this section, we show how to calculate the surface coverage of PA and the ratio of the quantities of PA remaining on the surface to those in the bulk droplet. The Langmuir adsorption model is assumed.

At surface-bulk equilibrium, the surface coverage θ_e and the bulk concentration C_{be} (molec m^{-3}) observe the following relationship:

$$\frac{\theta_e}{\sigma} = K_{sb} C_{be} (1 - \theta_e) \tag{5.14}$$

where σ (= 30 $Å^2$ $molec^{-1}$) is the effective cross section area of PA, and K_{sb} (= 2.01×10^{-4} m, Table 5.2) is the surface-bulk equilibrium constant.

The mass balance equation gives the second relationship between θ_e and C_{be}:

$$C_{b0} \frac{4}{3} \pi R_p^3 = C_{be} \frac{4}{3} \pi R_p^3 + \frac{\theta_e}{\sigma} 4 \pi R_p^2 \tag{5.15}$$

where C_{b0} (molec m^{-3}) and R_p (m) are the average concentration and the radius of the droplet, respectively.

The ratio of the quantity of PA on the surface to that in the bulk (S/V) is defined as:

$$S/V = \frac{3\theta_e}{\sigma C_{be} R_p} \tag{5.16}$$

Figure 5.8 shows an example of the surface coverage (θ_e) and surface-to-volume quantity ratio (S/V, dimensionless) of PA as a function of the droplet radius in a droplet system of an average concentration of 50 μM. The majority of PA ($\sim$ 98%) remains on the surface when the radius decreases to 10 μm. By comparison, for a droplet with a radius of 1 mm, $\sim$ 19% of PA is on the surface.

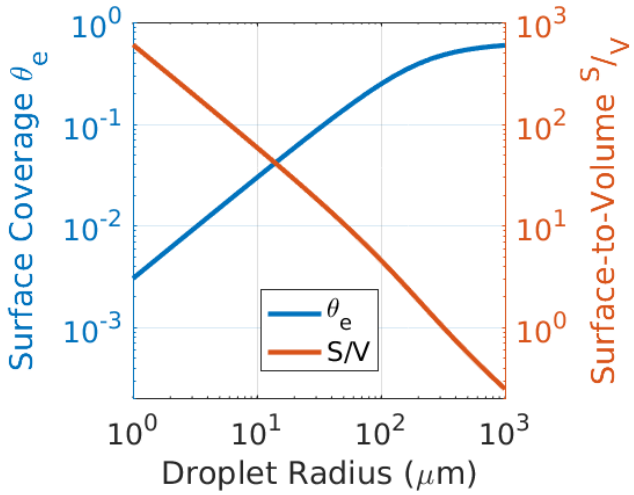

Figure 5.8: Equilibrium surface coverage (θ_e) and surface-to-volume quantity ratio (S/V) of PA as a function of the droplet radius in a droplet system of an average concentration of 50 μM.

5.5.3 Air-Surface-Water Equilibrium Constants

The water surface-gas phase partitioning coefficients (K_{sg}, in units of m^3 gas m^{-2} water surface) and the partitioning coefficients between water bulk and gas phase (K_{bg}, in units of m^3 gas m^{-3} water) for pinonic acid and its oxidation products were predicted with the software COSMOtherm (COSMOlogic, version 2017), which uses quantum-chemical calculations and statistical thermodynamics based on COSMO-RS (conductor-like screening model for real solvents) theory (Klamt, 2005; Klamt and Eckert, 2000). The water surface-water bulk phase partitioning coefficients (K_{sb}, in units of m^3 water m^{-2} water surface) were determined by the ratio $\frac{K_{sg}}{K_{bg}}$. The geometry of the molecules was optimized with TURBOMOLE (version 6.6, 2014, University of Karlsruhe & Forschungszentrum Karlsruhe GmbH, 1989-2007, TURBOMOLE GmbH, since 2007 available from www.turbomole.com) at the BP-TZVP level. COSMOconf (version 3.0, COSMOlogic) was then used to select a maximum of ten lowest energy conformers for each calculated molecule and generate COSMO files. Finally, partitioning coefficients were calculated with COSMOtherm (version C30_1705 with BP_TZVP_C30_1701 parameterization, COSMOlogic GmbH & Co. KG, Leverkusen, Germany, 2017) using the selected COSMO files as input. K_{bg} was calculated from COSMOtherm predicted Gibbs free energy of transfer between water and gas phase at 25 °C. K_{sg} was calculated based on the method described in Goss (2009). In brief, Gibbs free energy of transfer between an artificial vacuum phase and gas phase, and between interface and the vacuum phase were calculated for the target compounds at 25 °C. K_{sg} was then calculated from the adsorption free energy by applying a thermodynamic cycle. Prediction of K_{sg} by COSMOtherm was evaluated with 47 compounds with experimental data in the literature (Hartkopf and Karger, 1973; Roth et al., 2002) and a linear calibration was derived to correct the predicted data (Fig. 5.9).

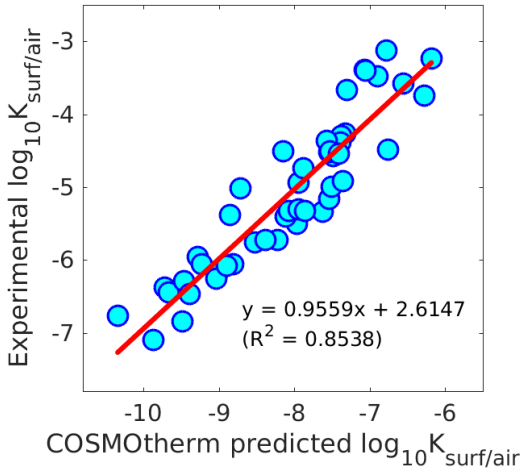

Figure 5.9: Correlation of COSMOtherm predicted $\log_{10} K_{sg}$ with experimental (Hartkopf and Karger, 1973; Roth et al., 2002) $\log_{10} K_{sg}$ at 15 °C. van 't Hoff equation is applied to estimate K_{sg} at 25 °C by assuming a constant ΔH between 15 and 25 °C, under which assumption the derived relationship remains the same.

Table 5.2: Equilibrium Constants for Typical Compounds

structure	formula	MW (g mol^{-1})	K_{sg} (m)	K_{sb} (= $\frac{K_{sg}}{K_{bg}}$, m)
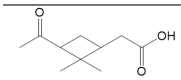	$C_{10}H_{16}O_3$	184	9.62×10^4	2.01×10^{-4}
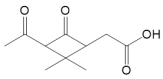	$C_{10}H_{14}O_4$	198	6.63×10^2	3.10×10^{-5}
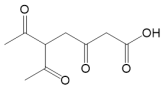	$C_9H_{12}O_5$	200	4.61×10^4	5.39×10^{-5}
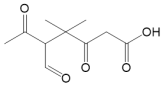	$C_{10}H_{14}O_5$	214	2.42×10^4	1.87×10^{-4}
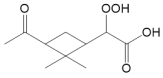	$C_{10}H_{16}O_5$	216	4.51×10^6	1.31×10^{-4}
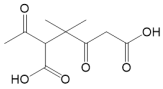	$C_{10}H_{14}O_6$	230	1.07×10^7	9.77×10^{-5}

5.5.4 Evaporation of PA from Droplet

In this section, we examine the extent to which the evaporation of PA from the droplet is significant during the experiment. We monitor the signal of PA on the surface of the hanging droplet (C_{b0} = 150 μM) at different exposure time (without introducing any OH) and the results are shown in Fig. 5.10. In the model, we assume the surface coverage of PA (θ_e = 0.832) is initially at equilibrium with the bulk PA concentration (C_{be} = 136 μM), and the bulk distribution is uniform. The bulk diffusivity of $\mathcal{D}_{b,\mathrm{PA}}$ is varied to evaluate if bulk diffusion is a rate-limiting step during the evaporation. The results, shown in Fig. 5.11, indicate that bulk diffusion can compensate for evaporation. For smaller bulk diffusivity, evaporation is limited to the surface regime. However, within the experimental period (< 100 s), evaporation-induced surface coverage shrinkage is found to be negligible, as supported by the observations. In the following simulation, a value of $\mathcal{D}_{b,\mathrm{PA}} = 10^{-10}$ m^2 s^{-1} is used, given the relatively large molecular size compared with OH ($\mathcal{D}_{b,\mathrm{OH}} = 2.3 \times 10^{-9}$ m^2 s^{-1}).

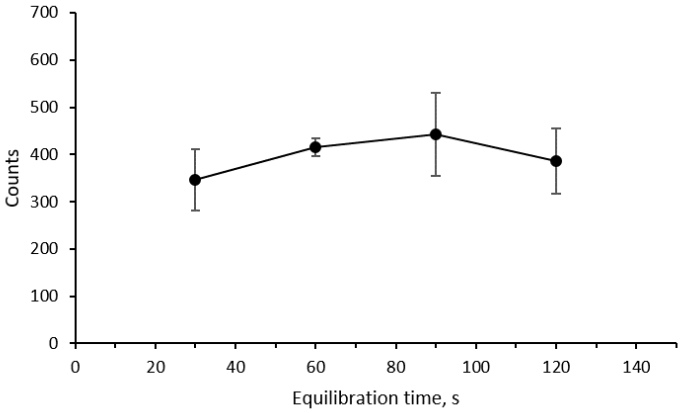

Figure 5.10: Experimental results of the signal of surface PA on the hanging droplet at different exposure time.

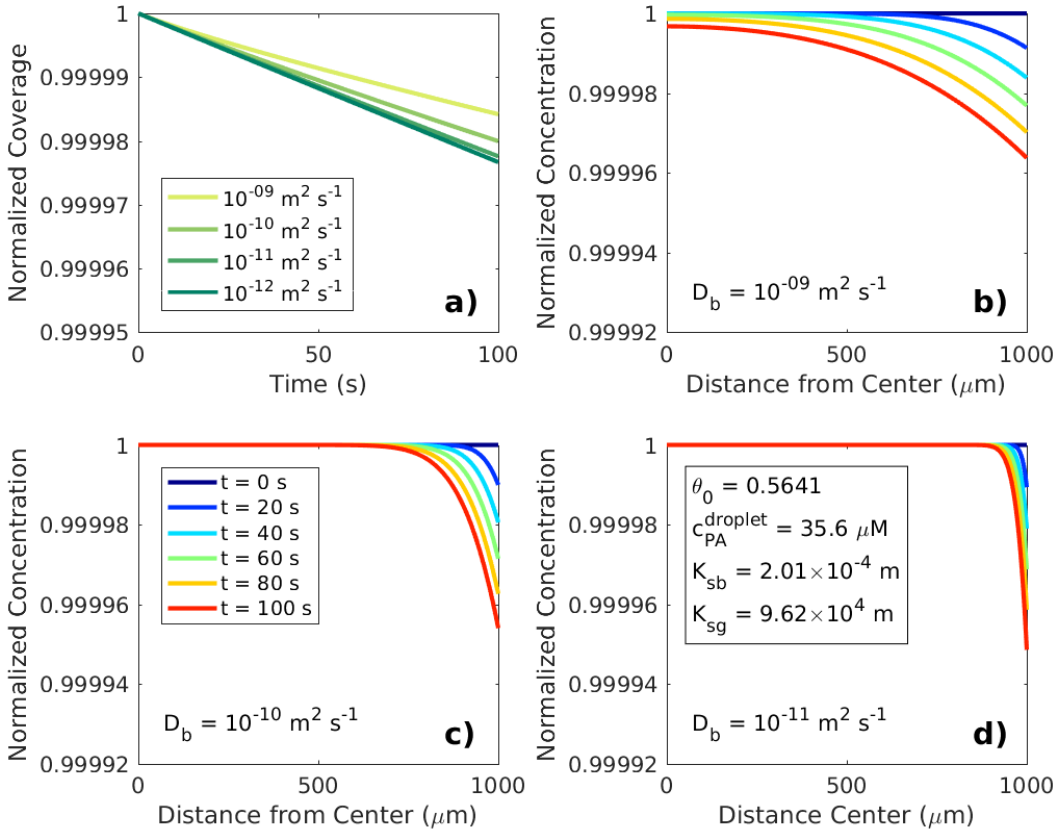

Figure 5.11: Simulation of PA evaporation when a droplet (radius = 1 mm) PA solution (150 μM) is exposed to ambient with zero gas-phase PA. a) Surface coverage of PA as a function of time at different bulk aqueous diffusivity. b) Bulk PA distribution along the radius at different exposure time when $\mathscr{D}_{b,\mathrm{PA}} = 10^{-9}$ m^2 s^{-1}. c) Bulk PA distribution along the radius at different exposure time when $\mathscr{D}_{b,\mathrm{PA}} = 10^{-10}$ m^2 s^{-1}. d) Bulk PA distribution along the radius at different exposure time when $\mathscr{D}_{b,\mathrm{PA}} = 10^{-11}$ m^2 s^{-1}.

5.5.5 Identification of PA + OH Products

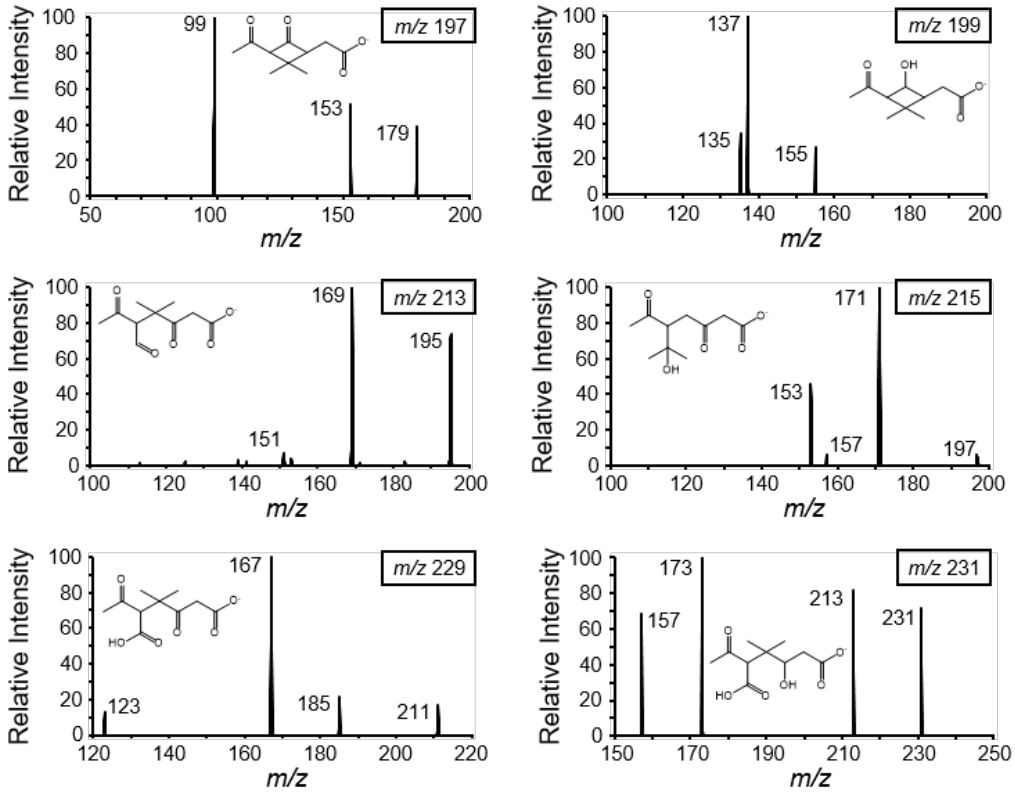

Figure 5.12: Experimental results of the CID (collision induced dissociation) signal of the 6 major PA products with proposed structures.

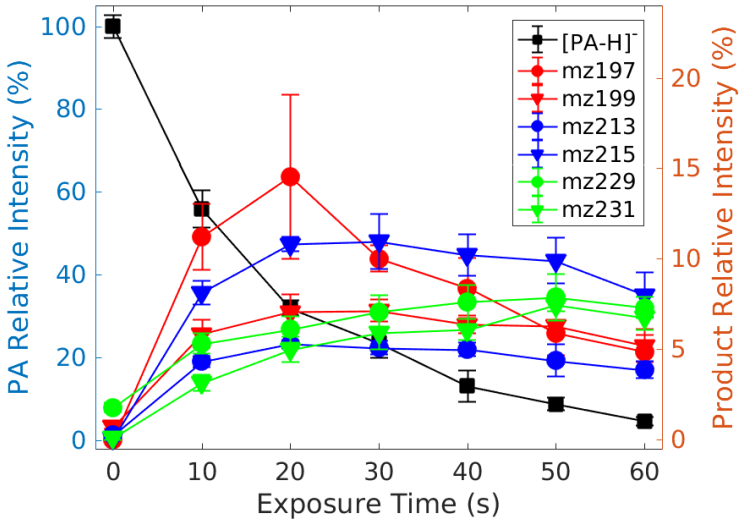

Figure 5.13: Temporal profiles of the relative peak area intensities of PA and its products .

5.5.6 SDS + OH Fitting

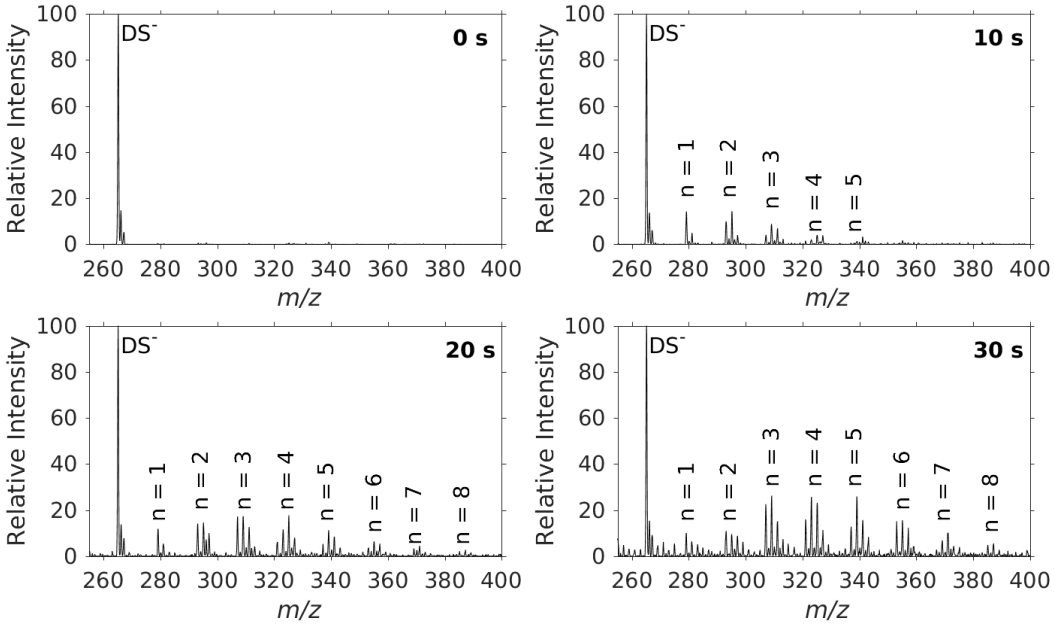

Figure 5.14: Mass spectra of SDS + OH oxidation at exposure time (0 s, 10 s, 20 s, and 30 s), reported as averages of replicate samples (N = 5). The peak intensities have been normalized with respect to the highest peak intensity in each mass spectra, i.e. DS^-. $n = 1$, $n = 2$, ..., mark the nth generation that contains n oxygen atoms in the SDS products.

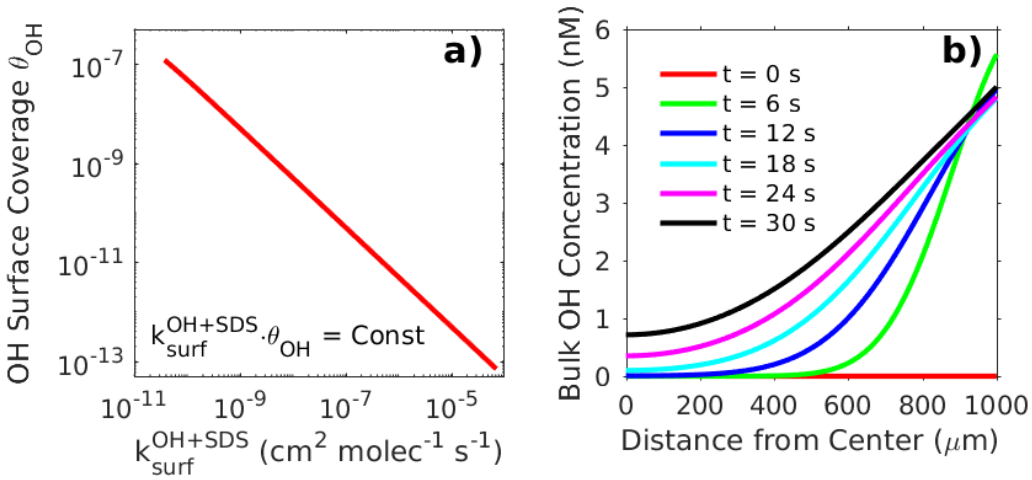

Figure 5.15: a) Inverse relationship between optimally fitted surface reaction rate constant for SDS + OH $k_{\text{surf}}^{\text{OH+SDS}}$ and the OH surface coverage θ_{OH}. b) Simulated bulk aqueous-phase OH distribution at different exposure times.

5.5.7 PA + OH and SDS + OH Fitting

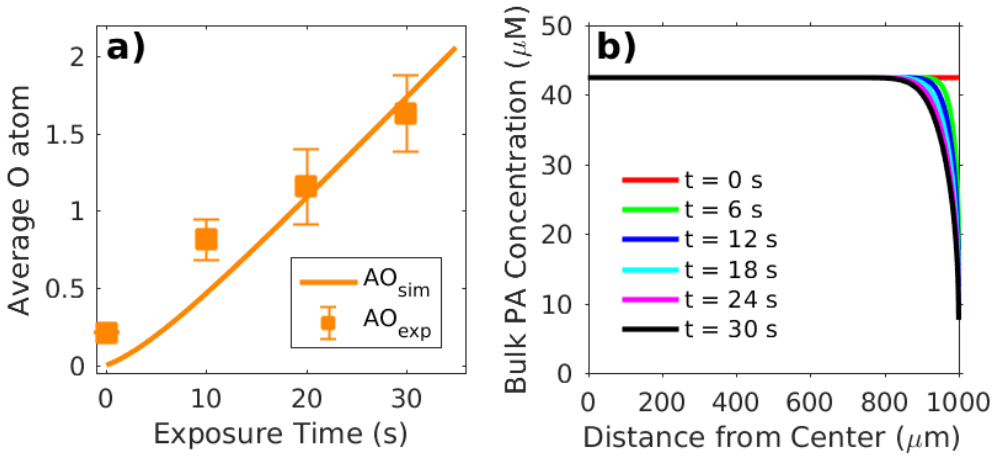

Figure 5.16: a) Experimental and fitting results of the average number of oxygen atoms incorporated into SDS products on the suspended droplet as a function of the exposure time. b) Simulated bulk aqueous-phase PA distribution at different exposure times.

5.5.8 Droplet Simulation

In this section, we show how to calculate the partition of PA among the gas phase, air-water interface, and the aqueous phase as functions of the droplet size, given the surface-gas (K_{sg} = 9.62×10^4 m) and surface-bulk (K_{sb} = 2.01×10^{-4} m) equilibrium constants. The Langmuir adsorption model is assumed to keep consistent with the model framework, so the expression is different from EQ. (2) in the manuscript, although this does not affect the conclusion that surface reaction is the largest sink of surface-active species at the air-water interface.

The overall PA concentration in the air parcel is $c_P = 0.5$ nmol m^{-3} air and the liquid water mixing ratio is $w_L = 3 \times 10^{-7}$ m^3 water m^{-3} air. The droplet radius (R) is in the range of $2.5 - 50 \times 10^{-6}$ m. We use g, s, and b to represent the concentration in the gas phase, surface, and the bulk aqueous phase in units of molec m^{-3} air, molec m^{-2} area, and molec m^{-3} water, respectively.

Based on a mass balance, there are two equations:

$$N\frac{4}{3}\pi R^3 = w_L \tag{5.17}$$

$$g + s \cdot N4\pi R^2 + b \cdot N\frac{4}{3}\pi R^3 = 10^{-9} c_P N_A \tag{5.18}$$

where N is the number concentration of the droplets and N_A is Avogadro's number.

From the equilibrium constant we have:

$$\frac{s}{g(1 - s\sigma)} = K_{sg} \tag{5.19}$$

$$\frac{s}{b(1 - s\sigma)} = K_{sb} \tag{5.20}$$

where $\sigma = 30 \times 10^{-20}$ Å^2 is the effective cross section area of PA. Combining EQs.(5.17) - (5.20), we can solve for N, g, s, and b.

Figure 5.17a shows the ratios of the fractions in the gas phase and in the bulk aqueous phase to that on the surface, as well as the number concentration of the droplet as functions of the droplet diameter. Because of the high surface activity of PA and high surface area concentration when the droplet radius is small, over 99% remains on the surface as $R < 10$ μm. Figure 5.17b shows the simulated temporal profiles of OH uptake coefficients on the surface of droplets of 5 μm and 100 μm, respectively.

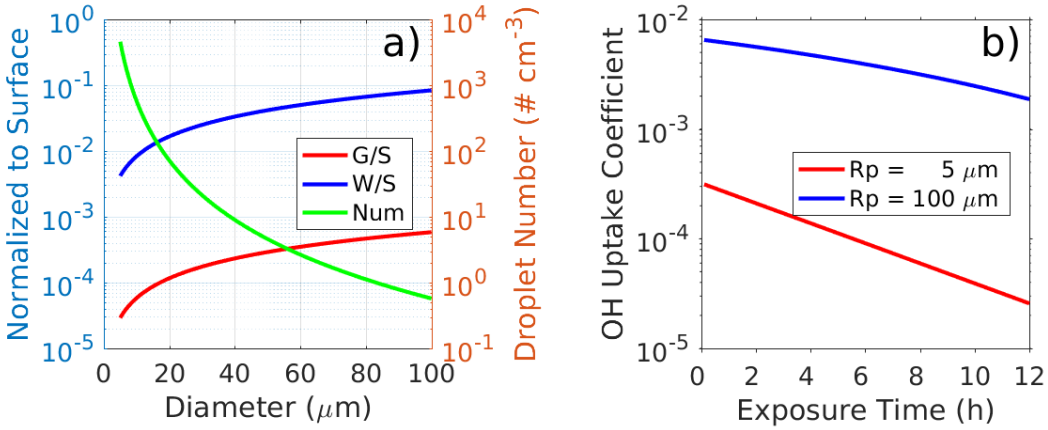

Figure 5.17: a) Ratios of the fractions of PA in the gas phase and in the bulk aqueous phase to that on the surface, as well as the number concentration of the droplet as functions of the droplet diameter. b) Simulated temporal profiles of OH uptake coefficients on the surface of droplets of 5 μm and 100 μm.

Chapter 6

CONCLUSIONS AND FUTURE WORK

This thesis has focused on characterizing and applying atmospheric reactors to study secondary organic aerosol (SOA) in the laboratory. The design and characterization of the Caltech PhotoOxidation flow Tube reactor (CPOT) led to the development of the advective-diffusive model (AD-PFR model). We proposed a unified theory to model the vapor-wall interaction and parameterized the processes. We also developed a multi-phase mass transport and reaction model to simulate the OH-initiated reactions occurring at the air-water interface of a droplet. Through Chapter 2 to Chapter 5, we stress that a proper interpretation of laboratory atmospheric chemistry study requires a well-characterized reactor and a well-defined model framework.

In addition to the work that has been carried out in this thesis, the methods we have developed can be applied to other aspects of SOA formation.

For example, Eq. 3.4 describing the cumulative residence time distribution in Chapter 3 can be combined with the parameterized vapor-wall interaction model in Chapter 4 to describe the signal delay in a sampling tube, which can be significant for instruments to detect those compounds with low volatilities. The Jimenez group in CU Boulder has made efforts on this topic. For example, Pagonis et al. (2017) proposed a vapor-wall interaction mechanism within a PFR model framework, similar to the absorption/desorption processes in chromatography, to describe the signal delay in Teflon sampling tube. This numerical model can reproduce the experimental data quite well, but is possible to be simplified into a single equation. One can follow the derivation of Deemter et al. (1956) for chromatography and use one or two key parameters in a key equation to represent the signal delay by sampling tubes.

Another on-going project is based on the multi-phase mass transport and reaction model in Chapter 5, which can be extended to a new comprehensive model to simulate single particle growth/evaporation by considering especially gas-particle interfacial interactions. Different from the model in Chapter 5 that assumes no water evaporation during the reaction, the single particle growth/evaporation model has a moving boundary, i.e., a typical Stefan problem. The concept of this model

is similar to that of the Kinetic Multi-layer model of GAs-Particle interactions in aerosols and clouds (KM-GAP, by M. Shiraiwa et al., 2012), however, instead of dividing the particle into multi-layer and treating each layer as a box model, the new model is based on the diffusion-reaction partial differential equation to represent the processes within the particle. This new model can help to evaluate the equilibration time between the gas- and particle- phases. Different from the traditional definition of equilibration time of gas- and particle- phases (Mai et al., 2015), the newly defined equilibrium time will consider only the equilibrium between the gas phase and the surface, which is more intuitive and can better reflect the interaction between the vapor and the particle.

BIBLIOGRAPHY

Abraham, M. H. and J. C. McGowan (1987). "The use of characteristic volumes to measure cavity terms in reversed phase liquid chromatography". In: *Chromatographia* 23.4, pp. 243–246. DOI: 10.1007/BF02311772.

Aljawhary, Dana, Ran Zhao, Alex K. Y. Lee, Chen Wang, and J. P. D. Abbatt (2016). "Kinetics, Mechanism, and Secondary Organic Aerosol Yield of Aqueous Phase Photo-Oxidation of α-Pinene Oxidation Products". In: *J. Phys. Chem. A* 120.9, pp. 1395–1407. DOI: 10.1021/acs.jpca.5b06237.

Aris, Rutherford (1956). "On the dispersion of a solute in a fluid flowing through a tube". In: *Proc. Roy. Soc. Lond. A Mat.* 235.1200, pp. 67–77. DOI: 10.1098/rspa.1956.0065.

Atkinson, Roger and Janet Arey (2003). "Atmospheric Degradation of Volatile Organic Compounds". In: *Chem. Rev.* 103.12, pp. 4605–4638. DOI: 10.1021/cr0206420.

Bagley, E. and F. A. Long (1955). "Two-stage sorption and desorption of organic vapors in cellulose acetate[1,2]". In: *J. Am. Chem. Soc.* 77.8, pp. 2172–2178. DOI: 10.1021/ja01613a038.

Barraza, Kevin M. (2018). "The Study of the Stepwise Hydroxyl Radical-Mediated Oxidation of Alkyl Surfactants at the Air-Water Interface". PhD thesis. California Institute of Technology.

Bates, Kelvin H., John D. Crounse, Jason M. St. Clair, Nathan B. Bennett, Tran B. Nguyen, John H. Seinfeld, Brian M. Stoltz, and Paul O. Wennberg (2014). "Gas phase production and loss of isoprene epoxydiols". In: *J. Phys. Chem. A* 118.7, pp. 1237–1246. DOI: 10.1021/jp4107958.

Bates, Kelvin H., Tran B. Nguyen, Alex P. Teng, John D. Crounse, Henrik G. Kjaergaard, Brian M. Stoltz, John H. Seinfeld, and Paul O. Wennberg (2016). "Production and Fate of C-4 Dihydroxycarbonyl Compounds from Isoprene Oxidation". In: *J. Phys. Chem. A* 120.1, 106–117. DOI: 10.1021/acs.jpca.5b10335.

Bean, J. K. and L. Hildebrandt Ruiz (2016). "Gas-particle partitioning and hydrolysis of organic nitrates formed from the oxidation of α-pinene in environmental chamber experiments". In: *Atmos. Chem. Phys.* 16.4, pp. 2175–2184. DOI: 10.5194/acp-16-2175-2016.

Beder, E. C., C. D. Bass, and W. L. Shackleford (1971). "Transmissivity and Absorption of Fused Quartz Between 0.22 μ and 3.5 μ from Room Temperature to 1500°C". In: *Appl. Opt.* 10.10, pp. 2263–2268. DOI: 10.1364/AO.10.002263.

Bernard, F., R. Ciuraru, A. Boréave, and C. George (2016). "Photosensitized Formation of Secondary Organic Aerosols above the Air/Water Interface". In: *Environ. Sci. Technol.* 50.16, pp. 8678–8686. DOI: 10.1021/acs.est.6b03520.

Bian, Q., A. A. May, S. M. Kreidenweis, and J. R. Pierce (2015). "Investigation of particle and vapor wall-loss effects on controlled wood-smoke smog-chamber experiments". In: *Atmos. Chem. Phys.* 15.19, pp. 11027–11045. DOI: 10.5194/acp-15-11027-2015.

Bilde, Merete and Spyros N. Pandis (2001). "Evaporation Rates and Vapor Pressures of Individual Aerosol Species Formed in the Atmospheric Oxidation of α- and β-Pinene". In: *Environ. Sci. Technol.* 35.16, pp. 3344–3349. DOI: 10.1021/es001946b.

Bird, R Byron, Warren E Stewart, and Edwin N Lightfoot (2007). *Transport Phenomena (revised)*. 2nd ed. New York: John Wiley & Sons, Inc.

Blando, James D and Barbara J Turpin (2000). "Secondary Organic Aerosol Formation in Cloud and Fog Droplets: a Literature Evaluation of Plausibility". In: *Atmos. Environ.* 34.10, pp. 1623–1632. DOI: 10.1016/S1352-2310(99)00392-1.

Boedeker (2017). *PTFE, FEP, and PFA Specifications*. URL: http://www.boedeker.com/feppfa_p.htm (visited on 01/23/2017).

Bonn, Boris, Gerhard Schuster, and Geert K. Moortgat (2002). "Influence of Water Vapor on the Process of New Particle Formation during Monoterpene Ozonolysis". In: *J. Phys. Chem. A* 106.12, pp. 2869–2881. DOI: 10.1021/jp012713p.

Bréon, Francois-Marie, Didier Tanré, and Sylvia Generoso (2002). "Aerosol Effect on Cloud Droplet Size Monitored from Satellite". In: *Science* 295.5556, pp. 834–838. DOI: 10.1126/science.1066434.

Bruns, E. A., I. El Haddad, A. Keller, F. Klein, N. K. Kumar, S. M. Pieber, J. C. Corbin, J. G. Slowik, W. H. Brune, U. Baltensperger, and A. S. H. Prévôt (2015). "Inter-comparison of laboratory smog chamber and flow reactor systems on organic aerosol yield and composition". In: *Atmos. Meas. Tech.* 8, pp. 2315–2332. DOI: 10.5194/amt-8-2315-2015.

Burkholder, J. B., S. P. Sander, J. P. D. Abbatt, J. R. Barker, R. E. Huie, C. E. Kolb, M. J. Kurylo, V. L. Orkin, D. M. Wilmouth, and P. H. Wine (2015). *Chemical Kinetics and Photochemical Data for Use in Atmospheric Studies, Evaluation No. 18*. JPL Publication 15-10, Jet Propulsion Laboratory, Pasadena.

Cappa, C. D., S. H. Jathar, M. J. Kleeman, K. S. Docherty, J. L. Jimenez, J. H. Seinfeld, and A. S. Wexler (2016). "Simulating secondary organic aerosol in a regional air quality model using the statistical oxidation model - Part 2: Assessing the influence of vapor wall losses". In: *Atmos. Chem. Phys.* 16.5, pp. 3041–3059. DOI: 10.5194/acp-16-3041-2016.

CARB (2018). *California Air Resources Board. Air Quality and Meteorological Information System*. URL: https://www.arb.ca.gov/aqmis2/aqdselect.php (visited on 04/07/2018).

Carslaw, Nicola (2007). "A New Detailed Chemical Model for Indoor Air Pollution". In: *Atmos. Environ.* 41.6, pp. 1164–1179. DOI: 10.1016/j.atmosenv.2006.09.038.

Chen, S., W. H. Brune, A. T. Lambe, P. Davidovits, and T. B. Onasch (2013). "Modeling organic aerosol from the oxidation of α-pinene in a Potential Aerosol Mass (PAM) chamber". In: *Atmos. Chem. Phys.* 13.9, pp. 5017–5031. DOI: 10.5194/acp-13-5017-2013.

CLOUD (2019). *CLOUD | CERN*. URL: https://home.cern/science/experiments/cloud (visited on 2019).

Compernolle, S., K. Ceulemans, and J.-F. Müller (2011). "EVAPORATION: a new vapour pressure estimation method for organic molecules including non-additivity and intramolecular interactions". In: *Atmos. Chem. Phys.* 11.18, pp. 9431–9450. DOI: 10.5194/acp-11-9431-2011.

Corner, J. and E. D. Pendlebury (1951). "The coagulation and deposition of a stirred aerosol". In: *Proc. Phys. Soc. B* 64.8, p. 645. DOI: 10.1088/0370-1301/64/8/304.

Crank, J. (1953). "A theoretical investigation of the influence of molecular relaxation and internal stress on diffusion in polymers". In: *J. Polym. Sci.* 11.2, pp. 151–168. DOI: 10.1002/pol.1953.120110206.

Crounse, John D., Karena A. McKinney, Alan J. Kwan, and Paul O. Wennberg (2006). "Measurement of gas-phase hydroperoxides by chemical ionization mass spectrometry". In: *Anal. Chem.* 78.19, pp. 6726–6732. DOI: 10.1021/ac0604235.

Crump, James G. and John H. Seinfeld (1981). "Turbulent deposition and gravitational sedimentation of an aerosol in a vessel of arbitrary shape". In: *J. Aerosol Sci.* 12.5, pp. 405–415. DOI: 10.1016/0021-8502(81)90036-7.

Danckwerts, P. V. (1953). "Continuous flow systems: Distribution of residence times". In: *Chem. Eng. Sci.* 2.1, pp. 1–13. DOI: 10.1016/0009-2509(53)80001-1.

Davidovits, P., J. T. Jayne, S. X. Duan, D. R. Worsnop, M. S. Zahniser, and C. E. Kolb (1991). "Uptake of gas molecules by liquids: a model". In: *J. Phys. Chem.* 95.16, pp. 6337–6340. DOI: 10.1021/j100169a048.

Davis, E James (2008). "Interpretation of uptake coefficient data obtained with flow tubes". In: *J. Phys. Chem. A* 112.9, pp. 1922–1932. DOI: 10.1021/jp074939j.

Davis, Mark E and Robert J Davis (2003). *Fundamentals of Chemical Reaction Engineering*. Courier Corporation.

Deemter, J. J. van, F. J. Zuiderweg, and A. Klinkenberg (1956). "Longitudinal diffusion and resistance to mass transfer as causes of nonideality in chromatography". In: *Chem. Eng. Sci.* 5.6, pp. 271–289. DOI: 10.1016/0009-2509(56)80003-1.

Demarque, Daniel P., Antonio E. M. Crotti, Ricardo Vessecchi, João L. C. Lopes, and Norberto P. Lopes (2016). "Fragmentation Reactions Using Electrospray Ionization Mass Spectrometry: An Important Tool for the Structural Elucidation and Characterization of Synthetic and Natural Products". In: *Nat. Prod. Rep.* 33.3, pp. 432–455. DOI: 10.1039/C5NP00073D.

Donahue, Neil M., James S. Clarke, Kenneth L. Demerjian, and James G. Anderson (1996). "Free-Radical Kinetics at High Pressure: A Mathematical Analysis of the Flow Reactor". In: *J. Phys. Chem.* 100.14, pp. 5821–5838. DOI: 10.1021/jp9525503.

Enami, Shinichi and A. J. Colussi (2017). "Efficient Scavenging of Criegee Intermediates on Water by Surface-Active *cis*-pinonic Acid". In: *Phys. Chem. Chem. Phys.* 19.26, pp. 17044–17051. DOI: 10.1039/C7CP03869K.

Enami, Shinichi and Yosuke Sakamoto (2016). "OH-Radical Oxidation of Surface-Active *cis*-Pinonic Acid at the Air-Water Interface". In: *J. Phys. Chem. A* 120.20, pp. 3578–3587. DOI: 10.1021/acs.jpca.6b01261.

EPA, US (2016). *Particulate Matter (PM) Basics*. URL: https://www.epa.gov/pm-pollution/particulate-matter-pm-basics.

Ervens, B., S. Gligorovski, and H. Herrmann (2003). "Temperature-Dependent Rate Constants for Hydroxyl Radical reactions with Organic Compounds in Aqueous Solutions". In: *Phys. Chem. Chem. Phys.* 5.9, pp. 1811–1824. DOI: 10.1039/B300072A.

Ervens, B., B. J. Turpin, and R. J. Weber (2011). "Secondary Organic Aerosol Formation in Cloud Droplets and Aqueous Particles (aqSOA): A Review of Laboratory, Field and Model Studies". In: *Atmos. Chem. Phys.* 11.21, pp. 11069–11102. DOI: 10.5194/acp-11-11069-2011.

Ervens, B. and R. Volkamer (2010). "Glyoxal Processing by Aerosol Multiphase Chemistry: Towards a Kinetic Modeling Framework of Secondary Organic Aerosol Formation in Aqueous Particles". In: *Atmos. Chem. Phys.* 10.17, pp. 8219–8244. DOI: 10.5194/acp-10-8219-2010.

Ezell, Michael J., Stanley N. Johnson, Yong Yu, Véronique Perraud, Emily A. Bruns, M. Lizabeth Alexander, Alla Zelenyuk, Donald Dabdub, and Barbara J. Finlayson-Pitts (2010). "A new aerosol flow system for photochemical and thermal studies of tropospheric aerosols". In: *Aerosol Sci. Tech.* 44.5, pp. 329–338. DOI: 10.1080/02786821003639700.

Faris, G. N. and R. Viskanta (1969). "An analysis of laminar combined forced and free convection heat transfer in a horizontal tube". In: *Int. J. Heat Mass Tran.* 12.10, pp. 1295–1309. DOI: 10.1016/0017-9310(69)90173-2.

Frezzotti, Aldo (2011). "Boundary conditions at the vapor-liquid interface". In: *Phys. Fluids* 23.3, p. 030609. DOI: 10.1063/1.3567001.

Fried, Erwin and Isaak E Idelchik (1989). *Flow Resistance: A Design Guide for Engineers*. Chem/Mats-Sci/E.

Frisch, H. L. (1980). "Sorption and transport in glassy polymers - a review". In: *Polym. Eng. Sci.* 20.1, pp. 2–13. DOI: 10.1002/pen.760200103.

Fuchs, N A (1964). *The Mechanics of Aerosols*. Pergamon, New York.

Galloway M. M., Loza C. L., Chhabra P. S., Chan A. W. H., Yee L. D., Seinfeld J. H., and Keutsch F. N. (2011). "Analysis of Photochemical and Dark Glyoxal Uptake: Implications for SOA Formation". In: *Geophys. Res. Lett* 38.17, p. L17811. DOI: 10.1029/2011GL048514.

George, I. J. and J. P. D. Abbatt (2010). "Heterogeneous oxidation of atmospheric aerosol particles by gas-phase radicals". In: *Nat. Chem.* 2.9, p. 713. DOI: 10.1038/nchem.806.

George, I. J., A. Vlasenko, J. G. Slowik, K. Broekhuizen, and J. P. D. Abbatt (2007). "Heterogeneous oxidation of saturated organic aerosols by hydroxyl radicals: uptake kinetics, condensed-phase products, and particle size change". In: *Atmos. Chem. Phys.* 7.16, pp. 4187–4201. DOI: 10.5194/acp-7-4187-2007.

Gormley, P. G. and M. Kennedy (1948). "Diffusion from a stream flowing through a cylindrical tube". In: *P. Roy. Irish Acad. A* 52, pp. 163–169.

Goss, Kai-Uwe (2009). "Predicting Adsorption of Organic Chemicals at the Air-Water Interface". In: *J. Phys. Chem. A* 113.44, pp. 12256–12259. DOI: 10.1021/jp907347p.

Grayson, J. W., M. Song, M. Sellier, and A. K. Bertram (2015). "Validation of the poke-flow technique combined with simulations of fluid flow for determining viscosities in samples with small volumes and high viscosities". In: *Atmos. Meas. Tech.* 8.6, pp. 2463–2472. DOI: 10.5194/amt-8-2463-2015.

Grimm, Ronald L. and J. L. Beauchamp (2003). "Field-Induced Droplet Ionization Mass Spectrometry". In: *J. Phys. Chem. B* 107.51, pp. 14161–14163. DOI: 10.1021/jp037099r.

– (2005). "Dynamics of Field-Induced Droplet Ionization: Time-Resolved Studies of Distortion, Jetting, and Progeny Formation from Charged and Neutral Methanol Droplets Exposed to Strong Electric Fields". In: *J. Phys. Chem. B* 109.16, pp. 8244–8250. DOI: 10.1021/jp0450540.

Grimm, Ronald L., Robert Hodyss, and J. L. Beauchamp (2006). "Probing Interfacial Chemistry of Single Droplets with Field-Induced Droplet Ionization Mass Spectrometry: Physical Adsorption of Polycyclic Aromatic Hydrocarbons and Ozonolysis of Oleic Acid and Related Compounds". In: *Anal. Chem.* 78.11, pp. 3800–3806. DOI: 10.1021/ac0601922.

Guenther, A. B., X. Jiang, C. L. Heald, T. Sakulyanontvittaya, T. Duhl, L. K. Emmons, and X. Wang (2012). "The Model of Emissions of Gases and Aerosols from Nature version 2.1 (MEGAN2.1): An Extended and Updated Framework for Modeling Biogenic Emissions". In: *Geosci. Model Dev.* 5.6, pp. 1471–1492. DOI: 10.5194/gmd-5-1471-2012.

Hartkopf, Arleigh and Barry L. Karger (1973). "Study of the interfacial properties of water by gas chromatography". In: *Acc. Chem. Res.* 6.6, pp. 209–216. DOI: 10.1021/ar50066a006.

Heath, Aubrey A. and Kalliat T. Valsaraj (2015). "Effects of Temperature, Oxygen Level, Ionic Strength, and pH on the Reaction of Benzene with Hydroxyl Radicals at the Air-Water Interface in Comparison to the Bulk Aqueous Phase". In: *J. Phys. Chem. A* 119.31, pp. 8527–8536. DOI: 10.1021/acs.jpca.5b05152.

Hodas, N., A. Zuend, W. Mui, R. C. Flagan, and J. H. Seinfeld (2015). "Influence of particle-phase state on the hygroscopic behavior of mixed organic-inorganic aerosols". In: *Atmos. Chem. Phys.* 15.9, 5027–5045. DOI: 10.5194/acp-15-5027-2015.

Holman, Jack Philip (2010). *Heat Transfer*. 10th ed. McGraw-Hill.

Houle, Frances A., Aaron A. Wiegel, and Kevin R. Wilson (2018). "Changes in Reactivity as Chemistry Becomes Confined to an Interface. The Case of Free Radical Oxidation of $C_{30}H_{62}$ Alkane by OH". In: *J. Phys. Chem. Lett* 9.5, pp. 1053–1057. DOI: 10.1021/acs.jpclett.8b00172.

Howard, Carleton J. (1979). "Kinetic measurements using flow tubes". In: *J. Phys. Chem.* 83.1, pp. 3–9. DOI: 10.1021/j100464a001.

Howell, Hilda and G. S. Fisher (1958). "The Dissociation Constants of Some of the Terpene Acids". In: *J. Am. Chem. Soc* 80.23, pp. 6316–6319. DOI: 10.1021/ja01556a038.

Hua, Wei, Dominique Verreault, and Heather C. Allen (2015). "Relative Order of Sulfuric Acid, Bisulfate, Hydronium, and Cations at the Air-Water Interface". In: *J. Am. Chem. Soc.* 137.43, pp. 13920–13926. DOI: 10.1021/jacs.5b08636.

Huang, Y., M. M. Coggon, R. Zhao, H. Lignell, M. U. Bauer, R. C. Flagan, and J. H. Seinfeld (2017). "The Caltech Photooxidation Flow Tube reactor: design, fluid dynamics and characterization". In: *Atmos. Meas. Tech.* 10.3, pp. 839–867. DOI: 10.5194/amt-10-839-2017.

IPCC (2013). *Climate Change 2013: The Physical Science Basis. Contribution of Working Group I to the Fifth Assessment Report of the Intergovernmental Panel on Climate Change*. Cambridge University Press, Cambridge, UK and New York, NY, USA.

Iqbal, M. and J. W. Stachiewicz (1966). "Influence of tube orientation on combined free and forced laminar convection heat transfer". In: *J. Heat Transf.* 88.1, pp. 109–116. DOI: 10.1115/1.3691452.

Ivanov, Andrey V., Sofia Trakhtenberg, Allan K. Bertram, Yulii M. Gershenzon, and Mario J. Molina (2007). "OH, HO_2, and Ozone Gaseous Diffusion Coefficients". In: *J. Phys. Chem. A* 111.9, pp. 1632–1637. DOI: 10.1021/jp066558w.

Jimenez, J. L., M. R. Canagaratna, N. M. Donahue, A. S. H. Prevot, Q. Zhang, J. H. Kroll, P. F. DeCarlo, J. D. Allan, H. Coe, N. L. Ng, A. C. Aiken, K. S. Docherty, I. M. Ulbrich, A. P. Grieshop, A. L. Robinson, J. Duplissy, J. D. Smith, K. R. Wilson, V. A. Lanz, C. Hueglin, Y. L. Sun, J. Tian, A. Laaksonen, T. Raatikainen, J. Rautiainen, P. Vaattovaara, M. Ehn, M. Kulmala, J. M. Tomlinson, D. R. Collins, M. J. Cubison, E, J. Dunlea, J. A. Huffman, T. B. Onasch, M. R. Alfarra, P. I. Williams, K. Bower, Y. Kondo, J. Schneider, F. Drewnick, S. Borrmann, S. Weimer, K. Demerjian, D. Salcedo, L. Cottrell, R. Griffin, A. Takami, T. Miyoshi, S. Hatakeyama, A. Shimono, J. Y. Sun, Y. M. Zhang, K. Dzepina, J. R. Kimmel, D. Sueper, J. T. Jayne, S. C. Herndon, A. M. Trimborn, L. R. Williams, E. C. Wood, A. M. Middlebrook, C. E. Kolb, U. Baltensperger, and D. R. Worsnop (2009). "Evolution of Organic Aerosols in the Atmosphere". In: *Science* 326.5959, pp. 1525–1529. DOI: 10.1126/science.1180353.

Jones, Stephanie H., Martin D. King, Andrew D. Ward, Adrian R. Rennie, Alex C. Jones, and Thomas Arnold (2017). "Are Organic Films from Atmospheric Aerosol and Sea Water Inert to Oxidation by Ozone at the Air-Water Interface?" In: *Atmos. Environ.* 161, pp. 274–287. DOI: 10.1016/j.atmosenv.2017.04.025.

Jonsson, Åsa M., Mattias Hallquist, and Evert Ljungström (2008). "Influence of OH Scavenger on the Water Effect on Secondary Organic Aerosol Formation from Ozonolysis of Limonene, Δ^3-Carene, and α-Pinene". In: *Environ. Sci. Technol.* 42.16, pp. 5938–5944. DOI: 10.1021/es702508y.

Kameel, F. Rifkha, M. R. Hoffmann, and A. J. Colussi (2013). "OH Radical-Initiated Chemistry of Isoprene in Aqueous Media. Atmospheric Implications". In: *J. Phys. Chem. A* 117.24, pp. 5117–5123. DOI: 10.1021/jp4026267.

Kang, E., M. J. Root, D. W. Toohey, and W. H. Brune (2007). "Introducing the concept of Potential Aerosol Mass (PAM)". In: *Atmos. Chem. Phys.* 7, pp. 5727–5744. DOI: 10.5194/acp-7-5727-2007.

Kang, E., D. W. Toohey, and W. H. Brune (2011). "Dependence of SOA oxidation on organic aerosol mass concentration and OH exposure: experimental PAM chamber studies". In: *Atmos. Chem. Phys.* 11, pp. 1837–1852. DOI: 10.5194/acp-11-1837-2011.

Karjalainen, P., H. Timonen, E. Saukko, H. Kuuluvainen, S. Saarikoski, P. Aakko-Saksa, T. Murtonen, M. Bloss, M. Dal Maso, P. Simonen, E. Ahlberg, B. Svenningsson, W. H. Brune, R. Hillamo, J. Keskinen, and T. Rönkkö (2016). "Time-resolved characterization of primary particle emissions and secondary particle formation from a modern gasoline passenger car". In: *Atmos. Chem. Phys.* 16.13, pp. 8559–8570. DOI: 10.5194/acp-16-8559-2016.

Kavouras, Ilias G., Nikolaos Mihalopoulos, and Euripides G. Stephanou (1999). "Secondary Organic Aerosol Formation vs Primary Organic Aerosol Emission: In Situ Evidence for the Chemical Coupling between Monoterpene Acidic Photooxidation Products and New Particle Formation over Forests". In: *Environ. Sci. Technol.* 33.7, pp. 1028–1037. DOI: 10.1021/es9807035.

Keller, Alejandro and Heinz Burtscher (2012). "A continuous photo-oxidation flow reactor for a defined measurement of the SOA formation potential of wood burning emissions". In: *J. Aerosol Sci.* 49, pp. 9–20. DOI: 10.1016/j.jaerosci.2012.02.007.

Khalizov, Alexei F., Michael E. Earle, Wayde J. W. Johnson, Gordon D. Stubley, and James J. Sloan (2006). "Development and characterization of a laminar aerosol flow tube". In: *Rev. Sci. Instrum.* 77.3, p. 033102. DOI: 10.1063/1.2175958.

Kim, Hugh I., Hyungjun Kim, Young Shik Shin, Luther W. Beegle, William A. Goddard, James R. Heath, Isik Kanik, and J. L. Beauchamp (2010a). "Time Resolved Studies of Interfacial Reactions of Ozone with Pulmonary Phospholipid Surfactants Using Field Induced Droplet Ionization Mass Spectrometry". In: *J. Phys. Chem. B* 114.29, pp. 9496–9503. DOI: 10.1021/jp102332g.

Kim, Hugh I., Hyungjun Kim, Young Shik Shin, Luther W. Beegle, Seung Soon Jang, Evan L. Neidholdt, William A. Goddard, James R. Heath, Isik Kanik, and J. L. Beauchamp (2010b). "Interfacial Reactions of Ozone with Surfactant Protein B in a Model Lung Surfactant System". In: *J. Am. Chem. Soc.* 132.7, pp. 2254–2263. DOI: 10.1021/ja908477w.

King, Martin D., Adrian R. Rennie, Katherine C. Thompson, Fleur N. Fisher, Chu Chuan Dong, Robert K. Thomas, Christian Pfrang, and Arwel V. Hughes (2009). "Oxidation of Oleic Acid at the Air-Water Interface and Its Potential Effects on Cloud Critical Supersaturations". In: *Phys. Chem. Chem. Phys.* 11.35, pp. 7699–7707. DOI: 10.1039/B906517B.

Klamt, Andreas (2005). *COSMO-RS From Quantum Chemistry to Fluid Phase Thermodynamics and Drug Design*. 1st ed. Elsevier: Amsterdam, The Netherlands.

Klamt, Andreas and Frank Eckert (2000). "COSMO-RS: a novel and efficient method for the a priori prediction of thermophysical data of liquids". In: *Fluid Ph. Equilibria* 172.1, pp. 43–72. DOI: 10.1016/S0378-3812(00)00357-5.

Krechmer, Jordan E., Matthew M. Coggon, Paola Massoli, Tran B. Nguyen, John D. Crounse, Weiwei Hu, Douglas A. Day, Geoffrey S. Tyndall, Daven K. Henze, Jean C. Rivera-Rios, John B. Nowak, Joel R. Kimmel, Roy L. Mauldin, Harald Stark, John T. Jayne, Mikko Sipilä, Heikki Junninen, Jason M. St. Clair, Xuan Zhang, Philip A. Feiner, Li Zhang, David O. Miller, William H. Brune, Frank N. Keutsch, Paul O. Wennberg, John H. Seinfeld, Douglas R. Worsnop, Jose L. Jimenez, and Manjula R. Canagaratna (2015). "Formation of low volatility organic compounds and secondary organic aerosol from isoprene hydroxyhydroperoxide

low-NO oxidation". In: *Environ. Sci. Technol.* 49.17, pp. 10330–10339. DOI: 10.1021/acs.est.5b02031.

Krechmer, Jordan E., Demetrios Pagonis, Paul J. Ziemann, and Jose L. Jimenez (2016). "Quantification of gas-wall partitioning in Teflon environmental chambers using rapid bursts of low-volatility oxidized species generated in situ". In: *Environ. Sci. Technol.* 50.11, pp. 5757–5765. DOI: 10.1021/acs.est.6b00606.

Kroll, Jesse H., Jared D. Smith, Dung L. Che, Sean H. Kessler, Douglas R. Worsnop, and Kevin R. Wilson (2009). "Measurement of fragmentation and functionalization pathways in the heterogeneous oxidation of oxidized organic aerosol". In: *Phys. Chem. Chem. Phys.* 11, pp. 8005–8014. DOI: 10.1039/B905289E.

Kumar, Manoj, Hao Li, Xiuhui Zhang, Xiao Cheng Zeng, and Joseph S. Francisco (Apr. 2018). "Nitric Acid-Amine Chemistry in the Gas Phase and at the Air-Water Interface". In: *J. Am. Chem. Soc.* DOI: 10.1021/jacs.8b03300.

La, Y. S., M. Camredon, P. J. Ziemann, R. Valorso, A. Matsunaga, V. Lannuque, J. Lee-Taylor, A. Hodzic, S. Madronich, and B. Aumont (2016). "Impact of chamber wall loss of gaseous organic compounds on secondary organic aerosol formation: explicit modeling of SOA formation from alkane and alkene oxidation". In: *Atmos. Chem. Phys.* 16.3, pp. 1417–1431. DOI: 10.5194/acp-16-1417-2016.

Lai, Chengyue, Yongchun Liu, Jinzhu Ma, Qingxin Ma, Biwu Chu, and Hong He (2015). "Heterogeneous Kinetics of *cis*-Pinonic Acid with Hydroxyl Radical under Different Environmental Conditions". In: *J. Phys. Chem. A* 119.25, pp. 6583–6593. DOI: 10.1021/acs.jpca.5b01321.

Lambe, A. T., A. T. Ahern, L. R. Williams, J. G. Slowik, J. P. S. Wong, J. P. D. Abbatt, W. H. Brune, N. L. Ng, J. P. Wright, D. R. Croasdale, D. R. Worsnop, P. Davidovits, and T. B. Onasch (2011a). "Characterization of aerosol photooxidation flow reactors: heterogeneous oxidation, secondary organic aerosol formation and cloud condensation nuclei activity measurements". In: *Atmos. Meas.Tech.* 4.3, pp. 445–461. DOI: 10.5194/amt-4-445-2011.

Lambe, A. T., P. S. Chhabra, T. B. Onasch, W. H. Brune, J. F. Hunter, J. H. Kroll, M. J. Cummings, J. F. Brogan, Y. Parmar, D. R. Worsnop, C. E. Kolb, and P. Davidovits (2015). "Effect of oxidant concentration, exposure time, and seed particles on secondary organic aerosol chemical composition and yield". In: *Atmos. Chem. Phys.* 15.6, pp. 3063–3075. DOI: 10.5194/acp-15-3063-2015.

Lambe, A. T., T. B. Onasch, P. Massoli, D. R. Croasdale, J. P. Wright, A. T. Ahern, L. R. Williams, D. R. Worsnop, W. H. Brune, and P. Davidovits (2011b). "Laboratory studies of the chemical composition and cloud condensation nuclei (CCN) activity of secondary organic aerosol (SOA) and oxidized primary organic aerosol (OPOA)". In: *Atmos. Chem. Phys.* 11, pp. 8913–8928. DOI: 10.5194/acp-11-8913-2011.

Lambe, A. T., Timothy B. Onasch, David R. Croasdale, Justin P. Wright, Alexander T. Martin, Jonathan P. Franklin, Paola Massoli, Jesse H. Kroll, Manjula R. Canagaratna, William H. Brune, Douglas R. Worsnop, and Paul Davidovits (2012). "Transitions from functionalization to fragmentation reactions of laboratory secondary organic aerosol (SOA) generated from the OH oxidation of alkane precursors". In: *Environ. Sci. Technol.* 46.10, pp. 5430–5437. DOI: 10.1021/es300274t.

Lee, Alex K. Y., P. Herckes, W. R. Leaitch, A. M. Macdonald, and J. P. D. Abbatt (2011). "Aqueous OH Oxidation of Ambient Organic Aerosol and Cloud Water Organics: Formation of Highly Oxidized Products". In: *Geophys. Res. Lett.* 38.11, p. L11805. DOI: 10.1029/2011GL047439.

Lee, Ben H., Felipe D. Lopez-Hilfiker, Claudia Mohr, Theo Kurtén, Douglas R. Worsnop, and Joel A. Thornton (2014). "An Iodide-adduct high-resolution time-of-flight chemical-ionization mass spectrometer: Application to atmospheric inorganic and organic compounds". In: *Environ. Sci. Technol.* 48.11, pp. 6309–6317. DOI: 10.1021/es500362a.

Lee, Ming-Tao, Fabrizio Orlando, Luca Artiglia, Shuzhen Chen, and Markus Ammann (2016). "Chemical Composition and Properties of the Liquid-Vapor Interface of Aqueous C1 to C4 Monofunctional Acid and Alcohol Solutions". In: *J. Phys. Chem. A* 120, pp. 9749–9758. DOI: 10.1021/acs.jpca.6b09261.

Li, R., Brett B. Palm, Amber M. Ortega, James Hlywiak, Weiwei Hu, Zhe Peng, Douglas A. Day, Christoph Knote, William H. Brune, Joost A. de Gouw, and Jose L. Jimenez (2015). "Modeling the radical chemistry in an oxidation flow reactor: Radical formation and recycling, sensitivities, and the OH exposure estimation equation". In: *J. Phys. Chem. A* 119.19, pp. 4418–4432. DOI: 10.1021/jp509534k.

Li, Xin, Thomas Hede, Yaoquan Tu, Caroline Leck, and Hans Ågren (2010). "Surface-Active *cis*-Pinonic Acid in Atmospheric Droplets: A Molecular Dynamics Study". In: *J. Phys. Chem. Lett.* 1.4, pp. 769–773. DOI: 10.1021/jz9004784.

Lignell, Hanna, Scott A. Epstein, Margaret R. Marvin, Dorit Shemesh, Benny Gerber, and Sergey Nizkorodov (2013). "Experimental and Theoretical Study of Aqueous *cis*-Pinonic Acid Photolysis". In: *J. Phys. Chem. A* 117, pp. 12930–12945. DOI: 10.1021/jp4093018.

Lim, Ho-Jin, Annmarie G. Carlton, and Barbara J. Turpin (2005). "Isoprene Forms Secondary Organic Aerosol through Cloud Processing: Model Simulations". In: *Environ. Sci. Technol.* 39.12, pp. 4441–4446. DOI: 10.1021/es048039h.

Lim, Y. B., Y. Tan, M. J. Perri, S. P. Seitzinger, and B. J. Turpin (2010). "Aqueous Chemistry and Its Role in Secondary Organic Aerosol (SOA) Formation". In: *Atmos. Chem. Phys.* 10.21, pp. 10521–10539. DOI: 10.5194/acp-10-10521-2010.

Linossier, I., F. Gaillard, M. Romand, and J. F. Feller (1997). "Measuring water diffusion in polymer films on the substrate by internal reflection fourier transform infrared spectroscopy". In: *J. Appl. Polym. Sci.* 66.13, pp. 2465–2473. DOI: 10.1002/(SICI)1097-4628(19971226)66:13<2465::AID-APP9>3.0.CO;2-G.

Liu, Benjamin Y. H. and K. W. Lee (1975). "An aerosol generator of high stability". In: *Am. Ind. Hyg. Assoc. J.* 36.12, pp. 861–865. DOI: 10.1080/00028897585073357.

Loza, C. L., Matthew M. Coggon, Tran B. Nguyen, Andreas Zuend, Richard C. Flagan, and John H. Seinfeld (2013). "On the Mixing and Evaporation of Secondary Organic Aerosol Components". In: *Environ. Sci. Technol.* 47.12, 6173–6180. DOI: 10.1021/es400979k.

Loza, C. L., J. S. Craven, L. D. Yee, M. M. Coggon, R. H. Schwantes, M. Shiraiwa, X. Zhang, K. A. Schilling, N. L. Ng, M. R. Canagaratna, P. J. Ziemann, R. C. Flagan, and J. H. Seinfeld (2014). "Secondary organic aerosol yields of 12-carbon alkanes". In: *Atmos. Chem. Phys.* 14.3, pp. 1423–1439. DOI: 10.5194/acp-14-1423-2014.

Loza, Christine L., Arthur W. H. Chan, Melissa M. Galloway, Frank N. Keutsch, Richard C. Flagan, and John H. Seinfeld (2010). "Characterization of vapor wall loss in laboratory chambers". In: *Environ. Sci. Technol.* 44.13, pp. 5074–5078. DOI: 10.1021/es100727v.

Mai, Huajun, Manabu Shiraiwa, Richard C. Flagan, and John H. Seinfeld (2015). "Under What Conditions Can Equilibrium Gas-Particle Partitioning Be Expected to Hold in the Atmosphere?" In: *Environ. Sci. Technol.* 49.19, pp. 11485–11491. DOI: 10.1021/acs.est.5b02587.

Martins-Costa, Marilia T. C., Francisco F. García-Prieto, and Manuel F. Ruiz-López (2015). "Reactivity of Aldehydes at the Air-Water Interface. Insights from Molecular Dynamics Simulations and ab initio Calculations". In: *Org. Biomol. Chem.* 13.6, pp. 1673–1679. DOI: 10.1039/C4OB02029D.

Matsunaga, Aiko and Paul J. Ziemann (2010). "Gas-wall partitioning of organic compounds in a Teflon film chamber and potential effects on reaction product and aerosol yield measurements". In: *Aerosol Sci. Technol.* 44.10, pp. 881–892. DOI: 10.1080/02786826.2010.501044.

Matthews, P. S. J., M. T. Baeza-Romero, L. K. Whalley, and D. E. Heard (2014). "Uptake of HO_2 radicals onto Arizona test dust particles using an aerosol flow tube". In: *Atmos. Chem. Phys.* 14.14, pp. 7397–7408. DOI: 10.5194/acp-14-7397-2014.

McDonald, A. T., R. W. Fox, and R. V. Van Dawoestine (1971). "Effects of swirling inlet flow on pressure recovery in conical diffusers". In: *AIAA J.* 9.10, pp. 2014–2018. DOI: 10.2514/3.6456.

McMurry, Peter H. and Daniel. Grosjean (1985). "Gas and aerosol wall losses in Teflon film smog chambers". In: *Environ. Sci. Technol.* 19.12, pp. 1176–1182. DOI: 10.1021/es00142a006.

McNeill, V. Faye, Joseph L. Woo, Derek D. Kim, Allison N. Schwier, Neal J. Wannell, Andrew J. Sumner, and Joseph M. Barakat (2012). "Aqueous-Phase Secondary Organic Aerosol and Organosulfate Formation in Atmospheric Aerosols: A Modeling Study". In: *Environ. Sci. Technol.* 46.15, pp. 8075–8081. DOI: 10.1021/es3002986.

McVay, R. C., Christopher D. Cappa, and John H. Seinfeld (2014). "Vapor-wall deposition in chambers: Theoretical considerations". In: *Environ. Sci. Technol.* 48.17, pp. 10251–10258. DOI: 10.1021/es502170j.

McVay, Renee C., Xuan Zhang, Bernard Aumont, Richard Valorso, Marie Camredon, Yuyi S. La, Paul O. Wennberg, and John H. Seinfeld (2016). "SOA formation from the photooxidation of α-pinene: systematic exploration of the simulation of chamber data". In: *Atmos. Chem. Phys.* 16.5, 2785–2802. DOI: 10.5194/acp-16-2785-2016.

Mehta, R. D. and P. Bradshaw (1979). "Design rules for small low speed wind tunnels". In: *Aeronaut. J.* 83.827, pp. 443–449. DOI: 10.1017/S0001924000031985.

Mikheev, Vladimir B., Nels S. Laulainen, Stephan E. Barlow, Michael Knott, and Ian J. Ford (2000). "The laminar flow tube reactor as a quantitative tool for nucleation studies: Experimental results and theoretical analysis of homogeneous nucleation of dibutylphthalate". In: *The Journal of Chemical Physics* 113.9, pp. 3704–3718. DOI: 10.1063/1.1287598.

Mitroo, D., Y. Sun, D. P. Combest, P. Kumar, and B. J. Williams (2018). "Assessing the degree of plug flow in oxidation flow reactors (OFRs): a study on a potential aerosol mass (PAM) reactor". In: *Atmos. Meas. Tech.* 11.3, pp. 1741–1756. DOI: 10.5194/amt-11-1741-2018.

Mori, Yasuo and Kozo Futagami (1967). "Forced convective heat transfer in uniformly heated horizontal tubes (2nd report, theoretical study)". In: *Int. J. Heat Mass Tran.* 10.12, pp. 1801–1813. DOI: 10.1016/0017-9310(67)90051-8.

Müller, L., M.-C. Reinnig, K. H. Naumann, H. Saathoff, T. F. Mentel, N. M. Donahue, and T. Hoffmann (2012). "Formation of 3-Methyl-1,2,3-Butanetricarboxylic Acid via Gas Phase Oxidation of Pinonic Acid - A Mass Spectrometric Study of SOA Aging". In: *Atmos. Chem. Phys.* 12.3, pp. 1483–1496. DOI: 10.5194/acp-12-1483-2012.

Nah, T., R. C. McVay, J. R. Pierce, J. H. Seinfeld, and N. L. Ng (2017). "Constraining uncertainties in particle-wall deposition correction during SOA formation in chamber experiments". In: *Atmos. Chem. Phys.* 17.3, pp. 2297–2310. DOI: 10.5194/acp-17-2297-2017.

Nah, T., R. C. McVay, X. Zhang, C. M. Boyd, J. H. Seinfeld, and N. L. Ng (2016). "Influence of seed aerosol surface area and oxidation rate on vapor wall deposition and SOA mass yields: a case study with α-pinene ozonolysis". In: *Atmos. Chem. Phys.* 16.14, pp. 9361–9379. DOI: 10.5194/acp-16-9361-2016.

Nguyen, T. B., Kelvin H. Bates, John D. Crounse, Rebecca H. Schwantes, Xuan Zhang, Henrik G. Kjaergaard, Jason D. Surratt, Peng Lin, Alexander Laskin, John H. Seinfeld, and Paul O. Wennberg (2015). "Mechanism of the hydroxyl radical oxidation of methacryloyl peroxynitrate (MPAN) and its pathway toward secondary organic aerosol formation in the atmosphere". In: *Phys. Chem. Chem. Phys.* 17.27, 17914–17926. DOI: 10.1039/C5CP02001H.

Nguyen, T. B., M. M. Coggon, K. H. Bates, X. Zhang, R. H. Schwantes, K. A. Schilling, C. L. Loza, R. C. Flagan, P. O. Wennberg, and J. H. Seinfeld (2014). "Organic aerosol formation from the reactive uptake of isoprene epoxydiols (IEPOX) onto non-acidified inorganic seeds". In: *Atmos. Chem. Phys.* 14.7, pp. 3497–3510. DOI: 10.5194/acp-14-3497-2014.

Nguyen, T. B., Geoffrey S. Tyndall, John D. Crounse, Alexander P. Teng, Kelvin H. Bates, Rebecca H. Schwantes, Matthew M. Coggon, Li Zhang, Philip Feiner, David O. Milller, Kate M. Skog, Jean C. Rivera-Rios, Matthew Dorris, Kevin F. Olson, Abigail Koss, Robert J. Wild, Steven S. Brown, Allen H. Goldstein, Joost A. de Gouw, William H. Brune, Frank N. Keutsch, John H. Seinfeld, and Paul O. Wennberg (2016). "Atmospheric fates of Criegee intermediates in the ozonolysis of isoprene". In: *Phys. Chem. Chem. Phys.* 18 (15), pp. 10241–10254. DOI: 10.1039/C6CP00053C.

Nozière, Barbara (2016). "Don't Forget the Surface". In: *Science* 351.6280, pp. 1396–1397. DOI: 10.1126/science.aaf3253.

Ogata, Akio and R.B. Banks (1961). "A solution of the differential equation of longitudinal dispersion in porous media". In: *U.S. Geol. Surv. Prof. Pap.* 34, 411–A. URL: https://pubs.er.usgs.gov/publication/pp411A.

Orlando, John J. and Geoffrey S. Tyndall (2012). "Laboratory Studies of Organic Peroxy Radical Chemistry: An Overview with Emphasis on Recent Issues of Atmospheric Significance". In: *Chem. Soc. Rev.* 41.19, pp. 6294–6317. DOI: 10.1039/C2CS35166H.

Ortega, A. M., D. A. Day, M. J. Cubison, W. H. Brune, D. Bon, J. A. de Gouw, and J. L. Jimenez (2013). "Secondary organic aerosol formation and primary organic aerosol oxidation from biomass-burning smoke in a flow reactor during FLAME-3". In: *Atmos. Chem. Phys.* 13, pp. 11551–11571. DOI: 10.5194/acp-13-11551-2013.

Ortega, A. M., P. L. Hayes, Z. Peng, B. B. Palm, W. Hu, D. A. Day, R. Li, M. J. Cubison, W. H. Brune, M. Graus, C. Warneke, J. B. Gilman, W. C. Kuster, J. de Gouw, C. Gutiérrez-Montes, and J. L. Jimenez (2016). "Real-time measurements of secondary organic aerosol formation and aging from ambient air in an oxidation

flow reactor in the Los Angeles area". In: *Atmos. Chem. Phys.* 16.11, pp. 7411–7433. DOI: 10.5194/acp-16-7411-2016.

Pagonis, D., Jordan E. Krechmer, J. de Gouw, J. L. Jimenez, and P. J. Ziemann (2017). "Effects of gas-wall partitioning in Teflon tubing and instrumentation on time-resolved measurements of gas-phase organic compounds". In: *Atmos. Meas. Tech.* 10.12, pp. 4687–4696. DOI: 10.5194/amt-10-4687-2017.

Palm, B. B., P. Campuzano-Jost, A. M. Ortega, D. A. Day, L. Kaser, W. Jud, T. Karl, A. Hansel, J. F. Hunter, E. S. Cross, J. H. Kroll, Z. Peng, W. H. Brune, and J. L. Jimenez (2016). "In situ secondary organic aerosol formation from ambient pine forest air using an oxidation flow reactor". In: *Atmos. Chem. Phys.* 16.5, pp. 2943–2970. DOI: 10.5194/acp-16-2943-2016.

Pankow, J. F. and W. E. Asher (2008). "SIMPOL.1: a simple group contribution method for predicting vapor pressures and enthalpies of vaporization of multifunctional organic compounds". In: *Atmos. Chem. Phys.* 8.10, pp. 2773–2796. DOI: 10.5194/acp-8-2773-2008.

Peng, Z., D. A. Day, A. M. Ortega, B. B. Palm, W. Hu, H. Stark, R. Li, K. Tsigaridis, W. H. Brune, and J. L. Jimenez (2016). "Non-OH chemistry in oxidation flow reactors for the study of atmospheric chemistry systematically examined by modeling". In: *Atmos. Chem. Phys.* 16.7, pp. 4283–4305. DOI: 10.5194/acp-16-4283-2016.

Peng, Z., D. A. Day, H. Stark, R. Li, J. Lee-Taylor, B. B. Palm, W. H. Brune, and J. L. Jimenez (2015). "HOx radical chemistry in oxidation flow reactors with low-pressure mercury lamps systematically examined by modeling". In: *Atmos. Meas. Tech.* 8.11, pp. 4863–4890. DOI: 10.5194/amt-8-4863-2015.

Pillar, Elizabeth A. and Marcelo I. Guzman (2017). "Oxidation of Substituted Catechols at the Air-Water Interface: Production of Carboxylic Acids, Quinones, and Polyphenols". In: *Environ. Sci. Technol.* 51.9, pp. 4951–4959. DOI: 10.1021/acs.est.7b00232.

Pope III, C. Arden, Richard T. Burnett, Michael J. Thun, Eugenia E. Calle, Daniel Krewski, Kazuhiko Ito, and George D. Thurston (2002). "Lung Cancer, Cardiopulmonary Mortality, and Long-term Exposure to Fine Particulate Air Pollution". In: *JAMA* 287.9, pp. 1132–1141. DOI: 10.1001/jama.287.9.1132.

Pöschl, U., Y. Rudich, and M. Ammann (2007). "Kinetic model framework for aerosol and cloud surface chemistry and gas-particle interactions - Part 1: General equations, parameters, and terminology". In: *Atmos. Chem. Phys.* 7.23, pp. 5989–6023. DOI: 10.5194/acp-7-5989-2007.

Prakash, R., D. Christopher, and K. Kumarrathinam (2014). "CFD analysis of flow through a conical exhaust diffuser". In: *Int. J. Res. Eng. Technol.* 3.11, pp. 239–248. DOI: 10.15623/ijret.2014.0323052.

Praske, Eric, John D. Crounse, Kelvin H. Bates, Theo Kurtén, Henrik G. Kjaergaard, and Paul O. Wennberg (2015). "Atmospheric fate of methyl vinyl ketone: Peroxy radical reactions with NO and HO2". In: *J. Phys. Chem. A* 119.19, pp. 4562–4572. DOI: 10.1021/jp5107058.

Praske, Eric, Rasmus V. Otkjær, John D. Crounse, J. Caleb Hethcox, Brian M. Stoltz, Henrik G. Kjaergaard, and Paul O. Wennberg (2018). "Atmospheric Autoxidation is Increasingly Important in Urban and Suburban North America". In: *Proc. Natl. Acad. Sci. U. S. A.* 115.1, pp. 64–69. DOI: 10.1073/pnas.1715540115.

Rossignol, Stéphanie, Liselotte Tinel, Angelica Bianco, Monica Passananti, Marcello Brigante, D. James Donaldson, and Christian George (2016). "Atmospheric Photochemistry at a Fatty Acid-Coated Air-Water Interface". In: *Science* 353.6300, pp. 699–702. DOI: 10.1126/science.aaf3617.

Roth, Christine M., Kai-Uwe Goss, and René P. Schwarzenbach (2002). "Adsorption of a Diverse Set of Organic Vapors on the Bulk Water Surface". In: *J. Colloid Interface Sci.* 252.1, pp. 21–30. DOI: 10.1006/jcis.2002.8446.

Ruehl, Christopher R., James F. Davies, and Kevin R. Wilson (2016). "An Interfacial Mechanism for Cloud Droplet Formation on Organic Aerosols". In: *Science* 351.6280, pp. 1447–1450. DOI: 10.1126/science.aad4889.

Russell, Glen A. (1957). "Deuterium-Isotope Effects in the Autoxidation of Aralkyl Hydrocarbons. Mechanism of the Interaction of Peroxy Radicals". In: *J. Am. Chem. Soc.* 79.14, pp. 3871–3877. DOI: 10.1021/ja01571a068.

Schilling Fahnestock, Katherine A., Lindsay D. Yee, Christine L. Loza, Matthew M. Coggon, Rebecca Schwantes, Xuan Zhang, Nathan F. Dalleska, and John H. Seinfeld (2015). "Secondary Organic Aerosol Composition from C12 Alkanes". In: *The Journal of Physical Chemistry A* 119.19, pp. 4281–4297. DOI: 10.1021/jp501779w.

Schwantes, R. H., Renee C. McVay, Xuan Zhang, Matthew M. Coggon, Hanna Lignell, Richard C. Flagan, Paul O. Wennberg, and John H. Seinfeld (2017a). "Science of the Environmental Chamber". In: *Advances in Atmospheric Chemistry*. World Scientific. Chap. 1 Science of the Environmental Chamber, pp. 1–93. DOI: 10.1142/9789813147355_0001.

Schwantes, R. H., K. A. Schilling, R. C. McVay, H. Lignell, M. M. Coggon, X. Zhang, P. O. Wennberg, and J. H. Seinfeld (2017b). "Formation of highly oxygenated low-volatility products from cresol oxidation". In: *Atmos. Chem. Phys.* 17.5, pp. 3453–3474. DOI: 10.5194/acp-17-3453-2017.

Schwantes, R. H., Alexander P. Teng, Tran B. Nguyen, Matthew M. Coggon, John D. Crounse, Jason M. St. Clair, Xuan Zhang, Katherine A. Schilling, John H. Seinfeld, and Paul O. Wennberg (2015). "Isoprene NO_3 oxidation products from the RO_2 + HO_2 pathway". In: *J. Phys. Chem. A* 119.40, pp. 10158–10171. DOI: 10.1021/acs.jpca.5b06355.

Schwantes, Rebecca H., Alexander P. Teng, Tran B. Nguyen, Matthew M. Coggon, John D. Crounse, Jason M. St Clair, Xuan Zhang, Katherine A. Schilling, John H. Seinfeld, and Paul O. Wennberg (2015). "Isoprene NO_3 Oxidation Products from the RO_2 + HO_2 Pathway". In: *J. Phys. Chem. A* 119.40, 10158–10171. DOI: 10.1021/acs.jpca.5b06355.

Schwarzenbach, Rene P., Philip M. Gschwend, and Dieter M. Imboden (2005). *Environmental Organic Chemistry*. 2nd. Hoboken, New Jersey: John Wiley & Sons, Inc. DOI: 10.1002/0471649643.

Sebastiani, F., R. A. Campbell, K. Rastogi, and C. Pfrang (2018). "Nighttime Oxidation of Surfactants at the Air-Water Interface: Effects of Chain Length, Head Group and Saturation". In: *Atmos. Chem. Phys.* 18.5, pp. 3249–3268. DOI: 10.5194/acp-18-3249-2018.

Seinfeld, J. H. and S. N. Pandis (2016). *Atmospheric Chemistry and Physics: From Air Pollution to Climate Change*. 3rd ed. Wiley Sons.

Seinfeld, John H. and James F. Pankow (2003). "Organic atmospheric particulate material". In: *Annu. Rev. Phys. Chem.* 54.1, pp. 121–140. DOI: 10.1146/annurev.physchem.54.011002.103756.

Sellier, M., J. W. Grayson, L. Renbaum-Wolff, M. Song, and A. K. Bertram (2015). "Estimating the viscosity of a highly viscous liquid droplet through the relaxation time of a dry spot". In: *J. Rheol.* 59.3, pp. 733–750. DOI: 10.1122/1.4917240.

Seltsam, M. M. (1995). "Experimental and theoretical study of wide-angle diffuser flow with screens". In: *AIAA J.* 33.11, pp. 2092–2100. DOI: 10.2514/3.12952.

Shiraiwa, M., C. Pfrang, T. Koop, and U. Pöschl (2012). "Kinetic multi-layer model of gas-particle interactions in aerosols and clouds (KM-GAP): linking condensation, evaporation and chemical reactions of organics, oxidants and water". In: *Atmos. Chem. Phys.* 12.5, pp. 2777–2794. DOI: 10.5194/acp-12-2777-2012.

Shiraiwa, Manabu, Markus Ammann, Thomas Koop, and Ulrich Pöschl (2011). "Gas uptake and chemical aging of semisolid organic aerosol particles". In: *Proc. Natl. Acad. Sci. U. S. A.* 108.27, pp. 11003–11008. DOI: 10.1073/pnas.1103045108.

Shiraiwa, Manabu, Lindsay D. Yee, Katherine A. Schilling, Christine L. Loza, Jill S. Craven, Andreas Zuend, Paul J. Ziemann, and John H. Seinfeld (2013). "Size distribution dynamics reveal particle-phase chemistry in organic aerosol formation". In: *Proc. Natl. Acad. Sci. U. S. A.* 110.29, pp. 11746–11750. DOI: 10.1073/pnas.1307501110.

Siegwarth, D. P., R. D. Mikesell, T. C. Readal, and T. J. Hanratty (1969). "Effect of secondary flow on the temperature field and primary flow in a heated horizontal tube". In: *Int. J. Heat Mass Tran.* 12.12, pp. 1535–1552. DOI: 10.1016/0017-9310(69)90090-8.

Simonen, P., E. Saukko, P. Karjalainen, H. Timonen, M. Bloss, P. Aakko-Saksa, T. Rönkkö, J. Keskinen, and M. Dal Maso (2017). "A new oxidation flow reactor for measuring secondary aerosol formation of rapidly changing emission sources". In: *Atmos. Meas. Tech.* 10.4, pp. 1519–1537. DOI: 10.5194/amt-10-1519-2017.

Slowik, J. G., J. P. S. Wong, and J. P. D. Abbatt (2012). "Real-time, controlled OH-initiated oxidation of biogenic secondary organic aerosol". In: *Atmos. Chem. Phys.* 12.20, pp. 9775–9790. DOI: 10.5194/acp-12-9775-2012.

Smith, J. D., J. H. Kroll, C. D. Cappa, D. L. Che, C. L. Liu, M. Ahmed, S. R. Leone, D. R. Worsnop, and K. R. Wilson (2009). "The heterogeneous reaction of hydroxyl radicals with sub-micron squalane particles: a model system for understanding the oxidative aging of ambient aerosols". In: *Atmos. Chem. Phys.* 9.9, pp. 3209–3222. DOI: 10.5194/acp-9-3209-2009.

Socorro, Joanna, Pascale S. J. Lakey, Lei Han, Thomas Berkemeier, Gerhard Lammel, Cornelius Zetzsch, Ulrich Pöschl, and Manabu Shiraiwa (2017). "Heterogeneous OH Oxidation, Shielding Effects, and Implications for the Atmospheric Fate of Terbuthylazine and Other Pesticides". In: *Environ. Sci. Technol.* 51.23, pp. 13749–13754. DOI: 10.1021/acs.est.7b04307.

Sonntag, Clemens von and Heinz-Peter Schuchmann (1991). "The Elucidation of Peroxyl Radical Reactions in Aqueous Solution with the Help of Radiation-Chemical Methods". In: *Angew. Chem. Int. Ed.* 30.10, pp. 1229–1253. DOI: 10.1002/anie.199112291.

Sparrow, E. M., J. P. Abraham, and W. J. Minkowycz (2009). "Flow Separation in a diverging conical duct: Effect of Reynolds number and divergence angle". In: *Int. J. Heat Mass Tran.* 52, pp. 3079–3083. DOI: 10.1016/j.ijheatmasstransfer.2009.02.010.

St. Clair, Jason M., David C. McCabe, John D. Crounse, Urs Steiner, and Paul O. Wennberg (2010). "Chemical ionization tandem mass spectrometer for the in situ measurement of methyl hydrogen peroxide". In: *Rev. Sci. Instrum.* 81.9, p. 094102. DOI: 10.1063/1.3480552.

St. Clair, Jason M., Jean C. Rivera-Rios, John D. Crounse, Hasse C. Knap, Kelvin H. Bates, Alex P. Teng, Solvejg Jørgensen, Henrik G. Kjaergaard, Frank N. Keutsch, and Paul O. Wennberg (2016). "Kinetics and products of the reaction of the first-generation isoprene hydroxy hydroperoxide (ISOPOOH) with OH". In: *J. Phys. Chem. A* 120.9, pp. 1441–1451. DOI: 10.1021/acs.jpca.5b06532.

Svishchev, Igor M. and Andriy Y. Plugatyr (2005). "Hydroxyl Radical in Aqueous Solution: Computer Simulation". In: *J. Phys. Chem. B* 109.9, pp. 4123–4128. DOI: 10.1021/jp046273o.

Tan, Anmin, André Ziegler, Bernhard Steinbauer, and Joachim Seelig (2002). "Thermodynamics of Sodium Dodecyl Sulfate Partitioning into Lipid Membranes". In: *Biophys. J.* 83.3, pp. 1547–1556. DOI: 10.1016/S0006-3495(02)73924-6.

Tan, Yi, Mark J. Perri, Sybil P. Seitzinger, and Barbara J. Turpin (2009). "Effects of Precursor Concentration and Acidic Sulfate in Aqueous Glyoxal-OH Radical Oxidation and Implications for Secondary Organic Aerosol". In: *Environ. Sci. Technol.* 43.21, pp. 8105–8112. DOI: 10.1021/es901742f.

Tavoularis, S (2005). *Measurement in Fluid Mechanics*. Cambridge University Press.

Taylor, Geoffrey Ingram (1953). "Dispersion of soluble matter in solvent flowing slowly through a tube". In: *Proc. R. Soc. Lond. A* 219.1137, pp. 186–203. DOI: 10.1098/rspa.1953.0139.

Taylor, W. D., T. D. Allston, M. J. Moscato, G. B. Fazekas, R. Kozlowski, and G. A. Takacs (1980). "Atmospheric photodissociation lifetimes for nitromethane, methyl nitrite, and methyl nitrate". In: *Int. J. of Chem. Kinet.* 12.4, pp. 231–240. DOI: 10.1002/kin.550120404.

Teng, Alexander P., John D. Crounse, and Paul O. Wennberg (2017). "Isoprene peroxy radical dynamics". In: *J. Am. Chem. Soc.* 139.15, pp. 5367–5377. DOI: 10.1021/jacs.6b12838.

Thomas, Daniel A., Matthew M. Coggon, Hanna Lignell, Katherine A. Schilling, Xuan Zhang, Rebecca H. Schwantes, Richard C. Flagan, John H. Seinfeld, and J. L. Beauchamp (2016). "Real-Time Studies of Iron Oxalate-Mediated Oxidation of Glycolaldehyde as a Model for Photochemical Aging of Aqueous Tropospheric Aerosols". In: *Environ. Sci. Technol.* 50.22, pp. 12241–12249. DOI: 10.1021/acs.est.6b03588.

Thornton, Joel and J. P. D. Abbatt (2005). "Measurements of HO_2 uptake to aqueous aerosol: Mass accommodation coefficients and net reactive loss". In: *J. Geophys. Res.: Atmos.* 110.D8. D08309. DOI: 10.1029/2004JD005402.

Tinel, Liselotte, Stéphanie Rossignol, Angelica Bianco, Monica Passananti, Sébastien Perrier, Xinming Wang, Marcello Brigante, D. James Donaldson, and Christian George (2016). "Mechanistic Insights on the Photosensitized Chemistry of a Fatty Acid at the Air/Water Interface". In: *Environ. Sci. Technol.* 50.20, pp. 11041–11048. DOI: 10.1021/acs.est.6b03165.

Tkacik, Daniel S., Andrew T. Lambe, Shantanu Jathar, Xiang Li, Albert A. Presto, Yunliang Zhao, Donald Blake, Simone Meinardi, John T. Jayne, Philip L. Croteau, and Allen L. Robinson (2014). "Secondary Organic Aerosol Formation from in-Use Motor Vehicle Emissions Using a Potential Aerosol Mass Reactor". In: *Environ. Sci. Technol.* 48.19, pp. 11235–11242. DOI: 10.1021/es502239v.

Tokarev, A., K. Friess, J. Machkova, M. Šipek, and Yu. Yampolskii (2006). "Sorption and diffusion of organic vapors in amorphous Teflon AF2400". In: *J. Polym. Sci. Pol. Phys.* 44.5, pp. 832–844. DOI: 10.1002/polb.20725.

Tropo (2014). *Vapour pressure of Pure Liquid Organic Compounds*. URL: http://tropo.aeronomie.be/models/evaporation_run.htm (visited on 06/11/2014).

Trump, Erica R., Scott A. Epstein, Ilona Riipinen, and Neil M. Donahue (2016). "Wall effects in smog chamber experiments: A model study". In: *Aerosol Sci. Technol.* 50.11, pp. 1180–1200. DOI: 10.1080/02786826.2016.1232858.

Vácha, Robert, Petr Slavíček, Martin Mucha, Barbara J. Finlayson-Pitts, and Pavel Jungwirth (2004). "Adsorption of Atmospherically Relevant Gases at the Air/Water Interface: Free Energy Profiles of Aqueous Solvation of N_2, O_2, O_3, OH, H_2O, HO_2, and H_2O_2". In: *J. Phys. Chem. A* 108.52, pp. 11573–11579. DOI: 10.1021/jp046268k.

Vereecken, Luc and Jozef Peeters (2002). "Enhanced H-Atom Abstraction from Pinonaldehyde, Pinonic Acid, Pinic Acid, and Related Compounds: Theoretical Study of C-H Bond Strengths". In: *Phys. Chem. Chem. Phys.* 4.3, pp. 467–472. DOI: 10.1039/B109370C.

Vestenius, M., H. Hellén, J. Levula, P. Kuronen, K. J. Helminen, T. Nieminen, M. Kulmala, and H. Hakola (2014). "Acidic Reaction Products of Monoterpenes and Sesquiterpenes in Atmospheric Fine Particles in a Boreal Forest". In: *Atmos. Chem. Phys.* 14.15, pp. 7883–7893. DOI: 10.5194/acp-14-7883-2014.

Vieth, W.R., J.M. Howell, and J.H. Hsieh (1976). "Dual sorption theory". In: *J. Membr. Sci.* 1, pp. 177–220. DOI: 10.1016/S0376-7388(00)82267-X.

Wang, Chen, Kai-Uwe Goss, Ying Duan Lei, J. P. D. Abbatt, and Frank Wania (2015). "Calculating Equilibrium Phase Distribution during the Formation of Secondary Organic Aerosol Using COSMOtherm". In: *Environ. Sci. Technol.* 49.14, pp. 8585–8594. DOI: 10.1021/acs.est.5b01584.

Wellen, Bethany A., Evan A. Lach, and Heather C. Allen (2017). "Surface pK_a of Octanoic, Nonanoic, and Decanoic Fatty Acids at the Air-Water Interface: Applications to Atmospheric Aerosol Chemistry". In: *Phys. Chem. Chem. Phys.* 19.39, pp. 26551–26558. DOI: 10.1039/C7CP04527A.

White, F M (2008). *Fluid Mechanics*. McGraw-Hill, New York.

Witkowski, Bartłomiej and Tomasz Gierczak (2017). "*cis*-Pinonic Acid Oxidation by Hydroxyl Radicals in the Aqueous Phase under Acidic and Basic Conditions: Kinetics and Mechanism". In: *Environ. Sci. Technol.* 51.17, pp. 9765–9773. DOI: 10.1021/acs.est.7b02427.

Wolf, David and Don H. White (1976). "Experimental study of the residence time distribution in plasticating screw extruders". In: *AIChE J.* 22.1, pp. 122–131. DOI: 10.1002/aic.690220115.

Wren, Sumi N., Brittany P. Gordon, Nicholas A. Valley, Laura E. McWilliams, and Geraldine L. Richmond (2015). "Hydration, Orientation, and Conformation of Methylglyoxal at the Air-Water Interface". In: *J. Phys. Chem. A* 119.24, pp. 6391–6403. DOI: 10.1021/acs.jpca.5b03555.

Xiao, Pin, Qian Wang, Wei-Hai Fang, and Ganglong Cui (2017). "Quantum Chemical Investigation on Photochemical Reactions of Nonanoic Acids at Air-Water Interface". In: *J. Phys. Chem. A* 121.22, pp. 4253–4262. DOI: 10.1021/acs.jpca.7b03123.

Yasmeen, F., R. Vermeylen, R. Szmigielski, Y. Iinuma, O. Böge, H. Herrmann, W. Maenhaut, and M. Claeys (2010). "Terpenylic Acid and Related Compounds: Precursors for Dimers in Secondary Organic Aerosol from the Ozonolysis of α- and β-Pinene". In: *Atmos. Chem. Phys.* 10.19, pp. 9383–9392. DOI: 10.5194/acp-10-9383-2010.

Ye, Penglin, Xiang Ding, Jani Hakala, Victoria Hofbauer, Ellis S. Robinson, and Neil M. Donahue (2016). "Vapor wall loss of semi-volatile organic compounds in a Teflon chamber". In: *Aerosol Sci. Technol.* 50.8, pp. 822–834. DOI: 10.1080/02786826.2016.1195905.

Yee, L. D., J. S. Craven, C. L. Loza, K. A. Schilling, N. L. Ng, M. R. Canagaratna, P. J. Ziemann, R. C. Flagan, and J. H. Seinfeld (2013). "Effect of chemical structure on secondary organic aerosol formation from C-12 alkanes". In: *Atmos. Chem. Phys.* 13.21, 11121–11140. DOI: 10.5194/acp-13-11121-2013.

Yeh, Geoffrey K. and Paul J. Ziemann (2014). "Alkyl nitrate formation from the reactions of C8-C14 n-alkanes with OH radicals in the presence of NOx: Measured yields with essential corrections for gas-wall partitioning". In: *J. Phys. Chem. A* 118.37, pp. 8147–8157. DOI: 10.1021/jp500631v.

– (2015). "Gas-wall partitioning of oxygenated organic compounds: Measurements, structure-activity relationships, and correlation with gas chromatographic retention factor". In: *Aerosol Sci. Technol.* 49.9, pp. 727–738. DOI: 10.1080/02786826.2015.1068427.

Zhang, X., Kevin M. Barraza, and J. L. Beauchamp (2018). "Cholesterol Provides Nonsacrificial Protection of Membrane Lipids from Chemical Damage at Air-Water Interface". In: *Proc. Natl. Acad. Sci. U. S. A.* 115.13, pp. 3255–3260. DOI: 10.1073/pnas.1722323115.

Zhang, X., Kevin M. Barraza, Kathleen T. Upton, and J. L. Beauchamp (2017). "Time Resolved Study of Hydroxyl Radical Oxidation of Oleic Acid at the Air-Water Interface". In: *Chem. Phys. Lett.* 683, pp. 76–82. DOI: 10.1016/j.cplett.2017.05.051.

Zhang, Xuan, Christopher D. Cappa, Shantanu H. Jathar, Renee C. McVay, Joseph J. Ensberg, Michael J. Kleeman, and John H. Seinfeld (2014). "Influence of vapor wall loss in laboratory chambers on yields of secondary organic aerosol". In: *Proc. Natl. Acad. Sci. U. S. A.* 111.16, pp. 5802–5807. DOI: 10.1073/pnas.1404727111.

Zhang, Xuan, Renee C. McVay, Dan D. Huang, Nathan F. Dalleska, Bernard Aumont, Richard C. Flagan, and John H. Seinfeld (2015). "Formation and evolution

of molecular products in α-pinene secondary organic aerosol". In: *Proc. Natl. Acad. Sci. U. S. A.* 112.46, 14168–14173. DOI: 10.1073/pnas.1517742112.

Zhang, Xuan, R. H. Schwantes, R. C. McVay, H. Lignell, M. M. Coggon, R. C. Flagan, and J. H. Seinfeld (2015). "Vapor wall deposition in Teflon chambers". In: *Atmos. Chem. Phys.* 15.8, pp. 4197–4214. DOI: 10.5194/acp-15-4197-2015.

Zhang, Y., M. S. Sanchez, C. Douet, Y. Wang, A. P. Bateman, Z. Gong, M. Kuwata, L. Renbaum-Wolff, B. B. Sato, P. F. Liu, A. K. Bertram, F. M. Geiger, and S. T. Martin (2015). "Changing shapes and implied viscosities of suspended submicron particles". In: *Atmos. Chem. Phys.* 15.14, pp. 7819–7829. DOI: 10.5194/acp-15-7819-2015.

Zhong, Jie, Manoj Kumar, Joseph S. Francisco, and Xiao Cheng Zeng (2018). "Insight into Chemistry on Cloud/Aerosol Water Surfaces". In: *Acc. Chem. Res.* 51.5, pp. 1229–1237. DOI: 10.1021/acs.accounts.8b00051.

Appendix A

IODOMETRY-ASSISTED LIQUID CHROMATOGRAPHY ELECTROSPRAY IONIZATION MASS SPECTROMETRY FOR ANALYSIS OF ORGANIC PEROXIDES: AN APPLICATION TO ATMOSPHERIC SECONDARY ORGANIC AEROSOL

Zhao, Ran, Christopher M. Kenseth, Yuanlong Huang, Nathan F. Dalleska, and John H. Seinfeld (2018). "Iodometry-Assisted Liquid Chromatography Electrospray Ionization Mass Spectrometry for Analysis of Organic Peroxides: An Application to Atmospheric Secondary Organic Aerosol". In: *Environ. Sci. Technol.* 52.4, pp. 2108–2117. DOI: 10.1021/acs.est.7b04863.

Environmental Science & Technology

Article

Cite This: Environ. Sci. Technol. 2018, 52, 2108−2117

pubs.acs.org/est

Iodometry-Assisted Liquid Chromatography Electrospray Ionization Mass Spectrometry for Analysis of Organic Peroxides: An Application to Atmospheric Secondary Organic Aerosol

Ran Zhao,*[,†] Christopher M. Kenseth,[†] Yuanlong Huang,[‡] Nathan F. Dalleska,[§] and John H. Seinfeld[†,∥]

[†]Division of Chemistry and Chemical Engineering, California Institute of Technology, Pasadena, California 91125, United States
[‡]Division of Geological and Planetary Sciences, California Institute of Technology, Pasadena, California 91125, United States
[§]Environmental Analysis Center, California Institute of Technology, Pasadena, California 91125, United States
[∥]Division of Engineering and Applied Science, California Institute of Technology, Pasadena, California 91125, United States

Supporting Information

ABSTRACT: Organic peroxides comprise a significant fraction of atmospheric secondary organic aerosol (SOA). Detection and quantification of particle-phase organic peroxides are highly challenging, and current efforts rely significantly on filter extraction and offline mass spectrometry (MS). Here, a novel technique, iodometry-assisted liquid chromatography electrospray ionization mass spectrometry (iodometry-assisted LC-ESI-MS), is developed and evaluated with a class of atmospherically relevant organic peroxides, α-acyloxyalkyl hydroperoxides, synthesized via liquid ozonolysis. Iodometry-assisted LC-ESI-MS unambiguously distinguishes organic peroxides, compensating for the lack of functional group information that can be obtained with MS. This technique can be versatile for a wide spectrum of environmental analytical applications for which a molecular-level identification of organic peroxide is required. Here, iodometry-assisted LC-ESI-MS is applied to the water-soluble organic carbon (WSOC) of α-pinene SOA. Unexpectedly, a limited number of detectable compounds in WSOC appear to be organic peroxides, despite the fact that spectroscopy-based iodometry indicates 15% of WSOC mass is associated with organic peroxides. This observation would be consistent with decomposition of multifunctional organic peroxides to small peroxides that can be quantified by spectroscopy-based iodometry but not by LC-ESI-MS. Overall, this study raises concerns regarding filter extraction-based studies, showing that assignment of organic peroxides solely on the basis of MS signatures can be misleading.

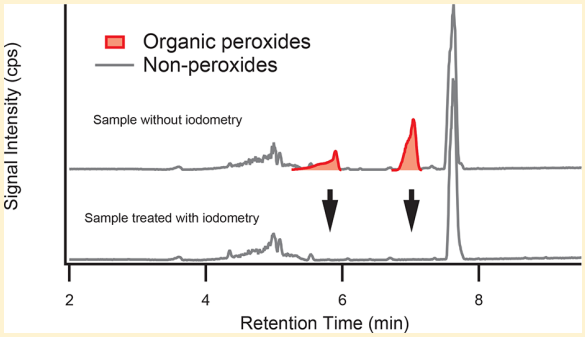

INTRODUCTION

Organic peroxides are ubiquitous in the atmospheric environment, participating in the oxidation of SO_2 to form acid rain,[1] serving as a reservoir for atmospheric oxidants,[2] and potentially contributing to the adverse health effects of air pollution.[3] Recent studies have revealed a critical role that organic peroxides play in the formation of secondary organic aerosol (SOA), submicrometer particulate matter that forms in the atmosphere via condensation of oxidation products of volatile organic compounds (VOCs).[4] Despite the prominent role that SOA plays in air quality and the global climate, our understanding of the reaction mechanisms and products of VOC oxidation remains incomplete. In particular, the identity and chemistry of organic peroxides represent important missing aspects.

On a global scale, biogenic monoterpenes ($C_{10}H_{16}$) are important precursors to SOA. Estimated global SOA production from mono- and sesquiterpenes varies from 14 to 246 Tg/year.[5,6] α-Pinene is the dominant monoterpene by mass[7] and is readily oxidized in the atmosphere by the major oxidants, O_3 and the OH radical. It has been established that SOA arising from α-pinene contains a substantial amount of total organic peroxides.[8,9] Quantification of organic peroxides in SOA extracts has been successful using spectroscopic techniques, such as iodometry.[8,10−12] Iodometry proceeds as $R_1OOR_2 + 2I^- + 2H^+ \rightarrow R_1OH + R_2OH + I_2$, followed by $I_2 + I^- \rightarrow I_3^-$,[13] where R_1 and R_2 represent any alkyl group or H. With acid catalysis, I^- reduces an organic peroxide molecule to the corresponding alcohols, liberating I_2 that subsequently forms I_3^- in an excess of I^-. The characteristic absorption of I_3^- reaches a peak at 350 nm and can be measured by ultraviolet−

Received: September 20, 2017
Revised: January 10, 2018
Accepted: January 25, 2018
Published: January 25, 2018

DOI: 10.1021/acs.est.7b04863
Environ. Sci. Technol. 2018, 52, 2108−2117

visible (UV−vis) spectrometry. As I^- reacts with essentially all types of organic peroxides,[14] iodometry determines the total organic peroxide content. Molecular-level identification of particle-phase organic peroxides is more challenging, because of the chemical complexity of SOA components, a lack of authentic organic peroxide chemical standards, and their chemical instability. A number of recent studies have reported decomposition of SOA organic peroxides in the particle phase[12,15] and the aqueous phase.[16]

Recent application of liquid chromatography electrospray ionization mass spectrometry (LC-ESI-MS) to extracted SOA components has significantly advanced our understanding of particle-phase organic compounds, including both monomers and dimers,[17−29] a number of which have been proposed to be organic peroxides. In particular, it is proposed that the stabilized Criegee intermediate (SCI) formed during ozonolysis can react with organic acids and form a class of hydroperoxy dimer esters, α-acyloxyalkyl hydroperoxides (αAAHPs).[15,17,18,30,31] The importance of α-AAHPs in the ambient atmosphere remains unclear, but a ≤16% contribution by mass to laboratory-generated SOA has been reported.[17] Additionally, gas-phase measurements using chemical ionization mass spectrometry have detected highly oxidized multifunctional organic compounds (HOMs), which bear multiple hydroperoxy functional groups and arise from repeated intramolecular hydrogen-abstraction reactions.[32,33] HOMs exhibit extremely low volatility, and their presence in the particle phase has been reported.[34−37] These studies have highlighted novel SOA formation pathways in which organic peroxides play a pivotal role. Determination of such organic peroxides at the molecular level is critical and is the only means of revealing the underlying mechanisms of formation of SOA.

Although ESI-MS is a versatile technique for a wide spectrum of organic compounds,[38,39] unambiguous identification of organic peroxides using MS-based techniques is challenging, given that MS provides limited information about functional groups. A number of studies have used ESI-MS to detect synthesized organic peroxides, including peracids,[40,41] alkylhydroperoxides,[42] peroxy esters,[29] diacyl peroxides,[43] and αAAHPs.[44] Despite the capability of ESI-MS for organic peroxide detection, detection of organic peroxide is highly sensitive to specific conditions employed in each ESI-MS instrument.

The primary objective of this study is to develop and demonstrate the applicability of a novel technique, iodometry-assisted LC-ESI-MS, to unambiguously distinguish organic peroxides present in a complex chemical matrix. The method is evaluated with αAAHPs synthesized via liquid-phase ozonolysis. For the first time, iodometry is employed not only to determine the total peroxide content but also to provide molecularly resolved information by coupling to LC-ESI-MS. We have applied iodometry-assisted LC-ESI-MS to investigate organic peroxides present in the water-soluble fraction of α-pinene SOA. Measurements of water-soluble organic carbon (WSOC) in SOA can be performed using filter extraction and/or the particle-into-liquid sampler (PILS).[45] WSOC has gained attention as a proxy for the oxygenated fraction of SOA[46] that can dissolve in cloudwater and undergo multiphase chemistry.[47−49]

EXPERIMENTAL SECTION

Chemicals. All chemicals were used without further purification. The following chemicals were purchased from Sigma-Aldrich: adipic acid (99%), α-pinene (>99%), benzoyl-peroxide (Luperox, 75%), *cis*-pinonic acid (98%), D-sorbitol (>98%), hydrogen peroxide (H_2O_2, 50% in water), lauroyl peroxide (Luperox, 97%), leucine enkephalin [>95%, high-performance liquid chromatography (HPLC) grade], *meso*-erythritol (>99%), pinic acid (custom-synthesized), potassium hydrogen phthalate (>99.95%), potassium iodide (KI, 99%), and *tert*-butyl hydroperoxide (Luperox, 50% in water). Chemicals were also purcahsed from other sources: acetonitrile (EMD), ammonium sulfate [$(NH_4)_2SO_4$, Mallinckrodt Chemicals], formic acid (Fluka, HPLC grade, 50% in water), glacial acetic acid (Macron Fine Chemicals), and methylhydroperoxide (synthesized).

SOA Generation and Collection. SOA was generated in the steady state Caltech photooxidation flow tube (CPOT) reactor,[50] details of which are given in section S1 of the Supporting Information. Briefly, α-pinene (175 ppb) and O_3 (1 ppm) reacted in the CPOT to generate SOA at room temperature without light or nitrogen oxides. No OH scavenger was added; therefore, α-pinene is oxidized primarily by O_3 with a contribution from the OH radical generated during ozonolysis. The total rate of gas flow through the CPOT was 12.5 L/min, giving rise to an average residence time of 3.5 min. Polydisperse $(NH_4)_2SO_4$ seed aerosol was generated by aerosolizing an aqueous solution (0.01 M) with a custom-built atomizer, followed by using a diffuser dryer and a neutralizer. The relative humidity (RH) in the CPOT was approximately 10%.

Approximately 10 L/min of flow from the CPOT was introduced through a Teflon filter (Pall Life Sciences, 47 mm diameter and 2 μm pore size) to collect SOA samples. A diffuser packed with activated charcoal was employed before the filter to remove O_3 and gas-phase species to prevent continuous on-filter reactions and further partitioning of gas-phase species to the collected particles. One filter sample was collected per experiment, with collection times of 15−18 h. The mass of collected particle samples was typically 1−2 mg. Filters were frozen at −16 °C immediately after collection. Note that we employed collection times longer than those in previous studies (0.6−4 h)[8,11,51,52] to overcome the detection limits of offline analyses and to maximize detection of compounds by LC-ESI-MS.

Synthesis of α-Acyloxyalkyl Hydroperoxides (αAAHPs). Two αAAHP species were synthesized as surrogates for multifunctional organic peroxides.[17,30,31] They were synthesized via liquid-phase ozonolysis with a method modified from a previous study.[44] Briefly, α-pinene (50 mM) and an organic acid (10 mM) were dissolved in acetonitrile. A 5 mL aliquot of this solution was bubbled with an air stream containing roughly 100 ppm of O_3 at a flow rate of 120 sccm for 5 min. The ozonolysis solution was immersed in an ice bath throughout the synthesis and storage to minimize decomposition.

The proposed pathway for formation of αAAHPs, as well as their structures, is shown in Figure 1. Briefly, α-pinene reacts with O_3 to form a primary ozonide that decomposes to form two possible Criegee intermediates. Upon interaction with the surrounding solvent molecules, stabilized Criegee intermediates (SCIs) are formed. The SCI reacts with the excess of the organic acid added to the solution, forming an αAAHP species with two possible structural isomers. Two organic acids, pinonic acid and adipic acid, were chosen in this work to synthesize two different αAAHPs. Pinonic acid was selected for

DOI: 10.1021/acs.est.7b04863
Environ. Sci. Technol. 2018, 52, 2108−2117

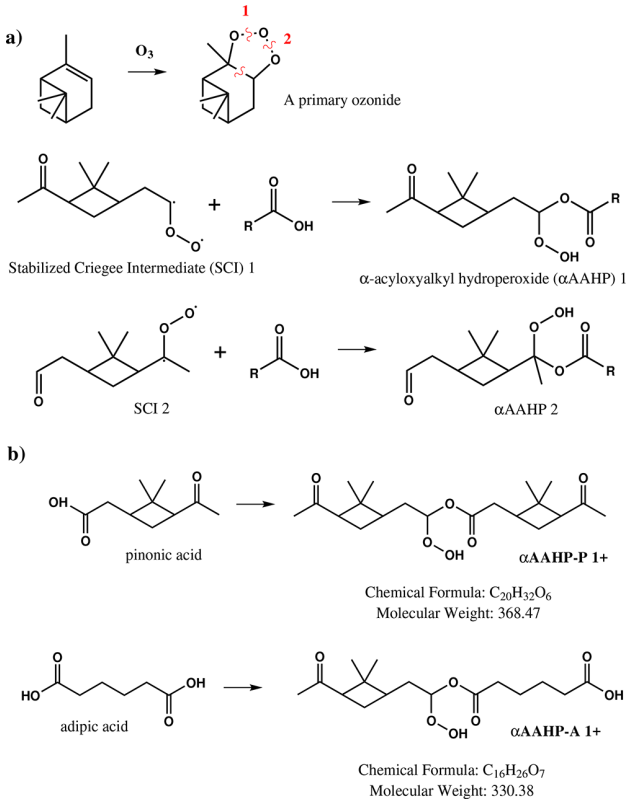

Figure 1. Schematic of the mechanism underlying the synthesis of the αAAHP species. Reactions in panel (a) illustrate the general reaction between a stabilized Criegee intermediate (SCI) and an organic acid, giving rise to αAAHP with two possible structural isomers. Reactions in panel (b) show the specific cases employed in this work to synthesize αAAHP-P and αAAHP-A. Only one structural isomer is shown for each of them.

its relevance in α-pinene oxidation. Adipic acid, being a diacid, contains an additional carboxylic acid functional group for which αAAHP-A is more easily detected by ESI^--MS. These two species are hereafter termed αAAHP-P and αAAHP-A, respectively.

Offline Chemical Analyses. The frozen filter samples were thawed and extracted in 10 mL of Milli-Q water (18.2 mΩ) by being mechanically shaken before in-depth chemical analyses were performed. Sonication was avoided to prevent potential artifacts.[10]

Total Organic Carbon (TOC). The total organic carbon (TOC) content of the SOA extracts was quantified using a TOC analyzer (OI Analytical model 1030W). The total carbon (TC) method was employed, wherein all the carbon-containing species (i.e., both organic and inorganic) are oxidized to CO_2 by sodium persulfate with phosphoric acid at 100 °C, with the CO_2 detected by nondispersive infrared detection. The TC content measured in a blank filter extract was subtracted as the background. The limit of detection is 0.6 ppm of C, determined as 3σ + the mean of the filter blank. The method was calibrated using potassium hydrogen phthalate, and the accuracy of the method was 5%, tested by measuring *meso*-erythritol and D-sorbitol solutions at known concentrations.

Iodometry. Formic acid or acetic acid was added to an aliquot of a WSOC sample to adjust the solution pH to 2 or 3, respectively. To this solution was added a concentrated potassium iodide (KI) aqueous solution, made fresh daily and purged with N_2 gas, such that the concentration of I^- in the solution was 60 mM. Immediately after the addition of KI, the solution was gently purged with N_2 and placed in an airtight vial in the dark for 1 h before the UV−vis measurement was conducted with a spectrophotometer (Shimadzu, UV-1601). The method was calibrated prior to each experiment against a set of H_2O_2 solutions, standardized with the molar absorptivity of H_2O_2 at 254 nm. The calibration accounts for the reaction of I^- with dissolved O_2 and confirms the linearity of the method. The detection limit of the current method is 1.5 μM H_2O_2 equivalent, determined as 3σ of the water blank.

Iodometry-Assisted LC-ESI-MS. The instrument and methods employed for the LC-ESI-MS analysis have been described previously.[22,23] Briefly, the instrument consists of a Waters ACQUITY UPLC I-Class system, coupled to a quadrupole time-of-flight mass spectrometer (Xevo G2-S QToF). LC separation was performed on an ACQUITY BEH C_{18} column (2.1 mm × 50 mm) held at 30 °C. The total flow rate was 0.3 mL min^{-1}, and the injection volume was 10 μL. LC uses two eluents: A [0.1% (v/v) formic acid in water] and B (100% acetonitrile). The gradient was programmed as follows: 100% A from 0 to 2.0 min, 10% A and 90% B from 2.0 to 10.2 min, and 100% A from 10.2 to 12 min. ESI settings were as follows: capillary voltage, 2.0 kV; sampling cone voltage, 40 V; source offset, 80 V; source temperature, 120 °C; desolvation temperature, 400 °C; cone gas, 30 L h^{-1}; desolvation gas, 650 L h^{-1}. Leucine enkephalin was employed as the lock mass for accurate mass determination. The method stability is within 5%, as determined by frequent consistency tests. The positive ($LC\text{-}ESI^+$-MS) and negative ($LC\text{-}ESI^-$-MS) modes were used under the same settings, and data were acquired and processed with MassLynx version 4.1.

For a number of samples, the iodometry method described above was applied prior to the LC-ESI-MS measurement. Formic acid was used to adjust the solution pH to 2. To ensure the completion of iodometry, the iodometry solutions were allowed to react for 5−7 h before the LC-ESI-MS measurement was conducted. As iodometry selectively reacts away organic peroxides, it is hypothesized that organic peroxide compounds can be elucidated by a comparison of iodometry-treated samples and nontreated samples. Four different conditions were examined to explore the effects of formic acid and iodide on WSOC: with neither formic acid nor KI (condition I), with formic acid (condition II), with KI (condition III), and with both formic acid and KI (condition IV). These four conditions maintain the same dilution ratio but with variable reagents added.

RESULTS AND DISCUSSION

Detection of Organic Peroxides. The LC-ESI-MS method separated and detected the two synthesized αAAHP species. Base peak intensity (BPI) chromatograms of an aqueous solution containing both αAAHPs are shown in Figure 2.

$LC\text{-}ESI^-$-MS detected αAAHP-A as its deprotonated form ($[M - H]^-$) due to the additional carboxylic acid functional group in the molecule (Figure 2a). Without a carboxylic acid functional group, αAAHP-P is not detected as the deprotonated form. Instead, a peak with a nominal mass of 183 Da appears at the retention time (t_R) corresponding to αAAHP-P, and its elemental composition is identical to that of the deprotonated pinonic acid ($C_{10}H_{15}O_3$). We propose that this peak is not pinonic acid, but instead a fragment of αAAHP-P because the t_R

DOI: 10.1021/acs.est.7b04863
Environ. Sci. Technol. 2018, 52, 2108−2117

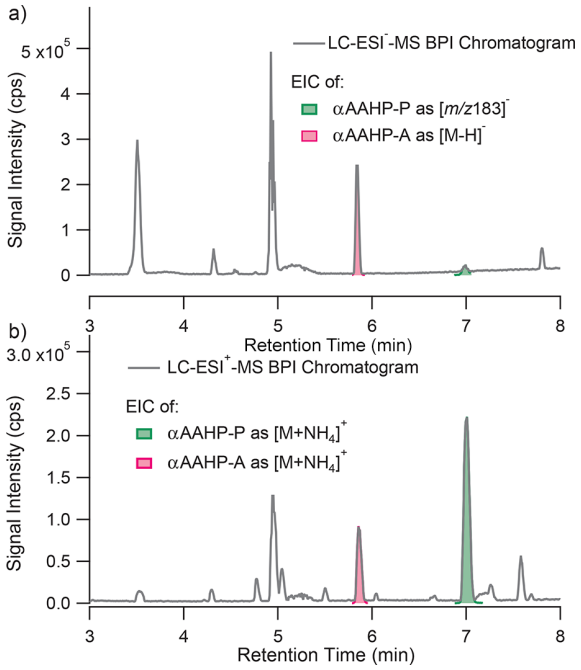

Figure 2. Base peak intensity (BPI) chromatogram of an aqueous solution containing αAAHP-P and αAAHP-A detected by (a) LC-ESI⁻-MS and (b) LC-ESI⁺-MS. Colored areas represent the extracted ion chromatograms (EICs) of these two αAAHP species.

of pinonic acid is 4.7 min. In addition, as we will discuss next, this m/z 183 fragment disappears when iodometry is applied, while pinonic acid does not. This observation gives rise to an important implication for the detection of SOA components, as a fraction of organic acids commonly observed by LC-ESI⁻-MS may have been fragments of αAAHP or other high-molecular weight compounds. LC-ESI⁺-MS has detected the αAAHP species predominantly as their ammonium clusters ($[M + NH_4]^+$) but also as their sodium clusters ($[M + Na]^+$). Note that the BPI chromatogram presents only the most intensive peak at each t_R.

To provide general guidance for future applications of ESI-MS in organic peroxide detection, we have also carefully evaluated the detection of organic peroxides using direct-infusion ESI-MS, which bypasses the LC component and directly injects the sample solution into the ESI-MS instrument (section S2 of the Supporting Information). Two commercially available organic peroxides, benzoyl peroxide and lauroryl peroxide, were chosen as representatives for ROOR species, while the synthesized αAAHP species were employed as those for multifunctional ROOH species. As expected, αAAHP-P is not detected by ESI⁻-MS as it does not contain any carboxylic functional group. ESI⁻-MS detects αAAHP-A as its $[M - H]^-$ and $[2M - H]^-$ forms. ESI⁺-MS detects all the four organic peroxides as their sodium clusters, as opposed to LC-ESI⁺-MS, in which ammonium clusters dominate. As sodium formate is introduced into the infusion system regularly for calibration, there can be a potential source of Na^+ in the system. On the other hand, the amount of Na^+ co-eluting with analytes during LC-ESI-MS is likely much smaller. Our results show that the difference in the ionization environment can likely change the mode of detection of organic peroxides. In future studies, the detectability of organic peroxides should be examined before any assumptions are made about their detection.

Characterization of Iodometry and the Total Peroxide Contents of α-Pinene SOA. Prior to application of iodometry to LC-ESI-MS, spectroscopy-based iodometry was performed to determine the total organic peroxide content of the WSOC samples. We performed measurements for five replicate filters. The H_2O_2 equivalent concentration of total organic peroxide ranged from 14 to 30 μM. Because the amount of SOA collected on each filter and the extraction efficiency vary, the measured total peroxide concentration of each filter extract was normalized to the measured TOC concentration.

The total peroxide content is commonly reported as molar yield (moles of organic peroxide per SOA mass) and mass yield (mass of organic peroxide per mass of SOA). Obtaining these values requires the average organic matter to organic carbon ratio (OM/OC) of SOA components and the average molecular weight of organic peroxides. Here, we assume the average OM/OC to be equivalent to that of pinic acid (i.e., 1.7), which is one of the most abundant compounds in α-pinene SOA,[7] while the average molecular weight of 300 g mol^{-1} for organic peroxides was adapted from previous studies.[8,52] With these assumptions, an average molar yield of $(4.8 \pm 1.2) \times 10^{-10}$ mol μg^{-1} and an average mass yield of 15 ± 3.7% were obtained from this study. As discussed with details in section S3.1 of the Supporting Information, this mass yield is lower but comparable to those reported in the literature.[8,11,51−55]

To improve our understanding of the current iodometry method, we have investigated the reaction kinetics of the iodometry reaction by monitoring the solution absorbance at 350 nm. We performed this experiment on WSOC as well as a number of individual peroxide solutions, including H_2O_2, *tert*-butyl hydroperoxide, and methyl hydroperoxide. The detailed results are presented in section S3.2 of the Supporting Information and Figure S3. Our results show that iodometry proceeds with different organic peroxides at different rates, with H_2O_2 reacting with iodide the most rapidly. The reaction with WSOC may not have reached completion after 1 h, at which point the UV measurement was taken in the current and a number of past studies,[8,10] giving rise to a potential underestimation of the total organic peroxide content (see section S.2 of the Supporting Information).

Iodometry-Assisted LC-ESI-MS. *Iodometry Performed on Non-Peroxide Species.* Iodometry was first performed on an aqueous solution containing each of three nonperoxide organic acids at 5 μM: adipic acid, pinonic acid, and pinic acid. These three organic acids can be readily detected by LC-ESI⁻-MS. An aliquot treated with iodometry (condition IV described in the Experimental Section) was compared with a control (condition II), and the BPI chromatograms are shown in section S4 of the Supporting Information. The peak intensities of the three organic acids treated with and without iodometry are essentially identical, confirming that iodide does not react with non-peroxide compounds. Another important observation is that the t_R of the three organic acids is not affected by iodometry. For the iodometry-treated sample, a large peak of iodide (127 Da) emerges at the beginning of the chromatogram (t_R < 2 min) but is directed to waste.

Iodometry Performed on αAAHP Species. Iodometry was performed on an acetonitrile solution containing both of the synthesized αAAHP species. Acetonitrile is used here to minimize hydrolysis of αAAHPs and to ensure that the spectral changes are induced by only iodometry. The solution was

DOI: 10.1021/acs.est.7b04863
Environ. Sci. Technol. 2018, 52, 2108−2117

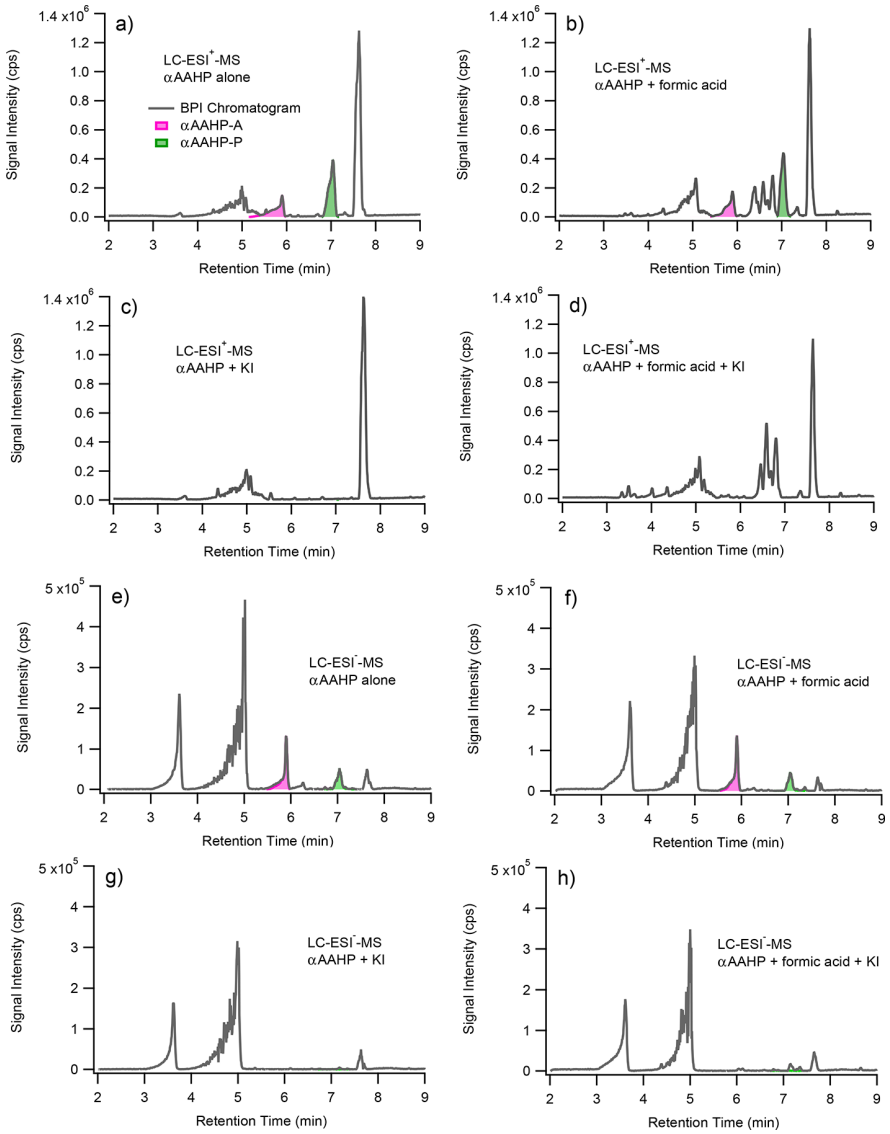

Figure 3. Results of iodometry performed on a mixture of synthesized αAAHP-P and αAAHP-A dissolved in acetonitrile. Results of LC-ESI$^+$-MS and LC-ESI$^-$-MS are presented in panels (a–d) and (e–h), respectively.

allowed to react for 2 h before LC-ESI-MS measurement. To the best of our knowledge, this is the first investigation of the iodometry reaction at the molecular level; therefore, detailed results are presented in Figure 3. Panels (a–d) of Figure 3 show the results obtained with LC-ESI$^+$-MS. When formic acid was added to the solution, several additional peaks appeared on the chromatogram, but the αAAHP peaks were unaffected (Figure 3b). When KI was added to the solution, either with or without formic acid, only the αAAHP peaks disappeared (Figure 3c,d). The excess of organic acid added to the solution for the synthesis likely made the solution sufficiently acidic, and iodometry proceeds without additional formic acid. A similar observation was obtained using LC-ESI$^-$-MS (Figure 3e–h). In particular, the m/z 183 peak at a t_R of 7 min disappears with iodometry, confirming that it is likely a fragment of αAAHP-P and unrelated to pinonic acid. These results illustrate that iodometry selectively reacts away organic peroxides with a negligible impact on non-peroxide species.

Effect of Iodometry on the SOA Extract. *Negative Mode (LC-ESI$^-$-MS).* Analysis of α-pinene SOA components using LC-ESI$^-$-MS has been reported in a number of studies, including our previous work.[17,18,20,22,26–28,56] The chromatogram and mass spectra recorded in this work are provided in section S5 of the Supporting Information. The BPI chromatogram obtained in this study (Figure S5a) reproduces well those of our previous study, confirming the reproducibility of the LC-ESI-MS method. Figure S5b shows the reconstructed mass spectrum, defined to be the sum of all mass spectra at t_R values from 2 to 9 min with a peak height of $\geq 2 \times 10^3$ counts per second (cps). The mass spectrum demonstrates a bimodal form, attributed to monomers and dimers in WSOC.[28,57,58] In Table S2, we provide a list of major peaks detected in this work. We did not conduct a detailed structural analysis, as this has already been done in a number of other studies.[17,23,35,59] Instead, we have annotated peaks that have been previously proposed as candidates of organic peroxides.

DOI: 10.1021/acs.est.7b04863
Environ. Sci. Technol. 2018, 52, 2108–2117

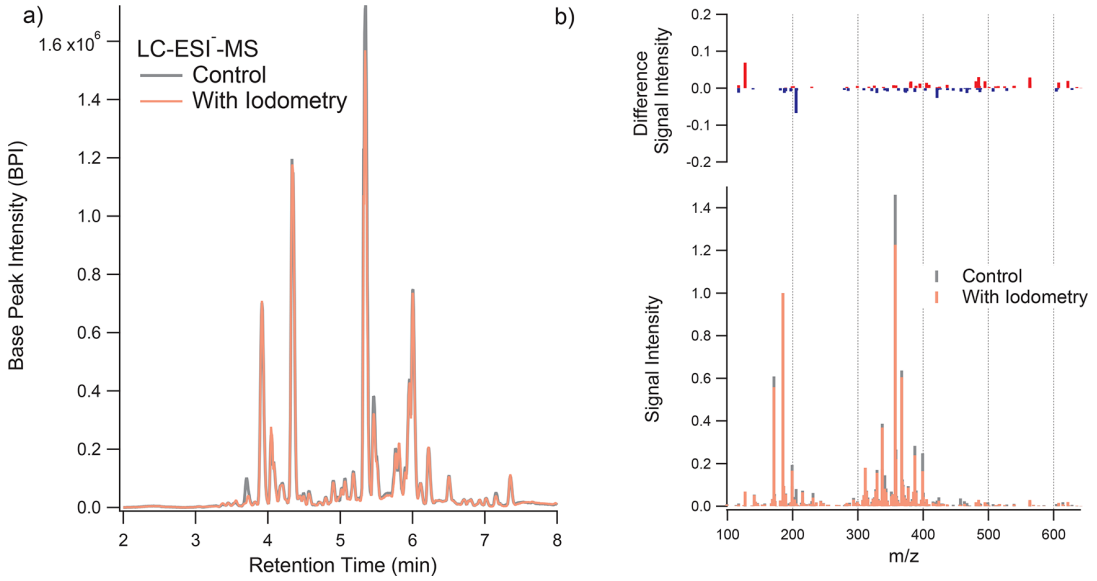

Figure 4. Comparison of a sample treated with and without iodometry, measured by LC-ESI⁻-MS. Comparison of the base peak intensity (BPI) chromatograms is shown in panel (a). The reconstructed mass spectra are shown in the bottom part of panel (b), where the peak intensities have been normalized to that of pinic acid ($[C_9H_{14}O_4 - H]^-$ at 185.08 Da). The top part of panel (b) shows a difference mass spectrum showing peaks that are depleted by >70% and those newly introduced by iodometry. Each BPI chromatogram and mass spectrum shown here is the average of triplicate measurements. The control sample refers to condition II described in the Experimental Section, while the iodometry sample refers to condition IV.

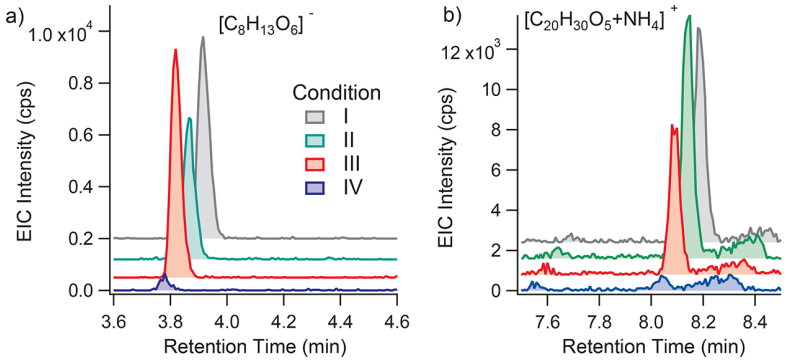

Figure 5. Extracted ion chromatogram (EIC) of two organic peroxide candidates: (a) $[C_8H_{13}O_6]^-$ from LC-ESI⁻-MS and (b) $[C_{20}H_{30}O_5 + NH_4]^+$ from LC-ESI⁺-MS. From top to bottom, the four traces represent iodometry conditions I–IV, respectively (see the Experimental Section).

We performed a comparison of samples treated with and without iodometry, and the results for LC-ESI⁻-MS are shown in Figure 4, focusing on the comparison between the sample treated with only formic acid (condition II) and that treated with both formic acid and KI (condition IV), as this comparison excludes any mass spectral changes induced by formic acid alone and best reflects changes induced by iodometry.

Iodometry did not induce significant changes in the BPI chromatograms or reconstructed mass spectra. The top panel of Figure 4b shows the difference mass spectrum between the control and iodometry samples. Given that the reactivity of αAAHP species has been exhibited (Figure 3), any organic peroxides present in the WSOC of α-pinene SOA should be depleted by the time of measurement. Therefore, only peaks that exhibit a significant change, i.e., either depleted by >70% or newly introduced by iodometry, are shown in the difference mass spectrum.

The only major peak that is depleted by iodometry and showed consistency between different filter samples is that of the deprotonated form of $C_8H_{14}O_6$ (205.071 Da, t_R of 3.71 min). The effect of iodometry on other major peaks is discussed in section S5 of the Supporting Information. The decay of $C_8H_{14}O_6$ on the BPI chromatogram can be observed (Figure 4a). The EICs of this compound are presented in Figure 5a, showing that $C_8H_{14}O_6$ is depleted only when both formic acid and KI are present. As the WSOC does not contain an excess of organic acids, compared to the synthesized αAAHPs in which an organic acid is added in excess for synthesis, it seems that additional formic acid is necessary for the iodometry reaction to proceed. We have attempted to perform MS^2 measurements on $C_8H_{14}O_6$, but the signal intensities of its fragments were too low to obtain structural information. $C_8H_{14}O_6$ has been observed previously and has been tentatively defined as an unknown carboxylic acid.[17] Results from this study suggest that this compound contains a peroxide functional group. Given the high oxygen/carbon ratio

DOI: 10.1021/acs.est.7b04863
Environ. Sci. Technol. 2018, 52, 2108−2117

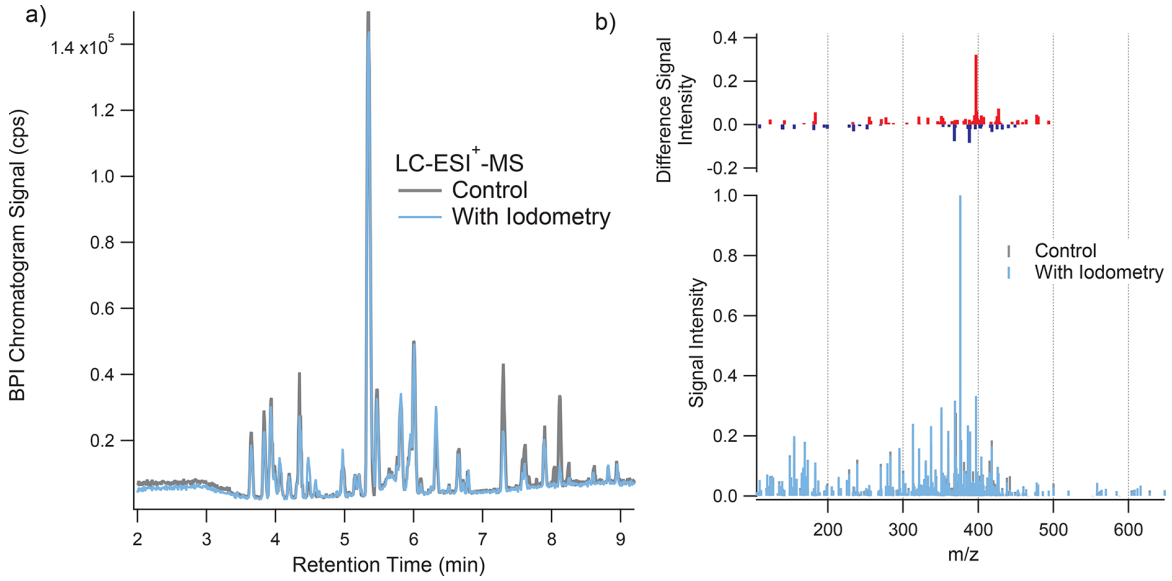

Figure 6. Comparison of a sample treated with and without iodometry, measured by LC-ESI$^+$-MS. Comparison of the base peak intensity (BPI) chromatograms is shown in panel (a). The reconstructed mass spectra are shown in the bottom part of panel (b), where the peak intensities have been normalized to that of pinyl-diaterpenyl ester ($[C_{17}H_{26}O_8 + Na]^+$ at 376.20 Da). The top part of panel (b) is a difference mass spectrum showing peaks that are depleted by >70% and those newly introduced by iodometry. Each BPI chromatogram and mass spectrum shown here is the average of triplicate measurements. The control sample refers to condition II described in the Experimental Section, while the iodometry sample refers to condition IV.

(O/C) of this compound, $C_8H_{14}O_6$ can potentially be a HOM species arising from intramolecular hydrogen abstraction (see Introduction). Alternatively, it can also be a compound similar to 3-methyl-1,2,3-butanetricarboxylic acid (MBTCA, $C_8H_{12}O_6$; t_R = 3.73 min), a well-established organic tracer for α-pinene SOA.[60−62]

Positive Mode (LC-ESI$^+$-MS). Driven by the abundance of organic acids, the use of ESI$^-$ has prevailed in molecular analyses of α-pinene SOA components. Only a few studies have employed ESI$^+$.[24,35,37,56,59,63] The BPI chromatogram recorded by LC-ESI$^+$-MS and its reconstructed mass spectrum are shown in panels (a) and (c) of Figure S5, respectively. A number of major compounds are detected in positive and negative modes, while some can be detected only by the positive mode, as clusters of H^+, Na^+, and NH_4^+. Because the polarity of ESI detection does not affect the chromatographic t_R, we have made peak assignments for the positive mode by comparison with peaks detected in the negative mode, and major compounds are listed in Table S3.

Comparison of a sample treated with and without iodometry is shown in Figure 6 in the same manner as in Figure 4. The only noticeable change on the BPI chromatograms is that two major peaks, appearing at t_R values of 7.3 and 8.1 min, disappear when iodometry is applied. Judging solely on the basis of the comparison of conditions II and IV, which is the case for Figure 6, these two peaks appear to be organic peroxides. However, a detailed investigation of these peaks under all four conditions, presented in section S6.1 of the Supporting Information, indicates that the addition of formic acid has introduced artifacts, and these two peaks are unlikely to be peroxides. Among all the peaks with a peak height of ≥2000 cps, five appear to be candidates for organic peroxides: $[C_8H_{10}O_3 + H]^+$ (155.07 Da), $[C_{10}H_{16}O_5 + NH_4]^+$ (234.13.34 Da), $[C_{10}H_{18}O_6 + NH_4]^+$ (252.15 Da), $[C_{20}H_{30}O_5 + NH_4]^+$ (368.24 Da), and $[C_{19}H_{30}O_7 + NH_4]^+$ (388.23 Da). The EICs of $[C_{20}H_{30}O_5 + NH_4]^+$ under condition I−IV are shown in Figure 5b, while those of the others are presented in section S6.2 of the Supporting Information. $[C_8H_{10}O_3 + H]^+$ and $[C_{10}H_{16}O_5 + NH_4]^+$ are detected as multiple peaks, and not all of them appear to be organic peroxides. This observation demonstrates the ability of iodometry-assisted LC-ESI-MS to resolve organic peroxides from non-peroxide isomers. The consistency of these observed trends has been confirmed with a separate filter sample. All five candidates for organic peroxides are detected as minor peaks and do not belong to the group of the 50 largest peaks summarized in Table S3. Their peak areas are 2−5% of that of pinyl-diaterpenyl ester, which is the largest peak detected by LC-ESI$^+$-MS. The effect of iodometry on other major peaks is presented in section S5 of the Supporting Information.

Explanations for the Absence of Organic Peroxides in WSOC. The absence of organic peroxides among the major products was unexpected, as α-pinene SOA has been believed to contain a high organic peroxide content.[9,64] In fact, our conventional iodometry measurement using UV−vis detected a total organic peroxide content comparable to that found in previous studies (Table S1). Many of the proposed organic peroxides from previous studies[17,18,23,59] are detected in this work with the corresponding elemental compositions (Table S2). However, none of these compounds decayed in response to the iodometry treatment. We have altered a number of experimental and instrumental conditions that can potentially affect iodometry and the detection of organic peroxides, including the temperature of the iodometry reaction and the ESI settings. Detailed results of these experiments are presented in section S7 of the Supporting Information. However, varying these factors did not explain the absence of major organic peroxide peaks.

The current LC-ESI-MS method is not quantitative, as determination of electrospray ionization efficiency for com-

DOI: 10.1021/acs.est.7b04863
Environ. Sci. Technol. 2018, 52, 2108−2117

pounds without definite structural information is difficult; therefore, the peak area of a compound does not directly reflect its concentration in the WSOC sample. With a computational approach, our previous study[23] has found that the ionization efficiencies of the dimer esters are 3−10 times higher than those of the monomeric compounds. Currently, we cannot rule out the possibility that LC-ESI-MS fails to detect certain organic peroxide species due to inefficient ionization. In particular, the major peaks detected by the current method include very few HOM compounds that typically exhibit O/C ratios of >0.7. It is likely that our method and/or instrument is less optimized toward HOMs than those of a number of previous studies.[34,35,37]

Alternatively, decomposition of organic peroxides may play an important role in filter extraction-based techniques. Decomposition can occur at different stages of the experiment. Highly labile organic peroxides may decompose in suspended particles before they can be collected.[12,15,23,52] Decomposition may also occur on the filter, with longer collection times leading to a loss of organic peroxide.[52] In future applications, the filter collection duration can be shortened from that in the current work (15−18 h) to minimize decomposition and evaporation. Finally, decomposition may occur after the SOA component is extracted to condensed phases, forming the OH radical[16] and H_2O_2.[53,55,65] Small and polar peroxides, such as H_2O_2, can contribute to the total peroxide content measured by the conventional, spectroscopy-based iodometry but cannot be detected by our LC-ESI-MS method, which is optimized for monomeric and dimeric oxidation products of α-pinene.

■ ENVIRONMENTAL IMPLICATIONS

With an emerging awareness of the role that organic peroxides play in SOA formation and the consequent health effects, identification of particle-phase organic peroxides has become a priority in atmospheric chemistry research. Employing advanced MS techniques, many recent studies have reported detection of particle-phase organic peroxides. However, structural assignment with MS is often based only on exact mass and/or fragmentation patterns, supported by feasible formation mechanisms, leaving room for potential misassignment due to a lack of structural information about functional groups. In this work, we have developed a novel technique, iodometry-assisted LC-ESI-MS, to unambiguously identify organic peroxides present in extracted SOA components at the molecular level.

Because of a lack of commercially available organic peroxides, characterization of our method was performed with synthesized α-acyloxyalkyl hydroperoxides (αAAHPs). Detection of αAAHPs was successful, but our results reveal concerns regarding the use of ESI-MS for the detection of organic peroxides. In particular, even with the same ESI-MS instrument, a difference in the ionization mode was observed between direct infusion and LC-ESI-MS, likely due to different ionization conditions. In future studies, the utility of LC-ESI-MS for organic peroxide identification should be thoroughly characterized.

The utility of iodometry-assisted LC-ESI-MS has been demonstrated with αAAHPs. Iodometry selectively reacts away organic peroxides with negligible interference with non-peroxide species. While iodometry-assisted LC-ESI-MS was applied in this work to study one specific issue related to atmospheric particulate matter, the versatility of this technique makes it applicable to a wide range of environmental applications that require the determination of organic peroxides at the molecular level.

Iodometry-assisted LC-ESI-MS was applied to the water-soluble organic carbon (WSOC) of α-pinene SOA collected from a flow tube reactor, following a standard sample collection procedure. Unexpectedly, only a limited number of detectable compounds, $C_8H_{14}O_6$ from the negative mode and five minor peaks from the positive mode, appeared to be organic peroxides. This observation is inconsistent with conventional, spectroscopy-based iodometry, which suggests that the average mass yield of organic peroxides is 15% in this system. We propose that the multifunctional organic peroxides may have decomposed to smaller peroxides that cannot be detected with the current LC-ESI-MS technique. Future studies should investigate the stability and decomposition mechanisms of organic peroxides on filters and in extraction solutions. Although this work focused only on the decay of organic peroxides during iodometry, an interesting direction would be the investigation of the corresponding alcohols arising from iodometry. Unlike organic peroxides, functionalized alcohols and polyols are commercially available, which may lead to new avenues for quantifying organic peroxides.

Our results raise significant concerns about all filter extraction-based studies of atmospheric SOA, showing that labile organic peroxides can be lost either during sample collection or after extraction. The use of MS prevails in the field of atmospheric chemistry, and the versatility of LC-ESI-MS has been proven by many studies. However, previously unrecognized considerations are required for the interpretation of MS data, particularly for the assignment of organic peroxides.

■ ASSOCIATED CONTENT

Supporting Information

The Supporting Information is available free of charge on the ACS Publications website at DOI: 10.1021/acs.est.7b04863.

Additional information about the generation and collection of SOA (section S1), detection of organic peroxides with direct-infusion ESI-MS (section S2), a comparison of the total organic peroxide content obtained in this work to those from previous studies and a detailed characterization of the iodometry method (section S3), results from iodometry performed on non-peroxide species (section S4), chromatograms and lists of major compounds detected by LC-ESI-MS (section S5), additional information about the analyses of iodometry-assisted LC-ESI-MS (section S6), and additional examination of various instrumental conditions for iodometry-assisted LC-ESI-MS (section S7) (PDF)

■ AUTHOR INFORMATION

Corresponding Author

*E-mail: rzhao@caltech.edu. Phone: +1 626-395-8928.

ORCID

Ran Zhao: 0000-0002-1096-7632
Christopher M. Kenseth: 0000-0003-3188-2336
John H. Seinfeld: 0000-0003-1344-4068

Notes

The authors declare no competing financial interest.

DOI: 10.1021/acs.est.7b04863
Environ. Sci. Technol. 2018, 52, 2108−2117

■ ACKNOWLEDGMENTS

The authors thank Dwight and Christine Landis for their generous contribution to the CPOT, Prof. Paul Wennberg for helpful discussion, Dr. John Crounse for assistance with UV−vis measurements, and Dr. Michelle Kim for the synthesis of methylhydroperoxide. LC-ESI-MS and TOC analyses were performed in the Environmental Analysis Center (EAC). This work was supported by National Science Foundation Grants AGS-1523500 and CHE-1508526. R.Z. also acknowledges support from a Natural Science and Engineering Research Council of Canada Postdoctoral Fellowship (NSERC-PDF).

■ REFERENCES

(1) Sakugawa, H.; Kaplan, I. R.; Tsai, W.; Cohen, Y. Atmospheric hydrogen peroxide. *Environ. Sci. Technol.* **1990**, *24*, 1452−1462.
(2) Pandis, S. N.; Seinfeld, J. H. Sensitivity analysis of a chemical mechanism for aqueous-phase atmospheric chemistry. *J. Geophys. Res.* **1989**, *94*, 1105−1126.
(3) Tao, F.; Gonzalez-Flecha, B.; Kobzik, L. Reactive oxygen species in pulmonary inflammation by ambient particulates. *Free Radical Biol. Med.* **2003**, *35*, 327−340.
(4) Seinfeld, J. H.; Pandis, S. N. *Atmospheric Chemistry and Physics: From Air Pollution to Climate Change*, 3rd ed.; John Wiley & Sons: Hoboken, NJ, 2016.
(5) Pye, H. O. T.; Chan, A. W. H.; Barkley, M. P.; Seinfeld, J. H. Global modeling of organic aerosol: the importance of reactive nitrogen (NO_x and NO_3). *Atmos. Chem. Phys.* **2010**, *10*, 11261−11276.
(6) Spracklen, D. V.; Jimenez, J. L.; Carslaw, K. S.; Worsnop, D. R.; Evans, M. J.; Mann, G. W.; Zhang, Q.; Canagaratna, M. R.; Allan, J.; Coe, H.; McFiggans, G.; Rap, A.; Forster, P. Aerosol mass spectrometer constraint on the global secondary organic aerosol budget. *Atmos. Chem. Phys.* **2011**, *11*, 12109−12136.
(7) Kanakidou, M.; et al. Organic aerosol and global climate modelling: a review. *Atmos. Chem. Phys.* **2005**, *5*, 1053−1123.
(8) Docherty, K. S.; Wu, W.; Lim, Y. B.; Ziemann, P. J. Contributions of organic peroxides to secondary aerosol formed from reactions of monoterpenes with O_3. *Environ. Sci. Technol.* **2005**, *39*, 4049−4059.
(9) Bonn, B.; von Kuhlmann, R.; Lawrence, M. G. High contribution of biogenic hydroperoxides to secondary organic aerosol formation. *Geophys. Res. Lett.* **2004**, *31*, L10108.
(10) Mutzel, A.; Rodigast, M.; Iinuma, Y.; Böge, O.; Herrmann, H. An improved method for the quantification of SOA bound peroxides. *Atmos. Environ.* **2013**, *67*, 365−369.
(11) Mertes, P.; Pfaffenberger, L.; Dommen, J.; Kalberer, M.; Baltensperger, U. Development of a sensitive long path absorption photometer to quantify peroxides in aerosol particles (Peroxide-LOPAP). *Atmos. Meas. Tech.* **2012**, *5*, 2339−2348.
(12) Krapf, M.; El Haddad, I.; Bruns, E. A.; Molteni, U.; Daellenbach, K. R.; Prévôt, A. S.; Baltensperger, U.; Dommen, J. Labile Peroxides in Secondary Organic Aerosol. *Chem.* **2016**, *1*, 603−616.
(13) Bloomfield, M. The spectrophotometric determination of hydroperoxide and peroxide in a lipid pharmaceutical product by flow injection analysis. *Analyst* **1999**, *124*, 1865−1871.
(14) Banerjee, D. K.; Budke, C. C. Spectrophotometric determination of traces of peroxides in organic solvents. *Anal. Chem.* **1964**, *36*, 792−796.
(15) Riva, M.; Budisulistiorini, S. H.; Zhang, Z.; Gold, A.; Thornton, J. A.; Turpin, B. J.; Surratt, J. D. Multiphase reactivity of gaseous hydroperoxide oligomers produced from isoprene ozonolysis in the presence of acidified aerosols. *Atmos. Environ.* **2017**, *152*, 314−322.
(16) Tong, H.; Arangio, A. M.; Lakey, P. S. J.; Berkemeier, T.; Liu, F.; Kampf, C. J.; Brune, W. H.; Pöschl, U.; Shiraiwa, M. Hydroxyl radicals from secondary organic aerosol decomposition in water. *Atmos. Chem. Phys.* **2016**, *16*, 1761−1771.
(17) Kristensen, K.; Watne, a. K.; Hammes, J.; Lutz, A.; Petäjä, T.; Hallquist, M.; Bilde, M.; Glasius, M. High-molecular weight dimer esters are major products in aerosols from α-pinene ozonolysis and the boreal forest. *Environ. Sci. Technol. Lett.* **2016**, *3*, 280−285.
(18) Kristensen, K.; Cui, T.; Zhang, H.; Gold, A.; Glasius, M.; Surratt, J. D. Dimers in α-pinene secondary organic aerosol: effect of hydroxyl radical, ozone, relative humidity and aerosol acidity. *Atmos. Chem. Phys.* **2014**, *14*, 4201−4218.
(19) Kristensen, K.; Enggrob, K. L.; King, S. M.; Worton, D. R.; Platt, S. M.; Mortensen, R.; Rosenoern, T.; Surratt, J. D.; Bilde, M.; Goldstein, A. H.; Glasius, M. Formation and occurrence of dimer esters of pinene oxidation products in atmospheric aerosols. *Atmos. Chem. Phys.* **2013**, *13*, 3763−3776.
(20) Yasmeen, F.; Vermeylen, R.; Szmigielski, R.; Iinuma, Y.; Böge, O.; Herrmann, H.; Maenhaut, W.; Claeys, M. Terpenylic acid and related compounds: precursors for dimers in secondary organic aerosol from the ozonolysis of α-and β-pinene. *Atmos. Chem. Phys.* **2010**, *10*, 9383−9392.
(21) Yasmeen, F.; Vermeylen, R.; Maurin, N.; Perraudin, E.; Doussin, J.-F.; Claeys, M. Characterisation of tracers for aging of α-pinene secondary organic aerosol using liquid chromatography/negative ion electrospray ionisation mass spectrometry. *Environ. Chem.* **2012**, *9*, 236−246.
(22) Zhang, X.; Dalleska, N. F.; Huang, D. D.; Bates, K. H.; Sorooshian, A.; Flagan, R. C.; Seinfeld, J. H. Time-resolved molecular characterization of organic aerosols by PILS+ UPLC/ESI-Q-TOFMS. *Atmos. Environ.* **2016**, *130*, 180−189.
(23) Zhang, X.; McVay, R. C.; Huang, D. D.; Dalleska, N. F.; Aumont, B.; Flagan, R. C.; Seinfeld, J. H. Formation and evolution of molecular products in α-pinene secondary organic aerosol. *Proc. Natl. Acad. Sci. U. S. A.* **2015**, *112*, 14168−14173.
(24) Witkowski, B.; Gierczak, T. Early stage composition of SOA produced by α-pinene/ozone reaction: α-Acyloxyhydroperoxy aldehydes and acidic dimers. *Atmos. Environ.* **2014**, *95*, 59−70.
(25) Hall, W. A., VI; Johnston, M. V. Oligomer content of α-pinene secondary organic aerosol. *Aerosol Sci. Technol.* **2011**, *45*, 37−45.
(26) Müller, L.; Reinnig, M.-C.; Warnke, J.; Hoffmann, T. Unambiguous identification of esters as oligomers in secondary organic aerosol formed from cyclohexene and cyclohexene/α-pinene ozonolysis. *Atmos. Chem. Phys.* **2008**, *8*, 1423−1433.
(27) Müller, L.; Reinnig, M.-C.; Hayen, H.; Hoffmann, T. Characterization of oligomeric compounds in secondary organic aerosol using liquid chromatography coupled to electrospray ionization Fourier transform ion cyclotron resonance mass spectrometry. *Rapid Commun. Mass Spectrom.* **2009**, *23*, 971−979.
(28) Kourtchev, I.; Doussin, J.-F.; Giorio, C.; Mahon, B.; Wilson, E. M.; Maurin, N.; Pangui, E.; Venables, D. S.; Wenger, J. C.; Kalberer, M. Molecular composition of fresh and aged secondary organic aerosol from a mixture of biogenic volatile compounds: a high-resolution mass spectrometry study. *Atmos. Chem. Phys.* **2015**, *15*, 5683−5695.
(29) Reinnig, M.-C.; Müller, L.; Warnke, J.; Hoffmann, T. Characterization of selected organic compound classes in secondary organic aerosol from biogenic VOCs by HPLC/MS^n. *Anal. Bioanal. Chem.* **2008**, *391*, 171−182.
(30) Mochida, M.; Katrib, Y.; Jayne, J. T.; Worsnop, D. R.; Martin, S. T. The relative importance of competing pathways for the formation of high-molecular-weight peroxides in the ozonolysis of organic aerosol particles. *Atmos. Chem. Phys.* **2006**, *6*, 4851−4866.
(31) Enami, S.; Colussi, A. J. Efficient scavenging of Criegee intermediates on water by surface-active cis-pinonic acid. *Phys. Chem. Chem. Phys.* **2017**, *19*, 17044−17051.
(32) Ehn, M.; Thornton, J. A.; Kleist, E.; Sipilä, M.; Junninen, H.; Pullinen, I.; Springer, M.; Rubach, F.; Tillmann, R.; Lee, B.; others.; et al. A large source of low-volatility secondary organic aerosol. *Nature* **2014**, *506*, 476−479.
(33) Crounse, J. D.; Nielsen, L. C.; Jørgensen, S.; Kjaergaard, H. G.; Wennberg, P. O. Autoxidation of organic compounds in the atmosphere. *J. Phys. Chem. Lett.* **2013**, *4*, 3513−3520.
(34) Mutzel, A.; Poulain, L.; Berndt, T.; Iinuma, Y.; Rodigast, M.; Böge, O.; Richters, S.; Spindler, G.; Sipilä, M.; Jokinen, T.; Kulmala, M.; Herrmann, H. Highly Oxidized Multifunctional Organic

DOI: 10.1021/acs.est.7b04863
Environ. Sci. Technol. 2018, 52, 2108−2117

Compounds Observed in Tropospheric Particles: A Field and Laboratory Study. *Environ. Sci. Technol.* **2015**, *49*, 7754−7761.
(35) Zhang, X.; et al. Highly oxygenated multifunctional compounds in α-pinene secondary organic aerosoll. *Environ. Sci. Technol.* **2017**, *51*, 5932−5940.
(36) Lee, B. H.; et al. Highly functionalized organic nitrates in the southeast United States: Contribution to secondary organic aerosol and reactive nitrogen budgets. *Proc. Natl. Acad. Sci. U. S. A.* **2016**, *113*, 1516−1521.
(37) Tu, P.; Hall, W. A.; Johnston, M. V. Characterization of highly oxidized molecules in fresh and aged biogenic secondary organic aerosol. *Anal. Chem.* **2016**, *88*, 4495−4501.
(38) Oss, M.; Kruve, A.; Herodes, K.; Leito, I. Electrospray ionization efficiency scale of organic compounds. *Anal. Chem.* **2010**, *82*, 2865−2872.
(39) Cech, N. B.; Enke, C. G. Practical implications of some recent studies in electrospray ionization fundamentals. *Mass Spectrom. Rev.* **2001**, *20*, 362−387.
(40) Steimer, S. S.; Kourtchev, I.; Kalberer, M. Mass spectrometry characterization of peroxycarboxylic acids as proxies for reactive oxygen species and highly oxygenated molecules in atmospheric aerosols. *Anal. Chem.* **2017**, *89*, 2873−2879.
(41) Ferdousi, B. N.; Islam, M. M.; Okajima, T.; Ohsaka, T. Electrochemical, HPLC and electrospray ionization mass spectroscopic analyses of peroxycitric acid coexisting with citric acid and hydrogen peroxide in aqueous solution. *Talanta* **2008**, *74*, 1355−1362.
(42) Nilsson, J.; Carlberg, J.; Abrahamsson, P.; Hulthe, G.; Persson, B.-A.; Karlberg, A.-T. Evaluation of ionization techniques for mass spectrometric detection of contact allergenic hydroperoxides formed by autoxidation of fragrance terpenes. *Rapid Commun. Mass Spectrom.* **2008**, *22*, 3593−3598.
(43) Yin, H.; Hachey, D. L.; Porter, N. A. Structural analysis of diacyl peroxides by electrospray tandem mass spectrometry with ammonium acetate: bond homolysis of peroxide-ammonium and peroxide-proton adducts. *Rapid Commun. Mass Spectrom.* **2000**, *14*, 1248−1254.
(44) Witkowski, B.; Gierczak, T. Analysis of α-acyloxyhydroperoxy aldehydes with electrospray ionization-tandem mass spectrometry (ESI-MS(n)). *J. Mass Spectrom.* **2013**, *48*, 79−88.
(45) Weber, R. J.; Orsini, D.; Daun, Y.; Lee, Y.-N.; Klotz, P. J.; Brechtel, F. A particle-into-liquid collector for rapid measurement of aerosol bulk chemical composition. *Aerosol Sci. Technol.* **2001**, *35*, 718−727.
(46) Kondo, Y.; Miyazaki, Y.; Takegawa, N.; Miyakawa, T.; Weber, R. J.; Jimenez, J. L.; Zhang, Q.; Worsnop, D. R. Oxygenated and water-soluble organic aerosols in Tokyo. *J. Geophys. Res.* **2007**, *112*, D01203 DOI: 10.1029/2006JD007056.
(47) Lee, A. K. Y.; Hayden, K. L.; Herckes, P.; Leaitch, W. R.; Liggio, J.; Macdonald, A. M.; Abbatt, J. P. D. Characterization of aerosol and cloud water at a mountain site during WACS 2010: secondary organic aerosol formation through oxidative cloud processing. *Atmos. Chem. Phys.* **2012**, *12*, 7103−7116.
(48) Herckes, P.; Valsaraj, K. T.; Collett, J. L., Jr A review of observations of organic matter in fogs and clouds: Origin, processing and fate. *Atmos. Res.* **2013**, *132*−*133*, 434−449.
(49) Blando, J. D.; Turpin, B. J. Secondary organic aerosol formation in cloud and fog droplets: a literature evaluation of plausibility. *Atmos. Environ.* **2000**, *34*, 1623−1632.
(50) Huang, Y.; Coggon, M. M.; Zhao, R.; Lignell, H.; Bauer, M. U.; Flagan, R. C.; Seinfeld, J. H. The Caltech Photooxidation Flow Tube reactor: design, fluid dynamics and characterization. *Atmos. Meas. Tech.* **2017**, *10*, 839−867.
(51) Epstein, S. A.; Blair, S. L.; Nizkorodov, S. A. Direct photolysis of α-pinene ozonolysis secondary organic aerosol: effect on particle mass and peroxide content. *Environ. Sci. Technol.* **2014**, *48*, 11251−11258.
(52) Li, H.; Chen, Z.; Huang, L.; Huang, D. Organic peroxides' gas-particle partitioning and rapid heterogeneous decomposition on secondary organic aerosol. *Atmos. Chem. Phys.* **2016**, *16*, 1837−1848.
(53) Badali, K. M.; Zhou, S.; Aljawhary, D.; Antiñolo, M.; Chen, W. J.; Lok, A.; Mungall, E.; Wong, J. P. S.; Zhao, R.; Abbatt, J. P. D. Formation of hydroxyl radicals from photolysis of secondary organic aerosol material. *Atmos. Chem. Phys.* **2015**, *15*, 7831−7840.
(54) Chen, X.; Hopke, P. K. Secondary organic aerosol from α-pinene ozonolysis in dynamic chamber system. *Indoor Air* **2009**, *19*, 335−345.
(55) Wang, Y.; Kim, H.; Paulson, S. E. Hydrogen peroxide generation from α- and β-pinene and toluene secondary organic aerosols. *Atmos. Environ.* **2011**, *45*, 3149−3156.
(56) Gao, Y.; Hall, W. H.; Johnston, M. Molecular composition of monoterpene secondary organic aerosol at low mass loading. *Environ. Sci. Technol.* **2010**, *44*, 7897−7902.
(57) Aljawhary, D.; Lee, A. K. Y.; Abbatt, J. P. D. High-resolution chemical ionization mass spectrometry (ToF-CIMS): application to study SOA composition and processing. *Atmos. Meas. Tech.* **2013**, *6*, 3211−3224.
(58) Zhao, R.; Aljawhary, D.; Lee, A. K. Y.; Abbatt, J. P. D. Rapid aqueous-phase photooxidation of dimers in the α-pinene secondary organic aerosol. *Environ. Sci. Technol. Lett.* **2017**, *4*, 205−210.
(59) Venkatachari, P.; Hopke, P. K. Characterization of products formed in the reaction of ozone with α-pinene: case for organic peroxides. *J. Environ. Monit.* **2008**, *10*, 966−974.
(60) Szmigielski, R.; Surratt, J. D.; Gómez-González, Y.; Van der Veken, P.; Kourtchev, I.; Vermeylen, R.; Blockhuys, F.; Jaoui, M.; Kleindienst, T. E.; Lewandowski, M.; Offenberg, J. H.; Edney, E. O.; Seinfeld, J. H.; Maenhaut, W.; Claeys, M. 3-methyl-1,2,3-butanetricarboxylic acid: An atmospheric tracer for terpene secondary organic aerosol. *Geophys. Res. Lett.* **2007**, *34*, L24811.
(61) Müller, L.; Reinnig, M.-C.; Naumann, K. H.; Saathoff, H.; Mentel, T. F.; Donahue, N. M.; Hoffmann, T. Formation of 3-methyl-1,2,3-butanetricarboxylic acid via gas phase oxidation of pinonic acid - a mass spectrometric study of SOA aging. *Atmos. Chem. Phys.* **2012**, *12*, 1483−1496.
(62) Aljawhary, D.; Zhao, R.; Lee, A. K.; Wang, C.; Abbatt, J. P. Kinetics, mechanism and secondary organic aerosol yield of aqueous phase photo-oxidation of α-pinene oxidation products. *J. Phys. Chem. A* **2016**, *120*, 1395−1407.
(63) Gao, S.; Keywood, M.; Ng, N. L.; Surratt, J.; Varutbangkul, V.; Bahreini, R.; Flagan, R. C.; Seinfeld, J. H. Low-molecular-weight and oligomeric components in secondary organic aerosol from the ozonolysis of cycloalkenes and α-pinene. *J. Phys. Chem. A* **2004**, *108*, 10147−10164.
(64) Jenkin, M. E. Modelling the formation and composition of secondary organic aerosol from α- and β-pinene ozonolysis using MCM v3. *Atmos. Chem. Phys.* **2004**, *4*, 1741−1757.
(65) Arellanes, C.; Paulson, S. E.; Fine, P. M.; Sioutas, C. Exceeding of Henry's law by hydrogen peroxide associated with urban aerosols. *Environ. Sci. Technol.* **2006**, *40*, 4859−4866.

DOI: 10.1021/acs.est.7b04863
Environ. Sci. Technol. 2018, 52, 2108−2117

Appendix B

A STEADY-STATE CONTINUOUS FLOW CHAMBER FOR THE STUDY OF DAYTIME AND NIGHTTIME CHEMISTRY UNDER ATMOSPHERICALLY RELEVANT NO LEVELS

Zhang, Xuan, John Ortega, Yuanlong Huang, Stephen Shertz, Geoffrey S. Tyndall, and John J. Orlando (2018). "A steady-state continuous flow chamber for the study of daytime and nighttime chemistry under atmospherically relevant NO levels". In: *Atmos. Meas. Tech.* 11.5, pp. 2537–2551. DOI: 10.5194/amt-11-2537-2018.

Atmos. Meas. Tech., 11, 2537–2551, 2018
https://doi.org/10.5194/amt-11-2537-2018

Atmospheric Measurement Techniques
Open Access
EGU

A steady-state continuous flow chamber for the study of daytime and nighttime chemistry under atmospherically relevant NO levels

Xuan Zhang[1,*], **John Ortega**[1,*], **Yuanlong Huang**[2], **Stephen Shertz**[1], **Geoffrey S. Tyndall**[1], **and John J. Orlando**[1]

[1]Atmospheric Chemistry Observation & Modeling Laboratory (ACOM), National Center for Atmospheric Research (NCAR), Boulder, CO, USA
[2]Department of Environmental Science and Engineering, California Institute of Technology, Pasadena, CA, USA
[*]These authors contributed equally to this work.

Correspondence: Xuan Zhang (xuanz@ucar.edu)

Received: 9 January 2018 – Discussion started: 12 January 2018
Revised: 4 April 2018 – Accepted: 6 April 2018 – Published: 3 May 2018

Abstract. Experiments performed in laboratory chambers have contributed significantly to the understanding of the fundamental kinetics and mechanisms of the chemical reactions occurring in the atmosphere. Two chemical regimes, classified as "high-NO" vs. "zero-NO" conditions, have been extensively studied in previous chamber experiments. Results derived from these two chemical scenarios are widely parameterized in chemical transport models to represent key atmospheric processes in urban and pristine environments. As the anthropogenic NO_x emissions in the United States have decreased remarkably in the past few decades, the classic "high-NO" and "zero-NO" conditions are no longer applicable to many regions that are constantly impacted by both polluted and background air masses. We present here the development and characterization of the NCAR Atmospheric Simulation Chamber, which is operated in steady-state continuous flow mode for the study of atmospheric chemistry under "intermediate NO" conditions. This particular chemical regime is characterized by constant sub-ppb levels of NO and can be created in the chamber by precise control of the inflow NO concentration and the ratio of chamber mixing to residence timescales. Over the range of conditions achievable in the chamber, the lifetime of peroxy radicals (RO_2), a key intermediate from the atmospheric degradation of volatile organic compounds (VOCs), can be extended to several minutes, and a diverse array of reaction pathways, including unimolecular pathways and bimolecular reactions with NO and HO_2, can thus be explored. Characterization experiments under photolytic and dark conditions were performed and, in conjunction with model predictions, provide a basis for interpretation of prevailing atmospheric processes in environments with intertwined biogenic and anthropogenic activities. We demonstrate the proof of concept of the steady-state continuous flow chamber operation through measurements of major first-generation products, methacrolein (MACR) and methyl vinyl ketone (MVK), from OH- and NO_3-initiated oxidation of isoprene.

1 Introduction

With the discovery of the role of biogenic volatile organic compounds (BVOCs) in urban photochemical smog (Chameides et al., 1988), the interactions of biogenic emissions with manmade pollution and their subsequent impact on the atmosphere's oxidative capacity and aerosol burden have received extensive studies in the ensuing decades (De Gouw et al., 2005; Ng et al., 2007; Goldstein et al., 2009; Surratt et al., 2010; Rollins et al., 2012; Shilling et al., 2013; Xu et al., 2015). A particular research focus has been understanding the influence of nitrogen oxides ($NO_x = NO+NO_2$) on the atmospheric oxidation cascades of BVOCs, which ultimately generate ozone (O_3) and secondary organic aerosols (SOA). Nitrogen oxides alter the distribution of BVOC oxidation products by primarily modulating the fate of peroxy radicals (RO_2), a key intermediate produced from the atmospheric degradation of VOCs by major oxidants including OH, O_3, and NO_3. In the absence of NO_x, RO_2 reacts predominantly with HO_2 radicals yielding organic peroxides and other products and, to a lesser extent, undergoes self- or

cross-reactions yielding carbonyls, alcohols, and multifunctional species. In the presence of elevated NO_x, the dominant fate of RO_2 is to react with NO leading to ozone production, and also to organic nitrates. During the night, RO_2 also reacts with NO_3 which is produced by the reaction between O_3 and NO_2. In addition, reaction of peroxyacyl radicals ($RC(O)O_2$) with NO_2 produces peroxyacyl nitrates that constitute a large reservoir of reactive nitrogen and a potentially important SOA precursor (Singh and Hanst, 1981; Nguyen et al., 2015).

Much of our understanding of the extent to which NO_x mediates the oxidation chemistry of BVOC in the atmosphere has been derived from measurements in laboratory chambers, where two extreme experimental conditions, i.e., "high-NO" vs. "zero-NO", were mostly performed to examine the reaction pathways of RO_2 radicals (Kroll and Seinfeld, 2008; Orlando and Tyndall, 2012; Ziemann and Atkinson, 2012). Results from these two chemical regimes have been widely incorporated into chemical transport models to represent key atmospheric processes in urban and pristine environments, respectively (Kanakidou et al., 2005). In the actual atmosphere, however, the fate of RO_2 radicals is rather more complicated than simply undergoing bimolecular reactions with NO / HO_2 as observed under the two extreme chamber conditions. It has been recently revealed that RO_2 radicals may undergo an internal H-shift followed by sequential O_2 addition, leading to highly oxygenated multifunctional peroxides (Ehn et al., 2014; Jokinen et al., 2015; Kurtén et al., 2015; Kirkby et al., 2016; Zhang et al., 2017). The rate of H-shift largely depends on the thermochemistry of the nascent alkyl radicals and can be reasonably fast, on a timescale of seconds to minutes (Crounse et al., 2013). Further, depending on the stability of the RO_2 precursor (alkyl radicals), RO_2 radicals may lose O_2 in competition with bimolecular reactions with NO, NO_3, RO_2, and HO_2. Recent theoretical and laboratory studies have found that the hydroxy peroxy radical conformers produced from isoprene photooxidation decompose readily to allylic radicals on timescales faster than bimolecular processes under atmospherically relevant NO and HO_2 levels (tens to hundreds of parts per trillion by volume). This highly dynamic system leads to formation of distinctly different products that depend on the concentrations of bimolecular reaction partners from those observed in chamber experiments under "high-NO" and "zero-NO" conditions (Teng et al., 2017).

Anthropogenic NO_x emissions in the United States have decreased remarkably in the past few decades (EPA, 2014), resulting in significant changes in the degradation mechanisms of BVOCs, especially in regions impacted by both background and polluted air masses such as the southeastern United States. However, the ultimate fate of peroxy radicals in environments with sub-ppb NO levels is still poorly constrained, in part due to a lack of consistent measurements under well-controlled conditions. Experimental approaches targeting a controlled NO level (sub-ppb to ppb) have been introduced over the years. For outdoor chambers, experiments were typically performed by exposing a gas mixture of O_3 / NO_x / VOCs or HONO / NO_x / VOCs to natural sunlight (Bloss et al., 2005; Karl et al., 2006). OH radicals were produced either via the photolysis of ozone and subsequent reaction of $O(^1D)$ with H_2O or directly from the photolysis of HONO. NO levels ranging from a few hundreds of ppt to a few ppb over the course of several hours of reactions have been reported. In the absence of any additional supply, NO will be eventually depleted in a closed chamber environment, and the initial "moderate-NO" condition will essentially transfer to the "zero-NO" condition. For indoor chambers, a "slow chemistry" scenario initiated by photolyzing methyl nitrite (CH_3ONO) under extremely low UV intensities as the OH radical source ($J_{CH_3ONO} \sim 10^{-5}\,s^{-1}$) was created to study the autoxidation chemistry of peroxy radicals produced from isoprene photooxidation (Crounse et al., 2011, 2012; Teng et al., 2017). The resulting NO and HO_2 mixing ratios are maintained at $\sim$ ppt level ($CH_3ONO + O_2 + h\nu \rightarrow HO_2 + NO + HCHO$) over the course of several hours of reaction, and the average OH concentration ($OH \sim 10^5$ molec cm^{-3}) is approximately 1 order of magnitude lower than that in the typical daytime ambient atmosphere. Another example relates to a recent method development in the potential aerosol mass (PAM) flow tube reactor where nitrous oxide (N_2O) was used to produce $\sim$ ppb level of NO ($O_3 + h\nu \rightarrow O_2 + O(^1D)$; $O(^1D) + N_2O \rightarrow 2NO$) (Lambe et al., 2017). Timescales for chemical reactions and gas–particle partitioning are ultimately limited to the mean residence time (~ 80 s) of the PAM reactor.

An alternative experimental platform to the batch-mode chamber and flow tube reactor described above is a well-mixed steady-state chamber with continuous feed of reactants and continuous withdrawal of reactor contents (Shilling et al., 2008). An attribute of the continuous flow steady-state chamber is that, by control of the inlet reactant concentrations and the ratio of mixing to residence timescales, it is possible to simulate atmospheric oxidation under stable conditions over a wide range of time periods and chemical scenarios. For example, a steady-state NO level at ~ 1 ppb was created by the continuously mixed flow chamber operation for the study of isoprene photooxidation chemistry (Liu et al., 2013). In this study, we present the development and characterization of the NCAR Atmospheric Simulation Chamber, which is operated in steady-state continuous flow mode for simulating atmospheric daytime and nighttime chemistry over chemical regimes not accessible in static chamber experiments. We focus on establishing an "intermediate NO" regime characterized by a constant steady-state NO level ranging from tens of ppt to a few ppb in the chamber. This particular chemical regime is well suited for the study of atmospheric behavior of RO_2 radicals, as they can survive up to minutes and embrace various reaction possibilities as opposed to reaction with NO, NO_3, HO_2, and RO_2 as their dominant fate observed in most batch-mode chamber

experiments. We employ the "intermediate NO" regimes to reexamine the daytime and nocturnal chemistry of isoprene through the measurements of two first-generation products, methacrolein (MACR) and methyl vinyl ketone (MVK).

2 Experimental

2.1 NCAR Atmospheric Simulation Chamber facilities

The NCAR Atmospheric Simulation Chamber consists of a 10 m^3 FEP Teflon (0.005 in. thick) bag that is housed in a cubic enclosure with UV reflective surfaces and a bank of 128 wall-mounted blacklight tubes (32 W, type F32T8/BL). To characterize photolytic conditions in the chamber, irradiance spectra were collected in the wavelength range of 180–600 nm at $\sim$ 0.8 nm resolution by a custom-built spectroradiometer, as shown in Fig. S1 in the Supplement (Petropavlovskikh et al., 2007). Photolysis frequencies were calculated based on the measured downwelling spectral actinic fluxes. The computed photolysis rate of NO_2 ($J_{NO_2} \sim 1.27 \times 10^{-3}\,s^{-1}$) agrees within 3 % with that measured by photolyzing 18.6 ppb NO_2 in the chamber and monitoring the NO production rate. The chamber is equipped with a standard set of measurements, including an integrated temperature and humidity probe (model 50U, VAISALA, CO) and a Magnehelic differential pressure indicating transmitter (model 605-11, Dwyer Instruments, IN). The chamber temperature is controlled at 295 K by the building's air conditioning system and increases to 305–306 K under maximum irradiation conditions. The relative humidity of the chamber air is below 10 % under dry conditions (the remaining water vapor is generated from methane combustion during the air purification process) and can be varied in the range of $\sim$ 10–50 % by flowing a portion of the purified dry flushing air into the chamber through a temperature-controlled water reservoir. Typical temperature and relative humidity profiles across the chamber under maximum irradiation conditions are given in Fig. S1 in the Supplement. The chamber internal pressure is maintained slightly above the ambient pressure to minimize the enclosure air contamination via penetration through the Teflon film.

Prior to each experiment, the chamber was flushed with purified dry air from an ultra high purity zero air generator (model 737, Aadco Instruments, OH) for $>$ 12 h until ozone and NO_x levels were below 1 ppb. During the operation of the steady-state continuous flow mode, the chamber was constantly flushed with purified dry air at 40 L min^{-1}, which gives an average chamber residence time of 4.17 h. The incoming and outgoing flows were balanced by a feedback control system that maintains a constant internal pressure of 1.2–4.9 $\times 10^{-4}$ atm above the ambient. The chamber is actively mixed by the turbulence created by the 40 L min^{-1} flushing air. The characteristic mixing time is defined as the time it takes for the measurement signal of a tracer compound (e.g., CO_2 and NO) to stabilize following a pulse injection. The average mixing time in the NCAR chamber was determined to be $\sim$ 9 min, which is $\sim$ 4 % of the residence time. Under such conditions, the gas- and particle-phase composition in the outflow can be assumed identical to that in the well-mixed core of the chamber.

To mimic daytime photochemistry in the continuous flow mode, steady-state OH mixing ratio was created by photolyzing hydrogen peroxide (H_2O_2) vapor that was continuously flowing into the chamber ($H_2O_2 + h\nu \rightarrow 2OH$, $J_{H_2O_2} \sim 4.33 \times 10^{-7}\,s^{-1}$). Specifically, a 20 mL syringe (NORM-JECT, Henke-Sass Wolf, MA) held on a syringe pump (model 100, KD Scientific, MA) kept at $\sim$ 4 °C was used to deliver H_2O_2 solution (1–30 wt %, Sigma Aldrich, MO) into a glass bulb that was gently warmed at $\sim$ 32 °C. The liquid delivery rate was sufficiently slow (100–300 µL min^{-1}) that all the H_2O_2 vapor was released into the glass bulb through evaporation of a small droplet hanging on the needle tip. An air stream (5 L min^{-1}) swept the H_2O_2 vapor into the chamber, resulting in an H_2O_2 mixing ratio in the range of 600 ppb to 16.22 ppm in the injection flow as a function of the concentration of H_2O_2 aqueous solution used. A spreadsheet (Table S2) for calculating the inflow H_2O_2 mixing ratio using the above input method is provided in the Supplement. As H_2O_2-laden air was continuously entering the chamber, it took approximately three turnover times ($\sim$ 12.5 h) for the desired H_2O_2 vapor mixing ratio to reach steady state in the chamber. The H_2O_2 vapor concentration in the chamber, though not measured, can be estimated from the steady-state OH mixing ratio derived from the observed exponential decay of a given parent hydrocarbon. Constant NO injection flow was achieved by diluting the gas flow from a concentrated NO cylinder (NO = 133.16 ppm, balance N_2) to a desired mixing ratio (0.1–100 ppb) using a set of mass flow controllers (Tylan FC260 and FC262, Mykrolis Corp., MA). The lowest steady-state NO level that can be achieved in the chamber is around 30 ppt (unpublished, NCAR). Note that for experiments performed in the absence of any VOC precursor, H_2O_2 and NO were the only two species that were continuously input into the chamber for the establishment of a combination of different photochemical conditions as denoted by the O_3 and NO_x measurements. For the isoprene photooxidation experiments, an isoprene standard (C_5H_8 = 531 ppm, balance N_2) was constantly injected into the chamber and diluted with the flushing air to achieve an inflow concentration of $\sim$ 20 ppb.

To mimic the nighttime chemistry in the continuous flow mode, steady-state NO_3 mixing ratio was created by constantly flowing diluted O_3 and NO air into the chamber ($NO + O_3 \rightarrow NO_2 + O_2$; $NO_2 + O_3 \rightarrow NO_3 + O_2$). The NO source can be replaced by NO_2, although the absolute absence of NO does not necessarily represent the actual atmospheric conditions. O_3 was produced by photolyzing O_2 in air at 185 nm using a mercury Pen-Ray lamp (UVP LLC, CA). Ozone concentration in the injection flow can

be controlled from 3.5 to 457 ppb automatically by adjusting the mercury lamp duty cycle. To study the $RO_2 + HO_2$ pathway, formaldehyde (CH_2O) was input into the chamber along with NO and O_3 to initiate HO_2 production ($NO_3 + CH_2O + O_2 \rightarrow HNO_3 + HO_2 + CO$). Formaldehyde aqueous solution (37 wt %, Sigma Aldrich, MO) was diluted with ultrapure water (Milli-Q, Merck Millipore, MA) to 0.2–1.0 wt % and continuously input into the chamber using the same method used for H_2O_2 input described above. It is worth noting that the formaldehyde aqueous solution contains 10–15 % methanol as stabilizer to prevent polymerization. The presence of methanol in the chamber does not significantly impact the nocturnal chemistry as it consumes OH and NO_3 radicals to generate formaldehyde and additional HO_2 ($CH_3OH + NO_3 \rightarrow HNO_3 + CH_2O + HO_2$, $CH_3OH + OH \rightarrow H_2O + CH_2O + HO_2$) (Atkinson et al., 2006). The use of formaldehyde as an HO_2 source mimics closely the atmospheric nighttime conditions in forest environments (Schwantes et al., 2015). To study the NO_3-initiated oxidation of isoprene, an injection flow of diluted isoprene ($\sim$ 10 ppb) was achieved using the procedure described above.

2.2 Analytical measurements

A suite of instruments was used to monitor gas-phase concentrations in the chamber outflow. O_3 was monitored by absorption spectroscopy with 0.5 ppb detection limit (model 49, Thermo Scientific, CO). The O_3 monitor was calibrated using an Ozone Primary Standard in the range of 0–200 ppb (model 49i-PS, Thermo Scientific, CO). The O_3 monitor used for chamber experiments was periodically checked with the primary standard and was shown to be stable over long periods of time (less than 1 ppb drift in over 1 year). NO was monitored by chemiluminescence with 0.5 ppb detection limit (model CLD 88Y, Eco Physics, MI). Zero-point and span calibrations of the NO_x monitor were performed prior to each experiment by supplying the instrument with pure N_2 gas and diluted NO, respectively. Multi-point calibration was performed on a weekly basis and has shown a good stability and linearity in the NO measurement ranging from 1 to 200 ppb. NO_x ($NO + NO_2$) measurements were performed using a photolytic converter that selectively converts NO_2 to NO upstream of the photo-multiplier tube in the CLD 88Y NO monitor. This converter uses two opposing arrays of UV LEDs shining into a cylindrical quartz mixing tube to achieve approximately 50 % conversion of NO_2 to NO per second. The total efficiency for the equipment described here is approximately 70 % as determined by measuring calibrated NO_2 standards. The sample path always includes the photolytic converter, and typical experiments cycle the power for the LED lights to switch between measuring NO (lights off) and NO_x (lights on). NO_2 concentrations were then determined by subtracting the NO from the adjacent NO_x measurements.

A customized proton transfer reaction quadrupole mass spectrometer (PTR-Q-MS) was used to measure volatile organic compounds including isoprene (C_5H_8), MACR (C_4H_6O), and MVK (C_4H_6O). The instrument was operated at 2.3 mbar drift pressure and 560 V drift voltage. Measurements reported here were obtained at a sampling rate of 10 Hz. In positive-mode operation, a given analyte [M] undergoes proton transfer reaction, producing an ion of the form $[M+H]^+$; that is, isoprene is detected as ion $C_5H_9^+$ (m/z 69) and MACR and MVK are both detected as ion $C_4H_7O^+$ (m/z 71). The instrument background was collected by sampling the chamber air for at least 30 min prior to each experiment. Measured ion intensities for isoprene ($C_5H_9^+$, m/z 69) and MACR and MVK ($C_4H_7O^+$, m/z 71) were calculated as the signal of each ion (counts per seconds) normalized to the total ion signal of H_3O^+. The instrument sensitivities towards isoprene, MACR, and MVK were calibrated with a mixture of diluted gas standards. The instrument sensitivity towards MACR is identical to that of MVK and, as a result, the sum of MACR and MVK concentration in the sampling air can be calculated by applying one calibration factor to the measured $C_4H_7O^+$ (m/z 71) signal intensity. Since artifacts in the measured $C_4H_7O^+$ signal can be produced through thermal decomposition of isoprene oxidation products, such as the peroxides, nitrates, and epoxides, on contact with hot metal surface (Liu et al., 2013; Nguyen et al., 2014b; Rivera-Rios et al., 2014), a cold-trap system was used to avoid bias in the interpretation of the PTR-Q-MS data. Specifically, a 1 m section of Teflon tubing was submerged in a low-temperature ethanol bath (-40 ± 2 °C) that could trap oxidized products less volatile than the authentic MACR and MVK standards after steady state was established in the chamber. The quantification of the sum of MACR and MVK was then based on the PTR-Q-MS measured $C_4H_7O^+$ (m/z 71) signal downstream of the cold trap.

3 Kinetic modeling

Reaction kinetics and mechanisms for the gas-phase photochemistry were extracted from the Master Chemical Mechanism (MCMv3.3.1, accessible at http://mcm.leeds.ac.uk/MCM/, last access: 4 January 2018). The inorganic reaction scheme includes 21 species and 48 reactions; the isoprene oxidation system includes 611 species and 1974 reactions. The kinetic schemes were implemented in MATLAB (Mathworks) to simulate the temporal profile of a given compound i in the chamber operated in the steady-state continuous flow mode:

$$\frac{dC_i}{dt} \cdot \tau = C_{i,0} + P_i - C_i - \sum k_i \cdot \tau \cdot C_i, \quad (1)$$

where C_i (molec cm^{-3}) is the gas-phase concentration of compound i in the well-mixed core of the chamber; $C_{i,0}$ (molec cm^{-3}) is the initial gas-phase concentration of com-

pound i in the injection flow; k_i (s^{-1}) is the pseudo-first-order rate coefficient for a chemical reaction that consumes compound i; τ (s) is the chamber mean residence time and can be calculated as the total chamber volume divided by the incoming and outgoing flow rate; and P_i (molec cm^{-3}) is the increment in the concentration of compound i through chemical production during one residence time. Note that two terms are neglected in Eq. (1), i.e., organic vapor condensation onto particles and deposition on the chamber wall. This is a reasonable simplification here due to the relatively high volatility ($\geq 10^{-1}$ atm) of compounds studied (Zhang et al., 2015b; Krechmer et al., 2016; Huang et al., 2018). Incorporation of these two terms into Eq. (1) is feasible given the vapor pressure of compound i, suspended particle size distribution, gas–particle and gas–wall partitioning coefficient, accommodation coefficients of compound i on particles and walls, and the effective absorbing organic masses on the wall (Zhang et al., 2014a, 2015b; Huang et al., 2016; McVay et al., 2016; Nah et al., 2016).

Model simulations used for comparison with chamber measurements were initialized using experimental conditions summarized in Table S1 in the Supplement. Model input parameters for all simulations include temperature (295 K at dark and 306 K under irradiation), local pressure (8.6×10^4 Pa), relative humidity (8 % at dark and 5 % under irradiation), light intensity ($J_{NO_2} = 1.27 \times 10^{-3}\ s^{-1}$ under irradiation and 0 at dark), chamber mean residence time (4.17 h), and input mixing ratios of H_2O_2 (0.11–16.2 ppm for photolytic experiments), NO (0.1–100 ppb for photolytic experiments and 10–20 ppb for dark experiments), O_3 (22–225 ppb for dark experiments), HCHO (0–600 ppb for dark experiments), and isoprene (19.9 ppb for photolytic experiments and 10.2 ppb for dark experiments). The model was propagated numerically for 25 h duration for each experiment.

4 Results and discussions

4.1 Optimal operating conditions for daytime photochemistry

Figure 1 shows the model-predicted steady-state mixing ratios of OH, HO_2, NO_3, NO, NO_2, and O_3 in the chamber after 20 h of photochemical reactions as a function of the H_2O_2 and NO concentrations in the continuous injection flow. Six blank chamber experiments were compared with simulations. In general, the model captures the evolution patterns of NO_x and O_3 well. The predicted mixing ratios of NO, NO_2, and O_3 agree within 69, 11, and 33 %, respectively, with the measurements (see Table S1 and Fig. S2 in the Supplement). The relatively large NO uncertainties originate from the measurements that were performed close to the instrument detection limit (0.5 ppb).

Simulated steady-state mixing ratios of OH radicals ($[OH]_{ss}$) range from $\sim 5 \times 10^5$ to $\sim 4 \times 10^6$ molec cm^{-3}, which over ~ 4 h chamber residence time would be roughly equivalent to ~ 1 to ~ 8 h of atmospheric OH exposure (1×10^6 molec cm^{-3}). As expected, $[OH]_{ss}$ increases with increasing NO influxes due to the enhanced NO_x / O_3 cycling but decreases with increasing H_2O_2 influxes due to the overwhelming reaction $OH + H_2O_2 \rightarrow H_2O + HO_2$. As a consequence, the steady-state mixing ratios of HO_2 radicals ($[HO_2]_{ss}$) reach up to $\sim 7 \times 10^9$ molec cm^{-3} when 16.2 ppm H_2O_2 is continuously injected into the chamber. If 110 ppb H_2O_2 is used instead, the resulting $[HO_2]_{ss}$ levels fall close to the ambient range ($\sim 10^8$ molec cm^{-3}).

Simulated steady-state NO mixing ratios in the chamber range from ~ 2 ppt to ~ 0.9 ppb from combinations of 0.1–20 ppb NO and 0.11–16.22 ppm H_2O_2 in the injection flow. The ratio of inflow NO concentration to the steady-state NO concentration in the chamber ranges from 5 to 93, demonstrating the importance of chemical removal in controlling the overall steady-state NO levels. O_3 accumulation is an inevitable consequence under photolytic conditions and, for example, the presence of 10 ppb O_3 leads to the chemical removal term ($k_{O_3+NO} \cdot [O_3] \cdot \tau$) in Eq. (1) that reduces the steady-state NO concentration by a factor of 60. It is worth noting that under all simulated conditions in the continuous flow mode, O_3 ($\sim$ 1–126 ppb) coexists with NO ($\sim$ 0.002–0.9 ppb). This particular chemical scenario, which is impossible to achieve in batch-mode reactors due to prompt conversion of NO to NO_2, could then be used to mimic ambient ozonolysis chemistry, for example, in forest regions that frequently encounter polluted air masses from nearby urban areas. The steady-state mixing ratios of NO_2 ($[NO_2]_{ss}$) exhibit a strong linear correlation with NO influxes. The use of less than 20 ppb NO in the injection flow results in a few to tens of ppb $[NO_2]_{ss}$, which is higher than the range typically found in the ambient. The potential "quenching" effect of NO_2 on RO_2 radicals through reversible termolecular reactions is discussed shortly.

In the so-called "high-NO_x" chamber experiments, the NO_3 radical is an unavoidable side-product when black lights are used as a representative of the solar radiation in mimicking the daytime photochemistry in the troposphere. The photolysis of NO_3, although its primary sink in the atmosphere, proceeds rather slowly ($J_{NO_3} \sim 1.8 \times 10^{-3}\ s^{-1}$) under the present chamber photolytic conditions, thereby leading to a significant accumulation of NO_3 radicals (7.9×10^4–2.8×10^8 molec cm^{-3}) at steady state. The simulated NO_3 / OH ratio dictates the extent to which the NO_3 (nighttime) chemistry competes with the OH-initiated (daytime) photochemistry. For compounds that are highly reactive towards NO_3 such as isoprene, NO_3-initiated oxidation accounts for up to ~ 60 % of the overall isoprene degradation pathways at the highest NO_3 / OH ratio (~ 255) simulated. Low concentrations of NO (< 20 ppb) and H_2O_2 (< 2 ppm) in the injection flow are therefore necessary to limit the interferences of NO_3-initiated chemistry. Again, taking isoprene as an example, the NO_3 oxidation pathway contributes less than 0.1 %

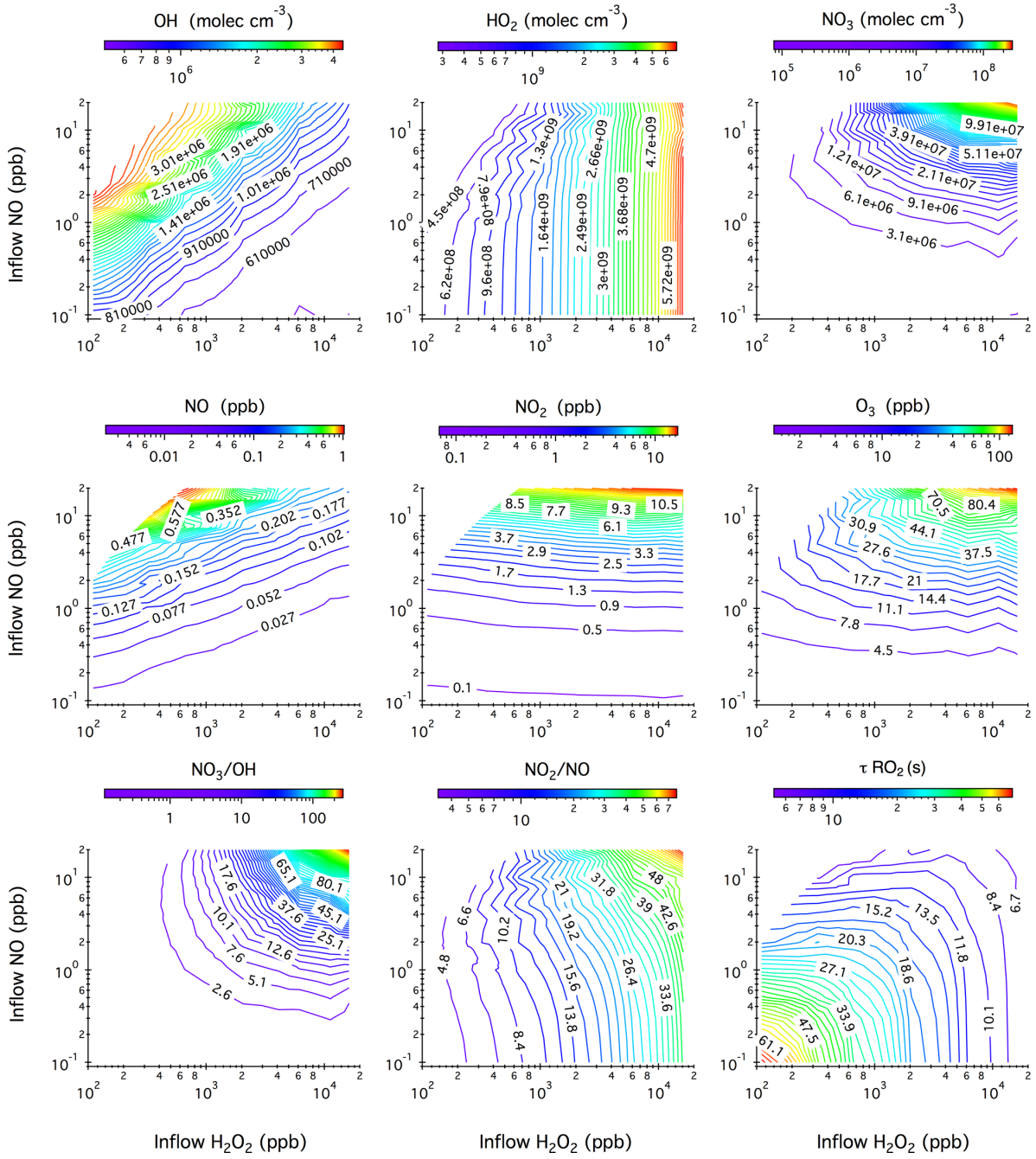

Figure 1. Contour plots showing the model-predicted steady-state mixing ratios of OH, HO_2, NO_3, NO, NO_2, and O_3 after 20 h of photochemical reactions in the chamber as a function of the concentrations of H_2O_2 and NO in the continuous injection flow. Also given here are the simulated NO_3 to OH ratio, NO_2 to NO ratio, and the lifetime of an RO_2 radical (τ_{RO_2}) with respect to reactions with NO and HO_2. Note that the ripples on the contour lines originate from the limited simulation datasets that are used to generate iso-response values.

of the overall isoprene degradation kinetics at the lowest NO_3 / OH ratio (~ 0.13) simulated here.

Also given in Fig. 1 is the calculated lifetime (τ_{RO_2}) of an RO_2 radical with respect to reactions with NO and HO_2 at 306 K. In most batch-mode chamber experiments, τ_{RO_2} of only several seconds or less can be achieved due to the presence of tens to hundreds of ppb levels of NO and HO_2. Here τ_{RO_2} could extend to 60 s or even longer with the continuous input of low mixing ratios of H_2O_2 (≤ 110 ppb) and NO (≤ 0.2 ppb). Note that the presence of tens of ppb NO_2 in the chamber might impose a "quenching" effect on the steady-state RO_2 level through rapid reversible reactions ($RO_2 + NO_2 + M \leftrightarrow RO_2NO_2 + M$). We evaluate this potential "quenching effect" using ethyl peroxy radical ($C_2H_5O_2$)

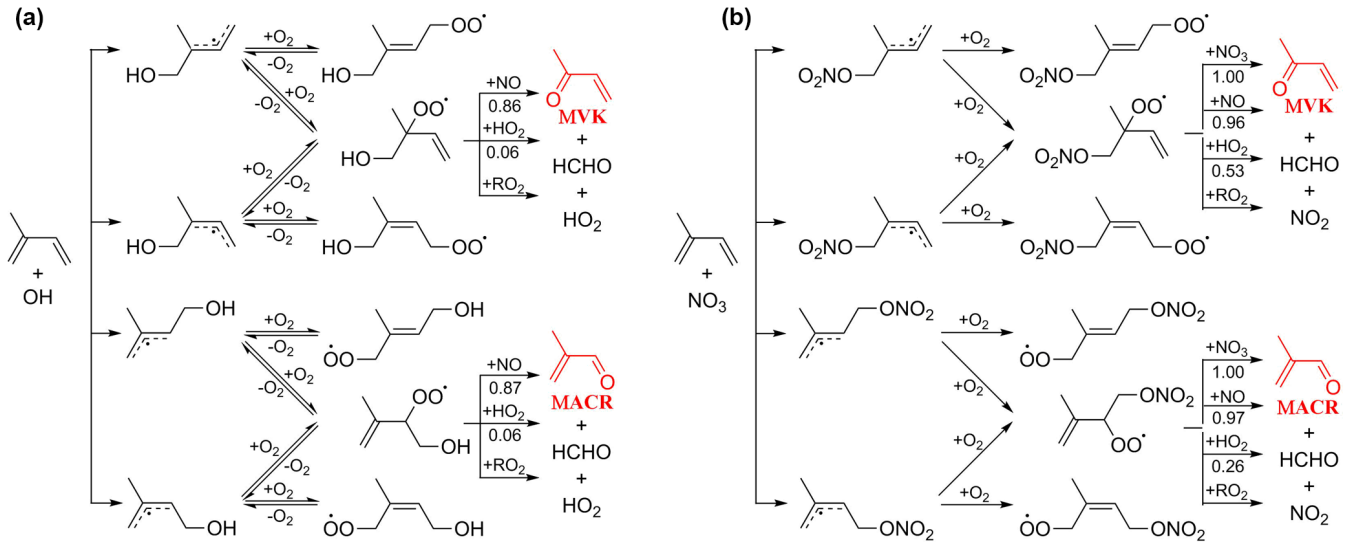

Figure 2. Representative mechanism for **(a)** OH- and **(b)** NO_3-initiated oxidation of isoprene that leads to the formation of MACR and MVK.

generated from OH oxidation of ethane as an example. Simulations shown in Fig. S3 in the Supplement reveal that incorporation of the $C_2H_5O_2 + NO_2 + M \leftrightarrow C_2H_5O_2NO_2 + M$ reaction into the mechanism in the presence of $\sim$ 1–80 ppb NO_2 does not notably change the behavior of $C_2H_5O_2$ radical. One exception is the peroxyacyl radical, which combines with NO_2 yielding peroxyacyl nitrate. For example, under 0.1–16 ppb $[NO_2]_{ss}$ as displayed in Fig. 1, we calculate that the time needed for peroxyacetyl radical ($CH_3C(O)O_2$) to reach equilibrium with peroxyacetyl nitrate ($CH_3C(O)O_2 + NO_2 + M \leftrightarrow CH_3C(O)O_2NO_2 + M$) ranges from $\sim$ 1 to $\sim$ 10 s, suggesting that the lifetime of peroxyacyl radicals is ultimately controlled by NO_2 instead of NO / HO_2 in the reaction system and, consequently, peroxyacyl radicals are not expected to be long-lived in the current chamber configuration.

We further compare the photochemical oxidation environment created here with the "intermediate-NO" conditions achieved by other chambers that employed the experimental approaches introduced earlier. In terms of the oxidizing power, all approaches are capable of maintaining an atmospheric relevant OH level ($\sim 10^6$ molec cm^{-3}) except the "slow chemistry" scenario that limits the photolysis rate of the OH precursor and results in an average OH mixing ratio of $\sim 10^5$ molec cm^{-3} (Crounse et al., 2012; Teng et al., 2017). At comparable OH levels, the overall atmospheric OH exposure achieved in the flow tube reactor is rather limited due to the short residence time (e.g., $\sim$ 80 s in the PAM reactor). In terms of the NO_x level, precisely controlled steady-state NO concentration can be achieved for an indefinite time period by operating chambers in the continuously mixed flow mode. However, NO_2 accumulates during the continuous oxidation process and the resulting NO_2 / NO ratio can be as much as an order of magnitude higher than that achieved in the static outdoor chambers.

4.2 Application to OH-initiated oxidation of isoprene

MACR and MVK are major first-generation products from the OH-initiated oxidation of isoprene in the presence of NO (Wennberg et al., 2018). They are produced from the decomposition of β-ISOPO alkoxy radicals that are primarily formed from the reaction of β-ISOPOO peroxy radicals (β-1-OH-2-OO and β-4-OH-3-OO) with NO; see mechanisms displayed in Fig. 2a. Reactions of β-ISOPOO peroxy radicals with HO_2 and RO_2 also partially yield β-ISOPO alkoxy radicals that ultimately lead to MACR and MVK, although these pathways are considered to be minor in the presence of hundreds to thousands of ppt NO in the atmosphere. The molar yields determined from previous studies range from 30 to 35 % for MVK and from 20 to 25 % for MACR under high-NO conditions (NO > 60 ppb) (Tuazon and Atkinson, 1990; Paulson and Seinfeld, 1992; Miyoshi et al., 1994; Ruppert and Becker, 2000; Sprengnether et al., 2002; Galloway et al., 2011; Liu et al., 2013). It has been recently shown that the six hydroxyl peroxy radicals (ISOPOO) produced from the initial OH addition to the double bonds of isoprene undergo rapid interconversion by removal or addition of O_2 that competes with bimolecular reactions under atmospherically relevant NO levels (Peeters et al., 2014; Teng et al., 2017). As a result, the distribution of ISOPOO radical isomers and their subsequent reaction products varies with their lifetimes with respect to bimolecular reactions. In the presence of hundreds of ppb NO as done by most previous experimental studies, the reaction of ISOPOO radicals with NO dominates over their interconversion, and the production of β-ISOPOO peroxy radical is less favored, leading the experiments to under-

estimate the MACR and MVK yields typically obtained in ambient conditions. Measurements by Karl et al. (2006) and Liu et al. (2013) conducted at NO concentrations comparable to the moderately polluted urban environment (~ 0.2 ppb in Karl et al. and ~ 1 ppb in Liu et al.) found higher MACR ($\sim 27\,\%$ in Karl et al. and $\sim 31.8\,\%$ in Liu et al.) and MVK ($\sim 41\,\%$ in Karl et al. and $\sim 44.5\,\%$ in Liu et al.) yields than other studies.

Here we perform a steady-state continuous-mode experiment to measure the production of MACR and MVK from the OH-initiated oxidation of isoprene in the presence of ~ 0.45 ppb NO. Figure 3 shows the observed and simulated temporal profiles of NO_x, O_3, C_5H_8, and C_4H_6O over 24 h photooxidation of isoprene. In this experiment, C_5H_8, H_2O_2, and NO were continuously fed into the chamber, with constant inflow concentrations of 19.9, 600, and 19 ppb, respectively. An outgoing flow at $40\,L\,min^{-1}$ continuously withdrew air from the chamber to balance the pressure. After approaching steady state, the sampling tube was submerged into a low-temperature ethanol bath ($-40 \pm 2\,^{\circ}C$) to trap oxidized products that would otherwise undergo thermal decomposition introducing interferences in the $C_4H_7O^+$ (m/z 71) signal. The measured concentrations of C_5H_8 and C_4H_6O upon cold trapping agree within 2.8 and 4.6 % uncertainties with the model simulations (see Fig. 3c and d).

To calculate the total molar yield ($Y_{C_4H_6O}$) of MACR and MVK, two reactions are considered:

$$C_5H_8 + OH \xrightarrow{k_1} Y_{C_4H_6O} \cdot C_4H_6O + \text{products}, \quad \text{(R1)}$$

$$C_4H_6O + OH \xrightarrow{k_2} \text{products}, \quad \text{(R2)}$$

where k_1 is the rate constant for OH reaction with isoprene, and k_2 is taken as the average of rate constants for OH reactions with MACR and MVK. Uncertainties associated with the simplification of k_2 in calculating the MACR and MVK yields will be discussed shortly. Note that the ozonolysis and NO_3-initiated oxidation in total account for less than 6 % of isoprene degradation pathway under current experimental conditions and are neglected in the calculation. The ozonolysis and photolysis in total account for $\sim 6\,\%$ of the C_4H_6O degradation pathway and are neglected here as well.

In the continuous-mode operation, two mass conservation equations are satisfied at steady state:

$$\frac{d[C_5H_8]_{ss}}{dt} = [C_5H_8]_0/\tau - [C_5H_8]_{ss}/\tau - k_1 \cdot [OH]_{ss} \cdot [C_5H_8]_{ss} = 0 \quad (2)$$

$$\frac{d[C_4H_6O]_{ss}}{dt} = Y_{C_4H_6O} \cdot k_1 \cdot [OH]_{ss} \cdot [C_5H_8]_{ss} - k_2 \cdot [OH]_{ss} \cdot [C_4H_6O]_{ss} - [C_4H_6O]_{ss}/\tau = 0 \quad (3)$$

where $[C_5H_8]_{ss}$ and $[C_4H_6O]_{ss}$ are the PTR-Q-MS measured steady-state concentrations of isoprene and the sum of MACR and MVK when using the cold trap, respectively, $[C_5H_8]_0$ is the initial concentration of isoprene, and τ is the chamber mean residence time and can be calculated as the total chamber volume divided by the incoming and outgoing flow rate. The steady-state OH radical concentration ($[OH]_{ss}$) can be derived by solving Eq. (2). The calculated $[OH]_{ss}$ (3.13×10^6 molec cm^{-3}) is 12 % higher than the model prediction (2.74×10^6 molec cm^{-3}). The molar yield of the sum of MACR and MVK from isoprene OH oxidation pathway in the presence of ~ 0.45 ppb NO is thus given by Eq. (4) and calculated as $76.7 \pm 5.8\,\%$:

$$Y_{C_4H_6O} = \frac{[C_4H_6O]_{ss} + k_2 \cdot [OH]_{ss} \cdot \tau \cdot [C_4H_6O]_{ss}}{k_1 \cdot [OH]_{ss} \cdot \tau \cdot [C_5H_8]_{ss}} \times f_{\beta\text{-ISOPOO+NO}}. \quad (4)$$

Here a 5.8 % uncertainty originates from the assumption that MACR + OH and MVK + OH proceed with equal reaction rate, although the rate constant for MVK + OH is $\sim 31\,\%$ lower than that of MACR + OH. Another potential uncertainty relates to the accuracy of the simulated steady-state HO_2 and RO_2 concentrations and the contribution of β-ISOPOO + HO_2 and β-ISOPOO + RO_2 reaction pathways to the overall β-ISOPOO fate. The fraction of β-ISOPOO radicals that reacts with NO ($f_{\beta\text{-ISOPOO+NO}}$) was predicted as 0.88, which was used here to scale the final MACR + MVK yield, see Eq. (4).

In summary, the measured yield of the sum of MACR and MVK in this study is close to that reported by Karl et al. (2006) and Liu et al. (2013), but ~ 27–$52\,\%$ higher than the majority of previous measurements performed under high-NO conditions (NO > 60 ppb). This is consistent with the dynamic nature of the six ISOPOO radical isomers that undergo rapid interconversion by addition or removal of O_2. In the presence of ~ 0.45 ppb NO as performed in this study, lifetimes of the β-1-OH-2-OO peroxy radical with respect to reaction with NO and loss of O_2 are estimated as 9.4 and 0.2 s, respectively, implying that the rapid interconversion between β-ISOPOO and δ-ISOPOO radicals essentially governs their distribution; under such conditions, the production of thermodynamically more stable β-ISOPOO isomers is favored, leading to higher yields of MACR and MVK. Here the reported MACR and MVK yield from isoprene OH oxidation in the presence of ~ 0.45 ppb NO represents an illustration of chamber operation at steady-state continuous flow mode for the establishment of certain experimental conditions that are not easily accessible from traditional batch-mode chamber experiments. A complete measurement of first-generation oxidation products from isoprene OH reaction under a wide range of NO levels (ISOPOO bimolecular lifetimes) will be forthcoming in a future publication.

4.3 Optimal operating conditions for nighttime chemistry

Figure 4 shows the model simulated steady-state mixing ratios of HO_2, NO_3, NO, NO_2, and O_3 after 16 h of dark reactions in the chamber as a function of the HCHO concen-

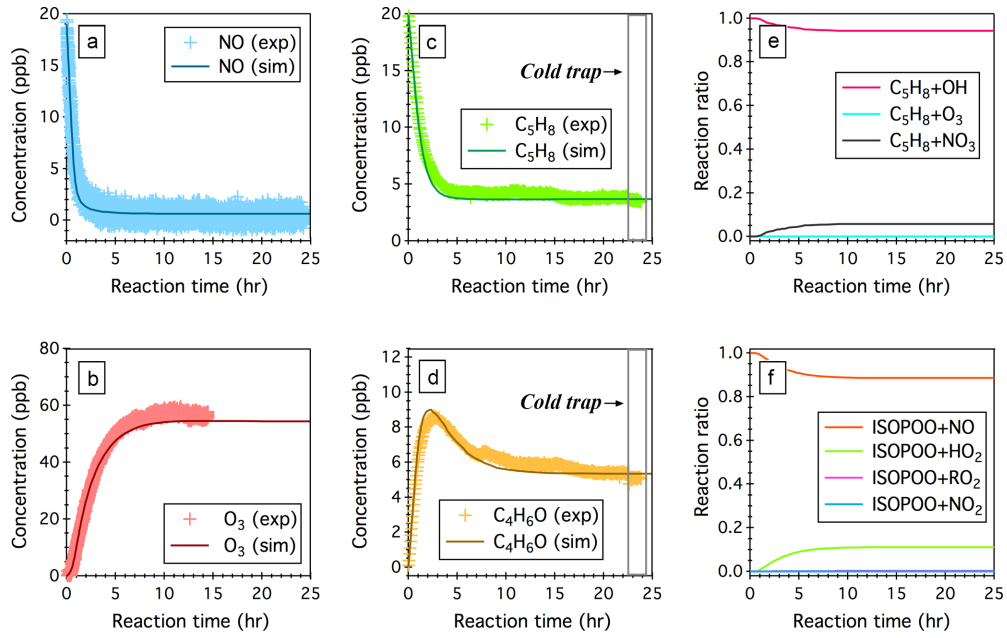

Figure 3. Simulated (sim.) and observed (exp.) temporal profiles of **(a)** NO, **(b)** O_3, **(c)** isoprene (C_5H_8), and **(d)** the sum of MACR and MVK (C_4H_6O) over 24 h OH-initiated oxidation of isoprene in the continuous flow mode chamber operation. Also displayed here include **(e)** simulated fractions of OH oxidation, ozonolysis, and NO_3 oxidation as the removal pathways of isoprene and **(f)** simulated fractions of ISOPOO radicals that react with NO, HO_2, RO_2, and NO_3. Time 0 is the point at which the chamber lights are turned on. Initial experimental conditions are 19 ppb NO, 0 ppb NO_2, 0 ppb O_3, 600 ppb H_2O_2, and 19.9 ppb C_5H_8, with continuous input of 600 ppb H_2O_2, 19 ppb NO, and 19.9 ppb C_5H_8 over the course of 24 h photochemical reactions.

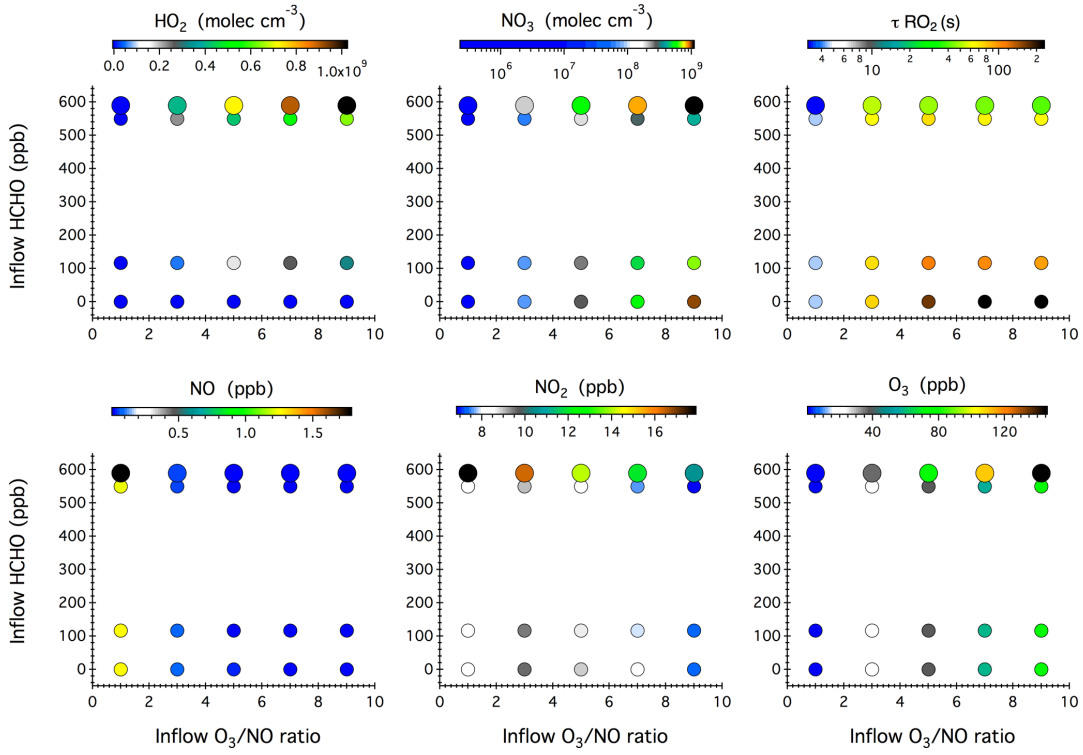

Figure 4. Simulated steady-state mixing ratios of HO_2, NO_3, NO, NO_2, and O_3 after 16 h of dark reactions in the chamber as a function of the concentrations of HCHO, NO, and O_3 in the continuous injection flow. The symbol size denotes different inflow NO concentrations, i.e., 10 and 20 ppb. Also given here is the calculated lifetime of an RO_2 radical (τ_{RO_2}) with respect to reactions with NO, NO_3, and HO_2.

tration and O_3 / NO ratio in the continuous chamber inflow. Blank experiments were compared with simulations in five cases (see Table S1 in the Supplement). The model captures the evolution patterns of NO_x and O_3 well. The observed mixing ratios of NO_2 and O_3 agree with the simulations to within 11 and 6 %, respectively (Fig. S4 in the Supplement).

Compared with the photochemical reaction schemes discussed earlier, the nocturnal chemistry is rather straightforward; that is, the inflow O_3 / NO ratio governs the steady-state concentrations of NO_3, NO_x, and O_3, while the inflow HCHO concentration ultimately controls the steady-state HO_2 level. Increasing the O_3 / NO ratio from 1 to 9 in the continuous inflow leads to increased NO_3 from 2.4×10^5 to 1.1×10^9 molec cm^{-3}, but decreased NO from 1.8 ppb to 20 ppt and decreased NO_2 from 18 to 7 ppb. At a fixed inflow O_3 / NO ratio, doubling the NO and O_3 concentrations leads to elevated NO_3, NO_x, and O_3 by a factor of 2.0–3.2, 1.5–2.0, and 1.4–2.0, respectively. The use of HCHO as an effective dark HO_2 source does not significantly impact the steady-state mixing ratios of NO_x and O_3, but slightly weakens the NO_3 production.

The calculated RO_2 lifetime (τ_{RO_2}) with respect to reactions with NO, NO_3, and HO_2 at 295 K ranges from 3 to 225 s. The highest τ_{RO_2} was achieved in the absence of any HCHO source and corresponds to a chemical regime that can be employed to study the intramolecular isomerization (autoxidation) pathway of RO_2 radicals, if any. Adding a continuous flow of HCHO to the system leads to the production of 10^7–10^9 molec cm^{-3} HO_2 radicals that then constitute a significant sink of RO_2 radicals and represents prevailing forest environments during nighttime.

4.4 Application to NO_3-initiated oxidation of isoprene

NO_3-initiated oxidation of isoprene proceeds by the NO_3 addition to the carbon double bonds followed by O_2 addition, yielding six distinct nitrooxy peroxy radicals (INOO), including two isomers (β-INOO) with O_2 added on the β-carbon to the nitrate group (see Fig. 2b for schematic illustration). The β-INOO radicals react further with NO_3, HO_2, NO, and RO_2, producing nitrooxy alkoxy radicals (β-INO) with molar yields of 1.00, 0.53, 0.97, and 0.40, respectively (Wennberg et al., 2018). The further decomposition of β-INO radicals produces MACR and MVK, together with HCHO and NO_2. Depending on the actual fate of β-INOO radicals, the yields of β-INO radicals can then vary from 0.4 to 1.0, resulting in a distinct distribution of final oxidation products. It is thus important to specify the ultimate fate of INOO radicals during quantification of oxidation products from isoprene reaction with NO_3. As an illustration, we performed one continuous-mode experiment that targets on controlling the steady-state fate of INOO radicals to be their reaction with NO and HO_2 (46 and 38 % INOO radicals are predicted to react with NO and HO_2, respectively, as shown in Fig. 5). Note that by adjusting the concentrations and fractions of inflow reactants (O_3, NO, HCHO, and C_5H_8), different chemical fates and lifetimes of INOO radicals can be achieved.

Figure 5 shows the observed and predicted temporal profiles of NO_x, O_3, C_5H_8, and C_4H_6O over 25 h of isoprene oxidation by NO_3, with continuous input of 10.2 ppb C_5H_8, 205 ppb O_3, and 59 ppb NO into the chamber and a balancing outgoing flow at 40 L min^{-1} carrying well-mixed reactants and products. It took $>$ 16 h to reach steady state for all the species displayed. In general, the model captures the trends of O_3 and NO well, while underpredicting the steady-state NO_2 by $\sim$ 26 %. After $\sim$ 18 h of dark reaction, the PTR-Q-MS sampling tubing was submerged into a cold ethanol bath (-40 ± 2 °C) to trap artifacts in the PTR-Q-MS measured $C_4H_7O^+$ (m/z 71) signal. The simulated steady-state concentration of isoprene agrees within 9 % with the measurements. The derived concentration of the sum of MACR and MVK from the measured $C_4H_7O^+$ ion intensity upon cold trapping is $\sim$ 1.1 ppb, which is $\sim$ 129 % higher than the model predictions ($\sim$ 0.48 ppb). This disagreement can be attributed, to a large extent, to the oversimplified representation of the six different INOO radicals as one δ-INOO isomer in the MCMv3.3.1 mechanism. As a result, the production of β-INOO radical, the important precursor of MACR and MVK, from NO_3-initiated oxidation of isoprene is suppressed in the simulations. The measured molar yield of the sum of MACR and MVK is 36.3 ± 12.1 %, with uncertainties arising from the fact that 10.5 % isoprene is predicted to react with OH as an additional source of MACR and MVK. Using this value, the fraction of β-INOO over the sum of nitrooxy peroxy radicals is estimated as 48.6 ± 16.2 %, which is close to that ($\sim$ 46.3 %) reported by Schwantes et al. (2015), although the estimated bimolecular lifetime of INOO radical in that study ($\sim$ 30 s) is lower than that predicted in the present work ($\sim$ 50 s). As discussed above, the hydroxyl peroxy radicals produced from OH oxidation of isoprene could undergo rapid interconversion through addition or removal of O_2 at atmospherically relevant lifetimes. This interconversion significantly impacts the subsequent chemistry of individual ISOPOO radical isomers in terms of reaction rates and product distributions. It is likely that the INOO radicals follow similar interconversion due to the small R-OO bond dissociation energy, although no experimental evidence exists. A full examination of the INOO chemistry, i.e., their kinetic and thermodynamic properties as well as their chemical fate at different lifetimes, will be the focus of future studies using this continuous flow chamber operation method.

5 Conclusions

We report here the development and characterization of the NCAR Atmospheric Simulation Chamber operated at steady-state continuous flow mode for simulating daytime and nocturnal chemistry under atmospherically relevant NO

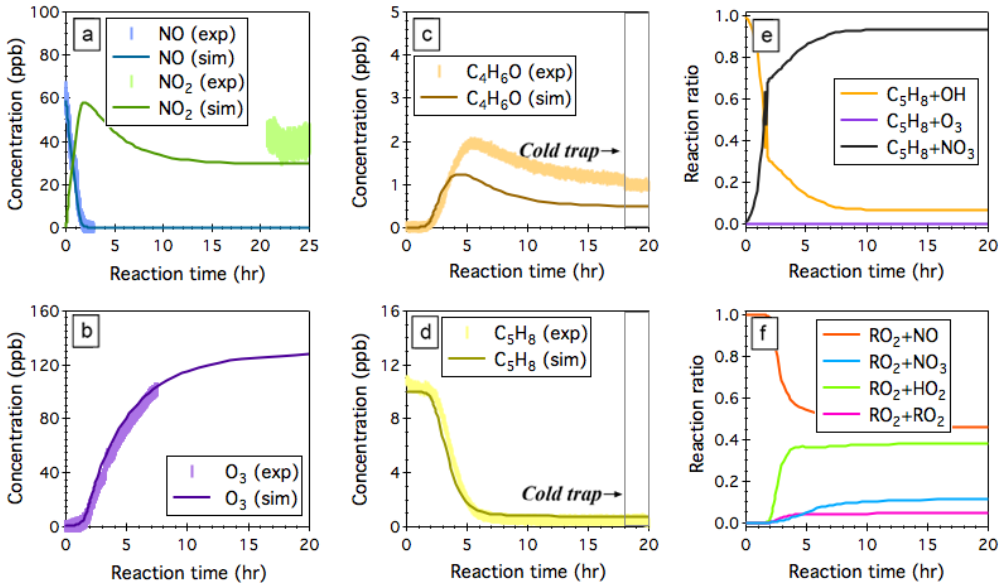

Figure 5. Simulated (sim.) and observed (exp.) evolution patterns of **(a)** NO_x, **(b)** O_3, **(c)** the sum of MACR and MVK (C_4H_6O), and **(d)** isoprene (C_5H_8) over 20 h NO_3-initiated oxidation of isoprene under continuous flow mode chamber operation. The fractions of isoprene that reacts with OH, O_3, and NO_3 are given in panel **(e)**, and the fractions of INOO radical that undergoes bimolecular reactions with NO, NO_3, HO_2, and RO_2 are given in panel **(f)**. Initial experimental conditions are 0 ppb O_3, 59 ppb NO_x, and 10.2 ppb C_5H_8, with continuous input of 205 ppb O_3, 59 ppb NO, and 10.2 ppb C_5H_8 over the course of 20 h dark reactions.

levels. The chamber is designed to achieve a well-controlled steady-state environment by continuous inflow of reactants and continuous withdrawal of reactor contents. We use a combination of kinetic modeling and chamber experiments to characterize the "intermediate-NO" chemical regime (tens of ppt to a few ppb) that can be achieved by precisely controlling the inlet reactant concentrations and the mixing/residence timescales of the chamber.

To mimic daytime photochemistry, continuous input of H_2O_2 and NO gases is required, resulting in steady-state OH mixing ratios of 10^5–10^6 molec cm^{-3} under irradiation. Under such conditions, the lifetime of a peroxy radical with respect to reaction with NO and HO_2 can be extended to 60 s or even longer, thus providing a unique environment to study all reaction possibilities of RO_2 radicals including the intramolecular isomerization (autoxidation) pathway. When studying OH-initiated chemistry, care needs to be taken to avoid a range of experimental conditions (e.g., inflow $H_2O_2 > 2$ ppm and NO > 20 ppb) where NO_3 oxidation might account for a large fraction of the overall degradation pathway of certain parent hydrocarbons such as alkenes.

To mimic nighttime chemistry, continuous input of NO (or NO_2) and O_3 is needed to produce steady-state NO_3 radicals in the range of 10^6–10^9 molec cm^{-3} in the dark. Under such conditions, an RO_2 radical can live up to 4 min prior to finding a bimolecular reaction partner (e.g., NO, NO_3, and HO_2), which were the dominant fates of RO_2 radicals in most batch-mode chamber experiments. Again, the long lifetime of RO_2 radicals achieved by the steady-state continuous-mode operation opens an avenue for close examination of RO_2 unimolecular (isomerization) pathways in nocturnal environments.

In simulating both daytime and nighttime chemistry with continuous flow operation method, O_3 accumulation is unavoidable. The extent to which ozonolysis interferes with OH- or NO_3-initiated oxidation chemistry depends on the steady-state O_3 concentration achieved in the chamber and its reactivity towards various parent VOCs. Taking isoprene as an example, ozonolysis accounts for < 1 and < 0.1 % of the overall isoprene degradation kinetics, respectively, under established steady-state photolytic and dark conditions described above.

In atmospheric chemistry, the terms "zero-NO" vs. "high-NO" have been widely used to classify photooxidation conditions and delineate the gas-phase fate of the peroxy radicals (RO_2) generated from VOCs oxidation (Zhang et al., 2010, 2014b, 2015a; He et al., 2011; Cappa et al., 2013; Zhang and Seinfeld, 2013; Loza et al., 2014; Nguyen et al., 2014a; Schilling Fahnestock et al., 2014; Krechmer et al., 2015; Gordon et al., 2016; Riva et al., 2016; Thomas et al., 2016; Schwantes et al., 2017a, b). In the so-called "high-NO" regime, reaction with NO dominates the fate of RO_2 radicals, whereas in the "zero-NO" regime, the RO_2 radicals primarily undergo reaction with HO_2 and, perhaps to a much lesser degree, self- or cross-combination. The importance of the "intermediate-NO" regime lies in the fact that at sub-ppb levels of NO, the $RO_2 + NO$ and $RO_2 + HO_2$ reactions are expected to co-exist and the RO_2 radical could survive up

to several minutes before encountering a partner (NO / HO_2) for bimolecular reactions. Under such conditions, the RO_2 radical isomers may undergo interconversion by addition or removal of O_2 and intramolecular isomerization (autoxidation) through H-shift. Here we use isoprene as an illustrative VOC to explore the fate of RO_2 radicals under sub-ppb NO. Future work will focus on detailed characterization of oxidation products from isoprene day- and nighttime chemistry with particular attention given to the controlled RO_2 fates and lifetimes.

Data availability. Data presented in this paper are available upon request to the corresponding author.

Supplement. The supplement related to this article is available online at: https://doi.org/10.5194/amt-11-2537-2018-supplement.

Competing interests. The authors declare that they have no conflict of interest.

Acknowledgements. The National Center for Atmospheric Research is operated by the University Corporation for Atmospheric Research, under the sponsorship of the National Science Foundation.

Edited by: Andreas Hofzumahaus
Reviewed by: Paul Seakins and one anonymous referee

References

Atkinson, R., Baulch, D. L., Cox, R. A., Crowley, J. N., Hampson, R. F., Hynes, R. G., Jenkin, M. E., Rossi, M. J., Troe, J., and IUPAC Subcommittee: Evaluated kinetic and photochemical data for atmospheric chemistry: Volume II – gas phase reactions of organic species, Atmos. Chem. Phys., 6, 3625–4055, https://doi.org/10.5194/acp-6-3625-2006, 2006.

Bloss, C., Wagner, V., Bonzanini, A., Jenkin, M. E., Wirtz, K., Martin-Reviejo, M., and Pilling, M. J.: Evaluation of detailed aromatic mechanisms (MCMv3 and MCMv3.1) against environmental chamber data, Atmos. Chem. Phys., 5, 623–639, https://doi.org/10.5194/acp-5-623-2005, 2005.

Cappa, C. D., Zhang, X., Loza, C. L., Craven, J. S., Yee, L. D., and Seinfeld, J. H.: Application of the Statistical Oxidation Model (SOM) to Secondary Organic Aerosol formation from photooxidation of C_{12} alkanes, Atmos. Chem. Phys., 13, 1591–1606, https://doi.org/10.5194/acp-13-1591-2013, 2013.

Chameides, W. L., Lindsay, R. W., Richardson, J., and Kiang, C. S.: The role of biogenic hydrocarbons in urban photochemical smog: Atlanta as a case study, Science, 241, 1473–1476, 1988.

Crounse, J. D., Paulot, F., Kjaergaard, H. G., and Wennberg, P. O.: Peroxy radical isomerization in the oxidation of isoprene, Phys. Chem. Chem. Phys., 13, 13607–13613, 2011.

Crounse, J. D., Knap, H. C., Ørnsø, K. B., Jørgensen, S., Paulot, F., Kjaergaard, H. G., and Wennberg, P. O.: Atmospheric fate of methacrolein. 1. Peroxy radical isomerization following addition of OH and O_2, J. Phys. Chem. A, 116, 5756–5762, 2012.

Crounse, J. D., Nielsen, L. B., Jørgensen, S., Kjaergaard, H. G., and Wennberg, P. O.: Autoxidation of organic compounds in the atmosphere, J. Phys. Chem. Lett., 4, 3513–3520, 2013.

De Gouw, J. A., Middlebrook, A. M., Warneke, C., Goldan, P. D., Kuster, W. C., Roberts, J. M., Fehsenfeld, F. C., Worsnop, D. R., Canagaratna, M. R., and Pszenny, A. A. P.: Budget of organic carbon in a polluted atmosphere: Results from the New England Air Quality Study in 2002, J. Geophys. Res.-Atmos., 110, D16305, https://doi.org/10.1029/2004JD005623, 2005.

Ehn, M., Thornton, J. A., Kleist, E., Sipilä, M., Junninen, H., Pullinen, I., Springer, M., Rubach, F., Tillmann, R., Lee, B., Lopez-Hilfiker, F., Andres, S., Acir, I.-H., Rissanen, M., Jokinen, T., Schobesberger, S., Kangasluoma, J., Kontkanen, J., Nieminen, T., Kurtén, T., Nielsen, L. B., Jørgensen, S., Kjaergaard, H. G., Canagaratna, M., Maso, M. D., Berndt, T., Petäjä, T., Wahner, A., Kerminen, V.-M., Kulmala, M., Worsnop, D. R., Wildt, J., and Mentel, T. F.: A large source of low-volatility secondary organic aerosol, Nature, 506, 476, https://doi.org/10.1038/nature13032, 2014.

EPA: Data from the 2011 National Emissions Inventory, Version 1, available at: http://www.epa.gov/air-emissions-inventories/2011-national-emissions-inventory-nei-data, last access: 2014.

Galloway, M. M., Huisman, A. J., Yee, L. D., Chan, A. W. H., Loza, C. L., Seinfeld, J. H., and Keutsch, F. N.: Yields of oxidized volatile organic compounds during the OH radical initiated oxidation of isoprene, methyl vinyl ketone, and methacrolein under high-NO_x conditions, Atmos. Chem. Phys., 11, 10779–10790, https://doi.org/10.5194/acp-11-10779-2011, 2011.

Goldstein, A. H., Koven, C. D., Heald, C. L., and Fung, I. Y.: Biogenic carbon and anthropogenic pollutants combine to form a cooling haze over the southeastern United States, P. Natl. Acad. Sci. USA, 106, 8835–8840, 2009.

Gordon, H., Sengupta, K., Rap, A., Duplissy, J., Frege, C., Williamson, C., Heinritzi, M., Simon, M., Yan, C., Almeida, J., Tröstl, J., Nieminen, T., Ortega, I. K., Wagner, R., Dunne, E. M., Adamov, A., Amorim, A., Bernhammer, A.-K., Bianchi, F., Breitenlechner, M., Brilke, S., Chen, X., Craven, J. S., Dias, A., Ehrhart, S., Fischer, L., Flagan, R. C., Franchin, A., Fuchs, C., Guida, R., Hakala, J., Hoyle, C. R., Jokinen, T., Junninen, H., Kangasluoma, J., Kim, J., Kirkby, J., Krapf, M., Kürten, A., Laaksonen, A., Lehtipalo, K., Makhmutov, V., Mathot, S., Molteni, U., Monks, S. A., Onnela, A., Peräkylä, O., Piel, F., Petäjä, T., Praplan, A. P., Pringle, K. J., Richards, N. A. D., Rissanen, M. P., Rondo, L., Sarnela, N., Schobesberger, S., Scott, C. E., Seinfeld, J. H., Sharma, S., Sipilä, M., Steiner, G., Stozhkov, Y., Stratmann, F., Tomé, A., Virtanen, A., Vogel, A. L., Wagner, A. C., Wagner, P. E., Weingartner, E., Wimmer, D., Winkler, P. M., Ye, P., Zhang, X., Hansel, A., Dommen, J., Donahue, N. M., Worsnop, D. R., Baltensperger, U., Kulmala, M., Curtius, J., and Carslaw, K. S.: Reduced anthropogenic aerosol radiative forcing caused by biogenic new particle formation, P. Natl. Acad. Sci. USA, 113, 12053–12058, 2016.

He, S., Chen, Z., and Zhang, X.: Photochemical reactions of methyl and ethyl nitrate: a dual role for alkyl nitrates in the nitrogen cycle, Environ. Chem., 8, 529–542, 2011.

Huang, D. D., Zhang, X., Dalleska, N. F., Lignell, H., Coggon, M. M., Chan, C. M., Flagan, R. C., Seinfeld, J. H., and Chan, C. K.: A note on the effects of inorganic seed aerosol on the oxidation state of secondary organic aerosol – α-pinene ozonolysis, J. Geophys. Res.-Atmos., 121, 12476–12483, 2016.

Huang, Y., Zhao, R., Charan, S. M., Kenseth, C. M., Zhang, X., and Seinfeld, J. H.: Unified theory of vapor-wall mass transport in Teflon-walled environmental chambers, Environ. Sci. Technol., 52, 2134–2142, 2018.

Jokinen, T., Berndt, T., Makkonen, R., Kerminen, V.-M., Junninen, H., Paasonen, P., Stratmann, F., Herrmann, H., Guenther, A. B., and Worsnop, D. R.: Production of extremely low volatile organic compounds from biogenic emissions: Measured yields and atmospheric implications, P. Natl. Acad. Sci. USA, 112, 7123–7128, 2015.

Kanakidou, M., Seinfeld, J. H., Pandis, S. N., Barnes, I., Dentener, F. J., Facchini, M. C., Van Dingenen, R., Ervens, B., Nenes, A., Nielsen, C. J., Swietlicki, E., Putaud, J. P., Balkanski, Y., Fuzzi, S., Horth, J., Moortgat, G. K., Winterhalter, R., Myhre, C. E. L., Tsigaridis, K., Vignati, E., Stephanou, E. G., and Wilson, J.: Organic aerosol and global climate modelling: a review, Atmos. Chem. Phys., 5, 1053–1123, https://doi.org/10.5194/acp-5-1053-2005, 2005.

Karl, M., Dorn, H. P., Holland, F., Koppmann, R., Poppe, D., Rupp, L., Schaub, A., and Wahner, A.: Product study of the reaction of OH radicals with isoprene in the atmosphere simulation chamber SAPHIR, J. Atmos. Chem., 55, 167–187, 2006.

Kirkby, J., Duplissy, J., Sengupta, K., Frege, C., Gordon, H., Williamson, C., Heinritzi, M., Simon, M., Yan, C., João, A., Tröstl, J., Nieminen, T., Ortega, I. K., Wagner, R., Adamov, A., Amorim, A., Bernhammer, A.-K., Bianchi, F., Breitenlechner, M., Brilke, S., Chen, X., Craven, J., Dias, A., Ehrhart, S., Flagan, R. C., Franchin, A., Fuchs, C., Guida, R., Hakala, J., Hoyle, C. R., Jokinen, T., Junninen, H., Kangasluoma, J., Kim, J., Krapf, M., Kürten, A., Laaksonen, A., Lehtipalo, K., Makhmutov, V., Mathot, S., Molteni, U., Onnela, A., Peräkylä, O., Piel, F., Petäjä, T., Praplan, A. P., Pringle, K., Rap, A., Richards, N. A. D., Riipinen, I., Rissanen, M. P., Rondo, L., Sarnela, N., Schobesberger, S., Scott, C. E., Seinfeld, J. H., Sipilä, M., Steiner, G., Stozhkov, Y., Stratmann, F., Tomé, A., Virtanen, A., Vogel, A. L., Wagner, A. C., Wagner, P. E., Weingartner, E., Wimmer, D., Winkler, P. M., Ye, P., Zhang, X., Hansel, A., Dommen, J., Donahue, N. M., Worsnop, D. R., Baltensperger, U., Kulmala, M., Carslaw, K. S., and Curtius, J.: Ion-induced nucleation of pure biogenic particles, Nature, 533, 521–526, 2016.

Krechmer, J. E., Coggon, M. M., Massoli, P., Nguyen, T. B., Crounse, J. D., Hu, W., Day, D. A., Tyndall, G. S., Henze, D. K., Rivera-Rios, J. C., Nowak, J. B., Kimmel, J. R., III, R. L. M., Stark, H., Jayne, J. T., Sipila, M., Junninen, H., Clair, J. M. S., Zhang, X., Feiner, P. A., Zhang, L., Miller, D. O., Brune, W. H., Keutsch, F. N., Wennberg, P. O., Seinfeld, J. H., Worsnop, D. R., Jimenez, J. L., and Canagaratna, M. R.: Formation of low volatility organic compounds and secondary organic aerosol from isoprene hydroxyhydroperoxide low-NO oxidation, Environ. Sci. Technol., 49, 10330–10339, 2015.

Krechmer, J. E., Pagonis, D., Ziemann, P. J., and Jimenez, J. L.: Quantification of gas-wall partitioning in Teflon environmental chambers using rapid bursts of low-volatility oxidized species generated in situ, Environ. Sci. Technol., 50, 5757–5765, 2016.

Kroll, J. H. and Seinfeld, J. H.: Chemistry of secondary organic aerosol: Formation and evolution of low-volatility organics in the atmosphere, Atmos. Environ., 42, 3593–3624, 2008.

Kurtén, T., Rissanen, M. P., Mackeprang, K., Thornton, J. A., Hyttinen, N., Jørgensen, S., Ehn, M., and Kjaergaard, H. G.: Computational study of hydrogen shifts and ring-opening mechanisms in α-pinene ozonolysis products, J. Phys. Chem. A, 119, 11366–11375, 2015.

Lambe, A., Massoli, P., Zhang, X., Canagaratna, M., Nowak, J., Daube, C., Yan, C., Nie, W., Onasch, T., Jayne, J., Kolb, C., Davidovits, P., Worsnop, D., and Brune, W.: Controlled nitric oxide production via $O(^1D) + N_2O$ reactions for use in oxidation flow reactor studies, Atmos. Meas. Tech., 10, 2283–2298, https://doi.org/10.5194/amt-10-2283-2017, 2017.

Liu, Y. J., Herdlinger-Blatt, I., McKinney, K. A., and Martin, S. T.: Production of methyl vinyl ketone and methacrolein via the hydroperoxyl pathway of isoprene oxidation, Atmos. Chem. Phys., 13, 5715–5730, https://doi.org/10.5194/acp-13-5715-2013, 2013.

Loza, C. L., Craven, J. S., Yee, L. D., Coggon, M. M., Schwantes, R. H., Shiraiwa, M., Zhang, X., Schilling, K. A., Ng, N. L., Canagaratna, M. R., Ziemann, P. J., Flagan, R. C., and Seinfeld, J. H.: Secondary organic aerosol yields of 12-carbon alkanes, Atmos. Chem. Phys., 14, 1423–1439, https://doi.org/10.5194/acp-14-1423-2014, 2014.

McVay, R. C., Zhang, X., Aumont, B., Valorso, R., Camredon, M., La, Y. S., Wennberg, P. O., and Seinfeld, J. H.: SOA formation from the photooxidation of α-pinene: systematic exploration of the simulation of chamber data, Atmos. Chem. Phys., 16, 2785–2802, https://doi.org/10.5194/acp-16-2785-2016, 2016.

Miyoshi, A., Hatakeyama, S., and Washida, N.: OH radical-initiated photooxidation of isoprene: An estimate of global CO production, J. Geophys. Res.-Atmos., 99, 18779–18787, 1994.

Nah, T., McVay, R. C., Zhang, X., Boyd, C. M., Seinfeld, J. H., and Ng, N. L.: Influence of seed aerosol surface area and oxidation rate on vapor wall deposition and SOA mass yields: a case study with α-pinene ozonolysis, Atmos. Chem. Phys., 16, 9361–9379, https://doi.org/10.5194/acp-16-9361-2016, 2016.

Ng, N. L., Chhabra, P. S., Chan, A. W. H., Surratt, J. D., Kroll, J. H., Kwan, A. J., McCabe, D. C., Wennberg, P. O., Sorooshian, A., Murphy, S. M., Dalleska, N. F., Flagan, R. C., and Seinfeld, J. H.: Effect of NO_x level on secondary organic aerosol (SOA) formation from the photooxidation of terpenes, Atmos. Chem. Phys., 7, 5159–5174, https://doi.org/10.5194/acp-7-5159-2007, 2007.

Nguyen, T. B., Coggon, M. M., Bates, K. H., Zhang, X., Schwantes, R. H., Schilling, K. A., Loza, C. L., Flagan, R. C., Wennberg, P. O., and Seinfeld, J. H.: Organic aerosol formation from the reactive uptake of isoprene epoxydiols (IEPOX) onto non-acidified inorganic seeds, Atmos. Chem. Phys., 14, 3497–3510, https://doi.org/10.5194/acp-14-3497-2014, 2014a.

Nguyen, T. B., Crounse, J. D., Schwantes, R. H., Teng, A. P., Bates, K. H., Zhang, X., St. Clair, J. M., Brune, W. H., Tyndall, G. S., Keutsch, F. N., Seinfeld, J. H., and Wennberg, P. O.: Overview of the Focused Isoprene eXperiment at the California Institute of Technology (FIXCIT): mechanistic chamber studies on the oxidation of biogenic compounds, Atmos. Chem. Phys., 14, 13531–13549, https://doi.org/10.5194/acp-14-13531-2014, 2014b.

Nguyen, T. B., Bates, K. H., Crounse, J. D., Schwantes, R. H., Zhang, X., Kjaergaard, H. G., Surratt, J. D., Lin, P., Laskin, A.,

and Seinfeld, J. H.: Mechanism of the hydroxyl radical oxidation of methacryloyl peroxynitrate (MPAN) and its pathway toward secondary organic aerosol formation in the atmosphere, Phys. Chem. Chem. Phys., 17, 17914–17926, 2015.

Orlando, J. J. and Tyndall, G. S.: Laboratory studies of organic peroxy radical chemistry: an overview with emphasis on recent issues of atmospheric significance, Chem. Soc. Rev., 41, 6294–6317, 2012.

Paulson, S. E. and Seinfeld, J. H.: Development and evaluation of a photooxidation mechanism for isoprene, J. Geophys. Res.-Atmos., 97, 20703–20715, 1992.

Peeters, J., Müller, J.-F. o., Stavrakou, T., and Nguyen, V. S.: Hydroxyl radical recycling in isoprene oxidation driven by hydrogen bonding and hydrogen tunneling: The upgraded LIM1 mechanism, J. Phys. Chem. A, 118, 8625–8643, 2014.

Petropavlovskikh, I., Shetter, R., Hall, S., Ullmann, K., and Bhartia, P. K.: Algorithm for the charge-coupled-device scanning actinic flux spectroradiometer ozone retrieval in support of the Aura satellite validation, J. Appl. Remote Sens., 1, 013540, https://doi.org/10.1117/1.2802563, 2007.

Riva, M., Budisulistiorini, S. H., Chen, Y., Zhang, Z., D'Ambro, E. L., Zhang, X., Gold, A., Turpin, B. J., Thornton, J. A., and Canagaratna, M. R.: Chemical characterization of secondary organic aerosol from oxidation of isoprene hydroxyhydroperoxides, Environ. Sci. Technol., 50, 9889–9899, 2016.

Rivera-Rios, J. C., Nguyen, T. B., Crounse, J. D., Jud, W., St Clair, J. M., Mikoviny, T., Gilman, J. B., Lerner, B. M., Kaiser, J. B., and Gouw, J. d.: Conversion of hydroperoxides to carbonyls in field and laboratory instrumentation: Observational bias in diagnosing pristine versus anthropogenically controlled atmospheric chemistry, Geophys. Res. Lett., 41, 8645–8651, 2014.

Rollins, A. W., Browne, E. C., Min, K. E., Pusede, S. E., Wooldridge, P. J., Gentner, D. R., Goldstein, A. H., Liu, S., Day, D. A., and Russell, L. M.: Evidence for NO_x control over nighttime SOA formation, Science, 337, 1210–1212, 2012.

Ruppert, L. and Becker, K. H.: A product study of the OH radical-initiated oxidation of isoprene: Formation of C 5-unsaturated diols, Atmos. Environ., 34, 1529–1542, 2000.

Schilling Fahnestock, K. A., Yee, L. D., Loza, C. L., Coggon, M. M., Schwantes, R., Zhang, X., Dalleska, N. F., and Seinfeld, J. H.: Secondary organic aerosol composition from C12 alkanes, J. Phys. Chem. A, 119, 4281–4297, 2014.

Schwantes, R. H., Teng, A. P., Nguyen, T. B., Coggon, M. M., Crounse, J. D., St. Clair, J. M., Zhang, X., Schilling, K. A., Seinfeld, J. H., and Wennberg, P. O.: Isoprene NO_3 oxidation products from the $RO_2 + HO_2$ Pathway, J. Phys. Chem. A, 119, 10158–10171, 2015.

Schwantes, R. H., McVay, R. C., Zhang, X., Coggon, M. M., Lignell, H., Flagan, R. C., Wennberg, P. O., and Seinfeld, J. H.: Science of the environmental chamber, Adv. Atmos. Chem., 1, 1–93, 2017a.

Schwantes, R. H., Schilling, K. A., McVay, R. C., Lignell, H., Coggon, M. M., Zhang, X., Wennberg, P. O., and Seinfeld, J. H.: Formation of highly oxygenated low-volatility products from cresol oxidation, Atmos. Chem. Phys., 17, 3453–3474, https://doi.org/10.5194/acp-17-3453-2017, 2017b.

Shilling, J. E., Chen, Q., King, S. M., Rosenoern, T., Kroll, J. H., Worsnop, D. R., McKinney, K. A., and Martin, S. T.: Particle mass yield in secondary organic aerosol formed by the dark ozonolysis of α-pinene, Atmos. Chem. Phys., 8, 2073–2088, https://doi.org/10.5194/acp-8-2073-2008, 2008.

Shilling, J. E., Zaveri, R. A., Fast, J. D., Kleinman, L., Alexander, M. L., Canagaratna, M. R., Fortner, E., Hubbe, J. M., Jayne, J. T., Sedlacek, A., Setyan, A., Springston, S., Worsnop, D. R., and Zhang, Q.: Enhanced SOA formation from mixed anthropogenic and biogenic emissions during the CARES campaign, Atmos. Chem. Phys., 13, 2091–2113, https://doi.org/10.5194/acp-13-2091-2013, 2013.

Singh, H. B. and Hanst, P. L.: Peroxyacetyl nitrate (PAN) in the unpolluted atmosphere: An important reservoir for nitrogen oxides, Geophys. Res. Lett., 8, 941–944, 1981.

Sprengnether, M., Demerjian, K. L., Donahue, N. M., and Anderson, J. G.: Product analysis of the OH oxidation of isoprene and 1, 3-butadiene in the presence of NO, J. Geophys. Res.-Atmos., 107, 4268, https://doi.org/10.1029/2001JD000716, 2002.

Surratt, J. D., Chan, A. W. H., Eddingsaas, N. C., Chan, M., Loza, C. L., Kwan, A. J., Hersey, S. P., Flagan, R. C., Wennberg, P. O., and Seinfeld, J. H.: Reactive intermediates revealed in secondary organic aerosol formation from isoprene, P. Natl. Acad. Sci. USA, 107, 6640–6645, 2010.

Teng, A. P., Crounse, J. D., and Wennberg, P. O.: Isoprene peroxy radical dynamics, J. Am. Chem. Soc., 139, 5367–5377, 2017.

Thomas, D. A., Coggon, M. M., Lignell, H., Schilling, K. A., Zhang, X., Schwantes, R. H., Flagan, R. C., Seinfeld, J. H., and Beauchamp, J. L.: Real-time studies of iron oxalate-mediated oxidation of glycolaldehyde as a model for photochemical aging of aqueous tropospheric aerosols, Environ. Sci. Technol., 50, 12241–12249, 2016.

Tuazon, E. C. and Atkinson, R.: A product study of the gas-phase reaction of Isoprene with the OH radical in the presence of NO_x, Int. J. Chem. Kinet., 22, 1221–1236, 1990.

Wennberg, P. O., Bates, K. H., Crounse, J. D., Dodson, L. G., McVay, R. C., Mertens, L. A., Nguyen, T. B., Praske, E., Schwantes, R. H., Smarte, M. D., St Clair, J. M., Teng, A. P., Zhang, X., and Seinfeld, J. H.: Gas-phase reactions of isoprene and its major oxidation products, Chem. Rev., 118, 3337–3390, https://doi.org/10.1021/acs.chemrev.7b00439, 2018.

Xu, L., Guo, H., Boyd, C. M., Klein, M., Bougiatioti, A., Cerully, K. M., Hite, J. R., Isaacman-VanWertz, G., Kreisberg, N. M., and Knote, C.: Effects of anthropogenic emissions on aerosol formation from isoprene and monoterpenes in the southeastern United States, P. Natl. Acad. Sci. USA, 112, 37–42, 2015.

Zhang, X. and Seinfeld, J. H.: A functional group oxidation model (FGOM) for SOA formation and aging, Atmos. Chem. Phys., 13, 5907–5926, https://doi.org/10.5194/acp-13-5907-2013, 2013.

Zhang, X., Chen, Z. M., and Zhao, Y.: Laboratory simulation for the aqueous OH-oxidation of methyl vinyl ketone and methacrolein: significance to the in-cloud SOA production, Atmos. Chem. Phys., 10, 9551–9561, https://doi.org/10.5194/acp-10-9551-2010, 2010.

Zhang, X., Cappa, C. D., Jathar, S. H., McVay, R. C., Ensberg, J. J., Kleeman, M. J., and Seinfeld, J. H.: Influence of vapor wall loss in laboratory chambers on yields of secondary organic aerosol, P. Natl. Acad. Sci. USA, 111, 5802–5807, 2014a.

Zhang, X., Schwantes, R. H., Coggon, M. M., Loza, C. L., Schilling, K. A., Flagan, R. C., and Seinfeld, J. H.: Role of ozone in SOA formation from alkane photooxidation, Atmos. Chem. Phys., 14, 1733–1753, https://doi.org/10.5194/acp-14-1733-2014, 2014b.

Zhang, X., McVay, R. C., Huang, D. D., Dalleska, N. F., Aumont, B., Flagan, R. C., and Seinfeld, J. H.: Formation and evolution of molecular products in α-pinene secondary organic aerosol, P. Natl. Acad. Sci. USA, 112, 14168–14173, 2015a.

Zhang, X., Schwantes, R. H., McVay, R. C., Lignell, H., Coggon, M. M., Flagan, R. C., and Seinfeld, J. H.: Vapor wall deposition in Teflon chambers, Atmos. Chem. Phys., 15, 4197–4214, https://doi.org/10.5194/acp-15-4197-2015, 2015b.

Zhang, X., Lambe, A. T., Upshur, M. A., Brooks, W. A., Gray Beì, A., Thomson, R. J., Geiger, F. M., Surratt, J. D., Zhang, Z., and Gold, A.: Highly oxygenated multifunctional compounds in α-pinene secondary organic aerosol, Environ. Sci. Technol., 51, 5932–5940, 2017.

Ziemann, P. J. and Atkinson, R.: Kinetics, products, and mechanisms of secondary organic aerosol formation, Chem. Soc. Rev., 41, 6582–6605, 2012.

Appendix C

RAPID AQUEOUS-PHASE HYDROLYSIS OF ESTER HYDROPEROXIDES ARISING FROM CRIEGEE INTERMEDIATES AND ORGANIC ACIDS

Zhao, Ran, Christopher M. Kenseth, Yuanlong Huang, Nathan F. Dalleska, Xiaobi M. Kuang, Jierou Chen, Suzanne E. Paulson, and John H. Seinfeld (2018). "Rapid Aqueous-Phase Hydrolysis of Ester Hydroperoxides Arising from Criegee Intermediates and Organic Acids". In: *J. Phys. Chem. A* 122.23, pp. 5190–5201. DOI: 10.1021/acs.jpca.8b02195.

THE JOURNAL OF PHYSICAL CHEMISTRY A

Article

Cite This: J. Phys. Chem. A 2018, 122, 5190−5201

pubs.acs.org/JPCA

Rapid Aqueous-Phase Hydrolysis of Ester Hydroperoxides Arising from Criegee Intermediates and Organic Acids

Ran Zhao,*[,†,‡] Christopher M. Kenseth,[†] Yuanlong Huang,[¶] Nathan F. Dalleska,[§] Xiaobi M. Kuang,[∥] Jierou Chen,[∥] Suzanne E. Paulson,[∥] and John H. Seinfeld[†,⊥]

[†]Devision of Chemistry and Chemical Engineering, California Institute of Technology, Pasadena, California 91125, United States

[¶]Division of Geological and Planetary Sciences, California Institute of Technology, Pasadena, California 91125, United States

[§]Environmental Analysis Center, California Institute of Technology, Pasadena, California 91125, United States

[∥]Department of Atmospheric and Oceanic Sciences, University of California—Los Angeles, Los Angeles, California 90095, United States

[⊥]Division of Engineering and Applied Science, California Institute of Technology, Pasadena, California 91125, United States

ABSTRACT: Stabilized Criegee intermediates react with organic acids in the gas phase and at the air−water interface to form a class of ester hydroperoxides, α-acyloxyalkyl hydroperoxides (αAAHPs). A number of recent studies have proposed the importance of αAAHPs to the formation and growth of secondary organic aerosol (SOA). The chemistry of αAAHPs has not been investigated due to a lack of commercially available chemical standards. In this work, the behavior of αAAHPs in condensed phases is investigated for the first time. Experiments were performed with two synthesized αAAHP species. αAAHPs decomposed rapidly in the aqueous phase, with the rate highly dependent on the solvent, temperature, solution pH, and other compounds present in the solution. The measured 1st-order decomposition rate coefficient varied between 10^{-3} and 10^{-5} s^{-1} under the conditions examined in this work. Elucidation of the reaction mechanism is complicated by byproducts arising from the synthetic procedure, but observations are consistent with a base-catalyzed hydrolysis of αAAHPs. The rapid hydrolysis of αAAHPs observed in this work implies their short lifetimes in ambient cloud and fog waters. Decomposition of αAAHPs likely gives rise to smaller peroxides, such as H_2O_2. The loss of αAAHPs is also relevant to filter extraction, which is commonly practiced in laboratory experiments, potentially explaining contradictory results reported in the existing literature regarding the importance of αAAHPs in SOA.

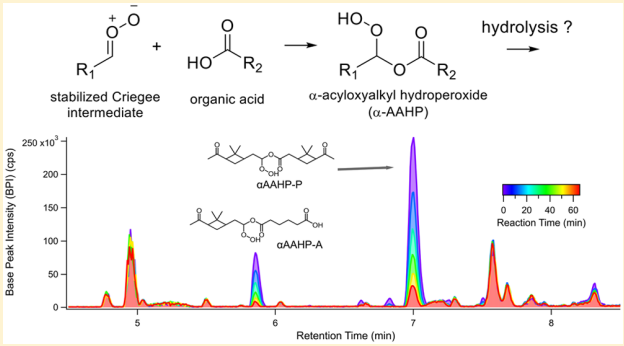

INTRODUCTION

Alkenes (e.g., isoprene and monoterpenes) comprise over half of the total volatile organic compounds (VOCs) emitted to Earth's atmosphere.[1] Owing to the reactivity of the C=C bond toward O_3, ozonolysis is a major sink of alkenes. Ozonolysis converts alkenes into oxygenated products that exhibit lower vapor pressures and contribute to the formation of secondary organic aerosol (SOA), a class of suspended organic particulate matter that affects air quality and global climate.[2] As shown in the generalized reaction scheme of alkene ozonolysis (Figure 1), O_3 first adds across the C=C bond, giving rise to a primary ozonide, which decomposes to a carbonyl compound and an excited carbonyl oxide referred to as the Criegee intermediate.[3] The Criegee intermediate is presented as a zwitterion in Figure 1, as it is the most stable configuration,[4] but it is also commonly referred to as a biradical in the literature. The Criegee intermediate can either undergo unimolecular decomposition or be stabilized upon collision with air (i.e., N_2 and O_2). The stabilized Criegee intermediate (SCI) can react bimolecularly with a wide spectrum of molecules collectively known as Criegee scavengers, among which organic acids are particularly efficient.[4,5] The reaction between the C_1 SCI and formic acid proceeds nearly at the collision limit,[6] with a rate coefficient larger than that of SCI + H_2O by 3 to 4 orders of magnitude.[7−9] The product arising from the SCI + organic acid reaction is an ester hydroperoxide, α-acyloxyalkyl hydroperoxide (αAAHP, Figure 1).[10] A number of studies have proposed that αAAHPs can contribute to SOA mass due to their low volatility, and alternatively, they can react further with another SCI to form compounds with even lower volatilities.[6,11]

Monoterpenes comprise a major fraction of global biogenic VOC emissions,[1] and the reaction products of monoterpene SCIs are of great importance to atmospheric chemistry. Recent studies have observed high molecular weight αAAHPs that are

Received: March 5, 2018
Revised: May 16, 2018
Published: May 21, 2018

DOI: 10.1021/acs.jpca.8b02195
J. Phys. Chem. A 2018, 122, 5190−5201

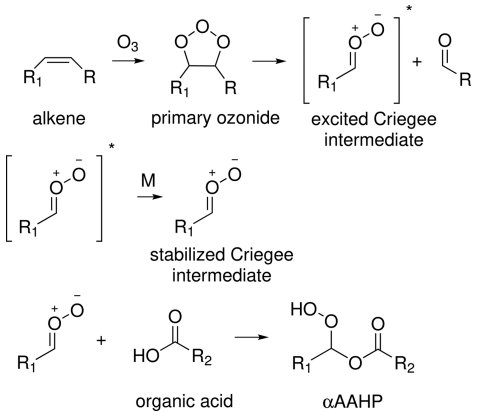

Figure 1. Schematic of the general atmospheric formation mechanism of α-acyloxyalkyl hydroperoxide (αAAHP).

likely attributable to the gas-phase reaction of monoterpene SCIs with organic acids.[12−15] Kristensen et al.[14] have proposed that αAAHPs are a major fraction of monoterpene SOA. The reaction of monoterpene SCIs with organic acids can also occur at the air−water interface, such as the surface of cloud droplets and aqueous aerosol. In particular, computational studies have shown that SCIs with hydrophobic substituents are relatively unreactive with water, allowing for reaction with other species, such as acids.[16−18] Recent experimental studies have provided supporting observations, showing that SCIs from monoterpenes and sesquiterpenes give rise to αAAHPs at the air−water interface.[19,20] While these studies suggest the importance of αAAHPs arising from monoterpenes, contradictory results have also been reported. A few studies have found that αAAHPs comprised only a minor fraction of α-pinene SOA extracted in organic or aqueous solvents.[21,22] Such contradictory results reflect the fact that the chemistry of αAAHPs has not been investigated in a systematic manner. Unrecognized reactions of αAAHPs are likely occurring in SOA and/or after sample collection.

Multifunctional organic peroxides, such as αAAHPs, comprise a highly complex, unresolved fraction of SOA. These organic peroxide species serve as reservoirs of important oxidants (e.g., the OH radical) and represent a class of reactive oxygen species (ROS), which are linked to adverse health effects of airborne particulate matter.[23,24] Despite their environmental significance, the chemistry of such multifunctional organic peroxides is poorly understood due to their complexity, lack of commercially available standards, and chemical instability. In particular, recent studies have demonstrated the labile nature of particle-bound organic peroxides.[25−27] Other studies have observed formation of H_2O_2 and the OH radical from the water extract of SOA, implying decomposition of larger organic peroxides.[28−30] In this work, two αAAHP species arising from the α-pinene SCIs are synthesized, and their condensed-phase chemistry is investigated for the first time. A specific objective is to understand the behavior of αAAHPs in the aqueous phase, which reflects their fate in cloudwater, aqueous aerosol, and aqueous solvents after extraction. We also attempt to determine the reaction mechanism of the decomposition of αAAHPs, with a particular interest in the extent to which they produce H_2O_2.

EXPERIMENTAL SECTION

Liquid Chromatography Electrospray Ionization Mass Spectrometry (LC-ESI-MS). An LC-ESI-MS technique is used here as the primary analytical method to characterize the synthesized αAAHPs and to monitor their decomposition. The same technique has been employed in a number of our previous studies.[21,31,32] A Waters ACQUITY UPLC I-Class system was coupled to a quadrupole time-of-flight MS (Xevo G2-S QToF). LC separation was performed on an AQUITY

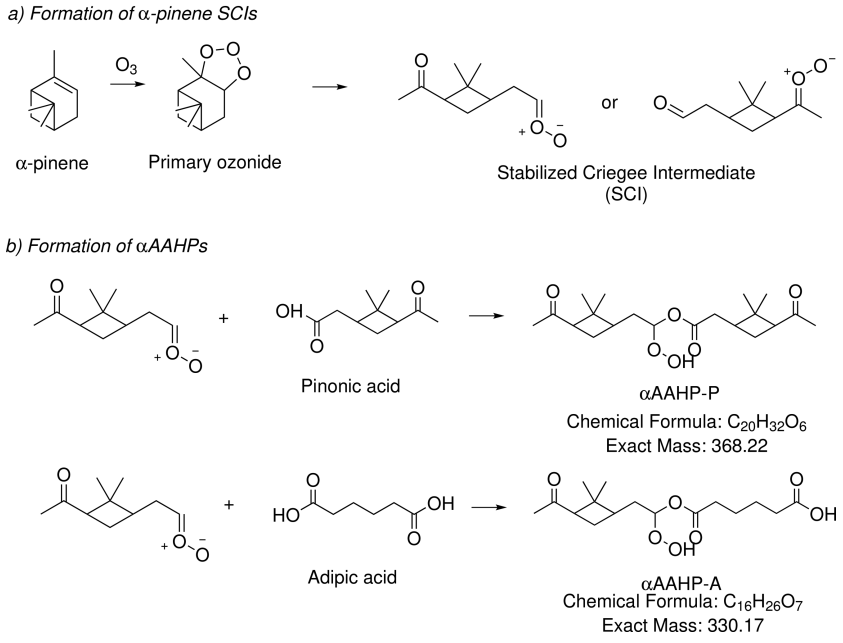

Figure 2. Synthetic pathways and possible structures of αAAHP-P and αAAHP-A. Simplified schematics for (a) the formation of α-pinene SCIs and (b) the formation of αAAHPs are shown. Ozonolysis of α-pinene gives rise to two possible SCIs, which subsequently form two αAAHP structural isomers upon reaction with an organic acid. For simplicity, only the αAAHPs arising from one SCI are shown in part b.

DOI: 10.1021/acs.jpca.8b02195
J. Phys. Chem. A 2018, 122, 5190−5201

BEH C_{18} column (1.7 μm, 2.1 × 50 mm), with the column temperature controlled at 30 °C. The injection volume was set at 10 μL, and the flow rate was 0.3 mL min^{-1}. The mobile phase gradient and ESI settings in this study are identical to those in Zhao et al.[21] and will not be discussed with further details here. Leucine enkephalin was employed as the lock mass for accurate mass determination. LC-ESI-MS was operated in both the positive (ESI(+)) and the negative (ESI(−)) modes. Generally, ESI(+) detects oxygenated compounds as ion clusters with Na^+, NH_4^+, or K^+, while ESI(−) detects compounds containing acidic protons in their deprotonated forms (i.e., as $[M - H]^-$). In this study, the instrument was operated primarily with ESI(+) as it detects both of the synthesized αAAHPs. ESI(−) was also employed to characterize αAAHPs and to elucidate the reaction mechanisms. Data were acquired and processed with MassLynx v.4.1 software. The reproducibility in the detected peak areas is within 5%, as determined by frequent consistency tests.

Synthesis of αAAHPs. Unless noted otherwise, all chemicals were purchased from Sigma-Aldrich without further purification. The synthetic procedure, adapted and modified from that of Witkowski and Gierczak,[33] is based on a liquid-phase ozonolysis of α-pinene. The SCIs generated from liquid-phase ozonolysis are forced to form αAAHPs in the presence of an excess amount of an organic acid. The chemical mechanisms behind the synthesis are shown in Figure 2. The synthetic procedure has been described elsewhere.[21] Briefly, α-pinene (50 mM) and an individual organic acid (10 mM) were dissolved in acetonitrile (EMD Millipore). A gentle stream of air (120 sccm) containing approximately 100 ppm of O_3 (generated from a custom-built O_3 generator) was bubbled through the acetonitrile solution. Synthesis of αAAHPs was carried out in an ice bath, and the solutions were stored in a freezer maintained at −16 °C. Two organic acids were selected to synthesize two different αAAHPs. Pinonic acid was selected for its relevance to monoterpene oxidation and its reactivity with SCIs.[14,19] Adipic acid was selected as representative of diacids. The two synthesized αAAHPs are herein referred to as αAAHP-P, and αAAHP-A, respectively (Figure 2). A synthetic control was also prepared by following the same synthetic procedures, except that no organic acid was added to force the formation of αAAHPs. The synthesized αAAHPs were not further purified due to their chemical instability; therefore, the solutions likely contain byproducts of liquid-phase α-pinene ozonolysis, e.g., through acid-catalyzed tautomerization of SCIs.[34]

Characterization of the Synthesized αAAHPs. The identity of the synthesized αAAHPs was first confirmed with the LC-ESI-MS technique. The synthetic control, αAAHP-A, and αAAHP-P were individually diluted by a factor of 50 to water acidified to pH 2 with H_2SO_4. The purpose of adding H_2SO_4 was to minimize decomposition of αAAHPs, which simplifies their characterization. As will be demonstrated in Results and Discussion, the decomposition of αAAHPs is found to be slow under acidic conditions. The diluted solutions were measured with LC-ESI-MS with both ESI(−) and ESI(+).

Iodometry was employed to confirm the peroxide functionality of αAAHPs. Iodometry is a method that selectively reduces organic peroxides into the corresponding alcohols.[35,36] It has been traditionally employed with UV−vis spectrometry to quantify the total peroxide content in a sample.[37,38] Our previous work has established a method to couple iodometry to LC-ESI-MS for a molecular-level analysis of organic peroxide; this method has been named iodometry-assisted LC-ESI-MS.[21] In the present work, both of the synthesized αAAHPs were first mixed and diluted by a factor of 50 in an aqueous solution, preacidified to pH 2 with H_2SO_4. In this case, acidifying the solution supplies the acid needed for iodometry. The solution was then divided into two aliquots. Potassium iodide (KI, 60 mM) was added to one aliquot to initiate iodometry, while no KI was added to the other aliquot as a control. Both aliquots were kept in the dark at room temperature. LC-ESI-MS measurement with ESI(+) was performed approximately 30 min after the addition of KI.

Hydrolysis of αAAHPs in Condensed Phases. The two αAAHPs were mixed and diluted simultaneously by a factor of 50 in an aqueous solution contained in a plastic LC-ESI-MS sample vial. The emphasis of the current work was placed on hydrolysis in the aqueous phase, but experiments were also performed in methanol and acetonitrile to explore the solvent effects. The sample vial was placed in a temperature-controlled sample holder, and the αAAHP signals were tracked over time using LC-ESI-MS. The temperature in the sample holder was adjusted to 7, 15, 25, and 35 °C to explore the temperature effect. The sample vials and aqueous solutions were preconditioned at the set temperatures before αAAHPs were added. The pH of the αAAHP solution at the default dilution ratio was 4.4 (monitored with a Thermo Scientific pH meter). Its acidity is likely due to the presence of residual pinonic acid and adipic acid used in the synthesis. To investigate the effect of solution pH on the decomposition of αAAHPs, experiments were also conducted in solutions with pH values either adjusted with H_2SO_4/NaOH or buffered with potassium hydrogen phthalate (KHP) (Baker Chemical Co.).

In the ambient atmosphere, αAAHPs are likely present in aqueous phases with highly complex chemical compositions, including numerous organic and inorganic compounds. To account for any matrix effect, we have also performed αAAHP hydrolysis experiments in an aqueous extract of SOA, generated from the reaction of O_3 and α-pinene in the Caltech PhotoOxidation flow Tube (CPOT) reactor.[39] The details of SOA generation, extraction, and characterization are provided in our previous work.[21] Briefly, α-pinene (175 ppb) and O_3 (1 ppm) were mixed in the CPOT in the absence of light, NO_x, and OH scavengers. The experiments were performed at room temperature and under dry conditions (RH < 10%). The average residence time in the CPOT was 3.5 min. Ammonium sulfate ($(NH_4)_2SO_4$) (Mallinckrodt Chemicals) seed aerosol was injected to assist formation of SOA and to minimize vapor-wall interactions. SOA generated in the CPOT was collected on a Teflon filter over 16 h. The filter was extracted to water by being mechanically shaken for 10 min, immediately before the hydrolysis experiments.

The pH of the SOA extract with diluted αAAHPs was measured to be 4.2. The $(NH_4)_2SO_4$ concentration, arising from the $(NH_4)_2SO_4$ seed aerosol, was approximately 200 μM, semiquantitatively determined by comparing the peak area of HSO_4^- observed by LC-ESI-MS to those from standard solutions of $(NH_4)_2SO_4$. The total organic carbon (TOC) in the water extract of SOA was measured to be 31 ppm carbon (ppmC) using a TOC analyzer (OI Analytical, Aurora model 1030w). The accuracy of the TOC instrument was within 5%.

High Performance Liquid Chromatography with Fluorescence Detection (HPLC-Fluorescence). The formation of H_2O_2 from αAAHPs was monitored with a HPLC-fluorescence instrument (Shimadzu RF-10AXL) located at the

DOI: 10.1021/acs.jpca.8b02195
J. Phys. Chem. A 2018, 122, 5190−5201

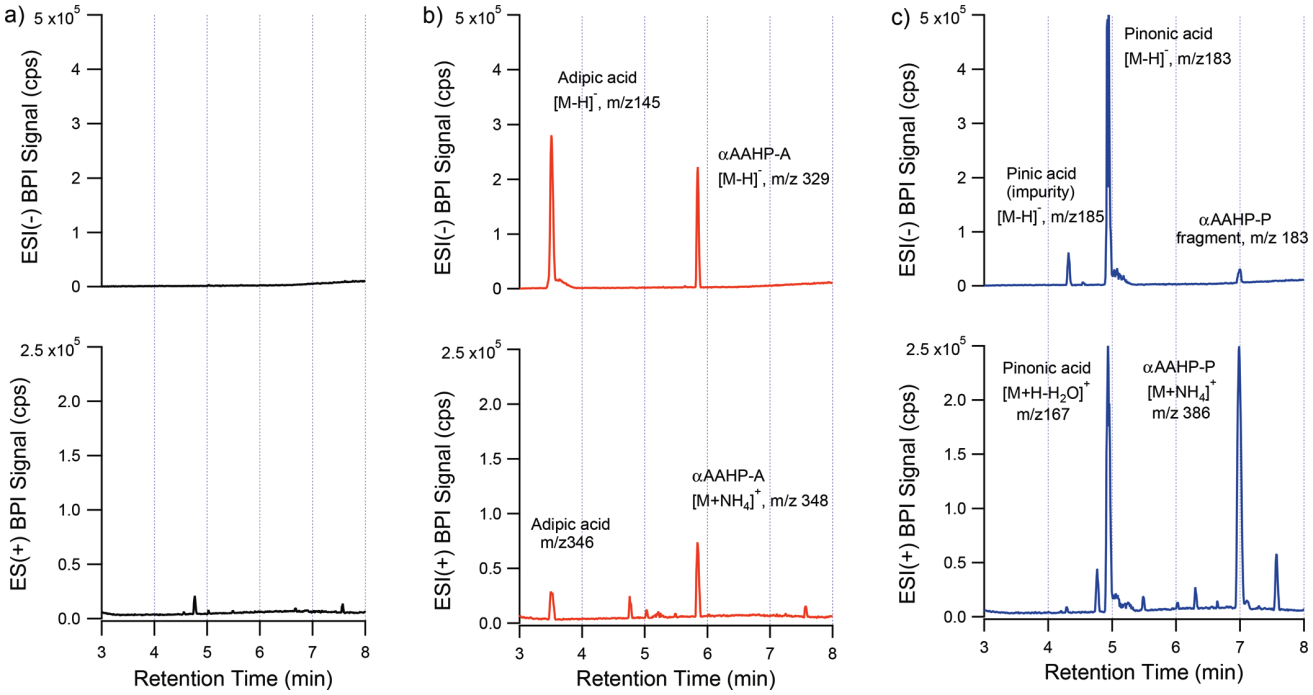

Figure 3. LC-ESI-MS BPI chromatograms of (a) the synthetic control, (b) αAAHP-A, and (c) αAAHP-P. The top panels show the results obtained with ESI(−) and the bottom panels show those obtained with ESI(+).

University of California—Los Angeles.[30,40−43] The technique is based on an LC separation of H_2O_2 and organic peroxides on a C_{18} reversed-phase column (GL Science Inc., 5 μm, 4.6 × 250 mm), followed by a postcolumn addition of a fluorescent reagent consisted of horseradish peroxidase (HRP) and *p*-hydroxyphenyl acetic acid (PHOPAA). With the catalytic assistance of HRP, PHOPAA selectively reacts with H_2O_2 and organic peroxides to form a fluorescent dimer, which was detected with a fluorescent detector. The excitation and emission wavelengths were set at 320 and 400 nm, respectively. The LC separation is based on an isocratic method with a 100% aqueous mobile phase containing 1 mM of H_2SO_4 (Fisher, 0.1 N, reagent grade) and 0.1 mM of ethylenediaminetetraacetic acid (EDTA) at a total flow rate of 0.6 mL min^{-1}. The length of the LC method was 10 min. The current LC method is optimized for the detection of H_2O_2 and polar organic peroxides. A pulse of acetonitrile (200 μL) was injected 3 min after the sample injection to facilitate the elution of less polar organic peroxides. The synthesized αAAHPs did not elute from the column and were not detected.

For the hydrolysis experiments, αAAHP-A or αAAHP-P was diluted by a factor of 250 in water and stored in the dark at room temperature. Aliquots (20 μL) of the experimental solution were injected into the HPLC-fluorescence instrument to monitor the formation of H_2O_2. The method was calibrated against standard H_2O_2 solutions, produced by diluting a commercial H_2O_2 solution (50% in water). The detection limit of the method was 10 nM. We have also performed control experiments in which the synthesized αAAHPs were diluted to the same ratio but in acetonitrile instead of water.

RESULTS AND DISCUSSION

Characterization of the Synthesized αAAHPs. Figure 3 shows the base peak intensity (BPI) chromatograms of the synthetic control, αAAHP-A, and αAAHP-P obtained with LC-ESI-MS. BPI chromatograms display the most intense peak at each given retention time (*RT*). Neither ESI(−) nor ESI(+) has detected any major compounds in the synthetic control (Figure 3a). αAAHPs are detected by both ESI(−) and ESI(+) (Figure 3, parts b and c), and the agreement between the detected and exact masses (Figure 2) is within ±10 ppm.

αAAHP-A emerges at *RT* = 5.8 min and is detected as $[M - H]^-$ (*m*/*z* 329) and $[2M - H]^-$ (*m*/*z* 659) by ESI(−). Along with αAAHP-A, residual adipic acid was also detected by ESI(−) at *RT* = 3.4 min, primarily as $[M - H]^-$ (*m*/*z* 145). ESI(+) detects αAAHP-A primarily as $[M + NH_4]^+$ (*m*/*z* 348), but also as $[M + Na]^+$ (*m*/*z* 353) and $[M + K]^+$ (*m*/*z* 369). Small organic acids, such as adipic acid, are not efficiently detected as $[M + Na]^+$ or $[M + NH_4]^+$. In fact, adipic acid is detected by ESI(+) primarily at *m*/*z* 346, which corresponds to a complex with iron ($[Fe^{3+}\cdot(M^-)_2]^-$). Iron is likely present at the ESI source or the injection system. We have confirmed that the isotope profile of this peak agrees with that of iron and that the peak area of *m*/*z* 346 is proportional to the adipic acid concentration. αAAHP-P (*RT* = 7 min) does not have any carboxylic groups and is not detected as $[M - H]^-$ by ESI(−), but instead as a fragment at *m*/*z* 183. The precursor of αAAHP-P, pinonic acid, is detected primarily as $[M - H]^-$ (*m*/*z* 183) by ESI(−) at *RT* = 4.9 min. Similar to the case of αAAHP-A, αAAHP-P is detected by ESI(+) primarily as $[M + NH_4]^+$ (*m*/*z* 386), but also as $[M + Na]^+$ (*m*/*z* 391) and $[M + K]^+$ (*m*/*z* 407). ESI(+) detects pinonic acid primarily in a dehydrated form, $[M + H - H_2O]^+$ (*m*/*z* 167), but also as the iron complex ($[Fe^{3+}\cdot(M^-)_2]^-$) at *m*/*z* 422, similar to the case of adipic acid. Besides the peaks of αAAHPs and their precursor organic acids, ESI(+) has detected a number of minor peaks likely attributable to byproducts arising from the current synthetic procedure. These byproducts do not contain acidic functionalities, as they are not detected by ESI(−).

DOI: 10.1021/acs.jpca.8b02195
J. Phys. Chem. A 2018, 122, 5190−5201

Figure 4 compares the ESI(+) BPI chromatograms of a mixture of the two αAAHPs treated with and without iodometry. The only major difference between the two BPI chromatograms is a complete attenuation of αAAHP peaks, confirming that they are organic peroxides. Iodometry induced negligible effects on the peaks of synthetic byproducts, indicating that most of these byproducts are nonperoxide species.

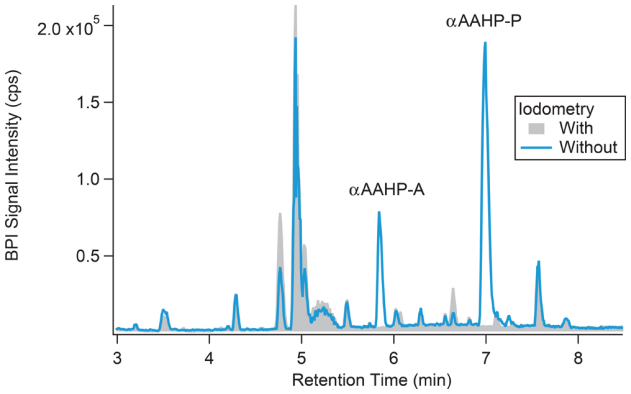

Figure 4. Characterization of the synthesized αAAHPs with iodometry-assisted LC-ESI-MS. ESI(+) BPI chromatograms of an aqueous solution treated with and without iodometry are compared.

Overall, it is confirmed that the synthesized αAAHPs are organic peroxides with the accurate masses and elemental compositions shown in Figure 2. However, we cannot distinguish structural isomers of αAAHPs with the current techniques. As shown in Figure 2a, α-pinene gives rise to two different SCIs, each leading to a distinct αAAHP structural isomer upon reaction with pinonic acid or adipic acid. The characterization also reveals that the αAAHP solutions contain numerous synthetic byproducts. The dominant byproducts are the residual precursor organic acids: adipic acid and pinonic acid. Their concentrations are determined to be approximately 200 μM in the synthetic solution diluted by a factor of 50. Although the majority of byproducts detected by LC-ESI-MS are nonperoxide species, there are likely undetected peroxide species. As will be discussed shortly, the HPLC-fluorescent technique detected a high initial background of H_2O_2, which is too polar to be retained by the LC method used in LC-ESI-MS. The presence of byproducts does not significantly affect the kinetic investigation of αAAHP decomposition but complicates the interpretation of the reaction mechanisms and will be discussed.

Decay of αAAHPs Signals in Condensed Phases. Figure 5 shows the ESI(+) BPI chromatograms recorded during an example experiment conducted in the aqueous phase at 25 °C with uncontrolled pH (4.4). The chromatograms are color-coded by the time at which each sample is injected to LC-ESI-MS, with that of the first sample defined as time 0. Both of the αAAHP species exhibit rapid decay, while the intensities of other nonperoxide peaks exhibit minimal changes during 1 h of reaction time. The inset of Figure 5 shows the 1st-order kinetic plots of the two αAAHPs recorded for the same experiment. The linearity of the plots indicates that the reaction is first-order. As discussed in the previous section, αAAHPs are detected by ESI(+) in multiple forms, including $[M + NH_4]^+$, $[M + Na]^+$, and $[M + K]^+$. Each of these three peaks exhibits decay at a very similar rate, and so only the dominant peak $[M + NH_4]^+$ is used for the kinetic analysis. We also conducted an experiment with pimelic acid added to the solution as an internal standard and monitored the signals of αAAHP-A and pimelic acid using ESI(−). The αAAHP-A decay rates with and without the internal standard differed by 8%, which is within the experimental uncertainties; the relative standard deviation of the hydrolysis rate at 25 °C is approximately 15%. As such, all the results discussed here are from experiments without an internal standard.

The effect of solvent on the decay rate of αAAHPs was investigated by performing the experiment at the same dilution ratio and temperature (25 °C), but in methanol and acetonitrile, which are the most commonly employed solvents for filter extraction and analysis. The decay profiles of αAAHP-P in the three solvents are shown in Figure 6. The decay rates of αAAHPs increase in the order of acetonitrile < methanol < water. The results for αAAHP-A exhibit the same trend and are not shown. The 1st-order decay rate coefficients (k^I) of αAAHPs and their corresponding e-folding lifetimes (τ_{avg}) in the three solvents are summarized in Table 1. The trend that

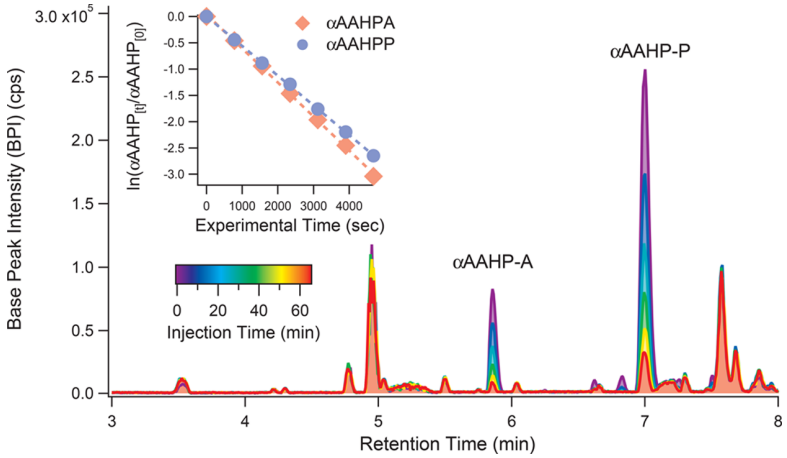

Figure 5. ESI(+) BPI chromatograms recorded in an example experiment at 25 °C with uncontrolled pH (4.4). Chromatograms are color-coded by the time each sample is injected to LC-ESI-MS. Time at which the first sample is injected is defined as time 0. The inset presents the 1st-order kinetic plots of the αAAHPs signal from the same experiment.

DOI: 10.1021/acs.jpca.8b02195
J. Phys. Chem. A 2018, 122, 5190−5201

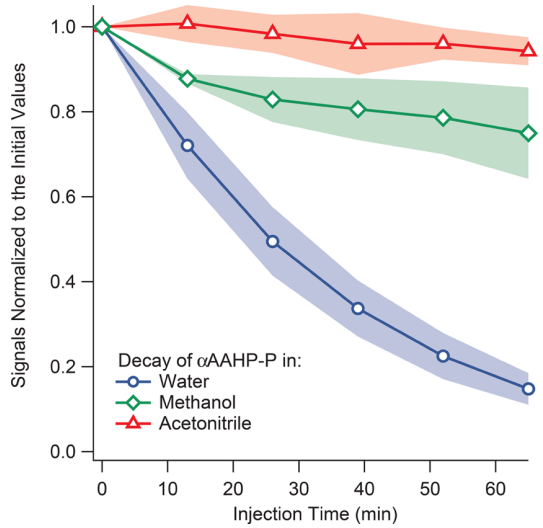

Figure 6. Decay of αAAHP-P in acetonitrile, methanol, and water. Experiments were performed at 25 °C with uncontrolled solution pH. The results represent the average of three replicates, with the error shading indicating one standard deviation.

αAAHPs are more reactive in polar and protic solvents is consistent with hydrolysis. We also note that when αAAHPs are stored in acetonitrile in a freezer maintained at −16 °C, their signals exhibit a slow decay of approximately 25% over the course of two weeks, indicating that they are highly stable under this condition.

Temperature Effects. The decomposition rates of αAAHPs appear to be highly temperature-dependent. The temperature dependences of the two αAAHPs are shown in Figure 7a, in the format of an Arrhenius plot (i.e., $\ln(k^1)$ vs $1/T$). The k^1 and τ_{avg} values at each temperature are summarized in Table 1. Decomposition of both αAAHPs is accelerated at higher temperatures, with their τ_{avg} values decreasing by roughly an order of magnitude from 7 to 35 °C. The slope of the Arrhenius plot is equivalent to $-E_a/R$, where E_a is the activation energy, and R is the gas constant. In this manner, the E_a values for αAAHP-A and αAAHP-P are obtained to be 62.6 ± 4.2 and 60.7 ± 6.7 kJ mol^{-1}, respectively. The uncertainty is obtained from that of the slope. These E_a values are comparable to but larger than those of simple alkyl esters, indicating that hydrolysis of αAAHPs is more sensitive to temperature than that of simple alkyl esters. For instance, E_a values for ethyl formate and diethyl ester are 37.4 and 44.9 kJ mol^{-1}, respectively.[44]

Effects of Solution pH. The effect of solution pH on the decomposition rate of αAAHPs is shown in Figure 7b. All of these experiments were performed at 25 °C. Decomposition of αAAHPs is highly pH dependent, proceeding more rapidly in basic solutions. The solid markers on Figure 7b represent those experiments in which the solution pH was adjusted with either H_2SO_4 or NaOH. These $\log_{10}(k^1)$ values exhibit a linear relationship with solution pH, indicating that the rate coefficients are proportional to the concentration of OH^- from pH 3.5 to 5.1. This is within the typical pH range for ambient cloud and fog waters.[45] The highest solution pH examined here is 5.1, as we found that the decomposition rate was too fast to be quantified by the current LC-ESI-MS method at higher pH values.

If organic acids are generated during decomposition of αAAHPs, the solution pH can be potentially altered during the course of an experiment. To account for this possibility, we also performed experiments in buffered solutions, and the results are shown in Figure 7b. The pH-dependence is similar in buffered and pH-adjusted solutions, indicated by the identical slopes between the two data series. However, the data of the buffered solutions is shifted up from those of the pH-adjusted solution, indicating more rapid decomposition of αAAHPs in buffers.

Matrix Effect. The faster decay of αAAHPs in buffers is likely the result of a matrix effect, which has also been observed in hydrolysis of other organic compounds.[44] The buffer solutions employed in the current work are generated by mixing KHP and NaOH. The KHP concentration ranges from 0.07 M (pH 5.0 buffer) and 0.1 M (pH 4.1 buffer), and that of NaOH ranges between 0.002 M (pH 5.0 buffer) and 0.03 M (pH 4.1 buffer). To explore the potential effect of Na^+ on hydrolysis of αAAHP, we performed a separate control experiment in which the decomposition of αAAHPs was monitored in an aqueous solution containing 0.015 M of Na_2SO_4. This experiment confirmed that Na^+ and SO_4^{2-} at this concentration do not accelerate the decomposition of αAAHPs. As such, KHP present in the buffers is likely responsible. Although KHP at the mM-level concentration is not atmospherically relevant, the fact that KHP accelerated αAAHP decomposition suggests that dissolved organic compounds in cloudwater may also be able to accelerate the decomposition of αAAHPs.

In the atmosphere, particle-phase αAAHPs are likely introduced into cloud and fog waters when the αAAHP-bearing particle is activated into a droplet, a process referred to as nucleation scavenging.[46] As such, in real cloudwater, αAAHPs are present with many other chemical components. The ideal way to investigate matrix effects of other cloudwater

Table 1. Summary of 1st-Order Decay Rates (k^1) and Corresponding e-Folding Lifetimes (τ_{avg}) of αAAHPs under a Variety of Experimental Conditions

			αAAHP-A		αAAHP-P	
solvent	T (°C)	pH[a]	k^1 (s^{-1})[b]	τ_{avg} (min)	k^1 (s^{-1})[b]	τ_{avg} (min)
acetonitrile	25	N.A.	(1.4 ± 0.8) × 10^{-5}	1200	(1.3 ± 0.8) × 10^{-5}	1200
methanol	25	N.A.	(8.9 ± 0.3) × 10^{-5}	190	(8.8 ± 0.2) × 10^{-5}	190
SOA	25	4.2	(6.9 ± 0.6) × 10^{-4}	24	(7.0 ± 0.4) × 10^{-4}	24
water	25	4.4	(5.8 ± 1.0) × 10^{-4}	29	(4.9 ± 0.7) × 10^{-4}	34
water	7	4.4	(1.3 ± 0.2) × 10^{-4}	110	(1.4 ± 0.1) × 10^{-4}	110
water	15	4.4	(2.3 ± 0.3) × 10^{-4}	72	(2.0 ± 0.3) × 10^{-4}	83
water	35	4.4	(1.6 ± 0.4) × 10^{-3}	11	(1.4 ± 0.4) × 10^{-3}	12

[a]Solution pH was uncontrolled in the listed experiments. [b]Uncertainties associated with k^1 are the standard deviation of three replicates.

DOI: 10.1021/acs.jpca.8b02195
J. Phys. Chem. A 2018, 122, 5190−5201

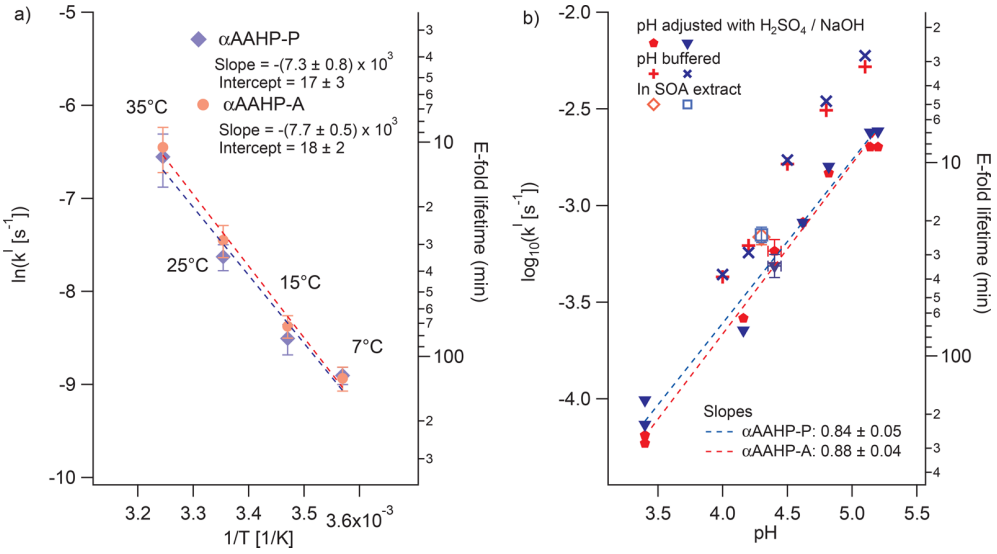

Figure 7. Temperature effect on the 1st-order decay rate of αAAHP (k^I), shown in part a as an Arrhenius plot (i.e., as ln(k^I) vs 1/T). These experiments were performed with the solution pH uncontrolled (~4.4). The effects of pH and solution matrix on k^I (in the $\log_{10}$ scale) are shown in part b. All of these experiments were performed at 25 °C. Red markers denote αAAHP-A, while blue markers represent αAAHP-P. For both parts a and b, the corresponding e-folding lifetimes are shown on the right axis. The uncertainty bars, where applicable, represent one standard deviation obtained from triplicate experiments.

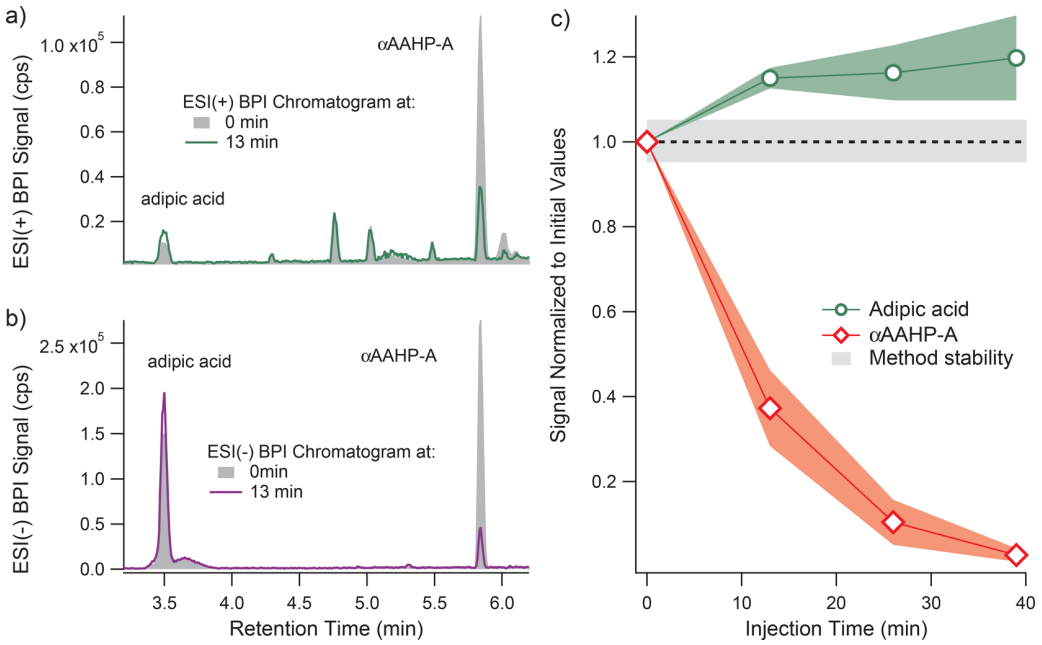

Figure 8. Change of signals in αAAHP-A hydrolysis experiment at 35 °C. The BPI chromatograms obtained with ESI(+) (a) and ESI(−) (b) at 0 and 13 min injection time are compared. The growth of the adipic acid signal and the decay of αAAHP-A signal as a function of injection time, measured with ESI(+), are shown in part c. Signals are normalized to the values obtained for the first injection, and the uncertainties correspond to the standard deviation of triplicate. The dashed line and the shaded area around it represent the stability (±5%) of the LC-ESI-MS method.

components is to use authentic cloudwater samples.[47,48] In the absence of such samples, we have taken a matrix-matching approach by extracting α-pinene SOA components and $(NH_4)_2SO_4$ into water to create an atmospherically relevant sample matrix. In the SOA extract, the k^I values were determined to be $(6.9 \pm 0.6) \times 10^{-4}$ and $(7.0 \pm 0.4) \times 10^{-4}$ for αAAHP-A and αAAHP-P, respectively. These values are significantly higher than those in water with the same pH (pH 4.2). The corresponding k^I values in pH 4.2 water are 3.2×10^{-4} and 3.6×10^{-4}, calculated with the pH-dependent curves shown in Figure 7b. Our results indicate that the presence of SOA compounds has doubled the decomposition rate of αAAHPs. Note that the hydrolysis experiment in the SOA extract was repeated in triplicate, and the uncertainty bars are shown in Figure 7b as a reference for the uncertainty range of this matrix-matching experiment.

As discussed in Experimental Section, the synthesized solutions contain organic acids and other byproducts. To

DOI: 10.1021/acs.jpca.8b02195
J. Phys. Chem. A 2018, 122, 5190−5201

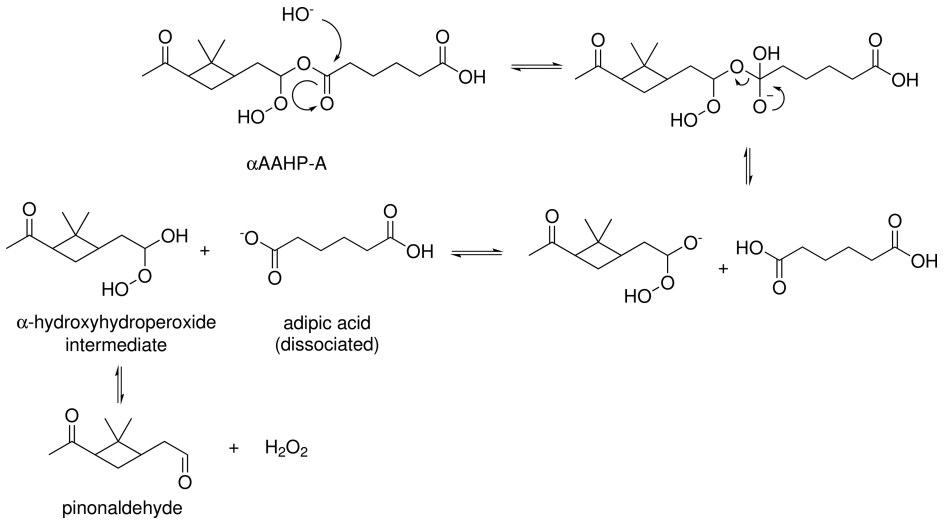

Figure 9. Base-catalyzed hydrolysis of αAAHP. The case of αAAHP-A is shown.

address the potential effect of the synthetic byproducts on the decomposition rate of αAAHPs, we performed an experiment with the αAAHPs diluted by an extra factor of two from the default dilution ratio (i.e., a dilution factor of 100 instead of 50) to reduce the concentration of byproducts. The k^1 values obtained at these two dilution ratios agree to within 7%. As hydrolysis, a 1st-order reaction, should not be affected by dilution alone, these results indicate that the effect of organic acids and synthetic byproducts on αAAHP decomposition is relatively small under the current experimental conditions.

The TOC concentration of the SOA water extract was measured to be 31 ppmC. Such a level of TOC is typically observed in polluted fog and cloudwater samples, such as those from Fresno, California, and Jeju Island, Korea.[46] We did not further perform a systematic investigation of the effect of each individual organic species on the hydrolysis rate of αAAHPs; it is an interesting direction for future studies.

Proposed Mechanism of αAAHP Decomposition. *Base-Catalyzed Hydrolysis.* We have attempted to derive the reaction mechanism of αAAHP decomposition by monitoring the growth of product peaks using LC-ESI-MS. However, as shown in Figure 5, none of the peaks exhibits significant changes in intensity besides those of the decaying αAAHPs. The only peaks that exhibit minor, yet consistent growth are those attributable to the precursor organic acids, i.e., adipic acid and pinonic acid. Tracking the growth of these peaks is complicated by the fact that high concentrations of these organic acids are present in the solution as byproducts of the αAAHP synthesis prior to the hydrolysis experiments. Growth of the organic acid peaks is most clearly observed when the decomposition of αAAHPs is more rapid, i.e., in experiments with high temperature or high solution pH. Parts a and b of Figure 8 show the BPI chromatograms of an αAAHP-A solution during a hydrolysis experiment at 35 °C; the growth of adipic acid is confirmed with both ESI(+) and ESI(−). The growing signal of adipic acid and the decaying signal of αAAHP-A during hydrolysis experiments at 35 °C are shown in Figure 8c. Signals are normalized to those at time = 0 (the first injection) for comparison. The growth of adipic acid is highly variable, but an average growth of 19 ± 9% is observed when αAAHP-A is nearly depleted. This magnitude of growth is larger than the method stability of the LC-ESI-MS (±5%). Production of pinonic acid from αAAHP-P is also observed, but to a less significant extent: 10 ± 3%. Such a small amount of pinonic acid production is close to the method stability. Our results highlight the importance of further purifying the synthesized αAAHPs in future studies, so that large residual acid signals do not mask signal growth due to αAAHP decomposition.

The observed pH-dependence and formation of organic acids are consistent with a base-catalyzed hydrolysis of αAAHPs, as shown by the case of αAAHP-A in Figure 9. The reaction proceeds via a nucleophilic addition of OH^- to the ester, yielding adipic acid and an α-hydroxyhydroperoxide (αHHP) intermediate that is in equilibrium with the corresponding aldehyde, pinonaldehyde, and H_2O_2.[49,50] The formation of H_2O_2 is qualitatively confirmed with the HPLC-fluorescence technique, with the results shown in Figure 10. As mentioned in Experimental, the synthesized solutions were diluted by a factor of 250 in water before the HPLC-fluorescence measurement. A high initial background of H_2O_2, 3.1 μM from αAAHP-A and 2.5 μM from αAAHP-P, is found in the

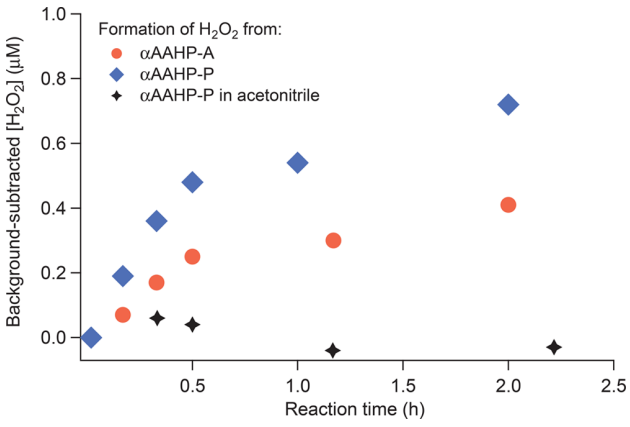

Figure 10. Production of H_2O_2 from αAAHPs diluted in water, measured using HPLC-fluorescence. The samples contain a high background of H_2O_2 from synthesis, which has been subtracted. The black trace shows the result of a control experiment, where αAAHP-P is dissolved in acetonitrile instead of water.

DOI: 10.1021/acs.jpca.8b02195
J. Phys. Chem. A 2018, 122, 5190−5201

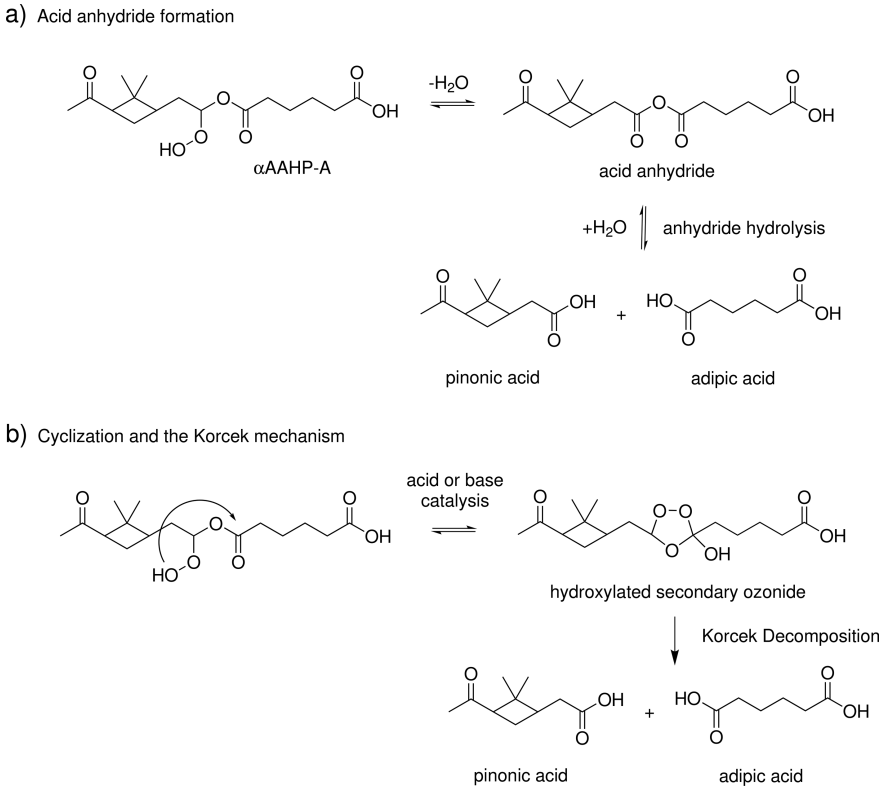

Figure 11. Other potential decomposition mechanisms of αAAHPs: (a) acid anhydride formation and (b) the Korcek mechanism. The cases for αAAHP-A are shown.

diluted aqueous solutions. We conducted a control experiment, in which αAAHP-P is diluted in acetonitrile instead of water. A similar initial H_2O_2 concentration (2.9 μM) is measured, but no further production of H_2O_2 is observed over the course of 2 h (Figure 10). The control experiment indicates that the initial H_2O_2 likely arises from the synthesis, and is not due to a rapid production upon dilution in water. The initial background has been subtracted from the results presented in Figure 10. When either αAAHP-A or αAAHP-P is diluted in water, a steady production of H_2O_2 is observed. While αAAHPs are depleted in approximately 1 h (as shown by the LC-ESI-MS results), the production of H_2O_2 continues over a much longer time. The HPLC-fluorescence results are consistent with the proposed mechanism (Figure 9), where αAAHPs are first converted into an αHHP intermediate, which likely generates H_2O_2 over a longer time scale. However, due to the impure nature of the synthesized solution, we cannot rule out the possibility that synthetic byproducts can also give rise to H_2O_2.

The observed base-catalyzed hydrolysis of αAAHPs is unique to aqueous-phase reactions. In fact, gas-phase decomposition of organic peroxides is often acid-catalyzed. Computational studies have shown that organic acids (e.g., formic acid) can form prereaction complexes with organic peroxides in the gas phase and reduce the energy barriers associated with their decomposition.[51,52] Conversely, in the aqueous phase, hydrolysis of αAAHPs is initiated via nucleophilic addition of OH^- to the ester functional group (Figure 9) The dependence of aqueous-phase decomposition on acid−base chemistry thus differentiates aqueous-phase mechanisms from their gas-phase counterparts.

Base-catalyzed hydrolysis in the aqueous phase has also been reported for a related class of organic hydroperoxides, αHHPs. In particular, the hydrolysis rates of hydroxymethyl hydroperoxide (HMP) and bis(hydroxymethyl) peroxide (BHMP) exhibit a linear relationship with the concentration of HO^- from pH 4 to 6.[53,54] This observation is similar to the case of αAAHPs observed in the current work. In general, hydrolysis reactions can be catalyzed by either acid or base.[44] We did not observe any signs of acid-catalyzed hydrolysis within the pH range studied here (pH 3.5 to 5.1), nor did we perform experiments under highly acidic conditions. However, acid-catalyzed hydrolysis of HMP and BHMP was observed in solutions with pH 1.5 or lower.[54] It will be of interest for future studies to investigate potential acid-catalyzed hydrolysis of αAAHPs in highly acidic solutions.

Other Potential Reaction Mechanisms. Besides the base-catalyzed hydrolysis mechanism, a number of other potential mechanisms have been proposed in previous work. The first mechanism is acid anhydride formation via loss of water from αAAHPs (Figure 11a). Studies of gas-phase ozonolysis of ethene in the presence of formic acid have observed the formation of formic acid anhydride, which likely arises from this reaction pathway.[7,55] A computational study[52] has shown that the presence of a third molecule, e.g., an organic acid, serves as the carrier of hydrogen and can efficiently lower the energy barrier of this reaction pathway. As shown in Figure 11a, the acid anhydride arising from αAAHP-A should undergo hydrolysis in the aqueous phase and give rise to pinonic acid and adipic acid. However, pinonic acid, which would have appeared at RT = 4.9 min, is not observed in the αAAHP-A hydrolysis experiments (Figure 8, parts a and b). Our results indicate that the acid anhydride pathway is unlikely a major reaction mechanism.

DOI: 10.1021/acs.jpca.8b02195
J. Phys. Chem. A 2018, 122, 5190−5201

The second reaction pathway considered here involves a cyclization reaction followed by decomposition, a route known as the Korcek mechanism.[56] The Korcek mechanism is particularly relevant to γ-ketohydroperoxides, forming a five-membered cyclic peroxide intermediate, which subsequently decomposes to a carbonyl compound and an organic acid.[57] In particular, Mutzel et al.[38] have proposed that the Korcek mechanism can be responsible for the loss of highly oxidized organic compounds present in SOA. As shown in Figure 11b, the cyclization of αAAHPs represents a special case of the Korcek mechanism, giving rise to a hydroxylated secondary ozonide intermediate. Information on the decomposition pathway of this hydroxylated secondary ozonide intermediate is limited.[58] In the case of αAAHP-A, the Korcek mechanism likely results in two organic acids, pinonic acid and adipic acid for the case of αAAHP-A. As already discussed for the acid anhydride pathway, production of pinonic acid is not observed in the current work, indicating that the Korcek mechanism is likely a minor reaction pathway.

CONCLUSION AND ENVIRONMENTAL IMPLICATIONS

A growing body of work suggests the importance of the reactions between stabilized Criegee intermediates (SCIs) and organic acids in the atmosphere.[5,6,14,18,20] The atmospheric fate of the resulting products, α-acyloxyalkyl hydroperoxides (αAAHPs), needs to be understood for in order to properly assess the environmental importance of SCI + organic acid chemistry. The current study presents the first systematic investigation of the behavior of αAAHPs in the condensed phase. Given a lack of commercially available standards, two αAAHPs were synthesized via liquid-phase ozonolysis of α-pinene. The most significant finding of the current work is a rapid decomposition of αAAHPs in the aqueous phase. The reaction rate is highly dependent on temperature and solution pH, with the observed e-folding lifetimes of αAAHPs ranging from 10 min (at 35 °C or pH 5) to over 100 min (at 7 °C or pH 3.5).

The observations have significant implications for the fate of αAAHPs in the atmosphere. It is now widely accepted that atmospheric aqueous phases, including cloud, fog, and aerosol liquid water, are important reaction media for organic compounds.[59−61] Highly functionalized organic compounds, such as αAAHPs arising from α-pinene ozonolysis, can be introduced into cloud and fog waters through nucleation scavenging. The pH of ambient cloud and fog waters varies between 2 and 7, depending on the chemical composition and the size of the droplets.[45] Larger droplets tend to be less acidic, as they are enriched in species arising from mineral dust and sea salt. Our study shows that base-catalyzed hydrolysis is likely the dominant decomposition pathway of αAAHPs in the cloud-water-relevant pH range. The rapid decay observed in this study implies that αAAHPs can be lost promptly when exposed to cloud and fog with pH values larger than 5. The stability of αAAHPs in aerosol liquid water is dependent on several competing factors and is difficult to predict. The pH values of aerosol liquid water tend to be lower, typically ranging between −1 and +3.[62] While we did not investigate the behavior of αAAHPs under such acidic conditions, studies on other types of organic hydroperoxide indicate that acid-catalyzed hydrolysis may become dominant in highly acidic solutions.[54] Aerosol liquid water also tends to contain a much higher concentration of organic compounds.[63,64] Observations from the current work show an acceleration of the αAAHP decomposition by dissolved organic compounds generated from α-pinene ozonolysis. The total organic carbon concentration used in the current work is 31 ppmC, equivalent to that in cloud and fog waters from polluted regions. However, extrapolation of the current results to highly complex ambient aerosol liquid water is difficult.

Rapid decomposition of αAAHPs can also occur in laboratory experiments when filter samples are extracted in aqueous or organic solvents. Such loss can potentially explain contradictory results reported in the existing literature regarding the importance of αAAHPs in SOA.[21,22] On the basis of the kinetic results obtained in this work, key suggestions can be made for future laboratory experiments targeting αAAHPs. Currently, the majority of chemical analyses of SOA components are based on filter collection, extraction, and off-line analyses. Our results suggest that the use of aprotic solvents, such as acetonitrile, can significantly reduce the decomposition of αAAHPs after extraction. If the use of aqueous solvents is unavoidable, the solution should be acidified and stored under lower temperatures to minimize αAAHP decomposition.

The reaction mechanism and the products arising from αAAHP decomposition are also of particular interest in atmospheric chemistry. The observed production of organic acids and H_2O_2 in this work is consistent with a base-catalyzed hydrolysis reaction of αAAHPs. The production of H_2O_2 is particularly important, given that H_2O_2 is a reactive oxygen species and is likely linked to adverse health effects of particulate matter pollution.[23] Formation of H_2O_2 in extracted SOA components has been previously observed and has been attributed to decomposition of larger organic peroxides.[28,30,40] αAAHP may represent one such H_2O_2 source. However, the interpretation of the reaction mechanism in the current work is significantly hindered by the presence of organic acids and synthetic byproducts that cannot be easily separated. Currently, we cannot rule out the possibility that H_2O_2 arises from compounds other than αAAHPs. Our results should be confirmed by future studies using pure αAAHP standards. A remaining question for the reaction mechanism of αAAHPs is the cause of their chemical instability. The water extract of α-pinene SOA contains a large number of nonperoxide dimer esters[31,65,66] that are much more stable than αAAHPs and do not exhibit a noticeable decay over a period of days. The hydroperoxide functional group likely introduces the observed chemical lability to αAAHPs, and base-catalyzed hydrolysis alone may not fully explain their rapid decomposition.

Finally, the two αAAHP species studied in this work exhibit similar dependence on all of the experimental conditions examined, implying that a generalized description for the reactivity of αAAHPs may be feasible. The current work focuses on two specific αAAHPs arising from α-pinene SCIs, which does not cover the diversity of SCI-derived organic species in the ambient atmosphere. Future studies should be extended to a wider spectrum of αAAHPs, including those arising from isoprene and other major alkenes.

AUTHOR INFORMATION

Corresponding Author

*(R.Z.) E-mail: rzhao@caltech.edu. Telephone: +1 626-395-8928.

DOI: 10.1021/acs.jpca.8b02195
J. Phys. Chem. A 2018, 122, 5190−5201

ORCID

Ran Zhao: 0000-0002-1096-7632
Christopher M. Kenseth: 0000-0003-3188-2336
Suzanne E. Paulson: 0000-0003-0855-7615
John H. Seinfeld: 0000-0003-1344-4068

Present Address

‡Department of Chemistry, University of Alberta, Edmonton, AB, Canada T6G 2G2

Notes

The authors declare no competing financial interest.

■ ACKNOWLEDGMENTS

The authors thank Dwight and Christine Landis for their generous contributions and Prof. Paul Wennberg for helpful discussions. LC-ESI-MS and TOC analyses were performed in the Caltech Environmental Analysis Center (EAC). This work was supported by National Science Foundation Grants AGS-1523500 and CHE-1508526. R.Z. also acknowledges support from the Natural Science and Engineering Research Council of Canada Postdoctoral Fellowship (NSERC-PDF).

■ REFERENCES

(1) Guenther, A.; Hewitt, C. N.; Erickson, D.; Fall, R.; Geron, C.; Graedel, T.; Harley, P.; Klinger, L.; Lerdau, M.; Mckay, W. A.; et al. A global model of natural volatile organic compound emissions. *J. Geophys. Res.* **1995**, *100*, 8873−8892.

(2) Seinfeld, J. H.; Pandis, S. N. *Atmospheric Chemistry and Physics: From Air Pollution to Climate Change*, 3rd ed.; John Wiley & Sons: Hoboken, NJ, 2016.

(3) Criegee, R. Mechanism of ozonolysis. *Angew. Chem., Int. Ed. Engl.* **1975**, *14*, 745−752.

(4) Osborn, D. L.; Taatjes, C. A. The physical chemistry of Criegee intermediates in the gas phase. *Int. Rev. Phys. Chem.* **2015**, *34*, 309−360.

(5) Taatjes, C. A.; Shallcross, D. E.; Percival, C. J. Research frontiers in the chemistry of Criegee intermediates and tropospheric ozonolysis. *Phys. Chem. Chem. Phys.* **2014**, *16*, 1704−1718.

(6) Welz, O.; Eskola, A. J.; Sheps, L.; Rotavera, B.; Savee, J. D.; Scheer, A. M.; Osborn, D. L.; Lowe, D.; Murray Booth, A.; Xiao, P.; et al. Rate coefficients of C1 and C2 Criegee intermediate reactions with formic and acetic acid near the collision limit: direct kinetics measurements and atmospheric implications. *Angew. Chem., Int. Ed.* **2014**, *53*, 4547−4550.

(7) Neeb, P.; Horie, O.; Moortgat, G. K. Gas-phase ozonolysis of ethene in the presence of hydroxylic compounds. *Int. J. Chem. Kinet.* **1996**, *28*, 721−730.

(8) Tobias, H. J.; Ziemann, P. J. Kinetics of the gas-phase reactions of alcohols, aldehydes, carboxylic acids, and water with the C13 stabilized Criegee intermediate formed from ozonolysis of 1-tetradecene. *J. Phys. Chem. A* **2001**, *105*, 6129−6135.

(9) Stone, D.; Blitz, M.; Daubney, L.; Howes, N. U.; Seakins, P. Kinetics of CH_2OO reactions with SO_2, NO_2, NO, H_2O and CH_3CHO as a function of pressure. *Phys. Chem. Chem. Phys.* **2014**, *16*, 1139−1149.

(10) Mochida, M.; Katrib, Y.; Jayne, J. T.; Worsnop, D. R.; Martin, S. T. The relative importance of competing pathways for the formation of high-molecular-weight peroxides in the ozonolysis of organic aerosol particles. *Atmos. Chem. Phys.* **2006**, *6*, 4851−4866.

(11) Sakamoto, Y.; Inomata, S.; Hirokawa, J. Oligomerization reaction of the criegee intermediate leads to secondary organic aerosol formation in ethylene ozonolysis. *J. Phys. Chem. A* **2013**, *117*, 12912−12921.

(12) Kristensen, K.; Enggrob, K. L.; King, S. M.; Worton, D. R.; Platt, S. M.; Mortensen, R.; Rosenoern, T.; Surratt, J. D.; Bilde, M.; Goldstein, A. H.; et al. Formation and occurrence of dimer esters of pinene oxidation products in atmospheric aerosols. *Atmos. Chem. Phys.* **2013**, *13*, 3763−3776.

(13) Kristensen, K.; Cui, T.; Zhang, H.; Gold, A.; Glasius, M.; Surratt, J. D. Dimers in α-pinene secondary organic aerosol: effect of hydroxyl radical, ozone, relative humidity and aerosol acidity. *Atmos. Chem. Phys.* **2014**, *14*, 4201−4218.

(14) Kristensen, K.; Watne, A. K.; Hammes, J.; Lutz, A.; Petäjä, T.; Hallquist, M.; Bilde, M.; Glasius, M. High-molecular weight dimer esters are major products in aerosols from α-pinene ozonolysis and the boreal forest. *Environ. Sci. Technol. Lett.* **2016**, *3*, 280−285.

(15) Kristensen, K.; Jensen, L.; Glasius, M.; Bilde, M. The effect of sub-zero temperature on the formation and composition of secondary organic aerosol from ozonolysis of α-pinene. *Environ. Sci. Processes Impacts* **2017**, *19*, 1220−1234.

(16) Zhu, C.; Kumar, M.; Zhong, J.; Li, L.; Francisco, J. S.; Zeng, X. C. New mechanistic pathways for Criegee−water chemistry at the air/water interface. *J. Am. Chem. Soc.* **2016**, *138*, 11164−11169.

(17) Zhong, J.; Kumar, M.; Zhu, C. Q.; Francisco, J. S.; Zeng, X. C. Surprising stability of larger Criegee intermediates on aqueous interfaces. *Angew. Chem., Int. Ed.* **2017**, *56*, 7740−7744.

(18) Kumar, M.; Zhong, J.; Zeng, X. C.; Francisco, J. S. Reaction of Criegee intermediate with nitric acid at the air−water interface. *J. Am. Chem. Soc.* **2018**, *140*, 4913−4921.

(19) Enami, S.; Colussi, A. J. Efficient scavenging of Criegee intermediates on water by surface-active cis-pinonic acid. *Phys. Chem. Chem. Phys.* **2017**, *19*, 17044−17051.

(20) Enami, S.; Colussi, A. J. Criegee chemistry on aqueous organic surfaces. *J. Phys. Chem. Lett.* **2017**, *8*, 1615−1623.

(21) Zhao, R.; Kenseth, C. M.; Huang, Y.; Dalleska, N. F.; Seinfeld, J. H. Iodometry-assisted liquid chromatography electrospray ionization mass spectrometry for analysis of organic peroxides - an application to atmospheric secondary organic aerosol. *Environ. Sci. Technol.* **2018**, *52*, 2108−2117.

(22) Witkowski, B.; Gierczak, T. Early stage composition of SOA produced by α-pinene/ozone reaction: α-Acyloxyhydroperoxy aldehydes and acidic dimers. *Atmos. Environ.* **2014**, *95*, 59−70.

(23) Tao, F.; Gonzalez-Flecha, B.; Kobzik, L. Reactive oxygen species in pulmonary inflammation by ambient particulates. *Free Radical Biol. Med.* **2003**, *35*, 327−340.

(24) Shiraiwa, M.; Ueda, K.; Pozzer, A.; Lammel, G.; Kampf, C. J.; Fushimi, A.; Enami, S.; Arangio, A. M.; Fröhlich-Nowoisky, J.; Fujitani, Y.; et al. Aerosol health effects from molecular to global scales. *Environ. Sci. Technol.* **2017**, *51*, 13545−13567.

(25) Krapf, M.; El Haddad, I.; Bruns, E. A.; Molteni, U.; Daellenbach, K. R.; Prévôt, A. S.; Baltensperger, U.; Dommen, J. Labile peroxides in secondary organic aerosol. *Chem.* **2016**, *1*, 603−616.

(26) Li, H.; Chen, Z.; Huang, L.; Huang, D. Organic peroxides' gas-particle partitioning and rapid heterogeneous decomposition on secondary organic aerosol. *Atmos. Chem. Phys.* **2016**, *16*, 1837−1848.

(27) Riva, M.; Budisulistiorini, S. H.; Zhang, Z.; Gold, A.; Thornton, J. A.; Turpin, B. J.; Surratt, J. D. Multiphase reactivity of gaseous hydroperoxide oligomers produced from isoprene ozonolysis in the presence of acidified aerosols. *Atmos. Environ.* **2017**, *152*, 314−322.

(28) Badali, K. M.; Zhou, S.; Aljawhary, D.; Antiñolo, M.; Chen, W. J.; Lok, A.; Mungall, E.; Wong, J. P. S.; Zhao, R.; Abbatt, J. P. D. Formation of hydroxyl radicals from photolysis of secondary organic aerosol material. *Atmos. Chem. Phys.* **2015**, *15*, 7831−7840.

(29) Tong, H.; Arangio, A. M.; Lakey, P. S. J.; Berkemeier, T.; Liu, F.; Kampf, C. J.; Brune, W. H.; Pöschl, U.; Shiraiwa, M. Hydroxyl radicals from secondary organic aerosol decomposition in water. *Atmos. Chem. Phys.* **2016**, *16*, 1761−1771.

(30) Arellanes, C.; Paulson, S. E.; Fine, P. M.; Sioutas, C. Exceeding of Henry's law by hydrogen peroxide associated with urban aerosols. *Environ. Sci. Technol.* **2006**, *40*, 4859−4866.

(31) Zhang, X.; McVay, R. C.; Huang, D. D.; Dalleska, N. F.; Aumont, B.; Flagan, R. C.; Seinfeld, J. H. Formation and evolution of molecular products in α-pinene secondary organic aerosol. *Proc. Natl. Acad. Sci. U. S. A.* **2015**, *112*, 14168−14173.

DOI: 10.1021/acs.jpca.8b02195
J. Phys. Chem. A 2018, 122, 5190−5201

(32) Zhang, X.; Dalleska, N. F.; Huang, D. D.; Bates, K. H.; Sorooshian, A.; Flagan, R. C.; Seinfeld, J. H. Time-resolved molecular characterization of organic aerosols by PILS+ UPLC/ESI-Q-TOFMS. *Atmos. Environ.* **2016**, *130*, 180−189.
(33) Witkowski, B.; Gierczak, T. Analysis of α-acyloxyhydroperoxy aldehydes with electrospray ionization-tandem mass spectrometry (ESI-MS(n)). *J. Mass Spectrom.* **2013**, *48*, 79−88.
(34) Kumar, M.; Busch, D. H.; Subramaniam, B.; Thompson, W. H. Barrierless tautomerization of Criegee intermediates via acid catalysis. *Phys. Chem. Chem. Phys.* **2014**, *16*, 22968−22973.
(35) Banerjee, D. K.; Budke, C. C. Spectrophotometric determination of traces of peroxides in organic solvents. *Anal. Chem.* **1964**, *36*, 792−796.
(36) Bloomfield, M. The spectrophotometric determination of hydroperoxide and peroxide in a lipid pharmaceutical product by flow injection analysis. *Analyst* **1999**, *124*, 1865−1871.
(37) Docherty, K. S.; Wu, W.; Lim, Y. B.; Ziemann, P. J. Contributions of organic peroxides to secondary aerosol formed from reactions of monoterpenes with O_3. *Environ. Sci. Technol.* **2005**, *39*, 4049−4059.
(38) Mutzel, A.; Poulain, L.; Berndt, T.; Iinuma, Y.; Rodigast, M.; Böge, O.; Richters, S.; Spindler, G.; Sipilä, M.; Jokinen, T.; et al. Highly oxidized multifunctional organic compounds observed in tropospheric particles: a field and laboratory study. *Environ. Sci. Technol.* **2015**, *49*, 7754−7761.
(39) Huang, Y.; Coggon, M. M.; Zhao, R.; Lignell, H.; Bauer, M. U.; Flagan, R. C.; Seinfeld, J. H. The Caltech Photooxidation Flow Tube reactor: design, fluid dynamics and characterization. *Atmos. Meas. Tech.* **2017**, *10*, 839−867.
(40) Wang, Y.; Kim, H.; Paulson, S. E. Hydrogen peroxide generation from α- and β-pinene and toluene secondary organic aerosols. *Atmos. Environ.* **2011**, *45*, 3149−3156.
(41) Wang, Y.; Arellanes, C.; Paulson, S. E. Hydrogen peroxide associated with ambient fine-mode, diesel, and biodiesel aerosol particles in Southern California. *Aerosol Sci. Technol.* **2012**, *46*, 394−402.
(42) Hasson, A. S.; Orzechowska, G.; Paulson, S. E. Production of stabilized Criegee intermediates and peroxides in the gas phase ozonolysis of alkenes: 1. Ethene, trans-2-butene, and 2,3-dimethyl-2-butene. *J. Geophys. Res. Atmos.* **2001**, *106*, 34131−34142.
(43) Hasson, A. S.; Ho, A. W.; Kuwata, K. T.; Paulson, S. E. Production of stabilized Criegee intermediates and peroxides in the gas phase ozonolysis of alkenes: 2. Asymmetric and biogenic alkenes. *J. Geophys. Res. Atmos.* **2001**, *106*, 34143−34153.
(44) Mabey, W.; Mill, T. Critical review of hydrolysis of organic compounds in water under environmental conditions. *J. Phys. Chem. Ref. Data* **1978**, *7*, 383−415.
(45) Collett, J. L.; Bator, A.; Rao, X.; Demoz, B. B. Acidity variations across the cloud drop size spectrum and their influence on rates of atmospheric sulfate production. *Geophys. Res. Lett.* **1994**, *21*, 2393−2396.
(46) Herckes, P.; Valsaraj, K. T.; Collett, J. L., Jr A review of observations of organic matter in fogs and clouds: origin, processing and fate. *Atmos. Res.* **2013**, *132-133*, 434−449.
(47) Boris, A. J.; Desyaterik, Y.; Collett, J. L. How do components of real cloud water affect aqueous pyruvate oxidation? *Atmos. Res.* **2014**, *143*, 95−106.
(48) Lee, A. K. Y.; Herckes, P.; Leaitch, W. R.; Macdonald, A. M.; Abbatt, J. P. D. Aqueous OH oxidation of ambient organic aerosol and cloud water organics: Formation of highly oxidized products. *Geophys. Res. Lett.* **2011**, *38*, GL047439.
(49) Zhao, R.; Lee, A. K. Y.; Abbatt, J. P. D. Investigation of aqueous-phase photooxidation of glyoxal and methylglyoxal by aerosol chemical ionization mass spectrometry: observation of hydroxyhydroperoxide formation. *J. Phys. Chem. A* **2012**, *116*, 6253−6263.
(50) Zhao, R.; Lee, A. K. Y.; Soong, R.; Simpson, A. J.; Abbatt, J. P. D. Formation of aqueous-phase α-hydroxyhydroperoxides (α-HHP): potential atmospheric impacts. *Atmos. Chem. Phys.* **2013**, *13*, 5857−5872.
(51) Kumar, M.; Busch, D. H.; Subramaniam, B.; Thompson, W. H. Role of tunable acid catalysis in decomposition of α-hydroxyalkyl hydroperoxides and mechanistic implications for tropospheric chemistry. *J. Phys. Chem. A* **2014**, *118*, 9701−9711.
(52) Aplincourt, P.; Ruiz-López, M. F. Theoretical study of formic acid anhydride formation from carbonyl oxide in the atmosphere. *J. Phys. Chem. A* **2000**, *104*, 380−388.
(53) Zhou, X.; Lee, Y. N. Aqueous solubility and reaction kinetics of hydroxymethyl hydroperoxide. *J. Phys. Chem.* **1992**, *96*, 265−272.
(54) Marklund, S.; et al. Simultaneous determination of bis (hydroxymethyl)-peroxide (BHMP), hydroxymethylhydroperoxide (HMP), and H_2O_2 with titanium (IV)-equilibria between peroxides and stabilities of HMP and BHMP at physiological conditions. *Acta Chem. Scand.* **1971**, *25*, 3517.
(55) Neeb, P.; Horie, O.; Moortgat, G. K. The nature of the transitory product in the gas-phase ozonolysis of ethene. *Chem. Phys. Lett.* **1995**, *246*, 150−156.
(56) Jensen, R. K.; Korcek, S.; Mahoney, L. R.; Zinbo, M. Liquid-phase autoxidation of organic compounds at elevated temperatures. 2. Kinetics and mechanisms of the formation of cleavage products in n-hexadecane autoxidation. *J. Am. Chem. Soc.* **1981**, *103*, 1742−1749.
(57) Jalan, A.; Alecu, I. M.; Meana-Pañeda, R.; Aguilera-Iparraguirre, J.; Yang, K. R.; Merchant, S. S.; Truhlar, D. G.; Green, W. H. New pathways for formation of acids and carbonyl products in low-temperature oxidation: the Korcek decomposition of γ-ketohydroperoxides. *J. Am. Chem. Soc.* **2013**, *135*, 11100−11114.
(58) Moshammer, K.; Jasper, A. W.; Popolan-Vaida, D. M.; Lucassen, A.; Dievart, P.; Selim, H.; Eskola, A. J.; Taatjes, C. A.; Leone, S. R.; Sarathy, S. M.; et al. Detection and identification of the keto-hydroperoxide ($HOOCH_2OCHO$) and other intermediates during low-temperature oxidation of dimethyl ether. *J. Phys. Chem. A* **2015**, *119*, 7361−7374.
(59) Ervens, B. Modeling the processing of aerosol and trace gases in clouds and fogs. *Chem. Rev.* **2015**, *115*, 4157−4198.
(60) McNeill, V. F. Aqueous organic chemistry in the atmosphere: sources and chemical processing of organic aerosols. *Environ. Sci. Technol.* **2015**, *49*, 1237−1244.
(61) Zhao, R.; Lee, A. K. Y.; Wang, C.; Wania, F.; Wong, J. P. S.; Zhou, S.; Abbatt, J. P. D. The Role of Water in Organic Aerosol Multiphase Chemistry: Focus on Partitioning and Reactivity. *Advances in Atmospheric Chemistry* **2017**, 95−184.
(62) Murphy, J. G.; Gregoire, P. K.; Tevlin, A. G.; Wentworth, G. R.; Ellis, R. A.; Markovic, M. Z.; VandenBoer, T. C. Observational constraints on particle acidity using measurements and modelling of particles and gases. *Faraday Discuss.* **2017**, *200*, 379−395.
(63) Arakaki, T.; Anastasio, C.; Kuroki, Y.; Nakajima, H.; Okada, K.; Kotani, Y.; Handa, D.; Azechi, S.; Kimura, T.; Tsuhako, A.; et al. A general scavenging rate constant for reaction of hydroxyl radical with organic carbon in atmospheric waters. *Environ. Sci. Technol.* **2013**, *47*, 8196−8203.
(64) Volkamer, R.; Ziemann, P. J.; Molina, M. J. Secondary organic aerosol formation from acetylene (C_2H_2): seed effect on SOA yields due to organic photochemistry in the aerosol aqueous phase. *Atmos. Chem. Phys.* **2009**, *9*, 1907−1928.
(65) Yasmeen, F.; Vermeylen, R.; Szmigielski, R.; Iinuma, Y.; Böge, O.; Herrmann, H.; Maenhaut, W.; Claeys, M. Terpenylic acid and related compounds: precursors for dimers in secondary organic aerosol from the ozonolysis of α-and β-pinene. *Atmos. Chem. Phys.* **2010**, *10*, 9383−9392.
(66) Müller, L.; Reinnig, M.-C.; Warnke, J.; Hoffmann, T. Unambiguous identification of esters as oligomers in secondary organic aerosol formed from cyclohexene and cyclohexene/α-pinene ozonolysis. *Atmos. Chem. Phys.* **2008**, *8*, 1423−1433.

DOI: 10.1021/acs.jpca.8b02195
J. Phys. Chem. A 2018, 122, 5190−5201

Appendix D

SYNERGISTIC O_3 + OH OXIDATION PATHWAY TO EXTREMELY LOW-VOLATILITY DIMERS REVEALED IN β-PINENE SECONDARY ORGANIC AEROSOL

Kenseth, Christopher M., Yuanlong Huang, Ran Zhao, Nathan F. Dalleska, J. Caleb Hethcox, Brian M. Stoltz, and John H. Seinfeld (2018). "Synergistic O_3 + OH oxidation pathway to extremely low-volatility dimers revealed in β-pinene secondary organic aerosol". In: *Proc. Natl. Acad. Sci. U.S.A.* 115.33, pp. 8301–8306. DOI: 10.1073/pnas.1804671115.

Synergistic O_3 + OH oxidation pathway to extremely low-volatility dimers revealed in β-pinene secondary organic aerosol

Christopher M. Kenseth[a], Yuanlong Huang[b], Ran Zhao[a], Nathan F. Dalleska[b], J. Caleb Hethcox[a], Brian M. Stoltz[a], and John H. Seinfeld[a,c,1]

[a]Division of Chemistry and Chemical Engineering, California Institute of Technology, Pasadena, CA 91125; [b]Division of Geological and Planetary Sciences, California Institute of Technology, Pasadena, CA 91125; and [c]Division of Engineering and Applied Science, California Institute of Technology, Pasadena, CA 91125

Edited by Joost A. de Gouw, University of Colorado Boulder, Boulder, CO, and accepted by Editorial Board Member A. R. Ravishankara July 2, 2018 (received for review March 16, 2018)

Dimeric compounds contribute significantly to the formation and growth of atmospheric secondary organic aerosol (SOA) derived from monoterpene oxidation. However, the mechanisms of dimer production, in particular the relevance of gas- vs. particle-phase chemistry, remain unclear. Here, through a combination of mass spectrometric, chromatographic, and synthetic techniques, we identify a suite of dimeric compounds ($C_{15–19}H_{24–32}O_{5–11}$) formed from concerted O_3 and OH oxidation of β-pinene (i.e., accretion of O_3- and OH-derived products/intermediates). These dimers account for an appreciable fraction (5.9–25.4%) of the β-pinene SOA mass and are designated as extremely low-volatility organic compounds. Certain dimers, characterized as covalent dimer esters, are conclusively shown to form through heterogeneous chemistry, while evidence of dimer production via gas-phase reactions is also presented. The formation of dimers through synergistic O_3 + OH oxidation represents a potentially significant, heretofore-unidentified source of low-volatility monoterpene SOA. This reactivity also suggests that the current treatment of SOA formation as a sum of products originating from the isolated oxidation of individual precursors fails to accurately reflect the complexity of oxidation pathways at play in the real atmosphere. Accounting for the role of synergistic oxidation in ambient SOA formation could help to resolve the discrepancy between the measured atmospheric burden of SOA and that predicted by regional air quality and global climate models.

secondary organic aerosol | synergistic oxidation | atmospheric accretion chemistry | dimer formation | monoterpenes

The oxidation of monoterpenes ($C_{10}H_{16}$) represents a substantial and well-established source of atmospheric secondary organic aerosol (SOA) (1, 2), which constitutes a dominant mass fraction (15–80%) of fine particulate matter ($PM_{2.5}$) (3) and exerts large but uncertain effects on Earth's radiative balance (4) as well as adverse impacts on regional air quality and human health (5, 6). High-molecular-weight, low-volatility dimeric compounds have been identified as significant components of both ambient (7–11) and laboratory-derived (12–22) monoterpene SOA, and have been implicated as key players in new particle formation and growth (9–14, 23–26), particle viscosity (27), and cloud condensation nuclei (CCN) activity (8, 24, 26).

Accumulating studies of α-pinene SOA indicate that a vast majority of these dimers are formed only through O_3- and not OH-initiated oxidation, despite the apparent monomeric building blocks being present in both oxidative systems (11–13). Particle-phase reactions of closed-shell monomers [e.g., aldol addition/condensation (15–18), (peroxy)hemiacetal/acetal formation (16, 21, 22), esterification (7, 18–21), and gem-diol formation (16, 17)] and gas-phase reactions involving early-stage oxidation products and/or reactive intermediates [e.g., stabilized Criegee intermediates (SCIs), carboxylic acids, and organic peroxy radicals (RO_2) (9–14, 23–26)] have been advanced as possible dimer formation pathways. However, the mechanisms underlying dimer production and the relative importance of gas- vs. particle-phase chemistry remain unresolved.

In this work, we investigate the formation, identity, and abundance of molecular products in SOA derived from the O_3- and OH-initiated oxidation of β-pinene, the second-most-abundant monoterpene emitted to the atmosphere (global emissions estimated at 19 Tg y^{-1}) (28). Through detailed chromatographic and mass spectrometric analysis, coupled with ^{13}C isotopic labeling and OH/SCI scavenging, we identify a reactive pathway to extremely low-volatility dimeric compounds in SOA formed from monoterpene ozonolysis involving reaction of O_3-derived products/intermediates with those generated from oxidation by OH produced in situ via vinyl hydroperoxide (VHP) decomposition. We present evidence for formation of these dimers via both gas- and particle-phase processes, underscoring the complexity of atmospheric accretion chemistry. In establishing that O_3 and OH can act in concert to form nontrivial yields of dimeric SOA constituents, we highlight the potential significance of synergistic oxidation in ambient aerosol formation.

Results and Discussion

Dimers in β-Pinene SOA. β-Pinene ozonolysis and photooxidation experiments were carried out in the Caltech dual 24 m^3 Teflon Environmental Chambers (CTEC) (*Materials and Methods*). A

Significance

Secondary organic aerosol (SOA) is ubiquitous in the atmosphere and plays a pivotal role in climate, air quality, and health. Monoterpenes, emitted in large quantities from forested regions, are a dominant source of SOA globally, with dimers having been identified as key contributors to particle formation and growth. Here, we establish the role of concerted oxidation by O_3 and OH as a significant route to dimer formation in SOA generated from β-pinene, the second-most-abundant monoterpene emitted to the atmosphere. Production of this class of dimers is found to occur through both gas- and particle-phase processes. Dimer formation via synergistic O_3 + OH oxidation could represent an appreciable source of "missing" SOA not included in current atmospheric models.

Author contributions: C.M.K. designed research; C.M.K., Y.H., and R.Z. performed research; J.C.H. and B.M.S. contributed new reagents/analytic tools; C.M.K., Y.H., R.Z., and N.F.D. analyzed data; and C.M.K. and J.H.S. wrote the paper.

The authors declare no conflict of interest.

This article is a PNAS Direct Submission. J.A.d.G. is a guest editor invited by the Editorial Board.

[1]To whom correspondence should be addressed. Email: seinfeld@caltech.edu.

This article contains supporting information online at www.pnas.org/lookup/suppl/doi:10.1073/pnas.1804671115/-/DCSupplemental.

Published online August 3, 2018.

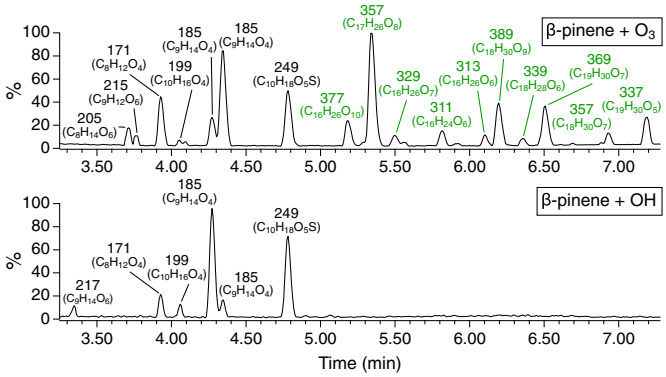

Fig. 1. UPLC/(−)ESI-Q-TOF-MS BPI chromatograms of SOA produced from the O_3- and OH-initiated oxidation of β-pinene after ∼4 h of reaction in the CTEC (*SI Appendix*, Table S1, Exps. 1 and 2). Numbers correspond to nominal *m/z* values of $[M-H]^-$ ions. Molecular formulas ($C_xH_yO_z$) were assigned with mass tolerances of <7 ppm and supported by associated ^{13}C isotope distributions. Chromatograms consist of monomeric (black) and dimeric (green) regions.

custom-modified particle-into-liquid sampler (PILS) integrated with ultra-performance liquid chromatography/electrospray ionization quadrupole time-of-flight mass spectrometry operated in negative ion mode [UPLC/(−)ESI-Q-TOF-MS] was used to characterize the time-resolved SOA molecular composition (*Materials and Methods*) (29). Base peak ion (BPI) chromatograms of the O_3- and OH-derived β-pinene SOA are shown in Fig. 1. The chromatographic fingerprint of the O_3 system displays distinct monomeric and dimeric regions. Conversely, while the identities of the monomers in both systems are similar, dimers measureable by PILS + UPLC/(−)ESI-Q-TOF-MS were not formed above the detection limit in the OH system, consistent with previous LC/(−)ESI-MS studies on dimer formation in α-pinene SOA (11–13). The monomers, on average, exhibit higher O:C ratios than the dimers, suggesting that deoxygenation (e.g., condensation) is operative in dimer formation (18, 21). That the dimers in the O_3-derived SOA elute at retention times (RT) distinct from those of the monomers and are undetected in SOA produced from OH oxidation demonstrates that they are authentic β-pinene SOA products rather than ion-source artifacts (e.g., noncovalent adducts) formed during the (−)ESI process.

The absence of detectable dimers in pinene photooxidation systems has prompted SCIs, specifically reaction of SCIs with first-generation carboxylic acids forming hydroperoxide esters (11, 12, 15), to be implicated as potential drivers of monoterpene accretion chemistry. However, we recently demonstrated that dimers identified in α-pinene SOA using LC/ESI-MS methods do not contain (hydro)peroxide moieties (30). Further, no clear reduction in dimer abundance was observed for SOA generated from β-pinene ozonolysis when either water vapor or formic acid was introduced as an SCI scavenger (*SI Appendix*, Fig. S1). These findings, together with modest SCI yields (15%) measured for α-pinene ozonolysis (31, 32), experimental and theoretical studies showing thermal unimolecular decay to be a dominant SCI loss process (32–34), and reported increases in dimer concentrations in α-pinene SOA with increasing relative humidity (RH) (11–13) despite the probable role of water vapor as an SCI scavenger, call into question the importance of SCI chemistry in monoterpene dimer production. The lack of peroxide dimers in α-pinene SOA also implies that gas-phase dimers formed via RO_2 self/cross-reactions ($RO_2 + RO_2 \rightarrow ROOR + O_2$) (23–26) do not retain their peroxide character (i.e., undergo chemical transformation/decomposition) following condensation to the particle phase, as previously suggested (13, 20, 23).

Although dimers in pinene SOA seem to form only through O_3- and not OH-initiated oxidation, scavenging of OH radicals produced as a byproduct of the hot Criegee VHP channel during α-pinene ozonolysis has been found to suppress the formation of certain dimeric species (11). To further explore this effect, steady-state β-pinene ozonolysis experiments were conducted in the Caltech Photooxidation Flow Tube (CPOT) in the presence and absence of cyclohexane as an OH scavenger (*Materials and Methods*). UPLC/(−)ESI-Q-TOF-MS was employed to measure the molecular composition of SOA samples collected on Teflon filters and extracted into H_2O (*Materials and Methods*). A group of 23 dimeric compounds, also present in the CTEC experiments, was identified whose formation was significantly inhibited (>65%) by introduction of the OH scavenger; four of the dimers are major peaks in the BPI chromatogram (Fig. 2). These dimers, with molecular formulas $C_{15-19}H_{24-32}O_{5-11}$ and O:C ratios ranging from 0.26 to 0.61, exhibit saturation mass concentrations (C^*) < 3×10^{-4} μg m^{-3} and are designated as extremely low-volatility organic compounds (ELVOC) (Table 1). Compounds with accurate masses/molecular formulas corresponding to 20 of the 23 identified dimers have been measured in recent monoterpene SOA formation experiments, and 18 such compounds have been observed in ambient SOA samples from forested regions dominated by monoterpene emissions (*SI Appendix*, Table S2). The clear conclusion from these experiments is that formation for this particular collection of dimeric species depends on both O_3 and OH oxidation, in either a concurrent or sequential manner.

Dimers from Ozonolysis of ^{13}C-β-Pinene. To determine the point in the O_3-initiated dimer formation pathway at which OH radical chemistry occurs (e.g., oxidation of the precursor hydrocarbon, gas-phase reaction with first-generation products, or heterogeneous aging of particle-bound dimers), the exocyclic double bond of β-pinene was exploited. ^{13}C-β-Pinene, labeled at the terminal vinylic carbon, was synthesized from ^{13}C-iodomethane and nopinone via Wittig olefination (Scheme 1). Ozonolysis of ^{13}C-β-pinene was carried out in the CPOT in the absence of an OH scavenger; SOA samples were collected on Teflon filters and extracted into H_2O. The *m/z* of 18 of the identified dimers (Table 1, types 1–3), including the four major BPI peaks, shifted by one mass unit on formation from ^{13}C-β-pinene, indicative of ^{13}C incorporation, while their RT remained unchanged. Recalling that reaction of ^{13}C-β-pinene with O_3 will cleave the ^{13}C label whereas on reaction with OH the label will be retained, the one-unit mass shift suggests that formation of the 18 dimers occurs via reaction, in either the gas or particle phase, of O_3-derived products/intermediates with products/intermediates generated from oxidation of β-pinene by OH produced via VHP decomposition. For those dimers that did not undergo a mass shift (Table 1, type 4), the observed dependence of their formation on OH can be rationalized, in addition to the scenarios above, in terms of a photooxidative pathway in which the labeled carbon is

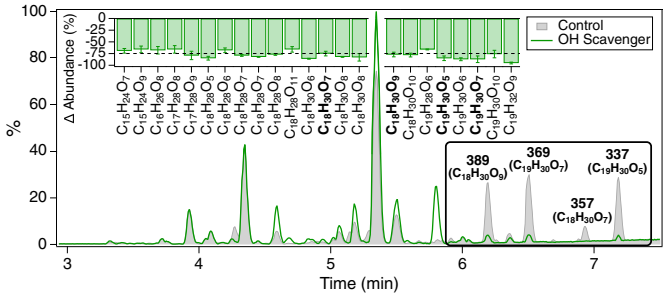

Fig. 2. UPLC/(−)ESI-Q-TOF-MS BPI chromatograms of SOA produced from the O_3-initiated oxidation of β-pinene in the CPOT in the presence and absence of cyclohexane as an OH scavenger (*SI Appendix*, Table S1, Exps. 7 and 8). Numbers correspond to nominal *m/z* values of $[M-H]^-$ ions; molecular formulas are given in parentheses. (*Inset*) Dimers that exhibited a significant decrease in abundance due to cyclohexane addition (Table 1), reported as a percent change relative to the control experiment and precise to <10%. Data for Control and OH Scavenger experiments are normalized to the total organic carbon content of the corresponding SOA samples (*SI Appendix*, S3.4) and are reported as averages of replicates (n = 3).

Table 1. Dimers identified in SOA produced from the O_3-initiated oxidation of β-pinene that exhibited a significant decrease in abundance (>65%) due to OH scavenging

Dimer type	Observed *m/z* (–)	RT, min	Molecular formula	Error, ppm	O:C	$\overline{OS}_C$[†]	logC*,[‡] μg m^{-3}	Exchangeable hydrogens	SOA mass fraction,[§,¶] %
1	323.1860	6.86	$C_{18}H_{28}O_5$	0.6	0.28	−1.00	−3.9	2	0.04–0.17
	355.1754	6.24	$C_{18}H_{28}O_7$	−0.8	0.39	−0.78	−7.6	4	0.11–0.36
	419.1525	4.70	$C_{18}H_{28}O_{11}$	−6.7	0.61	−0.33	−15.2	4	0.02–0.16
	373.1851	5.99	$C_{18}H_{30}O_8$	−2.9	0.44	−0.78	−9.4	4	0.07–0.23
	405.1764	4.49	$C_{18}H_{30}O_{10}$	0.7	0.56	−0.56	−13.2	5	0.06–0.62
	351.1828	5.73	$C_{19}H_{28}O_6$	5.7	0.32	−0.84	−6.1	2	0.10–0.41
	337.2027	7.16	$C_{19}H_{30}O_5$	3.6	0.26	−1.05	−4.3	2	0.46–2.01
	369.1916	6.48	$C_{19}H_{30}O_7$	0.8	0.37	−0.84	−7.9	4	2.23–9.24
2	341.1960	6.87	$C_{18}H_{30}O_6$	−1.2	0.33	−1.00	−5.7	2	0.06–0.24
	357.1919	6.91	$C_{18}H_{30}O_7$	1.7	0.39	−0.89	−7.6	3	0.39–1.60
	373.1851	5.70	$C_{18}H_{30}O_8$	−2.9	0.44	−0.78	−9.4	3	0.14–0.47
	389.1814	6.18	$C_{18}H_{30}O_9$	0.8	0.50	−0.67	−11.3	3	1.88–7.81
	353.1961	6.15	$C_{19}H_{30}O_6$	−0.8	0.32	−0.95	−6.1	3	0.14–0.60
3	315.1448	5.83	$C_{15}H_{24}O_7$	1.3	0.47	−0.67	−6.6	3	0.02–0.10
	347.1346	5.19	$C_{15}H_{24}O_9$	1.2	0.60	−0.40	−10.5	3	0.03–0.25
	375.1653	6.24	$C_{17}H_{28}O_9$	−0.5	0.53	−0.59	−11.0	3	0.02–0.24
	417.1769	6.76	$C_{19}H_{30}O_{10}$	1.9	0.53	−0.53	−13.5	2	0.06–0.62
	403.1963	6.28	$C_{19}H_{32}O_9$	−1.2	0.48	−0.74	−11.6	3	0.07–0.24
4	345.1549	5.36	$C_{16}H_{26}O_8$	0.1	0.50	−0.63	−8.8	2	0.05–0.50
	359.1714	5.89	$C_{17}H_{28}O_8$	2.2	0.47	−0.71	−9.1	3	0.32–1.07
	339.1822	6.34	$C_{18}H_{28}O_6$	4.1	0.33	−0.89	−5.7	2	0.46–1.93
	355.1754	5.27	$C_{18}H_{28}O_7$	−0.8	0.39	−0.78	−7.6	5	0.51–1.72
	371.1707	5.46	$C_{18}H_{28}O_8$	0.3	0.44	−0.67	−9.4	3	0.30–1.22

Dimers are grouped into four types based on structure and formation mechanism (see main text).

[†]Average carbon oxidation state ($\overline{OS}_C$ = 2 O:C − H:C).

[‡]Saturation mass concentration (C*). Estimated using empirical model developed by Donahue et al. (35).

[§]Calculated for β-pinene SOA produced from O_3-initiated oxidation in the CTEC (*SI Appendix*, Table S1, Exp. 1) after ∼4 h of reaction.

[¶]Upper and lower bounds represent mass fraction estimates derived from experimental and computational approaches, respectively. Uncertainties in experimental and computational approaches are estimated to be ±23% (relative) and a factor of 3, respectively. Details are provided in *SI Appendix*, S7.

eliminated following OH addition to β-pinene (36, 37) but prior to reaction with the O_3-derived species.

The steady-state CPOT experiments enabled collection of sufficient quantities of SOA mass for detailed structural analysis via collision-induced dissociation (CID) (*SI Appendix*, S3.5). MS/MS spectra of the ^{13}C-labeled dimers and their ^{12}C isotopologues revealed distinct OH-derived (^{13}C-mass-shifted) and O_3-derived (unshifted) fragmentation patterns (*SI Appendix*, Table S3). A group of eight dimeric compounds (Table 1, type 1) was identified with fragmentation patterns and relative peak intensities characteristic of covalent dimer esters, which have been reported to be significant components of monoterpene SOA (7, 10–13, 18–21). Specifically, (*i*) the elemental composition of the dimers is given by condensation of the O_3- and OH-derived monomeric product ions ($M_1 + M_2 - M_{H_2O} = M_D$) (7, 16), and (*ii*) assuming that the principal fragmentation occurs at the ester linkage, producing carboxyl and alkoxy fragment ions through neutral loss of the alcohol and dehydrated acid moieties, respectively, the carboxyl fragments and associated daughter ions are more intense than the alkoxy fragments and their daughter ions (Fig. 3) (20, 21, 38), in line with conventional charge accommodation behavior in (–)ESI-MS. For the remaining 10 dimers (Table 1, types 2 and 3), the O_3- and OH-derived fragmentation patterns were not indicative of known accretion chemistry (e.g., formal addition or condensation), and in most instances a reasonable OH-derived (^{13}C-mass-shifted) monomeric building block either could not be identified or failed to account for the observed OH-derived daughter ions (*SI Appendix*, Table S3). The structures of these dimers were not investigated further.

Based on comparison with MS/MS data for commercial standards and/or previously published MS/MS spectra, the O_3-derived monomeric building blocks of the dimer esters are attributed to one of three dicarboxylic acids, each a well-characterized pinene oxidation product that has been implicated in dimer formation: *cis*-pinic acid ($C_9H_{14}O_4$; Fig. 3*A*), *cis*-norpinic acid ($C_8H_{12}O_4$; Fig. 3*B*), and diaterpenylic acid ($C_8H_{14}O_5$; Fig. 3*C*) (7, 39) (*SI Appendix*, S6.1). Conversely, the OH-derived monomeric units are characterized by the ionic $[M-H]^-$ formulas $[C_{10}H_{15,17}O_{2-7}]^-$, indicative of OH addition to β-pinene ($C_{10}H_{16}$) followed by varying degrees of O_2 incorporation, isomerization, and bimolecular radical chemistry (36, 37). The daughter ions of the dicarboxylic acid and $[C_{10}H_{15,17}O_{2-7}]^-$ monomeric units are rationalized by successive neutral losses of H_2O (18 Da), CO_2 (44 Da), CH_2O (30 Da), and C_3H_6O (58 Da), all of which are established CID pathways (40–42). Notably, the loss of $^{13}CH_2O$ (31 Da) from the $[C_{10}H_{15,17}O_{2-7}]^-$ fragment is observed in the MS/MS spectrum of almost every ^{13}C-labeled dimer ester (Fig. 3 and *SI Appendix*, Table S3), consistent with the expected major addition of OH to β-pinene (83% of total OH reactivity) at the terminal vinylic carbon (36). Moreover, while the three dicarboxylic acids implicated as O_3-derived precursors were identified as major products in β-pinene SOA formed from ozonolysis (*SI Appendix*, S6.1), SOA products corresponding to the OH-derived monomeric building blocks (i.e., $C_{10}H_{16}O_{3,7}$ and $C_{10}H_{18}O_{2,4,6}$) were not detected.

To further constrain the structures of the dimer esters, β-pinene SOA filters were extracted into D_2O and analyzed via UPLC/(–)ESI-Q-TOF-MS using D_2O as the polar eluent (*SI Appendix*,

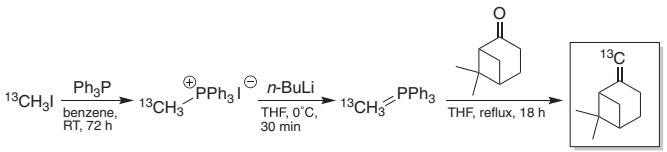

Scheme 1. Synthesis of ^{13}C-β-pinene via Wittig olefination (*SI Appendix*, S5).

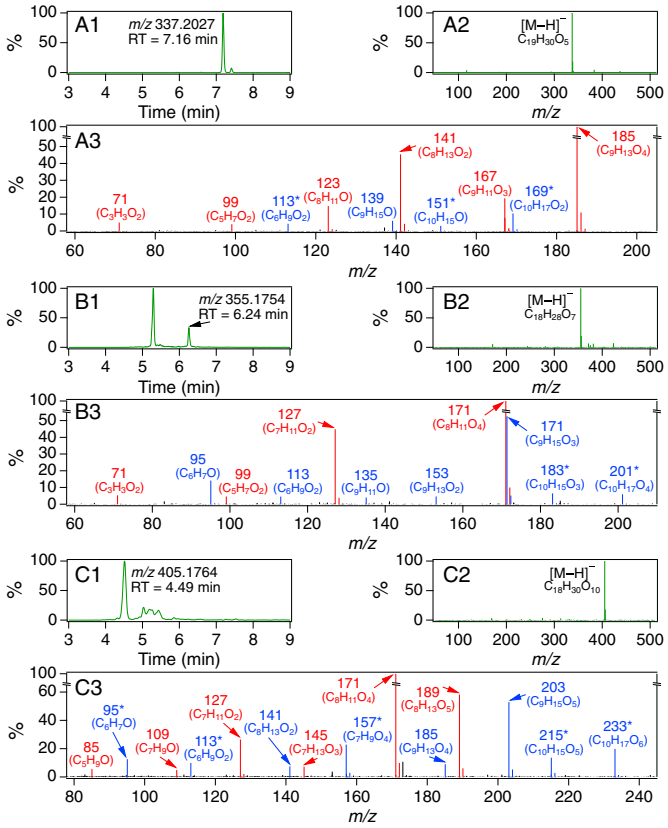

Fig. 3. Representative (*1*) extracted ion chromatograms, (*2*) MS spectra, and (*3*) MS/MS spectra, measured by UPLC/(–)ESI-Q-TOF-MS, of dimer esters in SOA produced from the O_3-initiated oxidation of β-pinene (Table 1, type 1) presumed to form from (*A*) *cis*-pinic acid ($C_9H_{14}O_4$), (*B*) *cis*-norpinic acid ($C_8H_{12}O_4$), and (*C*) diaterpenylic acid ($C_8H_{14}O_5$). MS/MS peaks are colored to denote O_3-derived (red) and OH-derived (blue) fragment ions. Numbers in MS/MS spectra correspond to nominal *m/z* values of $[M–H]^-$ fragment ions; ionic formulas $[C_xH_yO_z]^-$ are given in parentheses. *Indicates peaks that underwent a one-unit mass shift on formation from ^{13}C-β-pinene.

S3.6). This approach facilitated deuterium substitution (H → D) of labile hydrogens (e.g., –OH, –OOH, and –COOH) in the SOA constituents while preserving chromatographic separation, enabling quantification of the number of exchangeable hydrogens in the identified dimer molecules based on systematic shifts in *m/z* due to H/D exchange (Table 1 and *SI Appendix*, Fig. S4). Additionally, using our recently developed iodometry-assisted LC/ESI-MS assay for the molecular-level identification of organic peroxides (30), it was established that the 23 identified dimers do not contain hydroperoxide (ROOH) or organic peroxide (ROOR) functionalities (*SI Appendix*, S3.7). On the basis of these supporting experiments, the accurate mass (MS) and fragmentation (MS/MS) data, the inferred dicarboxylic acid structures of the O_3-derived monomers, and the prevailing mechanism of β-pinene photooxidation (36, 37), tentative molecular structures and fragmentation pathways for the dimer esters are proposed in *SI Appendix*, Table S4 and Fig. S10, respectively (*SI Appendix*, S6.1).

Mechanisms of Dimer Formation. To assess the relative contributions of gas- vs. particle-phase chemistry to the formation of dimers derived from concerted O_3 and OH oxidation, the temporal evolution of individual products in β-pinene SOA formed from ozonolysis in the CTEC was examined. Shown in Fig. 4 *A*–*C* are the particle-phase growth profiles of the eight dimer esters (Table 1, type 1) overlaid upon those corresponding to the dicarboxylic acid monomers (*cis*-pinic acid, *cis*-norpinic acid, and diaterpenylic acid) that were implicated as precursors based on detailed MS/MS analysis. The strong correlation between the particle-phase abundances of the dimer esters and their presumed dicarboxylic acid building blocks points toward a mechanism of heterogeneous formation, wherein the semivolatile dicarboxylic acids undergo traditional equilibrium gas-particle partitioning (43) with subsequent reactive uptake of the gas-phase, OH-derived monomers/intermediates on collision with particle surfaces to form ELVOC dimers. A heterogeneous rather than purely particle-phase mechanism is supported by the absence of monomers corresponding to the OH-derived dimer ester precursors in SOA generated from β-pinene ozonolysis. Such heterogeneous/multiphase accretion processes, leading to the production of high-molecular-weight oligomeric products, have recently been shown to contribute significantly to SOA formation in both biogenic and anthropogenic systems (44, 45).

The growth dynamics of the dimer esters can be contrasted against those shown in Fig. 4*D* for another group of dimers (Table 1, type 2) also produced from coupled O_3 and OH oxidation. These dimers achieve essentially their maximum, steady-state SOA concentrations after ∼2 h of reaction, whereas within the same time frame the dimer esters reach only ∼60% of their highest measured particle-phase abundances. Prompt formation and rapid particle-phase growth of the dimers in Fig. 4*D*, at rates faster than those observed for the monomers (Fig. 4 *A*–*C*), indicate production via gas-phase reactions of first-generation oxidation products/intermediates followed by irreversible condensation of the resulting ELVOC dimers onto existing aerosol surfaces. As the formation of these dimers was not significantly inhibited by introduction of SCI scavengers (*SI Appendix*, Fig. S1), they likely originate from closed-shell/radical species unique to the hot Criegee VHP channel. Although the identified dimers were found not to contain (hydro)peroxide functionalities (*SI Appendix*, S3.7), production of the dimers in Fig. 4*D* may be explained by gas-phase RO_2 self/cross-reactions (23–26, 46) with subsequent particle-phase decomposition leading to nonperoxide species (13, 20). Fast formation of particle-bound dimers during monoterpene ozonolysis has been reported in several recent studies (10–13, 20) and, together with their estimated low volatility, has been advanced to explain nucleation and initial growth of monoterpene SOA, both in laboratory studies without seed aerosol and in regions, such as the boreal forest, dominated by biogenic emissions (47).

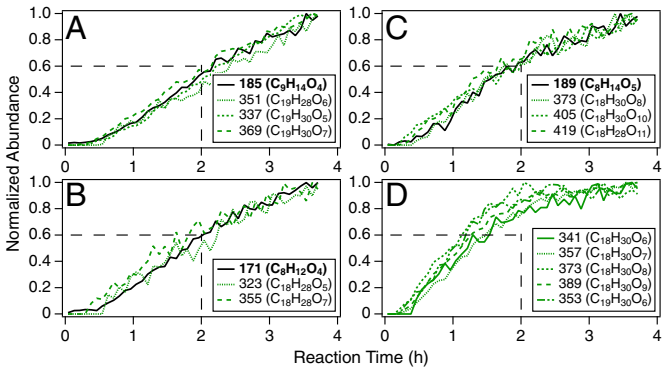

Fig. 4. Temporal profiles of molecular products in SOA produced from the O_3-initiated oxidation of β-pinene in the CTEC (*SI Appendix*, Table S1, Exp. 1), measured by PILS + UPLC/(–)ESI-Q-TOF-MS. Profiles are plotted as the particle-phase abundance of each species, normalized to the highest abundance observed over 4 h of reaction, as a function of reaction time. Discrete data points (5-min resolution) are presented as lines to aid the eye. Numbers correspond to nominal *m/z* values of $[M–H]^-$ ions; molecular formulas are given in parentheses. (*A*–*C*) Profiles of dimer esters (Table 1, type 1) and dicarboxylic acids implicated as precursors based on MS/MS analysis: (*A*) *cis*-pinic acid (*m/z* 185; $C_9H_{14}O_4$; RT 4.33), (*B*) *cis*-norpinic acid (*m/z* 171; $C_8H_{12}O_4$; RT 4.06), and (*C*) diaterpenylic acid (*m/z* 189; $C_8H_{14}O_5$; RT 3.32). (*D*) Profiles of dimers (Table 1, type 2) characterized by almost immediate formation and rapid particle-phase growth. Dashed lines (2 h, 0.6 abundance) are drawn to aid in comparison between growth profiles in *A*–*C* and *D*.

As a means of evaluating the hypothesized mechanism of heterogeneous dimer ester formation, β-pinene photooxidation experiments were conducted in the CTEC in the presence of seed aerosol composed of varying mass ratios of ammonium sulfate [$(NH_4)_2SO_4$] and *cis*-pinic acid, the only commercially available pinene-derived dicarboxylic acid (*Materials and Methods*). Consistent with the idea that introducing the O_3-derived dimer ester precursors into the particle phase of the OH system should promote otherwise negligible heterogeneous dimerization, the presence of *cis*-pinic acid in the $(NH_4)_2SO_4$ seed resulted in significant formation, proportional to the mass ratio of *cis*-pinic acid to $(NH_4)_2SO_4$, of the major dimer ester at *m/z* 337 ($C_{19}H_{30}O_5$) (Fig. 5), corroborating the indirect MS/MS (Fig. 3*A*) and kinetic (Fig. 4*A*) evidence for production from particle-bound *cis*-pinic acid. That the dimer ester at *m/z* 337 was not observed in OH-derived β-pinene SOA, with pure $(NH_4)_2SO_4$ seed, collected on a Teflon filter coated with *cis*-pinic acid excludes the possibility of dimer formation via accretion of condensed monomers, either on the filter or during the extraction process (*SI Appendix*, Fig. S11). Although the details of the mechanism forming the ester linkage remain unclear, the observed increase in dimer ester abundance at elevated RH (*SI Appendix*, Fig. S1) argues against production via conventional esterification (i.e., carboxylic acid + alcohol). Overall, these findings conclusively demonstrate the role of heterogeneous accretion chemistry in monoterpene SOA formation (*SI Appendix*, S6.2).

Surprisingly, these experiments also imply that a simple mass limitation of monomeric precursors in the particle phase is responsible for the absence of dimer esters in β-pinene SOA formed from OH-initiated oxidation. However, increased mass fractions of *cis*-pinic acid in SOA from α-pinene ozonolysis, relative to photooxidation, have been observed in a number of previous studies and have been invoked as a possible explanation for the lack of dimers containing *cis*-pinic acid in α-pinene photooxidation experiments (7, 12, 48). Indeed, in this study *cis*-pinic acid was found to comprise a much higher fraction of β-pinene SOA mass when formed from O_3- (13.4 ± 3.1%) rather than OH-initiated (1.7 ± 0.4%) oxidation (see *m/z* 185; RT 4.33 in Fig. 1), while significant but less pronounced disparities in SOA mass fraction between ozonolysis and photooxidation experiments were observed for *cis*-norpinic acid (1.4 ± 0.3% vs. 0.24 ± 0.06%) and diaterpenylic acid (0.71 ± 0.16% vs. 0.28 ± 0.06%) (*SI Appendix*, S7).

Although also suggested to arise from heterogeneous reaction of particle-phase *cis*-pinic acid (Fig. 4*A*), neither the prominent dimer ester at *m/z* 369 ($C_{19}H_{30}O_7$) nor the minor dimer ester at *m/z* 351 ($C_{19}H_{28}O_6$) was detected in the photooxidation experiments carried out with *cis*-pinic acid and $(NH_4)_2SO_4$ seed. One plausible explanation for the absence of these dimers is that the high HO_2 concentrations (~10^{10} molecules cm^{-3}) inherent in the use of H_2O_2 as an OH precursor (*SI Appendix*, S1.1) produce an oxidative environment in which the OH-derived RO_2 isomerization and bimolecular reaction channels are vastly different from those operative in the comparatively low-HO_2 (~10^7 molecules cm^{-3}) ozonolysis system (*SI Appendix*, S4) that form the $[C_{10}H_{17}O_4]^-$ and $[C_{10}H_{15}O_3]^-$ building blocks of the dimer esters at *m/z* 369 and 351, respectively (*SI Appendix*, Table S3). That $RO_2 + HO_2$ rate coefficients are typically order(s) of magnitude larger than those for $RO_2 + RO_2$ reactions (49) further compounds the disparity between these two RO_2 regimes. Conversely, for the dimer ester at *m/z* 337, although the structure of the $[C_{10}H_{17}O_2]^-$ building block is tentative (*SI Appendix*, Fig. S10 and Table S3), theoretical studies indicate that this monomer is able to form under both ozonolysis and photooxidation conditions from the $C_{10}H_{17}O_3$ hydroxy peroxy radical, produced from OH and subsequent O_2 addition to β-pinene, either via traditional $RO_2 + RO_2$ chemistry or through an OH-recycling pathway in the reaction with HO_2 (36, 50).

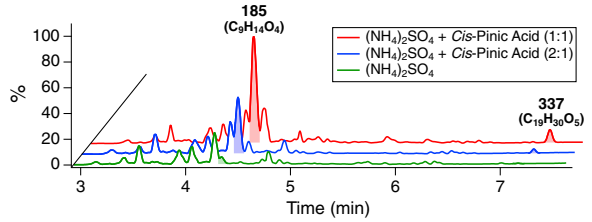

Fig. 5. UPLC/(−)ESI-Q-TOF-MS BPI chromatograms of SOA produced from the OH-initiated oxidation of β-pinene after ~4 h of reaction in the CTEC (*SI Appendix*, Table S1, Exps. 2–4). Experiments were conducted in the presence of seed aerosol at similar mass loadings but different mass ratios (see legend) of $(NH_4)_2SO_4$ and *cis*-pinic acid ($C_9H_{14}O_4$). Numbers correspond to nominal *m/z* values of $[M-H]^-$ ions; molecular formulas are given in parentheses. Shaded peaks correspond to *cis*-pinic acid and the dimer ester at *m/z* 337 ($C_{19}H_{30}O_5$). Chromatograms for each experiment are normalized to the area of the peak at RT 3.93 (*m/z* 171; $C_8H_{12}O_4$).

Atmospheric Implications. The production of dimeric compounds (Table 1, types 1–3) through concerted O_3 and OH oxidation accounts for an appreciable, heretofore-unidentified fraction (5.9–25.4%) of the total mass of β-pinene SOA derived from ozonolysis under the conditions employed in this work (Table 1). Although specifically revealed in SOA formation from β-pinene, this reactive pathway represents a potentially significant source of high-molecular-weight ELVOC to the atmosphere that is expected to be broadly applicable to other monoterpenes (*SI Appendix*, S8). Through detailed molecular composition and kinetic analysis, certain dimers are definitively shown to form through heterogeneous processes, while indirect evidence for dimer production via gas-phase routes is also presented. The importance of both gas- and particle-phase reactions to the formation of dimeric SOA constituents demonstrated in the current work underscores the complexity of atmospheric accretion chemistry, as well as the significant shortcomings in scientific understanding that preclude adequate characterization of its impact.

The O_3 + OH reactivity elucidated in β-pinene SOA also highlights the importance of understanding and accounting for the likely role of oxidative synergism in ambient aerosol formation, where SOA precursors are susceptible to concurrent oxidation by O_3 and OH. At present, SOA formation in atmospheric models is treated as an additive combination of products originating from the isolated oxidation of individual precursors (e.g., α-pinene + O_3 or isoprene + OH). In establishing that oxidants can act in concert to produce extremely low-volatility dimers in nontrivial yields, however, this study suggests that the tendency of current atmospheric models to systematically underpredict ambient SOA mass (1) may be due in part to the fact that discrete SOA formation mechanisms, parameterized by laboratory experiments that typically feature only one oxidant and a single SOA precursor, do not accurately reflect the intricate oxidation pathways at play in the real atmosphere. Revising the chemistry of monoterpene SOA formation in regional air quality and global climate models to account for the role of synergistic oxidation could help to resolve the discrepancy between model predictions and ambient measurements. However, parameterization of this reactivity requires additional work.

Materials and Methods

β-Pinene ozonolysis and photooxidation experiments were carried out in the CTEC and CPOT at ambient temperature (~295 K) and atmospheric pressure (~1 atm), under dry conditions (<10% RH), in the presence of $(NH_4)_2SO_4$ seed aerosol, and at mixing ratios of NO_x typical of the pristine atmosphere (<0.5 ppb). CTEC experiments were designed to mimic oxidation in ambient air, while those in the CPOT were used to elucidate dimer structures and formation mechanisms. For CTEC experiments with ~4-h duration, β-pinene (~120 ppb) was oxidized by O_3 (~200 ppb) in the absence of an OH scavenger or OH (~2×10^6 molecules cm^{-3}). Select photooxidation experiments were performed with mixed $(NH_4)_2SO_4$ and *cis*-pinic acid seed. For steady-state CPOT experiments, oxidation of β-pinene (~150 ppb) by O_3 (~1 ppm) proceeded in the presence and absence of scavengers for both OH (cyclohexane) and SCIs (water vapor and formic acid). In certain CPOT experiments, ^{13}C-β-pinene, synthesized from ^{13}C-iodomethane and nopinone via Wittig olefination

(Scheme 1), was used. Experimental conditions are reported in *SI Appendix*, Table S1 and described in detail in *SI Appendix*, S1.

β-Pinene mixing ratios were quantified with a gas chromatograph equipped with a flame ionization detector (GC/FID) (*SI Appendix*, S2). Aerosol size distributions and number concentrations were measured with a custom-built scanning mobility particle sizer (SMPS) (*SI Appendix*, S3.1). "Bulk" aerosol chemical composition was quantified with an Aerodyne high-resolution time-of-flight aerosol mass spectrometer (HR-ToF-AMS) (*SI Appendix*, S3.2). The molecular composition of β-pinene SOA collected by PILS during CTEC experiments (*SI Appendix*, S3.3) and on Teflon filters during steady-state CPOT and select CTEC experiments (*SI Appendix*, S3.4) was characterized off-line by UPLC/(−)ESI-Q-TOF-MS (*SI Appendix*, S3.5). Certain SOA filter samples were analyzed using D_2O in place of H_2O as the extraction solvent/polar eluent (*SI Appendix*, S3.6). Iodometry was coupled to UPLC/(−)ESI-Q-TOF-MS (30) to identify organic peroxides at the molecular level in β-pinene SOA (*SI Appendix*, S3.7). The Master Chemical Mechanism version 3.2 (MCMv3.2) (51) was used to simulate the concentration profiles of OH, HO_2, and RO_2 during β-pinene ozonolysis in the CTEC, as well as the fractions of β-pinene that react with O_3 vs. OH (*SI Appendix*, S4). Mass fractions of individual organic compounds in β-pinene SOA, along with associated uncertainties, were calculated as described in *SI Appendix*, S7.

ACKNOWLEDGMENTS. We thank Xuan Zhang, John Crounse, and Paul Wennberg for useful discussions. UPLC/(−)ESI-Q-TOF-MS was performed in the Caltech Environmental Analysis Center. This work was supported by National Science Foundation Grants AGS-1523500 and CHE-1508526. R.Z. acknowledges support from a Natural Science and Engineering Research Council of Canada Postdoctoral Fellowship. J.C.H. acknowledges support from the Camille and Henry Dreyfus Postdoctoral Program in Environmental Chemistry.

1. Hallquist M, et al. (2009) The formation, properties and impact of secondary organic aerosol: Current and emerging issues. *Atmos Chem Phys* 9:5155–5236.
2. Kanakidou M, et al. (2005) Organic aerosol and global climate modelling: A review. *Atmos Chem Phys* 5:1053–1123.
3. Jimenez JL, et al. (2009) Evolution of organic aerosols in the atmosphere. *Science* 326:1525–1529.
4. Intergovernmental Panel on Climate Change (2013) *Climate Change 2013: The Physical Science Basis*, eds Stocker TF, et al. (Cambridge Univ Press, Cambridge, UK).
5. Pope CA, 3rd, Ezzati M, Dockery DW (2009) Fine-particulate air pollution and life expectancy in the United States. *N Engl J Med* 360:376–386.
6. Cohen AJ, et al. (2017) Estimates and 25-year trends of the global burden of disease attributable to ambient air pollution: An analysis of data from the Global Burden of Diseases Study 2015. *Lancet* 389:1907–1918.
7. Yasmeen F, et al. (2010) Terpenylic acid and related compounds: Precursors for dimers in secondary organic aerosol from the ozonolysis of α- and β-pinene. *Atmos Chem Phys* 10:9383–9392.
8. Kourtchev I, et al. (2016) Enhanced volatile organic compounds emissions and organic aerosol mass increase the oligomer content of atmospheric aerosols. *Sci Rep* 6:35038.
9. Mohr C, et al. (2017) Ambient observations of dimers from terpene oxidation in the gas phase: Implications for new particle formation and growth. *Geophys Res Lett* 44:2958–2966.
10. Kristensen K, et al. (2013) Formation and occurrence of dimer esters of pinene oxidation products in atmospheric aerosols. *Atmos Chem Phys* 13:3763–3776.
11. Kristensen K, et al. (2016) High-molecular weight dimer esters are major products in aerosols from α-pinene ozonolysis and the boreal forest. *Environ Sci Technol Lett* 3:280–285.
12. Kristensen K, et al. (2014) Dimers in α-pinene secondary organic aerosol: Effect of hydroxyl radical, ozone, relative humidity and aerosol acidity. *Atmos Chem Phys* 14:4201–4218.
13. Zhang X, et al. (2015) Formation and evolution of molecular products in α-pinene secondary organic aerosol. *Proc Natl Acad Sci USA* 112:14168–14173.
14. Zhao Y, Wingen LM, Perraud V, Greaves J, Finlayson-Pitts BJ (2015) Role of the reaction of stabilized Criegee intermediates with peroxy radicals in particle formation and growth in air. *Phys Chem Chem Phys* 17:12500–12514.
15. Witkowski B, Gierczak T (2014) Early stage composition of SOA produced by α-pinene/ozone reaction: α-Acyloxyhydroperoxy aldehydes and acidic dimers. *Atmos Environ* 95:59–70.
16. Hall WA, 4th, Johnston MV (2012) Oligomer formation pathways in secondary organic aerosol from MS and MS/MS measurements with high mass accuracy and resolving power. *J Am Soc Mass Spectrom* 23:1097–1108.
17. Tolocka MP, et al. (2004) Formation of oligomers in secondary organic aerosol. *Environ Sci Technol* 38:1428–1434.
18. Reinhardt A, et al. (2007) Ultrahigh mass resolution and accurate mass measurements as a tool to characterize oligomers in secondary organic aerosols. *Anal Chem* 79:4074–4082.
19. Gao Y, Hall WA, Johnston MV (2010) Molecular composition of monoterpene secondary organic aerosol at low mass loading. *Environ Sci Technol* 44:7897–7902.
20. Müller L, Reinnig MC, Warnke J, Hoffmann T (2008) Unambiguous identification of esters as oligomers in secondary organic aerosol formed from cyclohexene and cyclohexene/α-pinene ozonolysis. *Atmos Chem Phys* 8:1423–1433.
21. Müller L, Reinnig MC, Hayen H, Hoffmann T (2009) Characterization of oligomeric compounds in secondary organic aerosol using liquid chromatography coupled to electrospray ionization Fourier transform ion cyclotron resonance mass spectrometry. *Rapid Commun Mass Spectrom* 23:971–979.
22. Docherty KS, Wu W, Lim YB, Ziemann PJ (2005) Contributions of organic peroxides to secondary aerosol formed from reactions of monoterpenes with O3. *Environ Sci Technol* 39:4049–4059.
23. Ehn M, et al. (2014) A large source of low-volatility secondary organic aerosol. *Nature* 506:476–479.
24. Jokinen T, et al. (2015) Production of extremely low volatile organic compounds from biogenic emissions: Measured yields and atmospheric implications. *Proc Natl Acad Sci USA* 112:7123–7128.
25. Kirkby J, et al. (2016) Ion-induced nucleation of pure biogenic particles. *Nature* 533:521–526.
26. Tröstl J, et al. (2016) The role of low-volatility organic compounds in initial particle growth in the atmosphere. *Nature* 533:527–531.
27. Kidd C, Perraud V, Wingen LM, Finlayson-Pitts BJ (2014) Integrating phase and composition of secondary organic aerosol from the ozonolysis of α-pinene. *Proc Natl Acad Sci USA* 111:7552–7557.
28. Guenther AB, et al. (2012) The Model of Emissions of Gases and Aerosols from Nature version 2.1 (MEGAN2.1): An extended and updated framework for modeling biogenic emissions. *Geosci Model Dev* 5:1471–1492.
29. Zhang X, et al. (2016) Time-resolved molecular characterization of organic aerosols by PILS + UPLC/ESI-Q-TOFMS. *Atmos Environ* 130:180–189.
30. Zhao R, Kenseth CM, Huang Y, Dalleska NF, Seinfeld JH (2018) Iodometry-assisted liquid chromatography electrospray ionization mass spectrometry for analysis of organic peroxides: An application to atmospheric secondary organic aerosol. *Environ Sci Technol* 52:2108–2117.
31. Donahue NM, Drozd GT, Epstein SA, Presto AA, Kroll JH (2011) Adventures in ozoneland: Down the rabbit-hole. *Phys Chem Chem Phys* 13:10848–10857.
32. Sipilä M, et al. (2014) Reactivity of stabilized Criegee intermediates (sCIs) from isoprene and monoterpene ozonolysis toward SO_2 and organic acids. *Atmos Chem Phys* 14:12143–12153.
33. Drozd GT, Kurtén T, Donahue NM, Lester MI (2017) Unimolecular decay of the dimethyl-substituted Criegee intermediate in alkene ozonolysis: Decay time scales and the importance of tunneling. *J Phys Chem A* 121:6036–6045.
34. Nguyen TL, Peeters J, Vereecken L (2009) Theoretical study of the gas-phase ozonolysis of β-pinene ($C_{10}H_{16}$). *Phys Chem Chem Phys* 11:5643–5656.
35. Donahue NM, Epstein SA, Pandis SN, Robinson AL (2011) A two-dimensional volatility basis set: 1. Organic-aerosol mixing thermodynamics. *Atmos Chem Phys* 11:3303–3318.
36. Vereecken L, Peeters J (2012) A theoretical study of the OH-initiated gas-phase oxidation mechanism of β-pinene ($C_{10}H_{16}$): First generation products. *Phys Chem Chem Phys* 14:3802–3815.
37. Kaminski M, et al. (2017) Investigation of the β-pinene photooxidation by OH in the atmosphere simulation chamber SAPHIR. *Atmos Chem Phys* 17:6631–6650.
38. Reinnig MC, Müller L, Warnke J, Hoffmann T (2008) Characterization of selected organic compound classes in secondary organic aerosol from biogenic VOCs by HPLC/MS^n. *Anal Bioanal Chem* 391:171–182.
39. Yasmeen F, et al. (2011) Characterisation of tracers for aging in α-pinene secondary organic aerosol using liquid chromatography/negative ion electrospray ionisation mass spectrometry. *Environ Chem* 9:236–246.
40. Grossert JS, Fancy PD, White RL (2005) Fragmentation pathways of negative ions produced by electrospray ionization of acyclic dicarboxylic acids and derivatives. *Can J Chem* 83:1878–1890.
41. Demarque DP, Crotti AE, Vessecchi R, Lopes JL, Lopes NP (2016) Fragmentation reactions using electrospray ionization mass spectrometry: An important tool for the structural elucidation and characterization of synthetic and natural products. *Nat Prod Rep* 33:432–455.
42. Kingston DG, Hobrock BW, Bursey MM, Bursey JT (1975) Intramolecular hydrogen transfer in mass spectra. III. Rearrangements involving the loss of small neutral molecules. *Chem Rev* 75:693–730.
43. Pankow JF (1994) An absorption model of gas-particle partitioning of organic compounds in the atmosphere. *Atmos Environ* 28:185–188.
44. Shiraiwa M, et al. (2013) Size distribution dynamics reveal particle-phase chemistry in organic aerosol formation. *Proc Natl Acad Sci USA* 110:11746–11750.
45. Barsanti KC, Kroll JH, Thornton JA (2017) Formation of low-volatility organic compounds in the atmosphere: Recent advancements and insights. *J Phys Chem Lett* 8:1503–1511.
46. Berndt T, et al. (2018) Accretion product formation from self- and cross-reactions of RO_2 radicals in the atmosphere. *Angew Chem Int Ed Engl* 57:3820–3824.
47. Glasius M, Goldstein AH (2016) Recent discoveries and future challenges in atmospheric organic chemistry. *Environ Sci Technol* 50:2754–2764.
48. Kourtchev I, et al. (2015) Molecular composition of fresh and aged secondary organic aerosol from a mixture of biogenic volatile compounds: A high-resolution mass spectrometry study. *Atmos Chem Phys* 15:5683–5695.
49. Orlando JJ, Tyndall GS (2012) Laboratory studies of organic peroxy radical chemistry: An overview with emphasis on recent issues of atmospheric significance. *Chem Soc Rev* 41:6294–6317.
50. Eddingsaas NC, Loza CL, Yee LD, Seinfeld JH, Wennberg PO (2012) α-pinene photooxidation under controlled chemical conditions–Gas-phase composition in low- and high-NO_x environments. *Atmos Chem Phys* 12:6489–6504.
51. Saunders SM, Jenkin ME, Derwent RG, Pilling MJ (2003) Protocol for the development of the Master Chemical Mechanism MCM v3 (Part A): Tropospheric degradation of non-aromatic volatile organic compounds. *Atmos Chem Phys* 3:161–180.